Downloaded from orbit.dtu.dk on: Apr 25, 2024

DTU Library

Osmotically driven flows in microfluidic channels and their relation to sugar transport in plants

Jensen, Kåre Hartvig

Publication date:
2011

Document Version
Publisher's PDF, also known as Version of record

Link back to DTU Orbit

Citation (APA):
Jensen, K. H. (2011). *Osmotically driven flows in microfluidic channels and their relation to sugar transport in plants*. Technical University of Denmark.

General rights
Copyright and moral rights for the publications made accessible in the public portal are retained by the authors and/or other copyright owners and it is a condition of accessing publications that users recognise and abide by the legal requirements associated with these rights.

- Users may download and print one copy of any publication from the public portal for the purpose of private study or research.
- You may not further distribute the material or use it for any profit-making activity or commercial gain
- You may freely distribute the URL identifying the publication in the public portal

If you believe that this document breaches copyright please contact us providing details, and we will remove access to the work immediately and investigate your claim.

DTU Nanotech
Department of Micro- and Nanotechnology

DTU

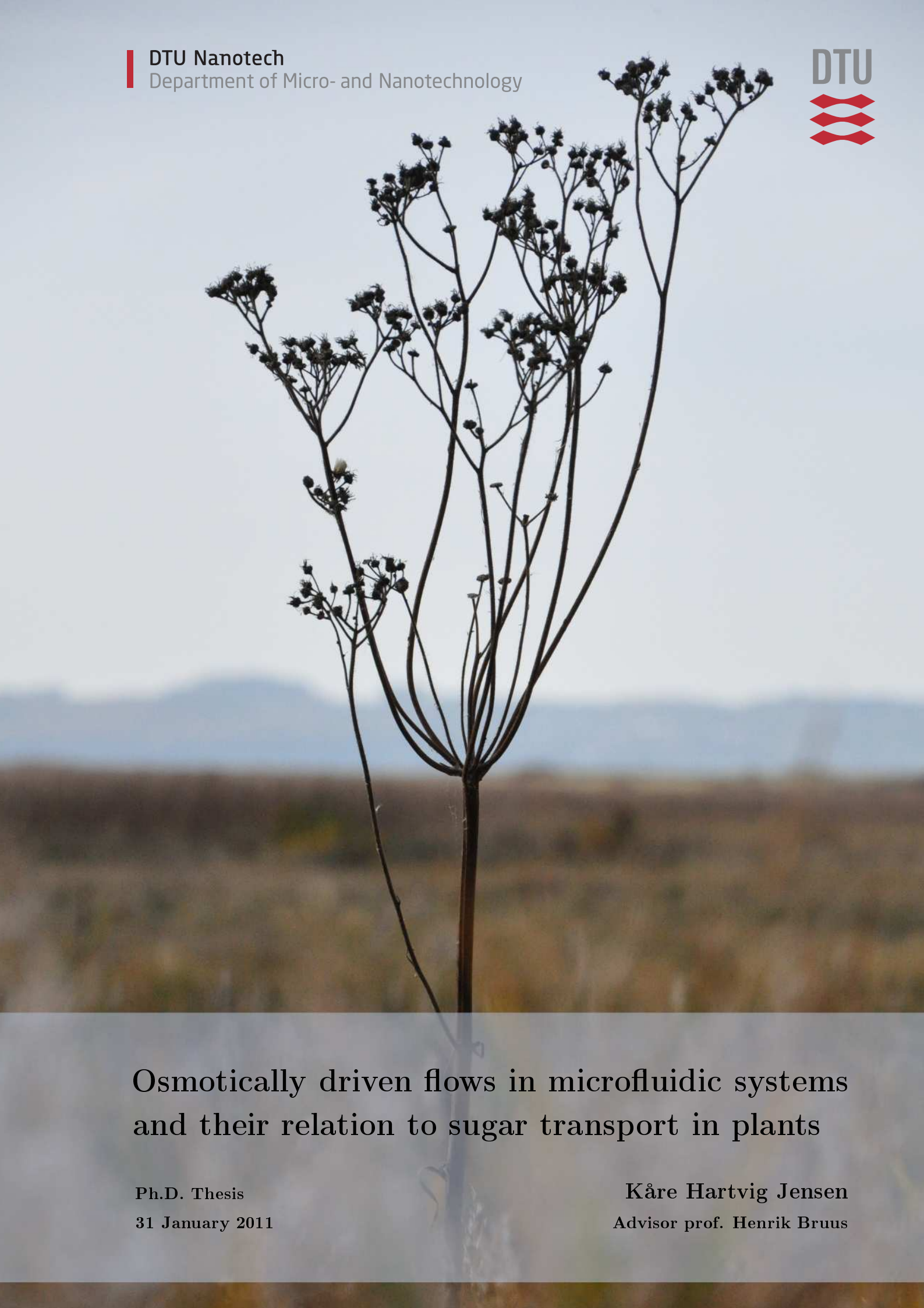

Osmotically driven flows in microfluidic systems and their relation to sugar transport in plants

Ph.D. Thesis

31 January 2011

Kåre Hartvig Jensen

Advisor prof. Henrik Bruus

Osmotically driven flows in microfluidic systems and their relation to sugar transport in plants

Copyright © Kåre Hartvig Jensen 2011
Cover photo: Kåre Hartvig Jensen and Jon Sullivan (www.pdphoto.org)
Typeset using LaTeX, PGF and TikZ

www.nanotech.dtu.dk/microfluidics
www.hartvig.de

Til min mormor,
der holdt så meget af blomster.

Abstract

The results in this thesis are part of the work carried out during the author's doctoral studies. The PhD project has been funded partly by the Danish National Research Foundation (grant no. 74) through the Center for Fluid Dynamics, and partly by the Department of Micro- and Nanotechnology at the Technical University of Denmark. The overall title for the PhD project is *Osmotically driven flow in microfluidic systems and their relation to sugar transport in plants*. The work has consisted of several smaller projects focusing on theory, and to some extend experiments, with osmotically driven flows as the predominant theme. This thesis contains selected parts of the results obtained. Other parts of the work have been published in peer-reviewed journals or presented at conferences, see Sec. 1.2.

The study of osmotically driven flows is motivated by phenomena observed in plants which have highly efficient vascular system that facilitates the transport of fluid and nutrients between distal parts of the organism. In this PhD project the author and co-workers[1] have studied one of these vascular system, the phloem, which is responsible for the distribution of sugar produced by photosynthesis and signaling molecules secreted in response to external or internal stimuli between distal parts of the plant. The phloem can be broadly comparable to a combination of the blood circulatory- and nervous systems found in animals, and it has long been debated which mechanism drives the translocation process. Since Ernst Münch's work in the 1930s it has been known that osmosis plays a very important role, but it is still largely unknown whether this mechanism can account for the rates of translocation observed in plants.

To get a fundamental understanding of osmotically driven flows, we have conducted a thorough theoretical study of these. This, coupled with a series of simple experiments, has allowed us to gain a new, quantitative, understanding of the transport process that occur in plants. The experiments were carried out in a microfluidic system. To mimic the situation in plants where the osmotic interaction occurs across cell membranes, we used a system where two channels (2.7 cm long, 200 μm wide and $50 - 200$ μm deep) were separated by a cellulose membrane. One channel was filled half way with an aqueous sugar solution, while the other channel was completely filled with water. Due to osmosis water moves from the water filled channel into the sugar-filled region and thereby pushes the sugar forwards. We have shown that the experiments, within a reasonable degree of accuracy, follow the predictions of the Münch theory.

With the understanding obtained from the above mentioned experiments, we have studied the main topic of this thesis: Theoretical aspects of osmotically driven flows. Although the basic equations have been known for at least half a century, there is a surprisingly poor understanding of the correlation between, say, a tree's height and the speed at which sugar is moving in phloem due to the osmotic flow process. To answer

[1] See the list of publications, Sec. 1.2, and the introduction to each chapter.

this and related questions, we have studied fundamental properties of osmotically driven flows, and have developed a simple model which we believe provides a reasonably accurate quantitative description of the transport process in the phloem. The model provides a basic understanding of the flow as a function of the parameters in the problem and is able to reproduce experimental data from *in vivo* measurements made on plants.

An interesting prediction of the model is that the osmotically driven Münch flow mechanism has a maximum in translocation velocity for a special value of the radius. The existence of such a maximum is quite easy to understand: the osmotic flow takes place across the cell surface and is therefore more effective in terms of the axial velocity for thinner tubes where the surface-to-volume ratio is larger. Very thin tubes, on the other hand, offer high viscous resistance to the flow, and thus there is an optimum radius where the osmotic pump is effective and the resistance not too large. We have derived an analytical expression for this radius which takes the form of an allometric scaling law relating the optimum radius of the phloem cells a_c to the length of the stem and the size of the leaf l_1. We thus find that at the radius $a_c^3 \propto l_1 l_2$, the osmotic flow mechanism yields the fastest possible translocation velocity. We have compared this prediction to plant data and have found good agreement between observations and our result for a group of plants varying several orders of magnitude in size. This finding suggests that the physical constraints imposed by the optimality of the Münch flow mechanism has played a significant role in the evolution of the phloem vascular system of plants.

Resumé

Resultaterne i denne afhandling er udarbejdet i løbet af forfatterens ph.d.-studier. Ph.d.-projektet er dels financieret af et af Danmarks Grundforskningsfond støttet projekt, Center for Fluid Dynamik (bevilling no. 74), og dels af Institut for Mikro- og Nanoteknologi ved Danmarks Tekniske Universitet. Den overordnede titel for ph.d.-projektet er *Osmotisk drevne strømninger i mikrofluide systemer og deres relation til sukkertransport i planter*. Arbejdet har bestået af flere mindre projekter med fokus på teori, og i nogen grad eksperimenter, med osmotisk drevne strømninger som det gennemgående tema. I den foreliggende afhandling gennemgås dele af de i løbet af projektet opnåede resultater. Andre dele af arbejdet er blevet publiceret i fagfællebedømte tidskrifter eller præsenteret ved konferencer, se afsnit 1.2.

Studiet af osmotisk drevne strømninger er motiveret af fænomener observeret i planter, der har meget effektive karsystemer, som sørger for at transportere væske, signal- og næringsstoffer. I dette ph.d.-projekt har forfatteren og samarbejdspartnere[2] studeret det ene af disse karsystemer, det såkaldte phloem, som sørger for at bringe signalstoffer og det sukker, der produceres gennem bladenes fotosyntese ned til rødderne eller ud til nye skud. Phloemet kan i store træk sammenlignes med en kombination af dyrs blodkredsløbs- og nervesystem, og det har længe været debatteret, hvad der driver sådanne strømninger. Siden Ernst Münchs arbejde i 1930'erne har det været kendt, at osmotiske trykforskelle spiller en meget vigtig rolle, men man ved stadig ikke, hvor stor en del af strømningerne, som kan forklares på denne måde. For at få en grundlænggende forståelse af osmotisk drevne strømninger har vi foretaget et grundigt teoretisk studie af disse. Det har, sammen med en række simple eksperimenter, givet os en ny forståelse for transportprocessen i planter.

Eksperimenterne er foretaget på mikrofluide systemer. For at efterligne situationen i planter, hvor den osmotiske vekselvirkning sker over cellemenbraner, har vi brugt et system, hvor to kanaler (2.7 cm lange, 200 μm bredde og $50 - 200$ μm dybe) er adskilt af en cellulosemembran. Den ene kanal fyldes halvt med en vandig sukkeropløsning, halvt med vand og den anden helt op med vand. Pga. osmose trænger vand fra den ene kanal ind i den anden og skubber således sukkeropløsningen fremad. Vi har vist, at eksperimenterne med rimelig nøjagtighed følger Münch-teoriens forudsigelser.

Med disse eksperimenter i bagagen har vi studeret hovedemnet i denne afhandling: Teoretiske aspekter af osmotisk drevne strømninger. Selv om de grundlæggende ligninger har været kendt i mere end et halvt århundrede, er der en forbavsende ringe forståelse for sammenhængen mellem f.eks. et træs højde og den hastighed, hvormed sukkerstoffer bevæger sig i phloemet. For at besvare dette og relaterede spørgsmål har vi studeret de fundamentale egenskaber ved osmotisk drevne strømninger. Vi har således udviklet en sim-

[2]Se publikationslisten, afsnit 1.2, samt introduktionen til de enkelte kapitler.

pel model, som beskriver transportprocessen i phloemet. Modellen giver en grundlæggende forståelse af strømningerne som funktion af de relevante parametre, og den er i stand til at reproducere eksperimentelle data fra *in-vivo* målinger på planter.

Modellen kommer desuden med mange interessante forudsigelser. En af dem er, at den osmotisk drevne strømningsmekanisme har den højeste effektivitet for en speciel radius af phloem-karene. Grunden til dette et, at den osmotiske strømning foregår via karenes overflade, og at den derfor er mere effektiv, jo mindre radius i karene er. På den anden side bliver den viskøse strømningsmodstand meget stor for små kar, og altså er der en særlig karradius, hvor disse to effekter er i balance, og hastigheden er størst mulig. Vi har udledt et analytisk udtryk for denne radius, der relaterer cellernes radius a_c til bladest størrelse l_1 og stammens længde l_2: $a_c^3 \propto l_1 l_2$. Vi finder god overensstemmelse mellem denne forudsigelse og data fra en stor gruppe planter, der varierer i længde over flere størrelsesordener. Dette resultat tyder på, at de fysiske begrænsninger i Münch-mekanismen har spillet en væsentlig rolle i udviklingen af planters phloem-kar system.

Preface

This thesis is submitted in partial fulfillment of the requirements for obtaining the degree of Doctor of Philosophy (Ph.D.) at the Technical University of Denmark. The work has been carried out at the Department of Micro- and Nanotechnology (DTU Nanotech) at the Technical University of Denmark from August 2007 to January 2011, within the Theoretical Microfluidics group. In the period from June to September 2008, and during shorter visits in 2009 and 2010, I worked in the lab of prof. Noel Michele Holbrook at Harvard University in Cambridge MA, USA. The Ph.D. project was supervised by prof. Henrik Bruus (main supervisor, DTU Nanotech), prof. Tomas Bohr (co-supervisor, DTU Physics) and while abroad by prof. Noel Michele Holbrook.

I would like to thank Henrik Bruus and Tomas Bohr for their dedicated effort as supervisors and for allowing me great freedom to pursue my research. Henrik introduced me to the field of microfluidics and I have benefited greatly from our many inspiring discussions. Tomas initiated my interest in phloem transport during my master studies at the University of Copenhagen and has continued to do so during this Ph.D. project.

I would also like to thank Missy Holbrook, Maciej Zwieniecki and members of their research groups for welcoming me at Harvard University and for providing me with invaluable insight on biological aspects of phloem transport. Jinkee Lee in particular played a significant role in the microfluidic experiments conducted during my stay abroad.

Much of the work I did on the hydraulic resistance of phloem sieve plates depends on measurements made by Daniel Mullendore and Michael Knoblauch, with whom I have had many stimulating correspondences.

I thank the people at DTU Nanotech and the TMF group in particular for providing a very nice and inspiring work environment.

Finally, I thank my family and Signe for always being there for me.

Kåre Hartvig Jensen
Department of Micro- and Nanotechnology
Technical University of Denmark
31 January 2011

Table of Contents

List of Figures **x**

List of Tables **xii**

List of Symbols **xiv**

1 Introduction **1**
1.1 Outline of the thesis . . . 3
1.2 Publications during the PhD project . . . 4

2 Osmotically driven flows in living and artificial systems **7**
2.1 Osmotically driven flows in living systems . . . 7
2.2 Vascular transport in plants . . . 8
2.2.1 The xylem . . . 8
2.2.2 The phloem . . . 11
2.3 Translocation in the phloem . . . 12
2.3.1 Mechanisms driving the flow . . . 12
2.3.2 Interaction between phloem and xylem . . . 14
2.4 Osmotically driven flows in artificial systems . . . 16
2.5 Technological applications of osmotically driven flows . . . 17
2.6 Conclusion . . . 18

3 Fluid mechanics of osmotically driven flows **19**
3.1 Background . . . 19
3.2 Osmosis . . . 20
3.2.1 Non-equilibrium thermodynamics . . . 20
3.2.2 Osmotically driven flow across a semipermeable membrane . . . 21
3.3 Equations of motion for osmotically driven flows . . . 22
3.3.1 Boundary conditions imposed by osmosis . . . 22
3.3.2 Equations of motion governing fluid flow . . . 22
3.3.3 Equations of motion governing solute transport . . . 24
3.4 Solution of the coupled concentration-flow problem . . . 24
3.5 Non-dimensional formulation of the equations of motion . . . 24
3.5.1 Non-dimensional equations of motion for fluid motion . . . 25

3.5.2 Non-dimensional equation of motion for solute transport 26
3.5.3 Summary of the non-dimensional equations of motion 27
3.5.4 Analytical solution of the flow problem 28
3.5.5 The Münch number 28
3.6 One-dimensional formulation of the equations of motion 31
3.7 Application of the equations of motion to translocation processes in plants . 31
3.7.1 An introduction to zone models 31
3.7.2 Characteristics properties of zone models 33
3.7.3 Common assumptions used in mathematical phloem transport models 34
3.8 Conclusion 36

4 Hydraulic resistance of sieve plates 39
4.1 Introduction to sieve plates 39
4.2 Characteristic properties of the flow inside sieve tube elements 40
4.2.1 Previous work on Stokes flow through small pores 42
4.2.2 Numerical simulation of the flow close to a sieve plates 43
4.3 Hydraulic resistance of sieve tubes 43
4.3.1 Hydraulic resistance of the cell lumen 44
4.3.2 Hydraulic resistance of the sieve plate 44
4.3.3 Hydraulic resistance of the sieve tube system 46
4.4 On the relationship between lumen and plate resistance 47
4.4.1 Effective hydraulic resistance 47
4.5 Conclusion 49

5 Mathematical analysis of the equations of motion 51
5.1 The 3–zone model 51
5.1.1 Formulation of the 3–zone model 51
5.1.2 A simplified mathematical treatment 52
5.1.3 Non-dimensional formulation of the equations of motion 53
5.2 Analytical solution of the 3–zone model 55
5.2.1 Solution for $M\ddot{u} \ll 1$ 55
5.2.2 Solution for $M\ddot{u} \gg 1$ 56
5.3 Solution summary for $\omega = 1$ 57
5.4 Comparison between numerical and analytical solutions 57
5.4.1 Numerical solutions of the 3–zone model 57
5.4.2 Comparison between numerical and analytical solutions 59
5.5 Conclusion and Summary 60

6 Optimality of the Münch mechanicsm 61
6.1 Introduction to optimality and allometric scaling laws 61
6.2 Comparison between the 3-zone model and plant velocity measurements . . 62
6.3 Optimality of the Münch mechanism 64
6.3.1 Allometric scaling law for the optimality of the Münch mechanism . 67
6.4 Comparison with plant data 68

6.4.1 Determining the scaling exponent . . . 68
6.4.2 Determining the scaling prefactor . . . 71
6.5 Discussion . . . 71
6.5.1 Lang's relay hypothesis . . . 72
6.5.2 Is osmosis adequate for translocation in tall trees? . . . 74
6.6 Conclusion . . . 74

7 Microfluidic Experiments 77
7.1 Abstract . . . 78
7.2 Introduction . . . 78
7.3 Experimental setup . . . 79
7.3.1 Chip design and fabrication . . . 79
7.3.2 Measurement setup and procedures . . . 79
7.4 Experimental results . . . 83
7.4.1 Dye tracking . . . 83
7.4.2 Particle tracking . . . 83
7.5 Theoretical analysis . . . 83
7.5.1 Equation of motion . . . 83
7.5.2 Corrections to the equation of motion . . . 87
7.6 Discussion . . . 88
7.6.1 Comparison of theory and experiment . . . 88
7.6.2 Osmotic pumps in lab-on-a-chip systems . . . 88
7.7 Conclusions . . . 89
7.8 Acknowledgements . . . 90

8 Self-consistent unstirred layers in osmotically driven flows 93
8.1 Abstract . . . 94
8.2 Introduction . . . 94
8.3 Governing equations and geometries . . . 96
8.3.1 Non-dimensional variables . . . 96
8.3.2 Steady state equations of motion - Stokes flow . . . 97
8.3.3 Geometries . . . 97
8.4 Numerical results for the left-right symmetric parallel plate problem . . . 99
8.5 Theory for the left-right symmetric parallel plate problem . . . 99
8.5.1 A detailed look at the concentration profile for $x < \ell_m$ . . . 101
8.5.2 A detailed look at the concentration profile for $x > \ell_m$ . . . 102
8.6 Results from other geometries . . . 103
8.7 Conclusion . . . 105
8.8 Numerical methods . . . 105
8.9 Solution of the diffusion-advection eigenvalue problem . . . 106

9 Conclusion and outlook 109

A Analytical solution of the 3-zone model **111**
A.1 Solution for $M\ddot{u} \ll 1$ . . . 112
A.1.1 Calculation of the constants $B_1, B_2, \ldots, B_6$ . . . 113
A.1.2 Additional results . . . 115
A.1.3 Calculation of $\bar{U}$ for $M\ddot{u} \ll 1$ . . . 115
A.2 Solution for $M\ddot{u} \gg 1$ . . . 117

B Horwitz's derivation of the equations of motion **121**
B.1 Conservation of volume . . . 121
B.2 Conservation of sugar . . . 123
B.2.1 Mathematical formulation of the loading/unloading processes . . . 123

C Themodynamics of osmosis **125**
C.1 Non-equlibrium thermodynamics . . . 125
C.2 Osmotically driven flow across non-ideal membranes . . . 126

D Sieve plate data **129**

E Paper published in the Journal of Fluid Mechanics (2009) **131**

F Paper published in the Journal of the Royal Society Interface (2011) **159**

Bibliography **176**

List of Figures

1.1 Sketch of sugar translocation in plants. 2

2.1 Schematic sketch of the phloem and xylem vascular systems found in plants. 9
2.2 SEM images of the phloem tissue of *Curcubita maxima* (squash). 10
2.3 Experimental data: Translocation velocities in xylem and phloem. 15
2.4 Sketch of biomimicking phloem transport experiments. 16

3.1 Sketch of the osmotic flow process. 20
3.2 Sketch of the geometry used in the derivation of the equations of motion. . . 23
3.3 Characteristic properties of the osmotically driven pipe flow solution. 29
3.4 Sketch of a zone model for translocation in the phloem. 32
3.5 Characteristics properties derived from zone models. 33

4.1 Sketch of the sieve tube element geometry. 40
4.2 SEM images of sieve plates. 41
4.3 Procedure for preparing numerical simulations of flow through sieve plates. . 44
4.4 Numerical simulation of flow close to a *Curcubita maxima* sieve plate. . . . 45
4.5 Comparative analysis of end wall resistivity in phloem sieve tubes. 48

5.1 Comparison between numerical and analytical solutions of the 3-zone model. 58
5.2 Comparison between numerical and analytical solutions of the 3-zone model. 59

6.1 Comparison between plant velocity measurements and theory. 63
6.2 Asymptotic behavior of $\bar{u}$. 65
6.3 Optimized velocity for osmotically driven flows. 66
6.4 Visual representation of plant data 69
6.5 Comparison between predicted scaling law and plant data 70
6.6 Lang's hypothesis. 73

7.1 Experimental microfluidic setup 80
7.2 Sketch of the osmotically driven flow in a microchannel 81
7.3 Images of the moving sugar front 82
7.4 Measured sugar front position as a function of time. 84
7.5 Average flow velocity as a function of time. 85
7.6 Front velocity obtained by particle tracking. 86

7.7 Time evolution of sugar concentration profile. 87
7.8 Comparison between experiment and theory. 89

8.1 Concentration distribution close to the membrane interface. 95
8.2 Sketch of the geometries considered. 98
8.3 Numerically computed concentration and velocity profiles. 100
8.4 Numerically computed concentration profiles. 101
8.5 Numerically computed membrane concentration. 104
8.6 Flow and concentration field for geometry (b) 105
8.7 Comparison between our numerical method and Pedley's analytical solution. 106

A.1 Plot of $U_X(X_2)$ as a function of B_1 for $\omega = 1$. 115
A.2 Plot of X as a function of $U_2(X)/U_1(X_1)$. 116
A.3 Plot of $f(\omega)$. 117

B.1 Sketch of the geometry used in Horwitz's derivation. 122

List of Tables

2.1 Characteristic physical parameters. 11

4.1 Experimental data: Sieve plate geometry. 42

6.1 Experimental data: Phloem velocities 75
6.2 Experimental data: Allometric scaling data 76

7.1 List of parameters for Chapter 7 91

8.1 List of parameters for Chap. 8 108

List of Symbols

Symbol	Description	Unit/value
A	Cross-section area	m^2
A_i	Integration constant	
a	Sieve tube radius	m
a_c	Optimized sieve tube radius	m
a_p	Sieve pore radius	m
$\bar{a}_p$	Average sieve pore radius	m
B	Scaling parameter	
B_i	Integration constant	
C	Concentration	
c	Concentration	$\mathrm{mol/m}^3$
c^*	c in the loading zone	$\mathrm{mol/m}^3$
c_2^*	c at the end of the translocation zone	$\mathrm{mol/m}^3$
c_3^*	c at the end of the unloading zone	$\mathrm{mol/m}^3$
Δc	Concentration difference	$\mathrm{mol/m}^3$
D	Diffusion coefficient	m^2/s
E	Elastic modulus	Pa
g	Gravitational acceleration	$9.82\ \mathrm{m/s}^2$
G	Geometric prefactor	
J_w	Non-dimensional trans-membrane water flux	
j_n'	Thermodynamic flux	
j_w	Trans-membrane water flux	$\mathrm{m}^3/(\mathrm{m}^2/\mathrm{s})$
K	Constant used in $Mü \gg 1$ calculation	
k_i	Loading/unloading reaction constant	
L_{nn}	Thermodynamic coupling constant	
L_p	Membrane permeability	m/(s Pa)
L_i	Zone length	
l	Characteristic length	m
ℓ	Sieve tube element length	m
ℓ_p	Sieve plate thickness	m
l_i	Zone length	m
M	Molar mass	kg/mol
$Mü$	Münch number	
m	Mass	kg
N_p	Number of pores per sieve plate	
P	Pressure	
Pe	Péclet number	
p	Pressure	Pa
Δp	Pressure difference	Pa

Continued on next page

Symbol	Description	Unit/value
$\mathfrak{p}$	Normal distribution function	1/m
Q	Volume flow per unit time	m^3/s
R	Radial coordinate	
$\mathbb{R}$	Gas constant	8.31 J/(K mol) [4]
$\mathcal{R}$	Hydraulic resistance	Pa/m^3
Re	Reynolds number	
r_c	Correlation coefficient	
r	Radial coordinate	m
S	Perimeter	m
s	Internal entropy	J/K
T	Time	
$\mathbb{T}$	Temperature	K
t	Time	s
U	1-D axial velocity	
$\bar{U}$	Mean velocity in the translocation zone	
$\mathbf{U}$	Velocity field	
U_R	Radial velocity	
U_X	Axial velocity	
u	1-D axial velocity	m/s
$\bar{u}$	Mean velocity in the translocation zone	m/s
$\mathbf{u}$	Velocity field	
u_r	Radial velocity	m/s
u_x	Axial velocity	m/s
V	Volume	m^3
$\bar{v}_w$	Molar volume of water	1.8×10^{-5} m^3/mol [67]
$\bar{v}_s$	Molar volume of solute	m^3/mol
α	Scaling exponent	
β	Scaling prefactor	
ϵ	Membrane thickness	m
η	Viscosity	Pa s
κ	Membrane pore radius	m
ω	Ratio of unloading to loading zone length	
ξ_n	Thermodynamic force	
Π	Osmotic pressure	Pa
ρ	Density	kg/m^3
σ_p	Sieve pore radius standard deviation	m
Υ	Sugar loading rate	
υ	Sugar loading rate	mol/(m^3 s)
ϕ	Covering fraction	
(x, y, z)	Cartesian coordinates	m
(X, Y, Z)	Cartesian coordinates	

Continued on next page

Symbol	Description	Unit/value
$\langle \square \rangle$	Average of function $\square$ taken over tube cross section	
$\partial_{\square}$	Partial derivative with respect to $\square$	

Chapter 1

Introduction

Osmosis is the passage of water from a region of high water concentration to a region of low water concentration through a semipermeable membrane. Scientific interest in the subject started in the middle of the eighteenth century with the discovery of osmosis by Abbé Jean-Antoine Nollet. It was soon realized that osmosis plays an important role in the transport of water in and out cells, and with the theoretical framework put in place by van't Hoff in the 1880s, the fundamental understanding of the phenomena was greatly improved [69].

One area of biology where osmotically driven flows turned out to be of particular importance is in plants. At the beginning of the twentieth century Ernst Münch published his now famous monograph "Die Stoffbewegungen in der Pflanze" [49]. He proposed that long-distance transport of sugar in plants is driven by osmosis and that it occurs in a microfluidic pipe network of cells spanning the entire length of the plant. His work revealed a wealth of phenomena of unanticipated complexity related to the fluid mechanics of osmotically driven flows that continue to pose intriguing questions today.

Münch's idea, illustrated in Fig. 1.1, was simple: In the leaves, sugar produced by photosynthesis is secreted into a network of cylindrical cells known as the phloem. Due to osmosis, the high concentration of sugar inside the phloem creates a flow of water across the semipermeable cell membrane. This in turn displace the liquid and sugar already present forwards, thereby creating a bulk flow of sugar from source to sink. At the sugar sink, e.g. the root, a fruit or other places of growth and storage, removal of sugar from the phloem causes the water to leave the cells since the osmotic driving force is no longer present.

The fundamental questions that arise from this hypothesis are e.g. how much sugar can be transported in this way? How fast can it move? What controls the rate of transport? How does the osmotic mechanism affect the structure of the plant? Is osmosis sufficient to account for the rates of translocation observed in plants? Ultimately these questions are all related to plant growth and are therefore of great both fundamental and practical importance.

The main focus in this thesis is put on a theoretical analysis of the fluid mechanics of osmotically driven flows, aimed at answering some of the questions posed above. To put the theoretical results in a biological context, the author has worked closely with

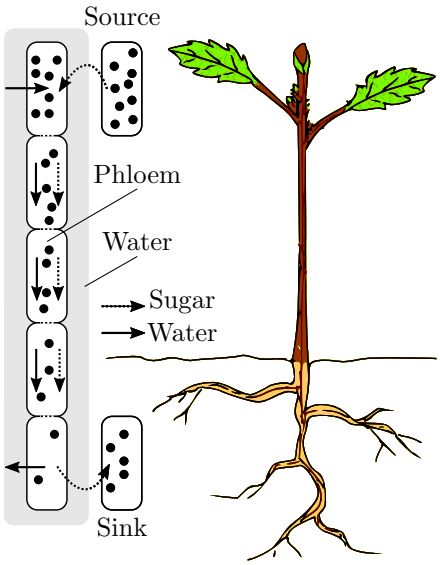

Figure 1.1: Schematic sketch of sugar translocation in plants according to the Münch hypothesis. In the source leaves, sugar (black dots) produced by photosynthesis is secreted into a network of cylindrical cells known as the phloem. Due to osmosis, the high concentration of sugar creates a flow of water across the semipermeable cell membrane from the surrounding tissue (solid arrows) into the phloem. This in turn displace the water and sugar (dashed arrows) already present forwards, thereby creating a bulk flow from sugar source to sugar sink. At the sink, e.g. the root, a fruit or other places of growth and storage, removal of sugar from the phloem causes the water to leave the cells since the osmotic driving force is no longer present. The loading and unloading processes are indicated by curved arrows. Adapted from [29], Fig. 1.

researchers performing *in-vivo* experiments on plants. This, together with a series of simple, biomimicking microfluidic experiments, have enabled us to gain a new understanding of the translocation processes that occur in plants.

1.1 Outline of the thesis

This thesis consists of 9 chapters. The bulk of the material presented has been published in the papers listed in Sec. 1.2. At the beginning of each chapter, a brief overview highlighting the contributions made by the author of the present thesis is given along with a list of relevant collaborators.

A list of the titles and a brief outline of the subjects treated is given below.

- **Chapter 2: Osmotically driven flows in living and artificial systems** This chapter provides an introduction to osmotically driven flows in artificial and living systems. Since the motivation for studying these flows comes primarily from phenomena observed in the phloem vascular system of plants, the basic principles of plant vascular biology are summarized. We discuss a number of experimental studies have been made on osmotically driven flows in artificial systems, some of which have significant technological applications.

- **Chapter 3: Fluid mechanics of osmotically driven flows** We introduce the basic concepts of osmosis and the relevant equations of motion for liquid and solute transport in osmotically driven flows. From these we derive an analytical solution for the osmotic flow and concentration problem in a cylindrical tube which leads directly to the one-dimensional equations of motion commonly used in the phloem transport literature. We discuss how these equations are applied in the literature to model transport processes in plants, and consider some of the characteristic properties of the models. Finally, we discuss some of the necessary assumptions for the equations of motion to be applicable.

- **Chapter 4: Hydraulic resistance of sieve plates** In chapter 3 we derived one-dimensional equations of motion for osmotically driven flows in cylindrical tubes with semipermeable walls. The translocation pathway found in plants does not, however, simply constitute one, long, continuous cylindrical tube. Rather, it consists of individual cells separated by sieve plates the presence which may contribute significantly to the overall hydraulic resistance of the translocation pathway. In this chapter we thus consider the effect of sieve plates on the flow inside the phloem sieve tubes. We show that the presence of the plates impose a significant amount of additional drag on the flow.

- **Chapter 5: Mathematical analysis of the equations of motion** In this chapter we study analytical and numerical solutions to the steady-state one-dimensional equations of motion derived in chapter 3. The equations are analyzed in a model consisting of 3 zones: a loading zone, a translocation zone and an unloading zone each representing different parts of the plant. We solve the equations of motion using

first a simple hydraulic resistor model and second a full analytical solution valid in the limit of very small and very large tube radii.

- **Chapter 6: Optimality of the Münch mechanism** In this chapter we apply the results of the 3-zone model introduced chapter 5 to translocation in plants. We begin by showing that the model is likely to be a concise representation of the processes that occur in plants by comparing experimental data to the predictions of the model. Then, we consider an interesting consequence of our results: The osmotic pumping mechanism has a maximum in translocation velocity for a special, optimal, value of the phloem sieve tube radius a_c. We derive an expression for a_c which takes the form of an allometric scaling law. At this particular value of the radius the Münch mechanism is optimized for rapid translocation of sugars in the phloem. We show that a large group of plants follow the predictions of the scaling law.
- **Chapter 7: Microfluidic experiments** Inspired by the biomimicking experiments of Münch, Eschrich *et al.*, and Lang discussed in chapter 2 the author and co-workers decided to design and fabricate microfluidic devices capable of biomimicking the processes that occur in the phloem vascular system of plants using channel dimension that approach those found in plants. This chapter is a description of the experiments, presented in the form of unabridged version of the paper [28].
- **Chapter 8: Self-consistent unstirred layers in osmotically driven flows** The one-dimensional equations of motion analyzed in chapters 3–6 were derived under the assumption that the concentration is well-mixed across the cross-section of the tube. This approximation is valid if the radial transport of solute molecules due to diffusion is much faster than the transport due to advection. In this chapter we study exactly when this condition is fulfilled in an idealized system.
- **Chapter 9: Conclusion and outlook** We present concluding remarks on our work on osmotically driven flows and give some directions for future research.

1.2 Publications during the PhD project

Papers in peer reviewed journals

1. K. H. Jensen, J. Lee, T. Bohr, H. Bruus, N. M. Holbrook and M. A. Zwieniecki
   Optimality of the Münch mechanism for translocation of sugars in plants
   Journal of The Royal Society Interface
   DOI: 10.1098/rsif.2010.0578 (2011) [29] (0 citations as of 31 January 2011).

2. K. H. Jensen, T. Bohr, and H. Bruus
   Self-consistent unstirred layers in osmotically driven flows
   Journal of Fluid Mechanics, Volume **662**, p. 197-208 (2010) [27] (0 citations).

3. K. H. Jensen, E. Rio, R. Hansen, C. Clanet and T. Bohr
   Osmotically driven pipe flows and their relation to sugar transport in plants
   Journal of Fluid Mechanics, Volume **636**, p. 371-396 (2009) [30] (2 citations).

4. K. H. Jensen, J. Lee, T. Bohr, and H. Bruus
   Osmotically driven flows in microchannels separated by a semipermeable membrane
   Lab Chip **9**, 2093-2099 (2009) [28] (4 citations).

5. K. H. Jensen, M.N. Alam, B. Scherer, A. Lambrecht and N.A. Mortensen
   Slow-light enhanced light-matter interactions with applications to gas sensing
   Optics Communications, Volume **281**, Issue 21, p. 5335-5339 (2008) [31] (5 citations)

First author conference contributions

1. K.H. Jensen, J. Lee, T. Bohr, J. Lee, N. M. Holbrook, M. Zwieniecki, Optimality of the Münch hypothesis for translocation of sugars in plants, International Conference on Plant Vascular Biology 2010, Colombus, USA. (2010)

2. K.H. Jensen, T. Bohr and H. Bruus, Concentration boundary layers in osmotic membrane transport processes, Annual Meeting of the APS Division of Fluid Dynamics, Minneapolis, USA, Paper MF.00002. Bull. Amer. Phys. Soc. **54** (19) (2009).

3. K.H. Jensen, T. Bohr and H. Bruus, Osmotically driven flows in microchannels and their relation to sugar transport in plants, 1st Nordic Meeting in Physics, Copenhagen, Paper BF.4 (2009).

Chapter 2

Osmotically driven flows in living and artificial systems

The present chapter provides an introduction to osmotically driven flows in artificial and living systems. Since the motivation for studying these flows comes primarily from phenomena observed in the phloem sugar transport system of plants, the basic principles of plant vascular biology are summarized. The introduced concepts are thoroughly described in the literature (see e.g. [12, 85, 73, 79, 23, 36]) and constitute the motivation for the work presented in this thesis. The subject will be presented as seen through the eyes of a physicist, and is not intended to be a complete review of the research field of plant vascular biology. What follows should however be a sufficiently complete description of the processes that takes place in plants to allow for a simple quantitative description of the process.

We end by discussing a number of experimental studies have been made on osmotically driven flows in artificial systems, some of which have significant technological applications.

For the biologically inclined reader it will be useful to know that throughout this thesis we are mainly concerned with transport processes that occur in angiosperms and that many of the geometric and hydraulic consideration are made with this class of plants in mind. This is of special importance in the discussion of sieve pores which are assumed to be open [37, 48]. This is not the case in gymnosperms [1] where the sieve pores are occluded by endoplasmic reticulum membrane complexes [68], and consequently the hydraulic resistance may be significantly higher.

2.1 Osmotically driven flows in living systems

Flows driven by osmosis are abundant in nature, the prime example being the flow of water across cell walls in virtually all living creatures. Here, osmosis facilitates the transport of

[1] Gymnosperms are characterized by having naked seeds, while the seeds of angiosperms are enclosed during pollination. The most abundant group of gymnosperms are conifers (e.g. pine trees) while angiosperms include all flowering plants. [73]

water across the plasma membrane either directly across the lipid bi-layer, or via membrane transport proteins such as aquaporins [17, 64].

While flow in and out of single cells have been studied extensively in the literature, the most interesting example, from a fluid mechanist's' point of view, of an osmotically driven flow is found in plants. Here, a network of cylindrical cells, known as the phloem, are responsible for transporting sugar from the leaves to places of growth or storage. In these cells, it is believed, osmosis creates a bulk flow of water, sugars, hormones, and signaling molecules over many tens of meters directed from source to sink in accordance with the basic needs of the plant [73]. This process, however, is not well understood on the quantitative level since direct measurements of translocation rates and driving forces are extremely difficult to make [53, 37, 36].

2.2 Vascular transport in plants

Terrestrial plants faces serious challenges if they are to survive on land. The key to survival and successful reproduction is the ability to acquire and retain a sufficient amount of water and nutrients for the plant to grow. In response to this, plants have developed roots and leaves. Roots provide mechanical stability and absorb water and nutrients from the soil while leaves absorb light and exchange gases with the atmosphere. As the plant grows, these two organs become increasingly separated in space and hence the time for responses to environmental stimuli to propagate is increased. This makes the distribution of water, nutrients, photosynthetic products and signaling molecules by passive means difficult. It is in response to this challenge that plants have developed long-distance vascular transport systems that allow the shoot and the root to exchange material and information in an elaborate and highly efficient way.

The vascular system of plants is made up of two parts: The phloem[2] and the xylem[3]. Both the phloem and the xylem are made up of cylindrical cells lying end-to-end in a microfluidic network spanning the entire length of the plant. The elements of phloem and xylem run in parallel to each other and are almost always found in close proximity, separated only by a few cells, as shown in Figs. 2.1 and 2.2. The two tissue types are discussed in detail below, and characteristic physical parameters are listed in table 2.1.

2.2.1 The xylem

The primary role of the xylem is to conduct water and nutrients from the roots to the rest of the plant [51]. The xylem consists of water-filled, cylindrical cells typically 100 μm in radius and with lengths ranging from 1 mm to several cm [85]. The cells are joined together at the ends to form a network running along the entire length of the plant. The mechanism driving flow in the xylem is believed to be evaporation from the leaves through stomata pores which open and close in response to changing conditions, such as light intensity, humidity, and CO_2 concentration in the atmosphere [73, 88]. This mechanism drives a

[2]The word phloem is derived the classical Greek word for bark, *phloios*.

[3]The word xylem is derived from the classical Greek word for wood, *xylon*.

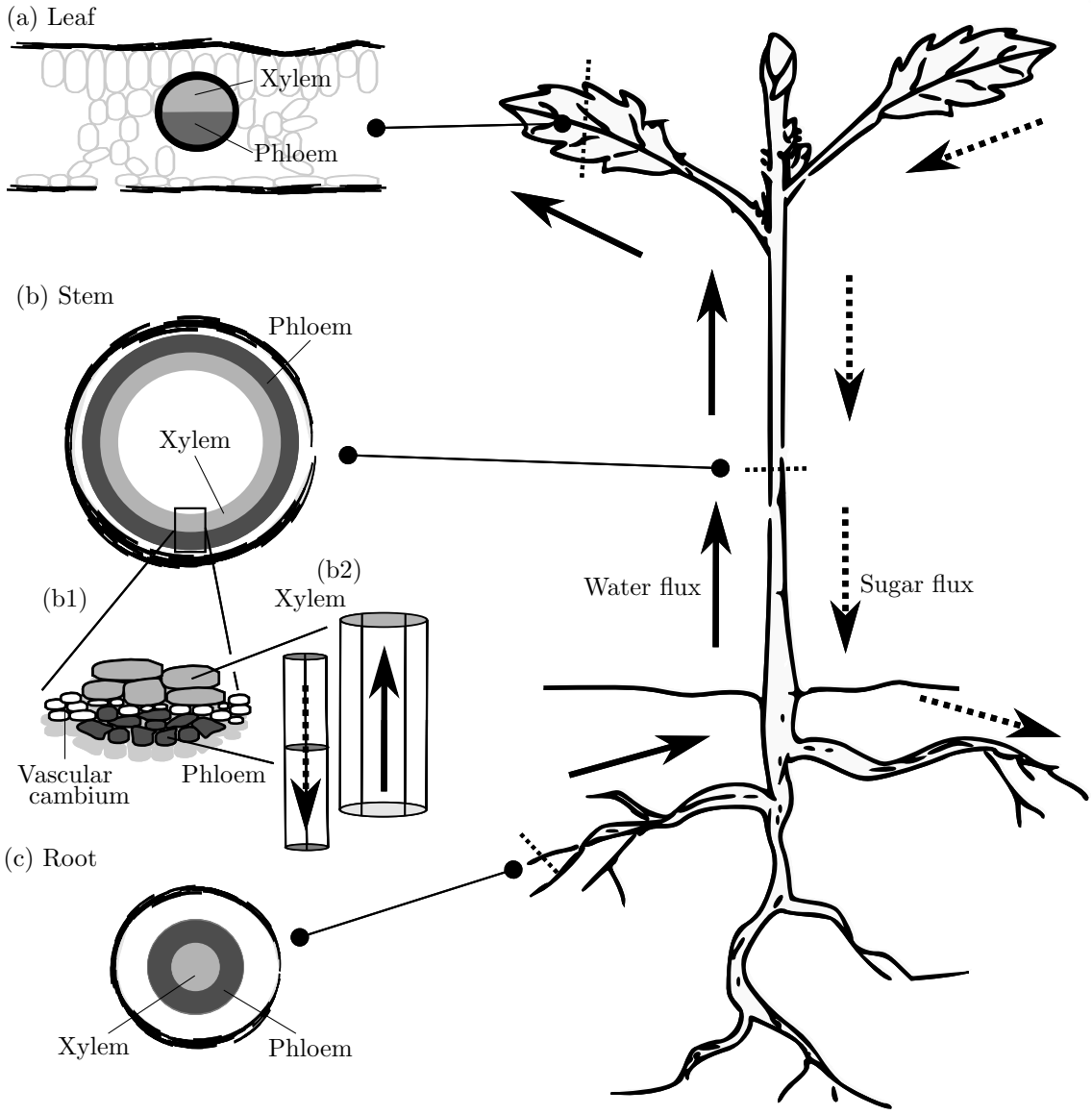

Figure 2.1: Schematic sketch of the phloem and xylem vascular systems found in plants. (a) In the leaf, the vascular tissue consisting of the phloem (dark gray) and xylem (light gray) is found in veins running parallel to the leaf surface located near the center of the cross section. (b-c) In the stem and roots, the vascular tissue is found close to the surface in either a continuous ring or in bundles. The xylem typically lies closer to the interior of the stem than the phloem as shown in (b1). Between the xylem and phloem is a meristem called the vascular cambium. This tissue divides off cells that will be become additional xylem and phloem as the plant grows. The cylindrical nature of the cells is illustrated in (b2), see also Fig. 2.2. The translocation pattern is indicated by the arrows. Water (solid arrows) is absorbed from the ground and moves towards the leaves driven by evaporation. Sugar (dashed arrows) is produced in the leaves and moves to places of growth or storage e.g. immature leaves, fruits or roots.

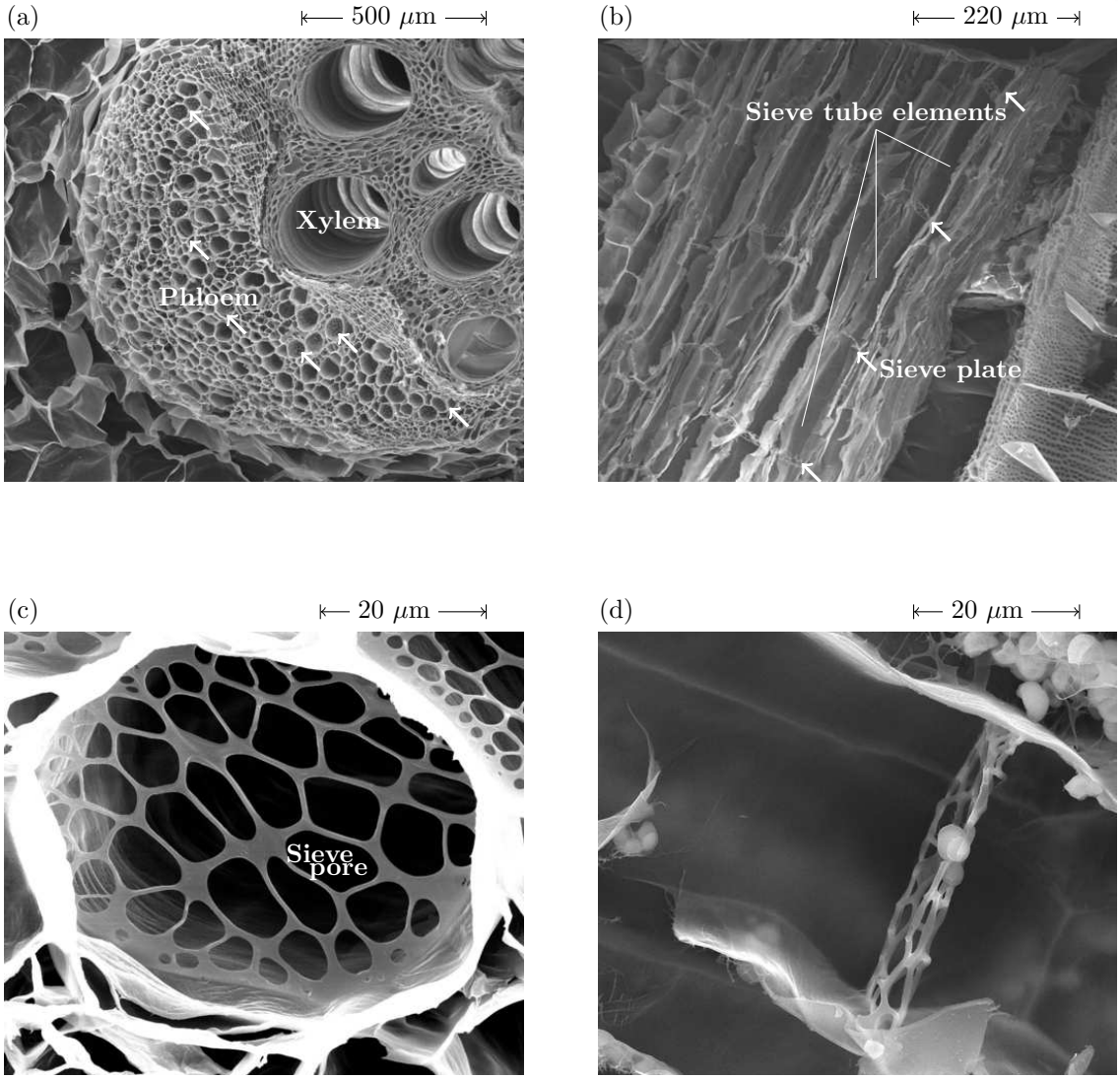

Figure 2.2: Scanning electron microscope (SEM) images of the phloem tissue of *Curcubita maxima* (squash), a plant which has very large (50 μm in diameter) but otherwise representative phloem sieve tube elements. (a) Horizontal cross-section of the vascular tissue (see Fig. 2.1(b1)) showing the phloem and xylem tissues. The position of a few of the sieve tube elements is indicated by the arrows. (b) Vertical cross section the phloem tissue showing the cylindrical nature of the sieve tube elements lying end to end. Individual sieve tubes are separated by sieve plates indicated by the arrows. (c) Frontal view of a sieve plate. About 50% of the plate are is covered by open sieve pores. (d) Side view of a sieve plate. SEM images courtesy of M. Knoblauch and D. L. Mullendore [48]. Reproduced with permission.

Table 2.1: Characteristic physical parameters relevant to vascular translocation processes in plants. Cell sizes refer to phloem sieve tube elements and xylem vessel elements.

Parameter	Phloem (P)	Xylem (X)	Reference
Cell radius	10 μm	100 μm	[48, 29](P), [85](X)
Cell length	100 μm − 1 mm	1 mm − 1 cm	[48](P), [85](X)
Flow velocity	1 m/h = 0.28 mm/s	10 m/h = 2.8 mm/s	[48, 29](P) [85](X)
Pressure	1 MPa	−1 MPa	[82] (P) [85](X)
Sugar concentration	0.1 M − 1 M	∼ 0 M	[73, 82] (P), [85](X)
Dry weight sugar transport	2.8×10^{-3} kg/(s m^2)		[12] (P)
Liquid viscosity	2×10^{-3} Pa s	1×10^{-3} Pa s	[79] (P), [73] (X)
Membrane permeability	5×10^{-14} m/(s Pa)		[79] (P)

flow with speeds of the order 10 m/h = 2.8 mm/s and the evaporation from the leaves causes the water column in the xylem to be under tension, with induced negative pressures of the order −1 MPa [85].

2.2.2 The phloem

The phloem is responsible for translocating the products of photosynthesis (i.e. sugars) from places of production, such as mature leaves, to places of growth or storage, such as immature leaves, fruits or roots. Besides sugar, signaling molecules are also transported in the phloem.

The phloem consists of several different types of cells: Sieve tube elements, in which the translocation of sugar takes place, companion cells that helps to regulate the metabolic activities of the sieve tube elements, phloem fibres that gives the plant mechanical strength, and phloem parenchyma which acts as storage [73]. As shown in Fig. 2.2(b), the sieve tube elements are cylindrical cells typically measuring 10 μm in radius and about 100 μm in length [80, 48]. They cover about 20 % of the area of the phloem [12] and contain a highly concentrated sugar solution (0.1 M − 1 M) as well as smaller amounts of signaling molecules, amino acids, proteins and a number of minerals [73]. The high sugar content means that the cells are under positive pressure, sometimes as high as 2.5 MPa [82].

The sieve tube elements are joined together end-to-end forming a network running along the entire length of the plant. During early stages of sieve tube element development, plasmodesmata in the end walls of adjacent immature sieve tube elements are converted into sieve pores usually a few ∼ 1 μm in diameter as shown in Fig. 2.2(c)-(d). When the sieve elements reaches maturity, these pores cover ∼ 50% of the end wall area and form what is known as a sieve plate. The pores allow the translocation stream to pass relatively freely between adjacent sieve elements, making the sieve tube a continuous pathway [48]. The primary role of the sieve plates is believed to be a defensive mechanism, sealing off the sieve elements by clogging the pores if the cell is mechanically damaged or heated. Thereby the plant prevents the valuable sugary content of the sieve elements from leaking [37].

As we shall see in chapter 4, the presence of sieve pores significantly increases the hydraulic resistance of the phloem sieve tube translocation pathway.

2.3 Translocation in the phloem

Long-distance transport of sugar in the phloem sieve tubes is an experimentally established fact [36]. The process, however, is not well understood on the quantitative level since direct measurements of translocation rates and driving forces are extremely difficult to make [53, 37, 36]. The fundamental problem is that the phloem is very sensitive to disturbances, ceasing flow when subjected to slight mechanical or thermal perturbations [37].

Early measurements of the rate of sugar transport in the phloem was conducted by weighing fruits at different instances in time. Using this technique, dry weight mass transfer rate of the order 1 g/(h cm^2) = 2.8×10^{-3} kg/s per m^2 of phloem area was found [12]. The problem with this type of experiment is that the only reliably measured quantity is the increase in dry weight per unit time. To get the actual translocation velocity one must make assumptions regarding the concentration of the sugar solution and the area fraction of the phloem in which the transport is taking place. To resolve this problem, more accurate measurement techniques using radioactive dye tracers emerged have since been used extensively, see [12] and references therein. More recently, nuclear magnetic resonance imaging has been used to measure phloem flow velocities [48, 89] although both dye and radioactive tracers remain in use to this day [37, 29]. All the above mentioned techniques find typical flow velocity in the sieve tube elements of the order 1 m/h = 0.28 mm/s, an order of magnitude slower than in the xylem. This velocity, with a sugar concentration of 1 M, gives a dry weight transfer rate of 0.1 kg/s of m^2 phloem sieve tube area, consistent with largest observed rate (5 g/(h cm^2) = 0.014 kg/s per m^2 of total phloem area [12]) since the sieve tubes cover only about 20% of the total phloem area.

2.3.1 Mechanisms driving the flow

To account for the rates of transport observed in the phloem, several different driving mechanisms have been proposed. We will discuss molecular diffusion and osmosis in detail below, but for a thorough analysis of other mechanisms which has been proposed, e.g. actin filament driven streaming and electro osmosis, see the review by MacRobbie [44].

Molecular diffusion

One of the first mechanisms suggest to be responsible for transport in the phloem was molecular diffusion. This hypothesis had many supporters, among them Julius Sachs, one of the leading plant physiologists of the 19th century [26]. The supporters of this theory envisaged that the transport of sugar was driven by a diffusive flux set up by the gradient in concentration between the sugar loading and unloading regions in the plant. Quantitative calculations by De Vries published in 1885 showed, however, that this process is much too slow to account for the observed rates of transport [35].

Following De Vries's calculations, Münch argues in [49] that the mass transfer due to diffusion can be estimated in the following way: In steady state the mass of sugar diffusing per unit time $\frac{\mathrm{d}m}{\mathrm{d}t}$ due to a difference in concentration Δc between two ends of a pipe of cross section area A and length l is

$$\frac{1}{A}\frac{\mathrm{d}m}{\mathrm{d}t} = MD\frac{\Delta c}{l}, \tag{2.1}$$

where M is the molar mass and D is the diffusion constant. For a sucrose solution with $M = 0.342$ kg/mol, $\Delta c = 1$ M, $D = 5 \times 10^{-10}$ m^2/s [4] and a pipe of length $l = 1$ m we find that

$$\left(\frac{1}{A}\frac{\mathrm{d}m}{\mathrm{d}t}\right)_{\text{Diff}} = 1.7 \times 10^{-7}\ \text{kg}/(\text{m}^2\ \text{s}), \tag{2.2}$$

which is four orders of magnitude smaller than the observed rate of mass transport. This calculation shows that diffusion alone cannot account for the observed long distance transport of sugar in plants [49, 12].

Osmosis

The most widely accepted explanation of translocation in the phloem dates back to the 1920s where the German scientist Ernst Münch proposed that the flow is passive and is driven by differences in osmotic pressure between sugar sources and sinks [49, 36]. Osmosis is the tendency of water to move across a semipermeable membrane from a region low solute concentration to a region of high concentration (see Sec. 3.2 and App. C). The osmotic pressure Π said to be driving the flow is directly proportional to the difference in concentration Δc across the membrane

$$\Pi = \mathbb{R}\mathbb{T}\Delta c, \tag{2.3}$$

where $\mathbb{R}$ is the gas constant and $\mathbb{T}$ is the temperature. With the sugar concentrations listed in table 2.1, we find $\Pi = 0.2 - 2$ MPa.

Münch envisaged a mass flow in the phloem sieve elements driven by an osmotic pressure gradient set up in the channel by the secretion (loading) of sugar into the sieve elements at the source leaves and the removal (unloading) of sugar in the source tissue, e.g. roots, fruits or other regions of growth and storage as illustrated in Fig. 1.1. The high concentration of sugar in the source region would create a flow across a semipermeable membrane into the phloem cells driven by osmosis. This would in turn displace the liquid already present downwards, thereby creating a bulk flow from source to sink. At the sink, removal of sugar from the phloem tissue would cause the water to leave the cells since the osmotic driving force is no longer present. The Münch hypothesis is also known as the pressure flow hypothesis [13] while the resulting flow is known as an osmotically driven pressure flow [80], an osmotically driven volume flow [16] or simply an *osmotically driven flow*.

A simple quantitative analysis of the Münch mechanism to estimate the flow velocities one would expect to find can be made in the following way. Consider the cylindrical sieve

tube elements lying end to end inside the plant. If they have a total length l and radius a, the volume Q flowing across the membrane surface per unit time is

$$Q = 2\pi a l L_p \Pi = 2\pi a l L_p \mathbb{R}\mathbb{T}\Delta c, \tag{2.4}$$

where L_p is the permeability of the membrane. The cross section area of the tube is $A = \pi a^2$, so the characteristic osmotic velocity u_{osm} inside the tube is

$$u_{\text{osm}} = \frac{Q}{A} = \frac{2}{a} l L_p \mathbb{R}\mathbb{T}\Delta c = \sigma l L_p \mathbb{R}\mathbb{T}\Delta c. \tag{2.5}$$

Here, σ is the surface to volume ratio of the tube

$$\sigma = \frac{S}{A} = \frac{2\pi a l}{\pi a^2 l} = \frac{2}{a}, \tag{2.6}$$

a crucial parameter in determining the flow velocity inside the tube. When σ is large, i.e. when the radius a is small, the flow velocities can become very large. Using the parameter values

$$l = 1 \text{ m}, \quad a = 10^{-5} \text{ m}, \quad L_p = 5 \times 10^{-14} \text{ m/(s Pa)}, \quad \text{and} \quad \mathbb{R}\mathbb{T}\Delta c = 1 \text{ MPa},$$

we find that

$$u_{\text{osm}} = 10^{-2} \text{ m/s}. \tag{2.7}$$

This number is two orders of magnitude larger than the observed flow velocity (2.8×10^{-4} m/s), but not unreasonable since the analysis does not take into account the viscous resistance of the fluid moving inside the narrow tube. We will derive a formula taking the viscosity into account in chapter 5, and show in chapter 6 that it agrees well with experimental data.

2.3.2 Interaction between the translocation processes in the phloem and the xylem

In the Münch hypothesis, the water entering the phloem due to osmosis comes from the surrounding tissue and thus ultimately from the xylem. Since the two tissues are separated only by a few cells and the hydrostatic pressure difference between them is measured in MPa (see Tab. 2.1), it is an open question how important the direct interaction between the flow in the phloem and the xylem is [24]. In a recent experiment, Windt *et al.* set out to investigate this by simultaneously measuring flow velocities in phloem and xylem of four different species under alternating day and night conditions [89]. As shown in Fig. 2.3, they demonstrated that the flow in the two tissues are largely independent, and that while the flow in the xylem exhibited large diurnal variations, the flow in the phloem is approximately constant throughout the day. Since large variations in xylem flow velocity implies large variations in pressure, we conclude on the basis of these experiments that the direct coupling between the flow in the phloem and in the xylem is in general weak, and that we therefore may treat the two systems separately.

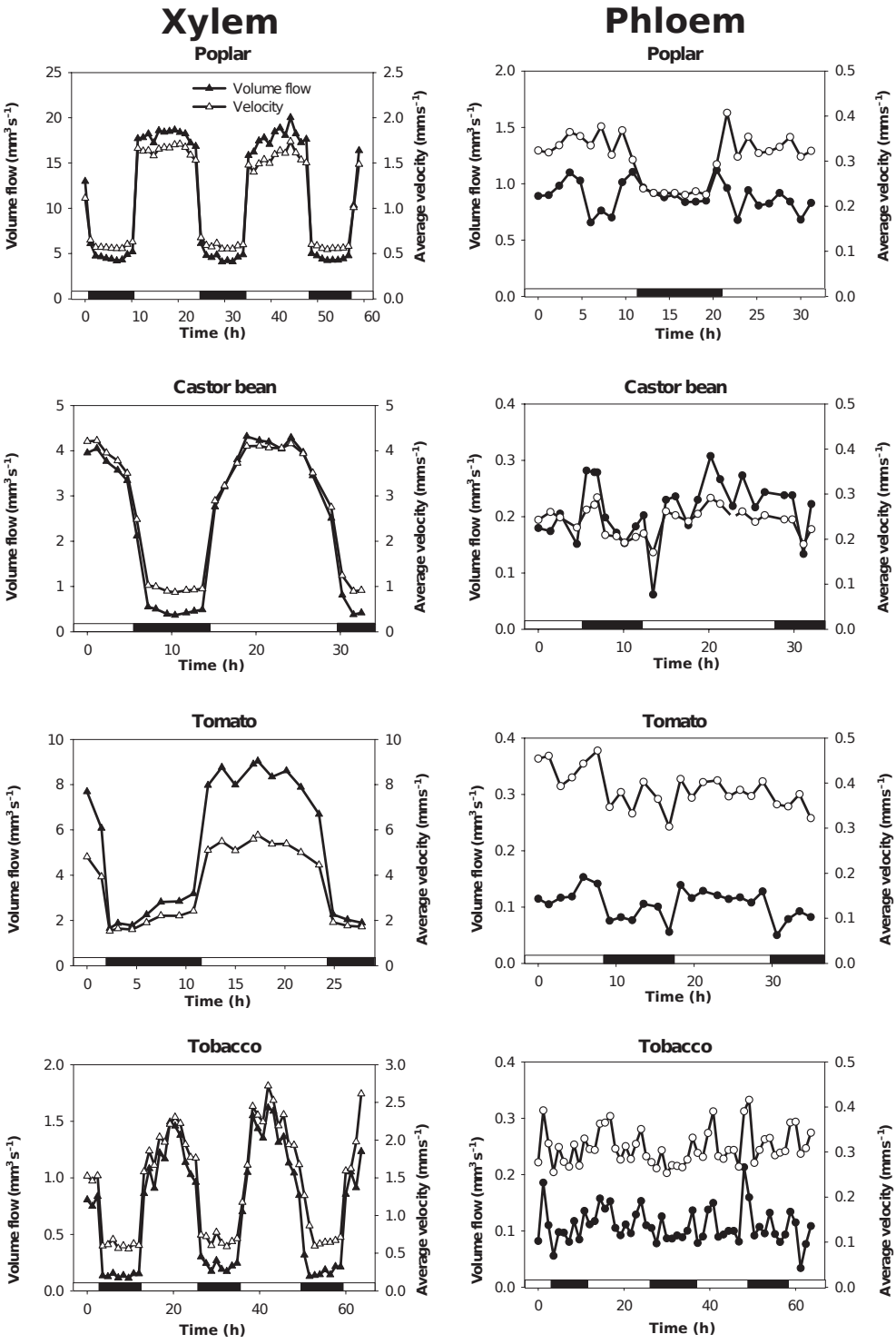

Figure 2.3: Translocation velocities measured as a function of time in the xylem (left column) and the phloem (right column) of four different species as indicated above the plots. The volume flow (closed symbols) and average linear velocity (open symbols) were measured using MRI over the course of 2 to 4 days. Black and white bars on the ordinate axis indicate day and night conditions. The translocation velocities measured in the xylem shows a strong dependence on these conditions, with high velocities observed during the day and low velocities during the night. Except for poplar, the velocities observed in the phloem are largely independent of the day/night conditions. From [89], Figs. 6 and 9. Reproduced with permission.

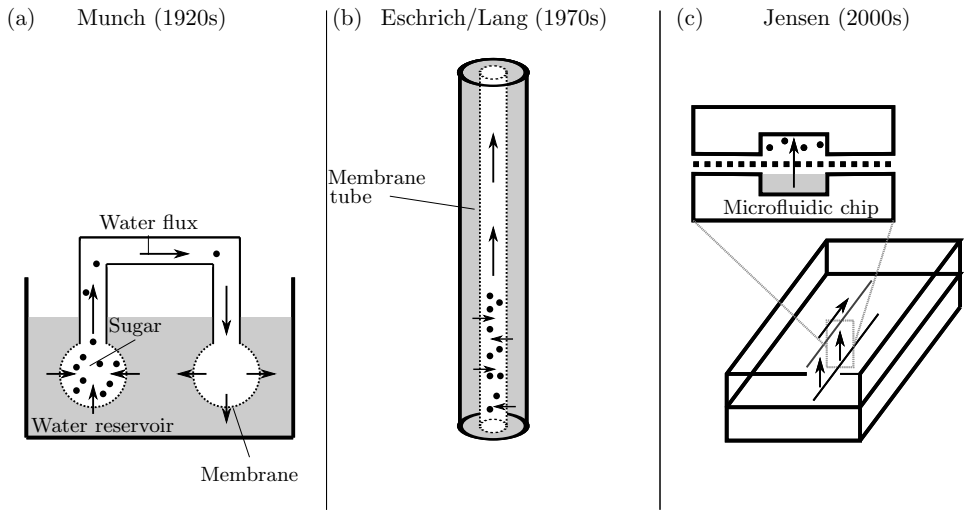

Figure 2.4: Schematics of three generations of biomimicking phloem transport experiments. (a) Ernst Münch [49], (b) Eschrich *et al.* and Lang [16, 40], and (c) the author of the present thesis, Jensen [28]. See Sec. 2.4 for a description each individual experimental setup.

2.4 Osmotically driven flows in artificial systems

Motivated primarily by osmotically driven flow in the phloem vascular system of plants, a number of experimental studies have been conducted using artificial "phloem cells" to study the fundamental physical processes [49, 16, 40, 55, 30, 28, 29]. These experiments, illustrated in Fig. 2.4 fall into three categories, historically and conceptually.

1920s: The work of Ernst Münch

Some of the first osmotic experiments related to translocation in plants were conducted by Ernst Münch in the 1920s [49] . His setup, shown in Fig. 2.4(a), consisted of two round-bottom flasks connected by a tube. Part of the surface of the flasks was covered by a semipermeable membrane. As he introduced sugar solutions of different concentration into the two flask and submerged them in a water bath, he observed a flow from the flask of high concentration to the flask of low concentration. He then went on to argue that, physically speaking, the plant constitutes a network of such connected osmotic parts, from which it would follows that osmotic flow also occurs since "same causes have same effects" ([49], p. 37, translation by Knoblauch & Peters [36]).

1970s: The work of Walter Eschrich *et al.* and Alexander Lang

A serious shortcoming of Münch's experiments is that the osmotic interaction takes place only in what corresponds to the loading and unloading regions, and not along the translocation region (i.e. the stem) as is the case in plants. In an attempt to investigate osmotically

driven flows in the translocation region, Eschrich *et al.* build experiments in the early 1970s to investigate the transient dynamics of a moving sugar front inside a cylindrical membrane tube [16]. Their setup, shown in Fig. 2.4(b), consisted of a long membrane tube ~ 1 cm in diameter fitted inside a water-filled glass tube. At the beginning of the experiment, a sugar solution was introduced into one end of the tube, which was then closed at both ends. The movement of the sugar front was subsequently observed for different sugar concentrations. They observed that the more concentrated the sucrose solution, the faster the front traveled. They also found that the velocity of the sugar front decayed exponentially in time as the front approached the far end of the tube. These experiments were later refined by the author of the present thesis during his master studies [30](See App. E, p. 131 for details) to allow for a better quantitative comparison between experiment and theory.

Following Eschrich *et al.*, Alexander Lang [40] build experiments to study steady-state osmotically driven flows. His setup, consisted again of a long, cm-sized, membrane tube submerged in a water bath. At one end a sucrose solution was introduced at a steady rate, and at the other end the tube was open at atmospheric pressure. At regular intervals along the membrane tube, several measurement stations were placed that enabled him to measure the local sugar concentration and pressure. He demonstrated that osmosis could create considerable bulk flows in narrow tubes, consistent with the Münch hypothesis.

2000s: Jensen *et al.*

While the experiments of Eschrich *et al.* and Lang were a major step forward in understanding the processes that drive translocation in plants, they still have the fundamental problem that the characteristic length-scale (i.e. tube diameter) are many orders of magnitude larger than what is observed in plants. Since osmosis is a surface phenomena in nature, this means that the ratio of surface to volume σ (cf. Eq. (2.6)) which controls the axial flow velocity is much smaller in plants than in the experiments. Experiments with channel radii in the relevant μm range have been possible since the early 2000s with the advent of modern microfluidic fabrication techniques [10].

In 2009-2011 the author and co-workers conducted a systematic survey of osmotically driven flows at the micrometre scale with osmotic interaction along the whole length of the microfluidic channel [28, 29]. The experiments, which are sketched in Fig. 2.4(c) and described in greater detail in chapter 7, studied osmotically driven flows in 200 μm wide and $50 - 200$ μm deep microchannels, thus approaching the length-scales found in plants.

2.5 Technological applications of osmotically driven flows

Osmotically driven flows have found numerous technological applications that falls into two categories: liquid handling and energy production.

In the 1970s, Theeuwes pioneered a pill-based osmotic delivery system for drugs [76]. In its simplest form, the system is constructed by coating an osmotically active solid drug with a semipermeable membrane. This membrane contains an orifice through which the dissolved drug is dispensed once the pill is submerged in water. The rate of delivery is

controlled by the water permeation characteristics of the semipermeable membrane surrounding the drug and the osmotic properties of the drug [76].

In 2009, the worlds first osmotic power plant began operations near Oslo, Norway. The power plant is located near the mouth of a river and uses the osmotic pressure difference between freshwater and the salty seawater to generate an osmotic pressure which drives a turbine. The plant is capable of producing 3 W per m^2 membrane area, a number which is continually increasing. The global potential of osmotic power is estimated to be 1500 T W h, equivalent to 50% of the total power production in the European Union [72].

2.6 Conclusion

In this chapter we have given an introduction to the motivation behind the topic studied in the present PhD thesis: translocation of sugars and signaling molecules in the phloem vascular system of plants.

In the following chapters, we will try to get an fundamental understanding of how these osmotically driven flows work. We will then attempt to answer fundamental questions such as how fast the sugar can move in plants using the osmotic pump? What controls the rate of transport? How does the osmotic mechanism affect the structure of the plant? Is osmosis sufficient to account for the rates of translocation observed in plants?

Chapter 3

Fluid mechanics of osmotically driven flows

From the processes occurring in plants, we now move on to a physical description of osmotically driven flows. In this chapter we thus first introduce the basic concepts of osmosis and the relevant equations of motion for liquid and solute transport. From these we derive an analytical solution for the osmotic flow and concentration problem in a cylindrical tube which leads directly to the one-dimensional transport equations commonly used in the phloem transport literature [79]. We finally discuss how these equations are applied to sugar transport in plants.

Most of the material presented can be found in the fluid mechanics and phloem translocation literature, but the derivation of the one-dimensional equation of motion for fluid transport in osmotically driven flows directly from an analytical solution to the Navier-Stokes equation is due to the author and has yet to be published. This also applies to the derivation of the one-dimensional equation of motion for sugar transport. The discussion of the characteristic properties of zone models given in Sec. 3.8 and Fig. 3.5 is due to the author. It was instrumental in obtaining the analytical solution to the equations of motion published in [29] and derived in Chapter 5. The term "Münch number" for the non-dimensional number $M\ddot{u}$ (see Sec. 3.5.5) was first introduced in [30] and was coined by the author and Tomas Bohr.

3.1 Background

With the advent of radioactive tracer experiments, the need for a quantitative description of the osmotically driven flow described by the Münch hypothesis became apparent in the 1950s (see [25] and references therein). One of the first to formulate the equations of motion in form of differential equations was Horwitz [25], who in 1958 investigated the theoretical background of radioactive tracer propagation observed in plants. His derivation (see Appendix B) rested on simple conservation principles and contains no detailed analysis of the fluid mechanics of osmotically driven flows.

In the present chapter, we will derive Horwitz's equations of motion based on the ther-

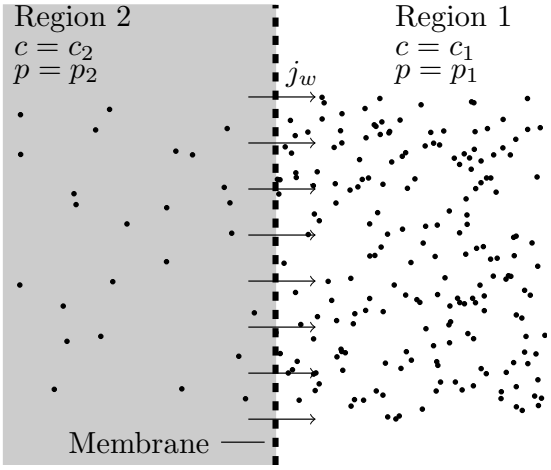

Figure 3.1: Sketch of the osmotic flow process. A semipermeable membrane (dashed line) separates two regions which contains aqueous solutions of a solute at concentrations c_1 and c_2 (proportional to the density of the black dots) and hydrostatic pressures p_1 and p_2 respectively. Osmosis and hydrostatic pressure drives a flow of water (arrows) across the membrane at a rate j_w given by Eq. (3.6).

[10]

modynamics of osmosis, the Navier-Stokes equation for fluid motion, and the convection-diffusion equation for solute transport.

3.2 Osmosis

Osmosis is the movement of water across a semipermeable membrane driven by a difference in chemical potential. It is important in many biological systems since virtually all biological membranes are semipermeable. In many cases these membranes are impermeable to large molecules, such as sugars, while permeable to water and small uncharged solutes [4].

3.2.1 Non-equilibrium thermodynamics

The process of osmosis can best be described by the formalism of non-equilibrium thermodynamics [67]. As discussed in Appendix C, we thus consider a linear phenomenological relation between a thermodynamic flux j_n' and the corresponding conjugate force ξ_n

$$j_n' = L_{nn}\xi_n. \tag{3.1}$$

Here, L_{nn} is a proportionality constant with the unit of conductance. The driving force ξ_n is related to the difference in chemical potential $\Delta\mu_n$ of the substance n between different regions of the system

$$\xi_n = \Delta\mu_n. \tag{3.2}$$

Eqns. (3.1)-(3.2) are valid close to equilibrium and Ohm's law of current flow, Fourier's law of heat flow, and Fick's law of diffusion are all familiar examples of Eq. (3.1).

It can be shown that the relation between the rate of internal entropy production $\partial_t s$, the absolute temperature $\mathbb{T}$, and the forces and fluxes is given by

$$\mathbb{T}\partial_t s = j'_n \xi_n. \tag{3.3}$$

The quantity $\mathbb{T}\partial_t s$ is known as the power dissipation function and is a measure of the tendency of the non-equilibrium process to proceed.

3.2.2 Osmotically driven flow across a semipermeable membrane

In the present discussion we consider the situation sketched in Fig. 3.1. An ideal semipermeable membrane separates two regions at pressures p_1 and p_2 which contains dilute aqueous solutions of a solute at concentrations c_1 and c_2. The membrane is permeable to water, but not to the solute. If the concentrations are low, the difference in chemical potential of the water $\Delta\mu_w$ across the membrane is given by

$$\Delta\mu_w = \bar{v}_w \left(p_2 - p_1\right) - \bar{v}_w \mathbb{R}\mathbb{T} \left(c_2 - c_1\right), \tag{3.4}$$

where $\bar{v}_w$ is the molar volume of water. We then have from Eq. (3.1) that the flux of water molecules j'_w is

$$j'_w = L_{ww}\bar{v}_w \left(\mathbb{R}\mathbb{T} \left(c_1 - c_2\right) - \left(p_1 - p_2\right)\right). \tag{3.5}$$

The volume of water j_w flowing across the membrane per unit area is then

$$j_w = \frac{j'_w \bar{v}_w}{\mathcal{A}} = L_p \left(\mathbb{R}\mathbb{T} \left(c_1 - c_2\right) - \left(p_1 - p_2\right)\right), \tag{3.6}$$

where $\mathcal{A}$ is the area of the membrane and $L_p = \frac{L_{ww}\bar{v}_w^2}{\mathcal{A}}$ is the permeability of the membrane, a material parameter that depends on the thickness of the membrane, the pore size, and the viscosity of the liquid. The general case where the membrane is permeable to the solute is discussed in Appendix C but will not be treated in the main text.

Osmotic pressure

If the system is is equilibrium, i.e. if $j_w = 0$, we find that the difference in pressure between the two sides of the membrane is

$$p_1 - p_2 = \mathbb{R}\mathbb{T}(c_1 - c_2) = \Pi \tag{3.7}$$

where $\Pi = \mathbb{R}\mathbb{T}(c_1 - c_2)$ is know as the osmotic pressure.

Entropy production and viscous power dissipation

The volume flux driven by osmotic and hydrostatic pressures is directly related to the entropy production through Eq. (3.3)

$$\mathbb{T}\partial_t s = j'_w \xi_w = A L_p \left(\mathbb{R}\mathbb{T} \left(c_1 - c_2\right) - \left(p_1 - p_2\right)\right)^2, \tag{3.8}$$

We immediately recognize this expression as the rate at which power is dissipated by the flow due to viscous friction inside the membrane.

3.3 Equations of motion for osmotically driven flows

Inspired by the geometry of the sieve tube elements discussed in Chapter 2, we now consider the motion of water and a solute (sugar) inside a long cylindrical tube of radius a as shown in Fig. 3.3. The tube is submerged in a reservoir of water at constant pressure p_2 and constant concentration c_2. For simplicity, we assume that the flow and concentration fields are rotationally symmetric such that the velocity $\mathbf{u}(r,x)$ and solute concentration $c_1(r,x)$ does not depend on the azimuthal position. The solute is moving due to the motion of the liquid and molecular diffusion. The wall of the tube is made from a semipermeable material (a membrane) of permeability L_p that allows water but not the solute to pass. Sugar is loaded/removed from the tube at a rate υ by an active mechanism decoupled from the osmotic pumping. For simplicity, we assume that υ is a function of the axial coordinate x only.

3.3.1 Boundary conditions imposed by osmosis

The presence of the membrane facilitates a flow of water driven by osmotic and hydrostatic pressure differences across the wall. This occurs at a rate given by Eq. (3.6) which imposes a boundary condition on the normal velocity component $\mathbf{n}\cdot\mathbf{u}$ at the membrane interface

$$\mathbf{n}\cdot\mathbf{u} = j_w = L_p(\mathbb{R}\mathbb{T}c - p), \quad \text{for} \quad r = a. \tag{3.9}$$

Here we have used the notation $p = p_1 - p_2$, and $c = c_1 - c_2$, and assume that $\mathbf{n}$ is a normal vector pointing into the tube. Additionally, the tangential velocity component is subject to the no-slip condition at the membrane interface

$$\mathbf{u} - (\mathbf{n}\cdot\mathbf{u})\mathbf{n} = \mathbf{0}, \quad \text{for} \quad r = a. \tag{3.10}$$

Finally, we require that no solute molecules move across the membrane

$$\mathbf{n}\cdot\left(-D\nabla c + c\mathbf{u}\right) = 0, \quad \text{for} \quad r = a, \tag{3.11}$$

where D is the diffusivity of the solute.

3.3.2 Equations of motion governing fluid flow

The motion of an incompressible Newtonian liquid is governed by the Navier-Stokes equation [10]

$$\rho\left(\partial_t\mathbf{u} + (\mathbf{u}\cdot\nabla)\mathbf{u}\right) = -\nabla p + \eta\nabla^2\mathbf{u}, \tag{3.12}$$

where t is time, ρ is the liquid density, η is the liquid viscosity, and the effect of gravity is included in the pressure. Since the liquid is incompressible, conservation of volume requires the solution to fulfill the continuity equation

$$\nabla\cdot\mathbf{u} = 0. \tag{3.13}$$

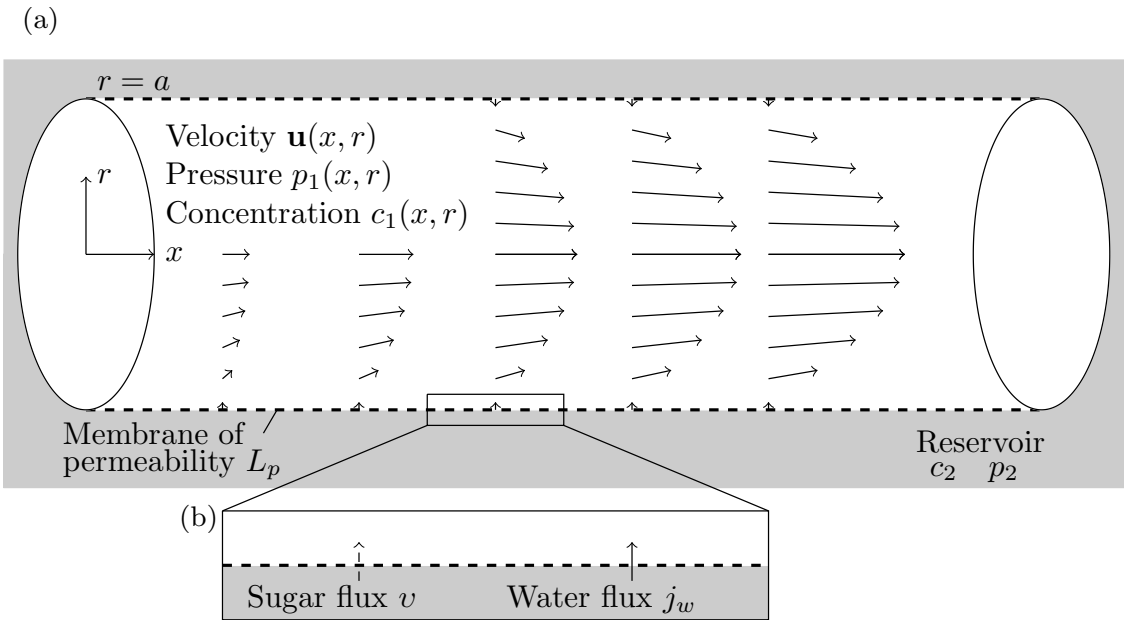

Figure 3.2: Sketch of the geometry used when deriving the equations of motion for osmotically driven flows. (a) An incompressible liquid (e.g. water) is moving inside a cylindrical tube of radius a with velocity $\mathbf{u}$ (arrows). The tube is submerged in a reservoir of water at constant pressure p_2 and constant concentration c_2. A solute of concentration c_1 is dissolved in the liquid and is moving due to the motion of the liquid and molecular diffusion. The tube is submerged in a large reservoir (gray region) and has a walls made from a semipermeable membrane (dashed line) with permeability L_p that allow the liquid but not the solute to pass. (b) Closeup of the situation at the membrane (dashed line). The presence of the membrane facilitates a flow of water driven by osmotic and hydrostatic pressure differences across the wall. This occurs at a rate j_w, given by Eq. (3.6), indicated by the solid arrow at the membrane interface (See Fig. 3.1). Sugar is loaded/removed from the tube at a rate υ by a mechanism decoupled from the osmotic pumping indicated by the dashed arrow. The osmotically driven flow across the membrane accelerates the liquid as it moves along the tube as indicated by the growing size of the arrows in (a).

In cylindrical coordinates these equations are

$$\rho\left(\partial_t u_x + u_r\partial_r u_x + u_x\partial_x u_x\right) = -\partial_x p + \eta\left(\partial_x^2 u_x + \frac{\partial_r u_x}{r} + \partial_r^2 u_x\right), \tag{3.14}$$

$$\rho\left(\partial_t u_r + u_r\partial_r u_r + u_x\partial_x u_r\right) = -\partial_r p + \eta\left(\partial_x^2 u_r + \frac{\partial_r u_r}{r} + \partial_r^2 u_r - \frac{u_r}{r^2}\right), \tag{3.15}$$

$$\partial_x u_x + \frac{u_r}{r} + \partial_r u_r = 0, \tag{3.16}$$

where the velocity $\mathbf{u} = (u_x, u_r)$. The boundary conditions are

$$u_r = -j_w \quad \text{for} \quad r = a, \tag{3.17}$$

$$u_x = 0 \quad \text{for} \quad r = a. \tag{3.18}$$

3.3.3 Equations of motion governing solute transport

The equation of motion for solute transport is the convection-diffusion equation [10]

$$\partial_t c + \mathbf{u}\cdot\nabla c = D\nabla^2 c + \upsilon. \tag{3.19}$$

In cylindrical coordinates this is

$$\partial_t c + u_r\partial_r c + u_x\partial_x c = D\left(\frac{1}{r}\partial_r\left(r\partial_r c\right) + \partial_x^2 c\right) + \upsilon. \tag{3.20}$$

The osmotic boundary condition given in Eq. (3.11) is

$$-D\partial_r c + c u_r = 0 \quad \text{for} \quad r = a. \tag{3.21}$$

3.4 Solution of the coupled concentration-flow problem

In order to obtain a full understanding of the coupled motion of water and the solute one needs to solve Eqns. (3.12) (3.13), and (3.19) with the appropriate osmotic boundary condition in Eqns. (3.9)-(3.11). Due to the coupling of the flow and concentration fields through the boundary conditions this is a formidable mathematical problem which has only been tackled analytically in a few special cases [59, 60, 56, 57, 58, 3, 27]. We we will discuss this in detail in Chapter 8, but for now we proceed by putting the equations of motion on non-dimensional form and applying the conditions relevant to plants.

3.5 Non-dimensional formulation of the equations of motion

To simplify the mathematical treatment of the equations of motion we use non-dimensional variables. Since the osmotically driven flow contains two characteristic velocity scales, the

axial velocity u_x^* and the radial velocity u_r^*, and two characteristic length scales, the tube length l and the tube radius a, we will non-dimensionalize in the following way

$$\begin{aligned} c &= c^* C', && (3.22)\\ u_x &= u_x^* U_X = 2L_p \mathbb{R}\mathbb{T} c^* \frac{l}{a} U_X, && (3.23)\\ u_r &= u_r^* U_R = 2L_p \mathbb{R}\mathbb{T} c^* U_R = \frac{a}{L} u_x^* U_R, && (3.24)\\ t &= t^* T = \frac{l}{u_x^*} T = \frac{a}{2L_p \mathbb{R}\mathbb{T} c^*} T, && (3.25)\\ x &= lX, && (3.26)\\ r &= aR, && (3.27)\\ p &= p^* P = \mathbb{R}\mathbb{T} c^* P, && (3.28)\\ \upsilon &= c^* \frac{2L_p \mathbb{R}\mathbb{T} c^*}{a} \Upsilon, && (3.29)\\ j_w &= 2L_p \mathbb{R}\mathbb{T} c^* J_w. && (3.30) \end{aligned}$$

Here, c^* is the characteristic concentration found in the tube.

3.5.1 Non-dimensional equations of motion for fluid motion

Using these variables, the equations of motion for the fluid motion are

$$H_1 \left(\partial_T U_X + U_R \partial_R U_X + U_X \partial_X U_X\right) = -H_3 \partial_X P + \left(\partial_X^2 U_X + H_4 \frac{\partial_R U_X}{R} + H_4 \partial_R^2 U_X\right), \quad (3.31)$$

$$H_2 \left(\partial_T U_R + U_R \partial_R U_R + U_X \partial_R U_R\right) = -H_3 \partial_R P + \left(\frac{1}{H_4} \partial_X^2 U_R + \frac{\partial_R U_R}{R} + \partial_R^2 U_R - \frac{U_R}{R^2}\right), \quad (3.32)$$

$$\partial_X U_X + \frac{U_R}{R} + \partial_R U_R = 0. \quad (3.33)$$

Here the four non-dimensional groups are

$$\begin{aligned} H_1 &= \frac{\rho u_x^* a}{\eta} = \frac{2\rho L_p \mathbb{R}\mathbb{T} c^* l}{\eta}, && (3.34)\\ H_2 &= \frac{\rho u_r^* a}{\eta} = \frac{2\rho L_p \mathbb{R}\mathbb{T} c^* a}{\eta}, && (3.35)\\ H_3 &= \frac{a}{2L_p \eta}, && (3.36)\\ H_4 &= \left(\frac{l}{a}\right)^2. && (3.37) \end{aligned}$$

H_1 and H_2 are the axial and radial Reynolds numbers which determine the relative importance of viscous and inertial forces. The importance of H_3 and the aspect ratio H_4 will

become clear in Sec. 3.5.5. Using the characteristic values relevant to plants [79]

$$L = 1\text{ m}, \quad a = 10^{-5}\text{ m}, \quad L_p = 5\times10^{-14}\text{ m/(s Pa)}, \quad \eta = 2\times10^{-3}\text{ Pa s},$$
$$\rho = 10^3\text{ kg/m}^3 \quad \text{and} \quad \mathbb{RT}c^* = 1\text{ MPa}$$

we find that

$$H_1 = 5\times10^{-2}, \tag{3.38}$$
$$H_2 = 5\times10^{-7}, \tag{3.39}$$
$$H_3 = 5\times10^{10}, \tag{3.40}$$
$$H_4 = 1\times10^{10}. \tag{3.41}$$

In this limit, the equations of motion simplify to

$$\partial_X P = \frac{2L_p\eta l^2}{a^3}\left(\frac{\partial_R U_X}{R} + \partial_R^2 U_X\right), \tag{3.42}$$
$$\partial_R P = 0, \tag{3.43}$$
$$\partial_X U_X + \frac{U_R}{R} + \partial_R U_R = 0. \tag{3.44}$$

The flow boundary conditions are

$$U_R = -J_W, \quad \text{for} \quad R = 1, \tag{3.45}$$
$$U_X = 0, \quad \text{for} \quad R = 1, \tag{3.46}$$

while the membrane transport equation is

$$J_w(X) = \frac{1}{2}\left(C(X,1) - P\right). \tag{3.47}$$

We note that the system of equations (3.42)-(3.44) corresponds to the Stokes equations in the lubrication limit [5, 3].

3.5.2 Non-dimensional equation of motion for solute transport

In non-dimensional variables, the equation of motion for solute transport is

$$\partial_T C' + U_R\partial_R C' + U_X\partial_X C' = H_5\left(\frac{1}{R}\partial_R\left(R\partial_R C'\right) + \frac{1}{H_4}\partial_X^2 C'\right) + \Upsilon. \tag{3.48}$$

H_4 is the aspect ratio given in Eq. (3.37) and H_5 is an inverse Péclet number

$$H_5 = \frac{D}{u_r^* a} = \frac{D}{2L_p\mathbb{RT}c^* a} = 5\times10^2, \tag{3.49}$$

with $D = 5\times10^{-10}$ m^2/s (Sucrose, [4]). At this point it is tempting to follow Aldis [3] and keep only terms of order H_5 in Eq. (3.48)

$$\frac{1}{R}\partial_R\left(R\partial_R C'\right) = 0. \tag{3.50}$$

This must imply that $C' = C'_0(X)$ if we require that $C'(R=0)$ is finite. Upon reinsertion in Eq. (3.48), this however yields that

$$\partial_T C' + U_X \partial_X C' = \frac{H_5}{H_4} \partial_X^2 C + \Upsilon \tag{3.51}$$

where that the radial diffusion term has now vanished and is clearly not the determining factor.

A more proper way of treating Eq. (3.48) is to consider the radial average of the transport equation, which is relevant since we are primarily interested in the axial transport of solute. Using the bracket notation

$$\langle f(X) \rangle = 2 \int_0^1 f(X,R) R \, \mathrm{d}R, \tag{3.52}$$

for the radial average of f we find from Eq. (3.48) that

$$\partial_T \langle C' \rangle + \partial_X \left(\langle C' U_X \rangle \right) = \frac{H_5}{H_4} \partial_X^2 \langle C' \rangle + \Upsilon. \tag{3.53}$$

Here we have used the osmotic boundary condition

$$-H_5 \partial_R C' + C' U_R = 0, \quad \text{for} \quad R = 1, \tag{3.54}$$

and the divergence equation (3.44) to cancel the radial diffusion terms. Note that $\langle \Upsilon \rangle = \Upsilon$ since the loading rate is independent of R by assumption. Since $\frac{H_5}{H_4} = 5 \times 10^{-8}$ we can safely disregard axial diffusion. Additionally, as we shall see in Chapter 8, the radial concentration distribution is nearly uniform at these low Péclet numbers. This allows us to write $\langle C' U_X \rangle = \langle C' \rangle \langle U_X \rangle$ such that

$$\partial_T \langle C' \rangle + \partial_X \left(\langle C' \rangle \langle U_X \rangle \right) = \Upsilon. \tag{3.55}$$

With the notation $C = \langle C' \rangle$ and $U = \langle U_X \rangle$ this becomes

$$\partial_T C + \partial_X \left(C U \right) = \Upsilon. \tag{3.56}$$

3.5.3 Summary of the non-dimensional equations of motion

In summary, the non-dimensional equations of motion are

$$\partial_X P = \frac{2 L_p \eta l^2}{a^3} \left(\frac{\partial_R U_X}{R} + \partial_R^2 U_X \right), \tag{3.57}$$

$$\partial_R P = 0, \tag{3.58}$$

$$\partial_X U_X + \frac{U_R}{R} + \partial_R U_R = 0, \tag{3.59}$$

$$\partial_T C + \partial_X (C U) = \Upsilon, \tag{3.60}$$

The boundary conditions are

$$U_R = -J_w = -\frac{1}{2} (C - P), \quad \text{for} \quad R = 1, \tag{3.61}$$

$$U_X = 0, \quad \text{for} \quad R = 1. \tag{3.62}$$

3.5.4 Analytical solution of the flow problem

Following Aldis [3] we notice that the flow problem can be solved using a squeeze flow profile

$$U_X(X,R) = 2(1-R^2)\Theta(X), \tag{3.63}$$
$$U_R(X,R) = J_w(X)\left(R^3-2R\right), \tag{3.64}$$

as illustrated in Fig. 3.3. Here, the quantity $\Theta(X)$ is given by

$$\Theta(X) = \Theta_0 + 2\int_{X_0}^{X} J_w(X')\,\mathrm{d}X' = \langle U_X\rangle = U(X), \tag{3.65}$$

and can be though of as an osmotic piston velocity. The constant Θ_0 and the lower limit X_0 on the integral takes into account the situation where only part of the tube is covered by the membrane which starts at $X = X_0$ with a flow profile $U_X(X_0,R) = 2(1-R^2)\Theta_0$. The velocity field given by Eqns. (3.63) and (3.64) fulfills the boundary conditions, the continuity equation and the pressure compatibility condition

$$\nabla \times \nabla^2 \mathbf{U} = 0, \tag{3.66}$$

which since the flow is rotationally symmetric corresponds to

$$\partial_X \partial_R P - \partial_R \partial_X P = 0. \tag{3.67}$$

Note that the solution given in Eqns. (3.63) and (3.64) does not in general fulfill the full Navier-Stokes equation (Eqns. (3.31)-(3.32)) or even the Stokes equation (Eqns. (3.31)-(3.32) with the left hand side put equal to zero).

We are now able to calculate the relation between the axial pressure gradient $\partial_X P$ and the radially averaged axial flow velocity $U(X)$

$$\partial_X P = -\frac{16L_p\eta l^2}{a^3}U(X) = -\frac{8H_4}{H_3}U(X) = M\ddot{u}\,U(X). \tag{3.68}$$

The formula is completely analogous to that found in conventional pipe flows, except for the fact that the axial flow velocity $U(X)$ is a function of the axial coordinate X. The non-dimensional Münch number $M\ddot{u}$ given by

$$M\ddot{u} = \frac{16L_p\eta l^2}{a^3}, \tag{3.69}$$

is discussed in Sec. 3.5.5 below.

3.5.5 The Münch number

The non-dimensional number $M\ddot{u}$ in Eq. (3.68) is known as the Münch number [30, 29]. It that characterizes the relative importance of hydraulic resistance along the tube to the

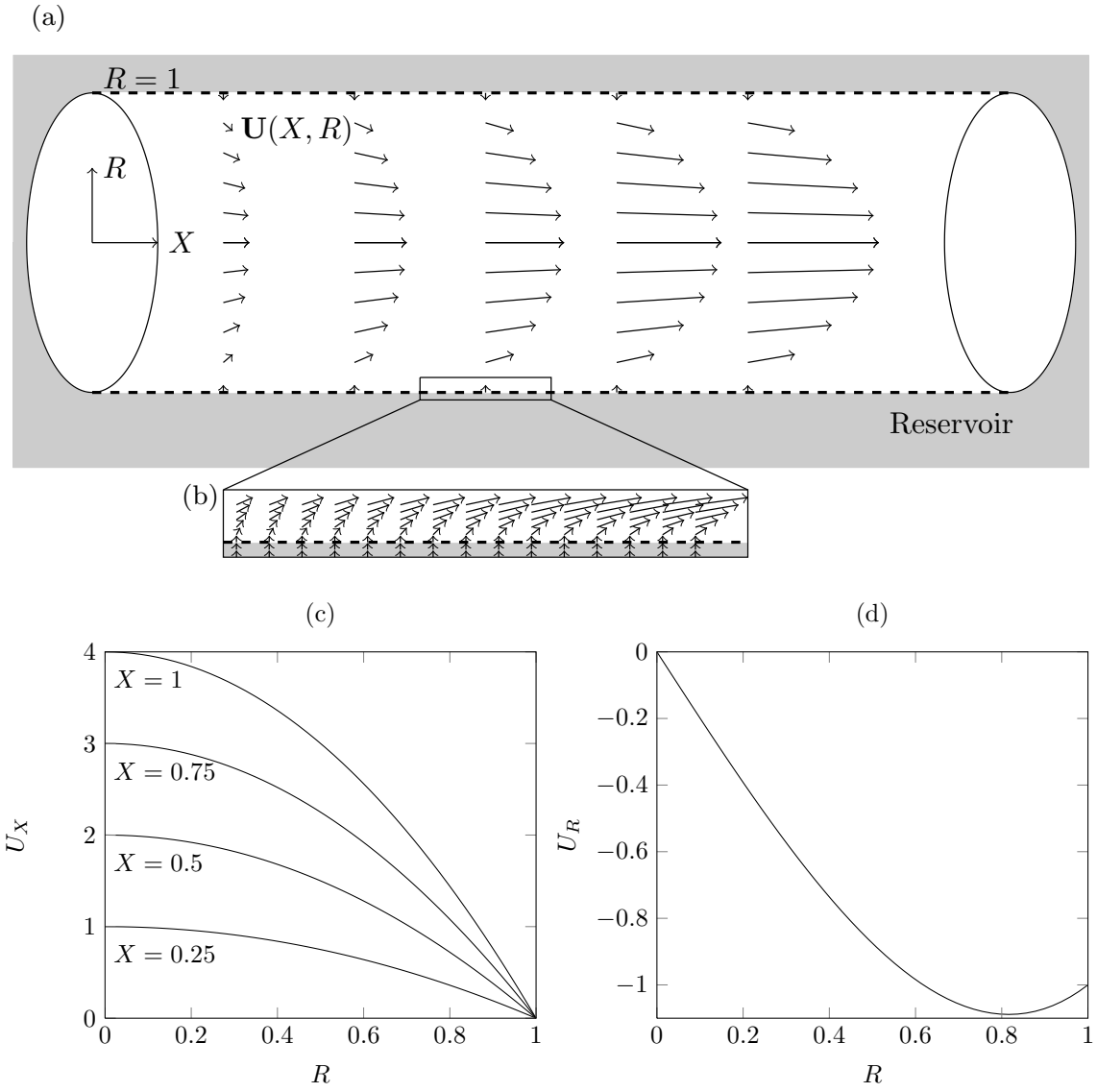

Figure 3.3: Characteristic properties of the osmotically driven pipe flow solution given in Eqns. (3.63) and (3.64). (a) Cross section plot in a vertical plane showing the velocity field $\mathbf{U}(X, R) = (U_X, U_R)$ (arrows) at various position along the tube in arbitrary units. (b) Same as in (a), but showing a closeup of the flow near the membrane interface (dashed line). (c) Axial flow velocity U_X plotted as a function of radius R at the axial positions X indicated below the graphs. (d) Radial flow velocity U_R plotted as a function of radius R. In (c) and (d), $X_0 = \Theta_0 = 0$ and $J_W(X) = 1$. Note that since J_w does not depend on X, the radial velocity U_R shown in (c) is constant as we move along the tube. This is generally not the case.

resistance across the membrane:

$$M\ddot{u} = \frac{8H_4}{H_3} = \frac{\text{Axial flow resistance}}{\text{Membrane flow resistance}} = \frac{\frac{8\eta l}{\pi a^4}}{\frac{1}{2\pi a l L_p}} \tag{3.70}$$

$$= \frac{16 L_p \eta l^2}{a^3}. \tag{3.71}$$

The Münch number is a function of the length of the tube l, the tube radius a, the membrane permeability L_p, and the liquid viscosity η. The product of the two latter parameters itself set a new length scale related to the properties of the membrane as discussed below. Using the values $l = 1$ m, $a = 10$ µm, $L_p = 5 \times 10^{-14}$ m/(Pa s), and $\eta = 2 \times 10^{-3}$ Pas we find that $M\ddot{u} = 1.6$. The magnitude of the Münch number varies greatly among different plant species with typical values between 1 and 10^3 [29].

The length-scale $L_p\eta$

The product $L_p\eta$ present in e.g. Eq. (3.71) has the dimension of length. Using the representative values given above, we find that it is of the order

$$L_p\eta = 10^{-16} \text{ m}. \tag{3.72}$$

A possible physical interpretation of this length is that it is related to the pore size in the semipermeable membrane. If we consider N pores of hydrodynamic radius κ and length ϵ in a membrane of area A the volume flow Q across a membrane subjected to a pressure difference Δp is

$$Q = \frac{\pi \kappa^4}{8\eta\epsilon} N \Delta p. \tag{3.73}$$

The number of pores N is taken to be proportional to $\frac{A}{\pi\kappa^2}$

$$N = \phi \frac{A}{\pi \kappa^2}, \tag{3.74}$$

where ϕ is the covering fraction. Using Eq. (3.74) we can write

$$Q = A\phi \frac{\kappa^2}{8\eta\epsilon} \Delta p. \tag{3.75}$$

From this formula, we identify the number $\phi\frac{\kappa^2}{8\eta\epsilon}$ as the permeability L_p. This means that the product $L_p\eta$ is related to the microscopic length scales in the following way

$$L_p\eta = \phi \frac{\kappa^2}{8\epsilon}. \tag{3.76}$$

At present, the author has no exact knowledge of the magnitude the parameters ϕ, κ and ϵ for the membranes found in phloem cells. If, however, we assume that the hydrodynamic pore size is, say, $\kappa = 0.1$ nm, the thickness of the membrane is $\epsilon = 100$ nm, and that the pores cover 1% of the surface area of the membrane, we find that $\phi\frac{\kappa^2}{8\epsilon} = 1.3 \times 10^{-16}$ m, a value consistent with Eq. (3.72).

3.6 One-dimensional formulation of the equations of motion

With the results derived in the previous sections, we can now present equations of motion for the average axial velocity U, the average pressure P, and the average concentration C. If we differentiate both sides of Eq. (3.65) we find that

$$\partial_X U = C - P. \tag{3.77}$$

With the result derived in Eq. (3.68) that $\partial_X P = -M\ddot{u}\, U$, this can be written as

$$\partial_X^2 U = \partial_x C + M\ddot{u}\, U, \tag{3.78}$$

The equation of motion for the solute is

$$\partial_T C + \partial_X (CU) = \Upsilon \tag{3.79}$$

Eqns. (3.78) and (3.79) constitutes the phloem transport equations used in the literature (see e.g. [79]). As we have seen in Sec. 3.5.4, they represent exact solutions to the equations of motion under appropriate assumptions. In dimensional units, they are

$$\partial_x^2 u = \frac{2L_p}{a}\left(RT\partial_x c + \frac{8\eta}{a^2}u\right), \tag{3.80}$$

$$\partial_t c + \partial_x (cu) = \upsilon, \tag{3.81}$$

which, as shown in Appendix B, are the same equations that Horwitz derived in his 1958 paper [25].

3.7 Application of the equations of motion to translocation processes in plants

We now move on to a discussion of how the equations of motion derived in the previous sections are applied to the processes that occur in plants as discussed in Chapter 2.

The equations of motion given in Eqns. (3.78)-(3.79) have been applied to translocation in the phloem and further analyzed by a large number of workers. Due to the complexity of the equation system, the general approach has been to use numerical methods to solve the problem for a specific set of parameters. For a very thorough review see Thompson and Holbrook [79] and related work in [80, 80, 81, 77, 23, 78]. It is, however, beyond the scope of this thesis to cover all aspect of these models in detail. Instead, we shall proceed by discussing some of the characteristic properties of the models.

3.7.1 An introduction to zone models

Common to the majority of models found in the literature is that they consider the plant as being split into a number of zones each representing different parts of the plant. Typically, three zones are used: A loading zone (the leaf), a translocation zone (the stem), and an unloading zone (the root) as sketched in Fig. 3.4. In the loading zone sugar is first

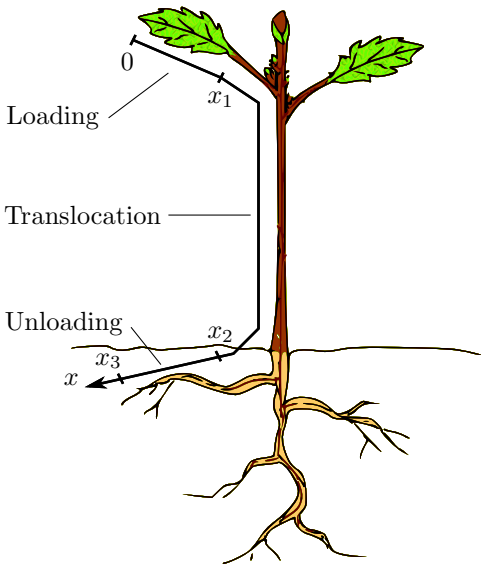

Figure 3.4: Sketch of a zone model for translocation in the phloem. In zone models, we think of the plant as being split into a number of zones representing different parts of the plant. In this case 3 zones are used: A loading zone (the leaf, $0 < x < x_1$), a translocation zone (the stem, $x_1 < x < x_2$), and an unloading zone (the root, $x_2 < x < x_3$). In the loading zone sugar is first secreted into the phloem tube. Driven by the osmotically generated flow, it then enters the translocation zone where no transport of sugar across the membrane takes place. Finally, it reaches the unloading zone where it is removed from the phloem. See also Fig. 1.1, p. 2. Adapted from [29], Fig. 1.

secreted into the phloem tube by a loading mechanism. Pushed forward by the osmotically generated flow, it then enters the translocation zone where no transport of sugar across the membrane takes place. Finally, it reaches the unloading zone where it is removed from the phloem. Between the different zones boundary conditions requiring continuity of the relevant physical quantities: velocity, concentration and pressure etc. are imposed.

In the literature, the translocation zone is always represented by a semipermeable membrane tube covering, say, the interval $x_1 \leq x \leq x_2$ as shown in Fig. 3.4. The mathematical representation of the loading and unloading zones are found in two fundamentally different forms. The first, and most common, introduced by Christy and Ferrier [13], uses a loading zone covering the interval $0 \leq x \leq x_1$ an and unloading zone covering the interval $x_2 \leq x \leq x_3$ as shown in Fig. 3.4. The length of the loading and unloading zones are usually equal and at $x = 0$ and $x = x_3$, the velocity is zero In each of the zones the loading function υ is chosen appropriately among a number of different candidates (see Sec. B.2.1 , p. 121 for examples). The second formulation, used by e.g. Pickard and Abraham-Shrauner [61] and Thompson and Holbrook [80], uses point sources/sinks located at the entrance ($x = x_1$) and exit ($x = x_2$) of the translocation zone. At these points, the injection rate of the concentration c and the velocity u are specified.

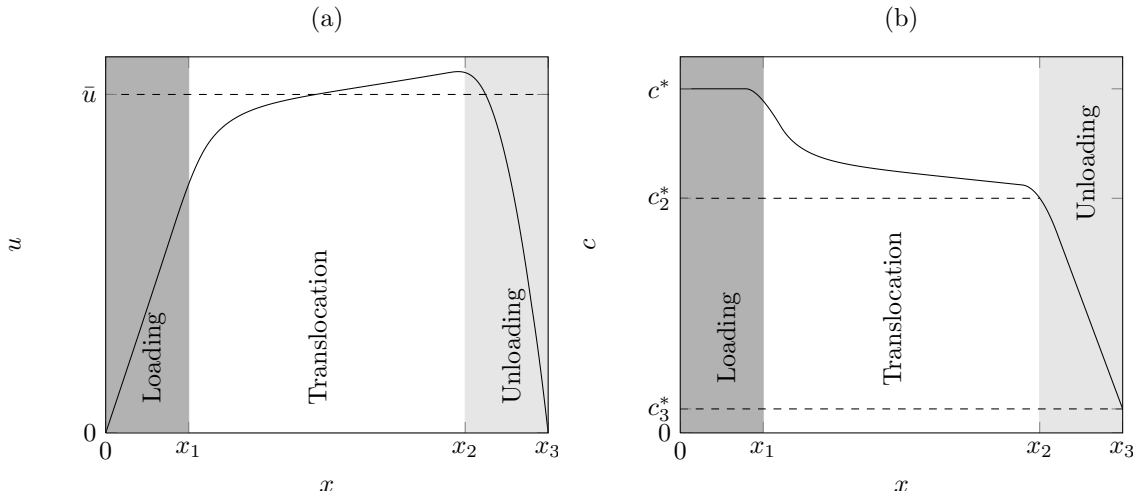

Figure 3.5: Characteristics properties of the velocity u and concentration c derived from numerical solution of zone models. (a) Velocity u (solid line) plotted as a function of axial position x. The characteristic average translocation velocity in the translocation zone $\bar{u}$ is indicated by the dashed line. (b) Concentration c (solid line) plotted as a function of axial position x. The concentrations in the loading zone c^*, at the end of the translocation zone c_2^* and at the end of the unloading zone c_3^* are indicated by dashed lines. See details in Sec. 3.7.2.

3.7.2 Characteristics properties of zone models

Having discussed the different mathematical models used to describe phloem transport is useful to step back and consider a few qualitative properties of the solutions that emerge from these models. Due to the complexity of the equations of motion given in Eqns. (3.80)-(3.81) coupled with the loading function υ, these are typically solved using numerical methods in steady state (i.e. $\partial_t c = 0$) [79]. Largely independent of the choice of loading function υ, the concentration c follows the pattern shown in Fig. 3.5(b). In the loading zone c is nearly constant at a level, say, $c = c^*$. In the translocation zone, the concentration is lowered as we move along the x-axis. This happens because the sugar solution is continually diluted by the influx of water across the membrane due to osmosis. In the unloading zone the concentration decays from an initial level c_2^*, determined by the flow in the translocation zone, to a level c_3^* much smaller than both c_2^* and c^* at the end of the unloading zone. The functional form of the decay depends on the dynamics of the flow problem, but in many cases it approximately linear [84, 70, 79]. In the loading and unloading zones, we can therefore approximate the concentration by

$$c(x) \simeq \begin{cases} c^* & \text{in the loading zone } (0 \le x \le x_1), \\ c_2^* \left(1 - \frac{x - x_2}{x_3 - x_2}\right) & \text{in the unloading zone } (x_2 \le x \le x_3). \end{cases} \tag{3.82}$$

The velocity follows the pattern shown in Fig. 3.5(a). In the loading zone, it rapidly increases due to the osmotic influx across the cell surface in the leaf. As we move along the translocation zone the velocity continues to increase as more and more water enter the translocation stream, although at a much slower pace than in the loading zone. We denote the characteristic velocity in the translocation zone $\bar{u}$. In the unloading zone, water gradually exits the cells before the velocity reaches zero at the end of the unloading zone.

From numerical solutions such as the one sketched in Fig. 3.5, quantitative information about the translocation process for a specific set of parameters (e.g. tube radius a, viscosity η, loading function υ etc.) can be derived. One can, e.g., deduce how fast and how much sugar can be transported from one end of the plant to the other for a specific set of parameters. Due to the very large number of parameters in the problem, however, one cannot in general determine the dependence of, say, the mean translocation speed, on the parameters in the without performing a very large set of simulations.

In Chapter 5 we take advantage of the simple form of the concentration profile given in Eq. 3.82 to determine analytical solutions that provide a thorough understanding of the dependence of the flow pattern on the parameters in the problem.

3.7.3 Common assumptions used in mathematical phloem transport models

In the previous sections, we have presented the zone model framework in which Horwitz's equation of motion (Eqns. (3.80)-(3.81)) are applied to translocation processes in plants. It is a widely debated issue whether this representation is at all meaningful in the sense that it provides an accurate description of the processes that occur in plants. In a recent review paper, Knoblauch and Peters [36] writes that

> While there is no shortage of mathematical formalizations of various aspects of phloem transport..., the question remains whether any such theoretical description mirrors physical reality in a biologically meaningful way can only be decided empirically. ([36], p. 1442)

At this point it is therefore useful to consider the assumptions necessary for the Horwitz zone model framework to be an accurate representation of the processes that occur in plant. A few of the most widely used assumptions are listed below (in *italic*) along with a discussion of their applicability.

1. *The membrane is permeable to water but perfectly impermeable to sugar.* The assumption that the membrane is ideal is generally regarded as valid [51, 73], although allowing for a sugar-permeable membrane does affect the flow, see Appendix C. As we will discuss in Chapter 8, the concentration and flow patterns close to the membrane are, even in the impermeable case, very complicated. See e.g. [15].

2. *The membrane is rigid.* The assumption that the membrane is rigid implies that the radius a of the cells are constant and thus independent of the intracellular pressure p. Thompson and Holbrook investigated the effect of including this by allowing the

radius to vary as $a \propto a_0 \exp(p - p_0)$. They found that it was of "*little biological significance*" ([79], p. 435).

3. *The osmotic pressure is a linear function of the concentration.* At low concentrations, the osmotic pressure of sucrose is proportional to the concentration [47]. At higher concentrations, one must take into account the non-linearity of the osmotic pressure. At $c = 1$ M, this corresponds to a $\sim 10\%$ increase in the osmotic pressure [79].

4. *The viscosity of the liquid does not depend on the sugar concentration.* At low concentrations, the viscosity of the liquid is approximately linear in the sugar concentration and the typical viscosity is $\sim 2 \times 10^{-3}$ Pas. At higher concentration, the viscosity increases exponentially, significantly increasing the hydraulic resistance [7, 79].

5. *The volume of the sugar dissolved in water is negligible.* The partial molar volume of sucrose dissolved in water is 2.2×10^{-4} m^3/mol. A 1 M aqueous solution will thus have a volume $\sim 20\%$ larger than if the volume of the sucrose were neglected. Not including this effect leads to an underestimation of the flow velocity [79].

6. *The velocity field, the concentration, and the pressure are essentially one-dimensional and can each be modelled using a single component.* These assumptions were discussed in Sec. 3.5, and are widely regarded as being valid [79].

7. *There is no interaction between the phloem and the xylem.* As discussed in Sec. 2.3.2, experiments have shown that in many species the interaction between the flow in the phloem and in the xylem does not appear to be significant [89]. Several theoretical workers, however, have claimed otherwise. See e.g. [24].

8. *The concentration of sugar in the tissue surrounding the phloem does not depend on the axial position* This is equivalent to stating that the concentration c_2 in the reservoir surrounding the phloem (Fig. 3.1) is constant. Generally, the argument for the validity of this assumption is that the sugar concentration in the xylem is very low [38]. Other adjacent cells may, however, contain significant amounts of sugar [73] something which may also lead to a change in the pressure inside the sieve tubes [82].

9. *The presence of sieve plates does not affect the flow.* Sieve plates are perforated structures that separate adjacent phloem sieve tube elements. Since only $\sim 50\%$ of their area is open they are bound to impose drag on the flow. It has been speculated that the drag is in fact very large [80], but a thorough analysis of the fluid mechanics of this problem has not been undertaken so far. In Chapter 4 we study this problem in detail.

10. *The phloem can be modeled as a collection of individual phloem tubes spanning the entire length of the plant. There is no interaction between two parallel phloem tubes.* This assumption is almost certainly not valid, since it is well known that flow between adjacent sieve tube elements can occur [73]. On the other hand, the difficulty

in evaluating the quantitative importance of this assumption is that the network structure of the phloem is still largely unknown [36].

It is far from obvious that the assumptions listed above will not have a significant influence on the applicability of the results predicted by the models. Some attempts have been made to resolve this by studying models that take some of the effects described above into account, see e.g. [13, 84, 79, 24]. It is, however, still very difficult to asses which assumptions have the greatest influence on the flow.

To resolve this, one must take one small step at a time. In the following chapter, we thus investigate the effect of the presence of sieve plates on the flow. We do this not because it is necessarily the most important assumption, but because it amenable to a simple physical analysis.

We end by noting that all the above mentioned assumptions pose questions for future research. Among them, the author finds that assumption 10 is of particular interest since the network structure of the phloem and its influence on the flow has not yet been fully understood [36].

3.8 Conclusion

In this chapter, we have studied the fluid mechanics of osmotically driven flows. We have seen that the motion of a solution of water and sugar moving inside the a cylindrical tube with semipermeable walls can be described by two non-dimensional partial differential equations for the average axial velocity U and concentration C:

$$\partial_X^2 U = \partial_x C + M\ddot{u}\, U, \tag{3.83}$$

$$\partial_T C + \partial_X (CU) = \Upsilon. \tag{3.84}$$

The equations depends on a single non-dimensional number $M\ddot{u}$

$$M\ddot{u} = \frac{16 L_p \eta l^2}{a^3}, \tag{3.85}$$

which characterizes the relative importance of hydraulic resistance along the tube to resistance across the membrane. These equations were derived directly from an approximated analytical solution of the Navier-Stokes equation. The validity of this solution depends on the relative size of the non-dimensional groups H_1, H_2, H_3, H_4 and H_5 as discussed in Sec. 3.5.1 and 3.5.2.

We have further discussed how the equations of motion for osmotically driven flows are applied to phloem transport in the literature. We have presented some of the characteristic results that come out of these models, and have found that many of these models, although quantitatively different, display many of the same qualitative features. Of particular importance is the realization that most models yields concentration and velocity profiles similar to those shown in Fig. 3.4. This permits us to describe the concentration in a very simple manner in the loading and unloading zones, cf. Eq. (3.82), thus simplifying the mathematical treatment of the equations of motion significantly.

Further, we have discussed some of the necessary assumptions for the equations of motion to be a relevant physical representation of the processes that occur in plants. The qualitative and quantitative effects of many of these on the translocation process are still unresolved, and pose significant questions for future research in the field.

Chapter 4

The effect of sieve plates on the hydraulic resistance of the phloem translocation pathway

In Chapter 3 we derived one-dimensional equations of motion for osmotically driven flows in cylindrical semipermeable tubes. By looking at Fig. 2.2(b)-(d) on page 10 it quickly becomes apparent that the phloem sieve tube elements put together do not simply constitute one, long, continuous cylindrical tube. Rather, it consists of individual cells separated by sieve plates the presence of which may contribute significantly to the overall hydraulic resistance of the translocation pathway

No proper fluid mechanical analysis of this problem has been published so far, in part due to the lack of reliable anatomical data on the structure of the sieve plates. Such data has been made available recently by Mullendore *et al.* [48] and the author is in great depth to Daniel Mullendore and Michale Knoblauch (Washington State University) for making these available to the present study. In this chapter we thus consider the effect of sieve plates on the flow inside the phloem sieve tubes. We show that the presence of the plates impose a significant amount of additional drag on the liquid.

The analysis of the hydraulic resistance of sieve plates presented in this chapter is due to the author and constitutes work in progress. A manuscript written in collaboration with Daniel Mullendore, Michael Knoblauch, Noel Michele Holbrook, Tomas Bohr and Henrik Bruus is currently under preparation for submission to a peer-reviewed journal.

4.1 Introduction to sieve plates

In the previous chapter, we saw that the equations of motion for the flow of water and sugar through the phloem depends on the non-dimensional Münch number $M\ddot{u}$

$$M\ddot{u} = \frac{\text{Axial flow resistance}}{\text{Membrane flow resistance}} = \frac{\mathcal{R}}{\mathcal{R}_M} = \frac{16 L_p \eta l^2}{a^3}, \tag{4.1}$$

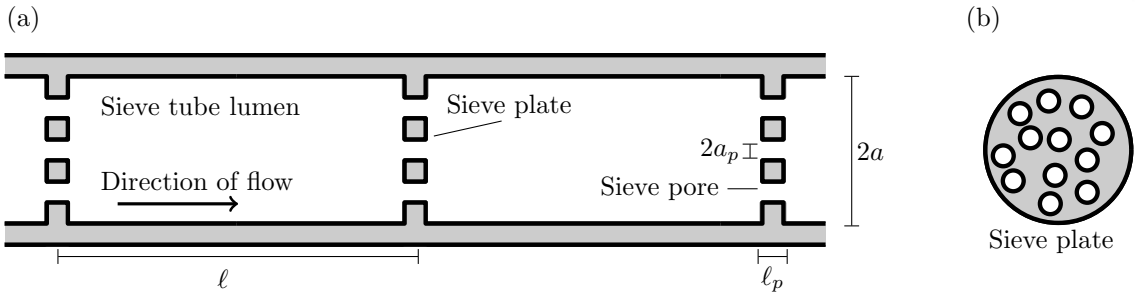

Figure 4.1: Sketch of the phloem sieve tube element geometry. (a) Adjacent sieve tube elements of length ℓ and radius a are separated by thin sieve plates of length ℓ_p perforated by small holes with radius a_p known as sieve pores. (b) End view of a sieve plate. See Fig. 4.2 for examples of sieve plate structures found in plants.

where $\mathcal{R}$ is the axial and $\mathcal{R}_M$ is the membrane hydraulic resistance of the phloem respectively.

As sketched in Fig. 4.1, adjacent phloem cells are separated by thin sieve plates perforated by small holes known as sieve pores. The plates are believed to impose a significant amount of drag [80] thus leading to an increase in $\mathcal{R}$ and *Mü*. Using a novel visualization method Mullendore *et al.* [48] recently investigated the detailed structure of cell walls and sieve plates using scanning electron microscopy as shown in Fig. 4.2. Using their data, we are able to quantify this increase in resistance.

4.2 Characteristic properties of the flow inside sieve tube elements

The data given in Table 4.1, collected by Mullendore *et al.* [48] and Thompson and Holbrook [80], shows that the sieve tube elements has a radius a of about 10 µm and a length ℓ of $0.1 - 1$ mm. Each sieve plate has $50 - 400$ approximately circular pores evenly distributed to cover $\sim 50\%$ of the plate area. The mean radius of the pores $\bar{a}_p$ vary from $0.1 - 2.5$ µm and the radii of the individual pores are normally distributed with a standard deviation σ_p of about $0.25\bar{a}_p$. The thickness of the plate ℓ_p is comparable in size to the radius of the pores.

To characterize the flow inside the sieve tube element, we consider first the situation in the sieve tube lumen, i.e. far away from the sieve plate. The lumen Reynolds number Re_l is given by

$$Re_l = \frac{\rho u_l a}{\eta}, \tag{4.2}$$

where u_l is the characteristic flow velocity inside the cell lumen. From Table 2.1, p. 11, we find that $u_l \simeq 2.8 \times 10^{-4}$ m/s. With $a = 10^{-5}$ m, $\eta = 2 \times 10^{-3}$ and $\rho = 10^3$ kg/m^3 we have that

$$Re_l = 1.4 \times 10^{-3}. \tag{4.3}$$

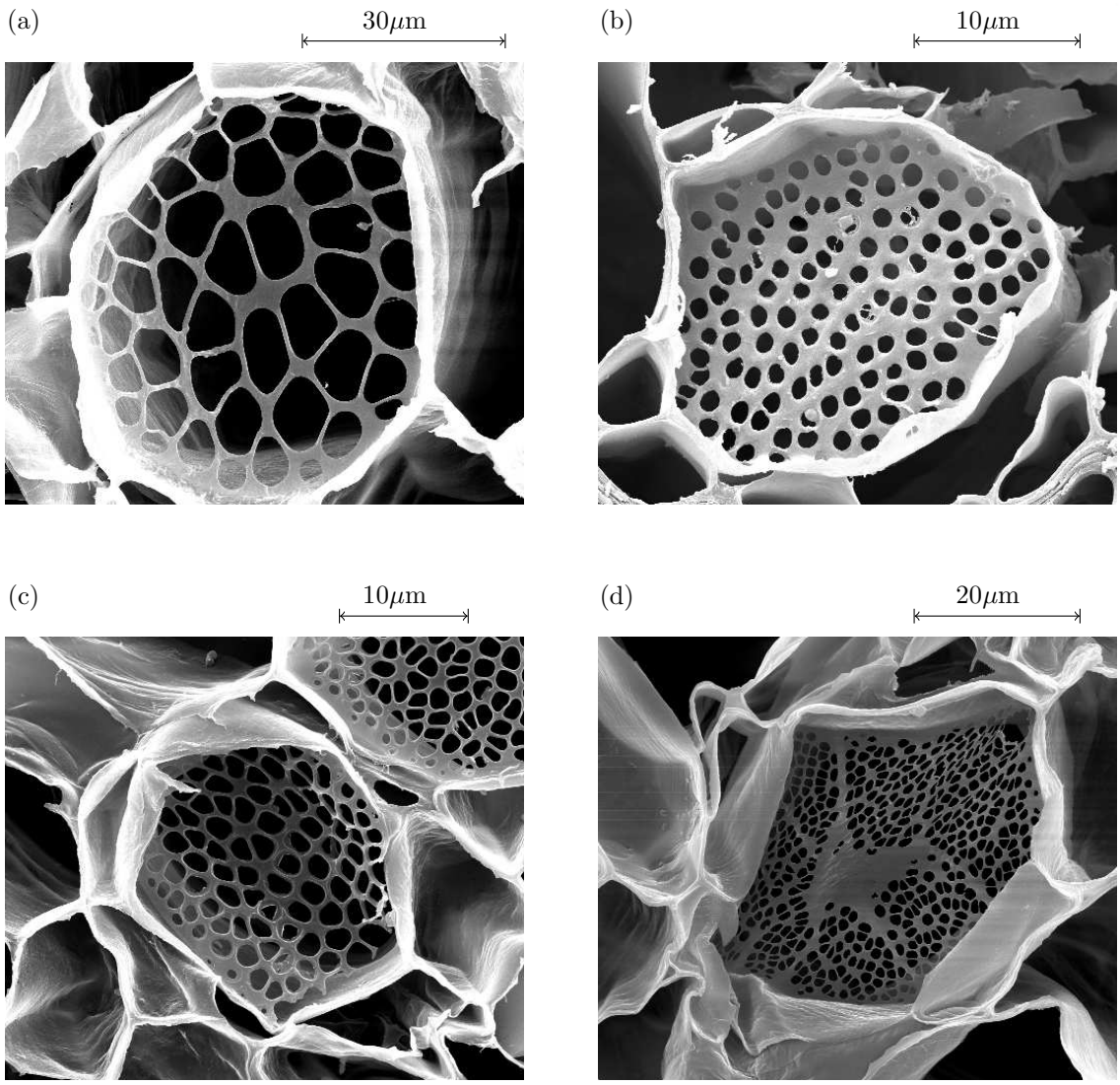

Figure 4.2: Scanning electron microscope (SEM) images of sieve plates. (a) *Curcubita maxima* (Squash). (b) *Phyllostachys nuda* (Bamboo). (c) *Phaseolus vulgaris* (Green bean). (d) *Ricinus communis* (Castor bean). On average, about 50% of the sieve plate area is covered by open pores. SEM images courtesy of M. Knoblauch and D. L. Mullendore [48]. Reproduced with permission.

Table 4.1: Sieve tube element data from [48](1-5) and [80](6-19). Sieve tube radius a, sieve tube element length ℓ average pore radius $\bar{a}_p$, pore thickness ℓ_p, and number of pores per plate N_p.

No.	Species	a [μm]	ℓ [μm]	$\bar{a}_p$ [μm]	ℓ_p [μm]	N_p
1	*Cucurbita maxima*	25.65 ± 2.97	341 ± 77	2.54 ± 0.86	1.27 ± 0.29	54.8 ± 11.9
2	*Phaseolus vulgaris*	10.13 ± 1.13	140 ± 38	0.73 ± 0.24	0.43 ± 0.11	95.4 ± 31.7
3	*Solanum lycopersicum*	10.70 ± 1.40	130 ± 90	0.61 ± 0.15	0.52 ± 0.12	121.3 ± 30.0
4	*Ricinus communis*	16.22 ± 1.60	255 ± 122	0.52 ± 0.14	0.24 ± 0.05	371.9 ± 79.0
5	*Phyllostachys nuda*	11.60 ± 1.00	1052 ± 244	0.61 ± 0.13	0.39 ± 0.10	105.6 ± 12.7
6	*Pinus strobus*	10.9	1580	0.35	2.5	720
7	*Festuca arundinacea*	3	100	0.3	0.5	33
8	*Beta vulgaris*	5	200	0.1	0.4	1250
9	*Glycine max* (petiole)	4.2	125	0.35	1.1	58
10	*Glycine max* (stem)	6.6	156	0.6	1.2	81
11	*Glycine max* (root)	5.1	137	0.5	1.0	60
12	*Gossypium barbadense*	11	210	0.5	1.0	160
13	*Sabal palmetto*	18	700	0.95	0.5	287
14	*Yucca flaccida*	10	460	0.26	0.4	1746
15	*Robinia pseudoacacia*	10	180	1.25	0.5	21
16	*Tilia americana*	15	350	0.6	0.8	625
17	*Ulmus americana*	18	190	2.0	1.0	50
18	*Cucurbita melopepo*	40	250	2.4	0.5	120
19	*Vitis vinifera*	18	500	0.7	3.5	661

For the flow close to a sieve plate we use the plate Reynolds number Re_p

$$Re_p = \frac{\rho u_p a_p}{\eta}. \tag{4.4}$$

Here, a_p is the radius of the pores and u_p is the flow velocity inside the pores. If the pores cover 50% of the plate area, u_p is twice as large as the lumen velocity, i.e. $u_p = 2u_l$. If the pore radius a_p is, say, 10 times smaller than the cell radius a, we find that the pore Reynolds number Re_p is

$$Re_p = 2.8 \times 10^{-4}. \tag{4.5}$$

Both Reynolds numbers Re_l and Re_p are sufficiently small that we may treat the flow inside the cells as Stokes flow. This corresponds to ignoring the left-hand side of the Navier-Stokes Eqns. (3.14)-(3.15), an approximation which simplifies the problem considerably.

4.2.1 Previous work on Stokes flow through small pores

A large number of workers have studied Stokes flow through small pores both experimentally and theoretically. Using an elegant experiment, Johansen [34] found that for $Re_p \leq 30$ the flow close to a pore is left-right symmetric and laminar[1]. He also found that the length of the region upstream affected by the presence of the pore is very short, and roughly equal to the pore diameter $2a_p$.

[1] In fact, it remains laminar until $Re_p \simeq 10^3$ but symmetry is broken above $Re_p = 30$.

Theoretically, low Reynolds number flow through pores have been studied extensively for very short pores [66, 65, 20, 33, 86] and for pores of finite length [14]. Most relevant to the present discussion is the work of Dagan *et al.* who showed in [14] that to within an accuracy of 1% the resistance of a single pore $\mathcal{R}_{p,1}$ of finite length ℓ_p in an infinite plane is given by

$$\mathcal{R}_{p,1} = \frac{8\eta\ell_p}{\pi a_p^4} + \frac{3\eta}{a_p^3}. \tag{4.6}$$

The first term on the right-hand side is the well-know formula for the resistance of a cylindrical pipe. The second term represents the resistance of a pore in an infinitely thin plate and was first derived for a circular pore by Sampson [66] and later generalized to other shapes by Roscoe [65] and Hasimoto [20].

In plants, the sieve plate and pores are embedded in a larger circular tube. The effect of the surrounding pipe walls on the resistance of the pore was studied by Jeong [33] and shown to be negligible as long as $\frac{a_p}{a} \leq 0.3$. The effect of neighboring pores was investigated semi-analytically by Wang [86] who showed that the resistance differed only by a few percent from that found in Eq. (4.6) for covering fractions less than $\leq 50\%$.

4.2.2 Numerical simulation of the flow close to a sieve plates

To test the applicability of the results found in the literature we have conducted numerical simulations of the flow through sieve plates. Using COMSOL 3.5a, a commercial computational fluid dynamics software package, we have calculated numerical approximations to the flow in the Stokes flow approximation using a 3-D version of the finite-element solver used in [27], see Chapter 8. The procedure for importing the actual sieve plate structures into the simulation workspace is shown in Fig. 4.3. After a careful meshing procedure and a thorough convergence analysis we find flow patterns similar to those shown in Fig. 4.4. An important qualitative feature of the flow is that it is relatively undisturbed until a very short distance from the plate. This distance is of the order $2\bar{a}_p$, the mean diameter of the pores, in good agreement with the results found by Johansen [34]. Close to the plate the flow is disturbed by the presence of the plate and the fluid must change direction in order to pass through the pores. This phenomena gives rise to the Sampson-term $\frac{3\eta}{a_p^3}$ in Eq. (4.6).

4.3 Hydraulic resistance of sieve tubes

We shall now proceed to calculate the hydraulic resistance of a single sieve tube element which consists of two parts: A cell lumen and a sieve plate as shown in Fig. 4.1. When calculating the hydraulic resistance of the tube $\mathcal{R}_t$, we thus consider two resistances acting in series

$$\mathcal{R}_t = \mathcal{R}_l + \mathcal{R}_p, \tag{4.7}$$

where $\mathcal{R}_l$ is the resistance of the cell lumen and $\mathcal{R}_p$ is the resistance of the sieve plate.

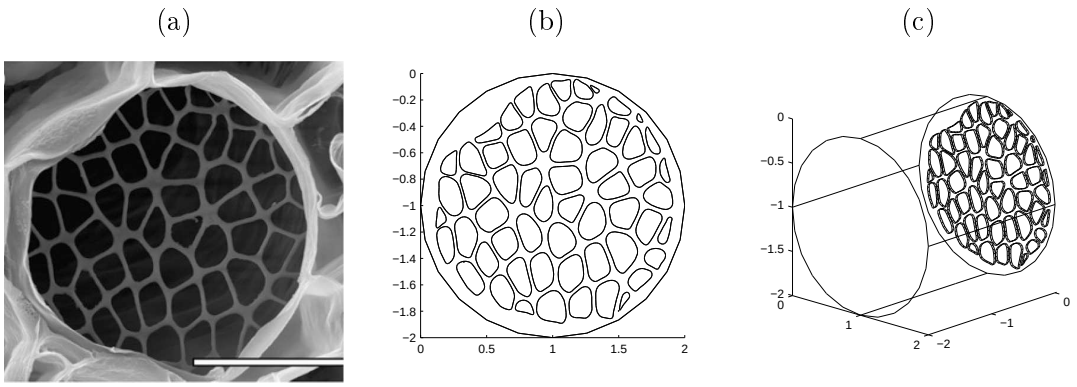

Figure 4.3: Procedure for preparing numerical simulations of flow through sieve plates. In (a), a SEM image of a sieve plate found in *Curcubita maxima* is shown. From [48], scale bar 20 μm. In (b), a front view of the extracted pore structure is shown. In (c), the plate has been place inside a 3-D cylindrical tube, ready for use in COMSOL 3.5a. The results of the simulation can be found in Fig. 4.4.

4.3.1 Hydraulic resistance of the cell lumen

For a cylindrical cell of length ℓ and radius r, the hydraulic resistance is given by [10]

$$\mathcal{R}_l = \frac{8\eta\ell}{\pi r^4}. \tag{4.8}$$

4.3.2 Hydraulic resistance of the sieve plate

In the literature, several different methods for calculating the resistance of a sieve plates have been proposed [80, 48]. Generally, the idea is to consider the plate as a collection of individual pores acting in parallel. This gives a hydraulic resistance of

$$\mathcal{R}_p = \left(\sum_{i=1}^{N_p} R_{P,i}^{-1} \right)^{-1}, \tag{4.9}$$

where $R_{P,i}$ is the hydraulic resistance of each individual pore. Thompson and Holbrook [80] suggests that one uses

$$\mathcal{R}_{p,i}^{T} = \frac{8\eta\ell_p}{\pi\bar{a}_p^4} + \frac{3\eta}{\bar{a}_p^3}. \tag{4.10}$$

This takes into account both terms found by Dagan *et al.* in Eq. (4.6) but uses the mean value of the pore radius $\bar{a}_p$ rather than taking the sum over the individual pores, an approach used, presumably because only the mean value of pore radii was not known at the time.

Having measured the sizes of 10^4 individual pores, the summation approach was used recently by Mullendore [48] who suggested that the resistance of each individual pore $R_{P,i}$

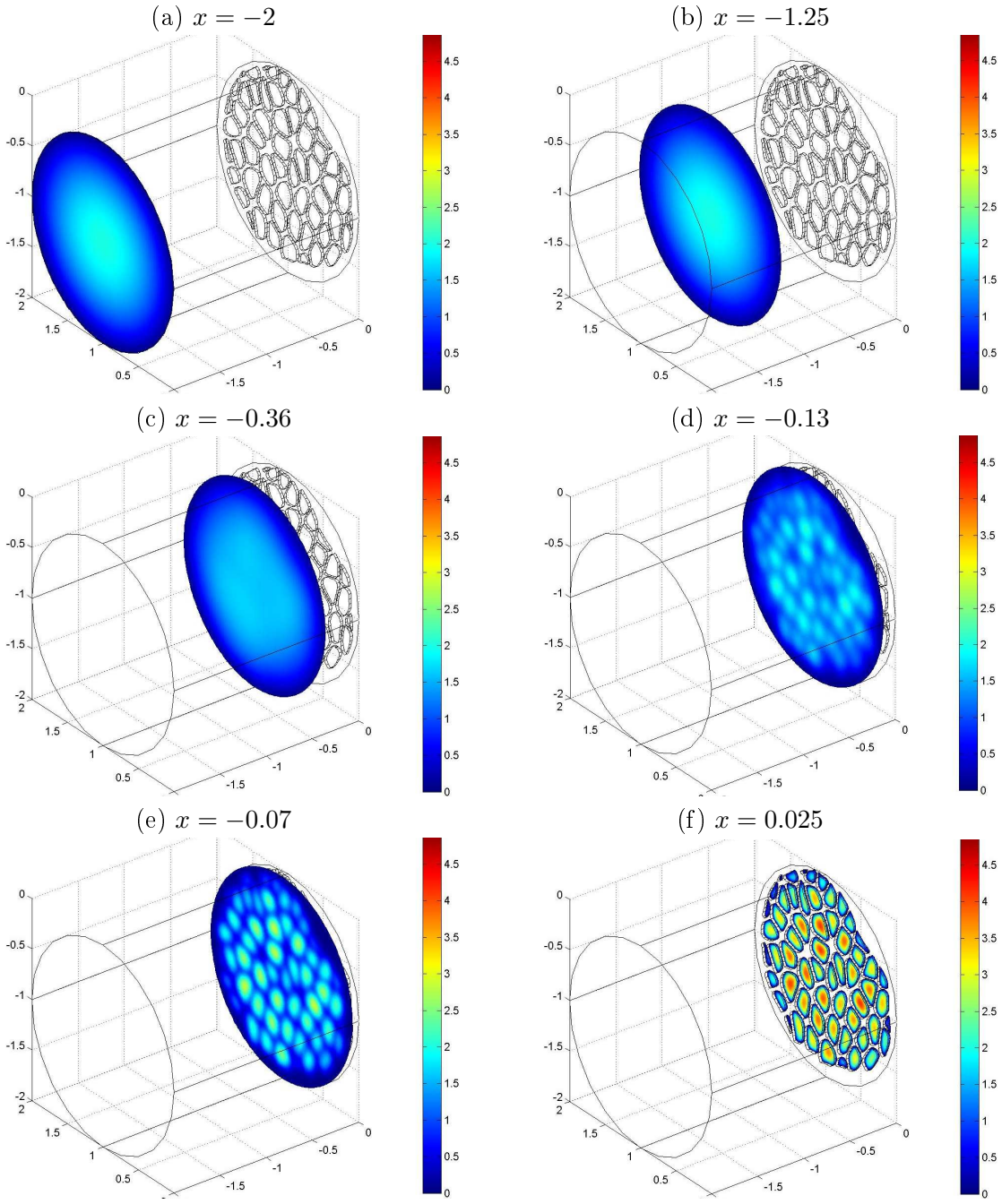

Figure 4.4: Numerical simulation of flow close to a *Curcubita maxima* sieve plate. The liquid is moving from left to right. (a)-(f) Contour plot of the magnitude of the flow velocity (red fast, blue slow in arbitrary units) at the positions indicated above the plots. The pores start at $x = 0$ and have a typical diameter of 0.1 in these units. The flow profile in (a) and (b) is the well known parabolic profile found in pressure driven pipe flows. Close to the sieve plate (c)-(f), the flow is disturbed by the presence of the plate and the fluid must change direction in order to pass through the pores (f).

could be written as

$$\mathcal{R}_{p,i}^{M} = \frac{8\eta\ell_p}{\pi a_{p,i}^4} \tag{4.11}$$

such that the sum in Eq. (4.9) is taken over the individual pores of differing radii. Compared to Eq. (4.6) this, however, only takes into account the first term in Dagans formula.

Taking both effects into account, we propose that a more accurate way of calculating $R_{P,i}$ is to use

$$\mathcal{R}_{p,i} = \frac{8\eta\ell_p}{\pi a_{p,i}^4} + \frac{3\eta}{a_{p,i}^3}. \tag{4.12}$$

To get an idea of the quantitative difference between Eqns. (4.10), (4.11) and (4.12) we consider the data given in Appendix D. Here the radii of the pores from the *Curcubita maxima* sieve plate shown in Fig. 4.2(a) are given. We find that

$$\mathcal{R}_p^T = 6.14 \times 10^{12} \text{ Pa s/m}^3, \tag{4.13}$$

$$\mathcal{R}_p^M = 7.49 \times 10^{11} \text{ Pa s/m}^3, \tag{4.14}$$

$$\mathcal{R}_p = 4.21 \times 10^{12} \text{ Pa s/m}^3, \tag{4.15}$$

calculated with $\eta = 2 \times 10^{-3}$ Pa s. We observe that both $\mathcal{R}_p^T$ and $\mathcal{R}_p^M$ differ significantly from $\mathcal{R}_p$, being that they are 1.5 times larger and 5 times smaller than $\mathcal{R}_p$ respectively.

4.3.3 Hydraulic resistance of the sieve tube system

With the results derived in Eqns. (4.8) and (4.12) we have for the total tube resistance $\mathcal{R}_t$ that

$$\mathcal{R}_t = \frac{8\eta\ell}{\pi a^4} + \left(\sum_{i=1}^{N_p} \left(\frac{8\eta\ell_p}{\pi a_{p,i}^4} + \frac{3\eta}{a_{p,i}^3} \right)^{-1} \right)^{-1}. \tag{4.16}$$

An important observation is that with the knowledge that the pore radii are normally distributed with mean $\bar{a}_p$ and standard deviation σ_p we can approximated this by

$$\mathcal{R}_t \simeq \frac{8\eta l}{\pi a^4} + \left(N_p \int_0^\infty \mathfrak{p}(a_p) \left(\frac{8\eta l_p}{\pi a_p^4} + \frac{3\eta}{a_p^3} \right)^{-1} \mathrm{d}a_p \right)^{-1}, \tag{4.17}$$

where $\mathfrak{p}(a_p)$ is normal probability density function

$$\mathfrak{p}(a_p) = \frac{1}{\sqrt{2\pi\sigma_p^2}} \exp\left(-\frac{(\bar{a}_p - a_p)^2}{2\sigma_p^2} \right). \tag{4.18}$$

For the data given in Appendix D, the expression in Eq. (4.17) gives $\mathcal{R}_p = 4.12 \times 10^{12}$ Pa s/m^3, very close to the value in Eq. (4.15).

4.4 On the relationship between lumen and plate resistance

Having established Eq. (4.17) as an approximate expression for the resistance of the sieve tube, we can now apply it to the data in Table 4.1. To best interpret the results, we calculate the lumen and plate parts separately and compare their magnitudes. In Fig. 4.5, the sieve plate resistance $\mathcal{R}_p$ is plotted as a function of the lumen resistance $\mathcal{R}_l$. Both were calculated from Eq. (4.17) using data from table 4.1 and under the assumption that $\eta = 2 \times 10^{-3}$ Pa s. For data points 6–19 we assume that $\sigma_p = 0.25\bar{a}_p$.

By looking at the plot, we observe what appears to be a linear relation between the two, i.e. $\mathcal{R}_p \propto \mathcal{R}_l$. A least squares regression [75] gives

$$\mathcal{R}_P = (2.54 \pm 0.42)\mathcal{R}_L, \tag{4.19}$$

with a correlation coefficient of $r_c = 0.78$ While the trend of the plot in Fig. 4.5 is clear, it is obvious that many effects are influencing the relation between plate and lumen resistance. As an example it is interesting to consider, say, plant no. 13 which is *Sabal palmetto*, a palm tree that lies some distance from the $\mathcal{R}_P = 2.54\mathcal{R}_L$ line. In this plant the sieve tubes are found inside the stem, rather than right under the bark which is usually the case in trees, and are thus mechanically protected against insects and other predators [22]. This may in part explain why it has such a relatively low plate resistance.

One may, however, speculate that Eq. (4.19) points in the direction of the existence of a general allometric scaling law for the sieve plate resistance. Such a law is known to exist for the xylem, where structures similar to sieve plates also separate adjacent vascular cells. Sperry *et al.* found that $R_P \simeq R_L$ [71]. The reasoning behind this is, in simple terms that the relation $R_P \simeq R_L$ minimizes the hydraulic resistance of the xylem. At present, this type of argument does not seem to be applicable to the phloem.

4.4.1 Effective hydraulic resistance

As a consequence of Eq. (4.19) we conclude that the hydraulic resistance of the phloem translocation pathway is significantly increased by the presence of the sieve plates. On average, the resistance is 3.5 times higher than the lumen resistance.

$$\mathcal{R}_t = \mathcal{R}_L + \mathcal{R}_P = 3.5R_L = 3.5\frac{8\eta\ell}{\pi a^4}. \tag{4.20}$$

We can thus think of the viscosity as being 3.5 times higher due to the presence of the sieve plates. Writing $\eta_{\text{eff}} = 3.5\eta$ we find that

$$\mathcal{R}_t = \frac{8\eta_{\text{eff}}\ell}{\pi a^4}. \tag{4.21}$$

This increase in effective viscosity means that the Münch number given in Eq. (4.1) is effectively 3.5 times larger since it should include the effect of the added viscosity. From now on we thus write

$$M\ddot{u} = \frac{16L_p\eta_{\text{eff}}L^2}{a^3}. \tag{4.22}$$

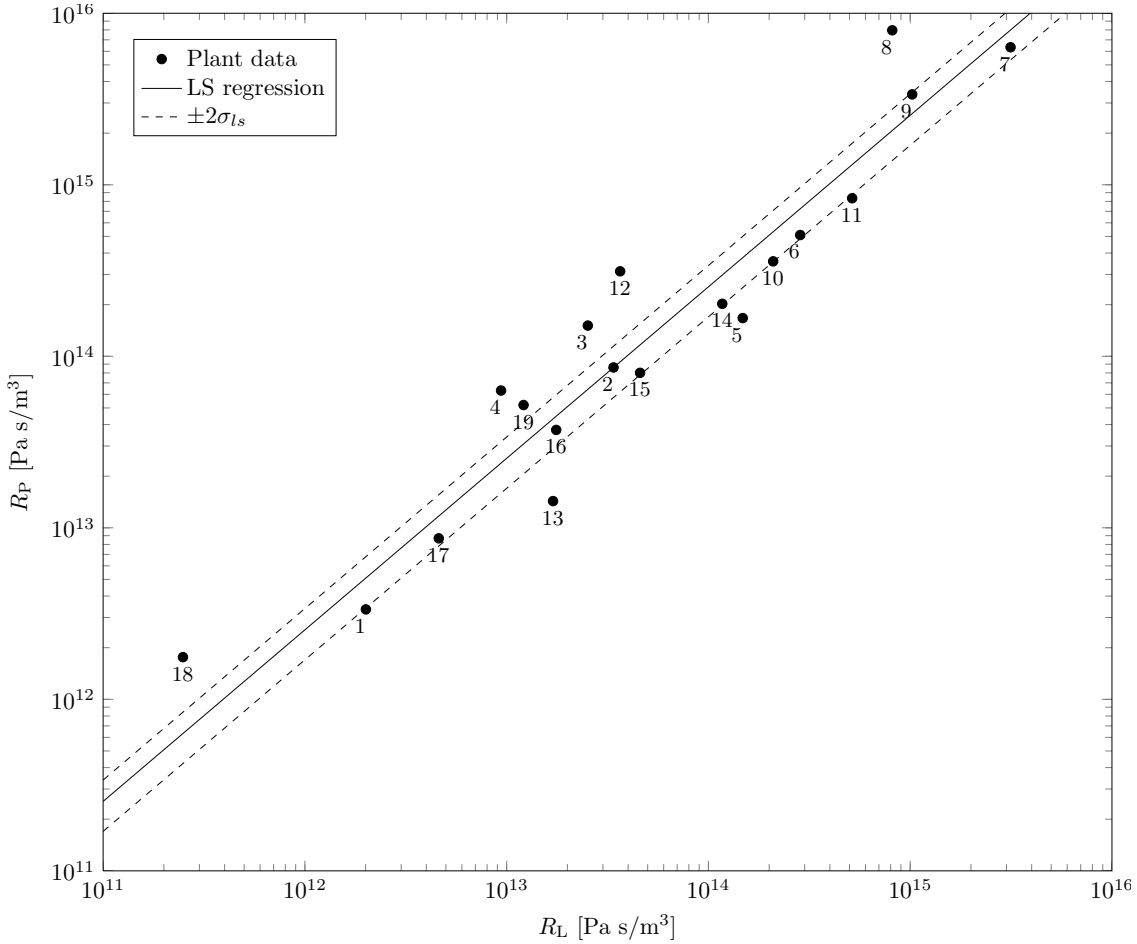

Figure 4.5: Comparative analysis of end wall resistivity in phloem sieve tubes. The sieve plate resistance R_P is plotted as a function of the lumen resistance R_L calculated from Eq. (4.17) using the data in Table 4.1. For data points $6-19$, we assume that $\sigma_p = 0.25\bar{a}_p$. A least squares regression gives $R_P = (2.54 \pm 0.42)R_L$ with $r_c = 0.78$.

4.5 Conclusion

I this chapter, we have studied the effect of sieve plates on the hydraulic resistance of the phloem translocation pathway. We have derived an analytical expression for the resistance based on fact that the flow occurs at low Reynolds numbers and that the pore radii are normally distributed.

Using published data on the structure of sieve plates, we have found an approximately linear relationship between the plate $\mathcal{R}_p$ and lumen $\mathcal{R}_l$ resistance: $\mathcal{R}_P = (2.54 \pm 0.42)\mathcal{R}_L$. This implies that the presence of sieve plates increases the hydraulic resistance of the entire sieve tube element by a factor of ~ 3.5. In the context of the one-dimensional equations of motion derived in Chap. 3 we include this effect by introducing an effective viscosity $\eta_{\text{eff}} = 3.5\eta$ into the Münch number cf. Eq. (4.22).

Chapter 5

Mathematical analysis of the equations of motion

In this chapter we study analytical and numerical solutions to the steady-state one-dimensional equations of motion derived in Chapter 3. The equations are analyzed in a zone model using first a simple hydraulic resistor model and second a full analytical solution in the limits $M\ddot{u} \ll 1$ and $M\ddot{u} \gg 1$. The dependence of the average axial translocation velocity $\bar{U}$ on the parameters in the problem is determined in the form of an approximate analytical expression for the full range of $M\ddot{u}$ numbers.

The solutions to the equations of motion was derived by the author in collaboration with Tomas Bohr and Henrik Bruus. A condensed version of the derivation was published in [29]. Additional technical details of the analytical solution procedure can be found in Appendix A.

A detailed treatment of time dependent osmotic flows was published in [30] (see Appendix E) and will not be covered in the main text.

5.1 The 3–zone model

5.1.1 Formulation of the 3–zone model

In this chapter we think of the plant as being split into three zones as shown in Fig. 3.4, p. 32. Specifically we use a loading zone (zone 1, $0 < x < x_1$) of length l_1, a translocation zone (zone 2, $x_1 < x < x_2$) of length l_2 and an unloading zone (zone 3, $x_2 < x < x_3$) of length l_3. We use the boundary conditions $u(0) = u(x_3) = 0$ and require that the velocity and its first derivative with respect to x is continuous across all internal boundaries. By Eq. (3.77), p. 31, this assumption implies that the pressure p and concentration c is also continuous across the internal boundaries. Further, we assume that the concentration c can be written as

$$c(x) \simeq \begin{cases} c^* & \text{in zone 1 } (0 < x < x_1), \\ c_2^* \left(1 - \frac{x - x_2}{x_3 - x_2}\right) & \text{in zone 3 } (x_2 < x < x_3), \end{cases} \tag{5.1}$$

where c^* is the characteristic concentration found in the loading zone and c_2^* is the concentration at the entrance to the unloading zone. The equations of motion were derived in Chapter 3 and are give by

$$\partial_x^2 u = \frac{2L_p}{a}\left(\mathbb{R}\mathbb{T}\partial_x c + \frac{8\eta_{\text{eff}}}{a^2}u\right), \tag{5.2}$$

$$\partial_x(cu) = \upsilon \tag{5.3}$$

The loading υ rate is not explicitly specified, but assumed to lead to concentration profiles of the form given in Eq. (5.1). Note that we now use the effective viscosity η_{eff} introduced in Chapter 4 to take the effect of sieve plates into account.

To be able to compare the results of this model to velocity measurements made on plants we define the average translocation velocity $\bar{u}$ to be the mean value of the velocity in the translocation zone as

$$\bar{u} = \frac{1}{x_2 - x_1}\int_{x_1}^{x_2} u(x)\,\mathrm{d}x. \tag{5.4}$$

The goal of the following mathematical analysis will be to determine this velocity as a function of the parameters in the problem.

5.1.2 A simplified mathematical treatment

Before we move on to a rigorous mathematical treatment of the model, we will try to described the flow in a simple manner, so as to get an idea of what kind of results we should expect from the full model. Let us therefore consider the phloem translocation pathway as a series of hydraulic resistances (see e.g. [10]) that the water has to overcome in order to move from source to sink. The three resistances are

$$\mathcal{R}_1 = \frac{1}{2\pi a l_1 L_p} + \frac{8\eta_{\text{eff}} l_1}{\pi a^4} \simeq \frac{1}{2\pi a l_1 L_p}, \tag{5.5}$$

$$\mathcal{R}_2 = \frac{8\eta_{\text{eff}} l_2}{\pi a^4}, \tag{5.6}$$

$$\mathcal{R}_3 = \frac{1}{2\pi a l_3 L_p} + \frac{8\eta_{\text{eff}} l_3}{\pi a^4} \simeq \frac{1}{2\pi a l_3 L_p}. \tag{5.7}$$

Here, we approximate the resistance in the loading and unloading zones $\mathcal{R}_1$ and $\mathcal{R}_3$ by the hydraulic resistance associated with moving across the membrane and disregard the resistance of the flow along the tube[1]. If we assume for simplicity that $l_1 = l_3$, the total resistance is simply the sum of the three resistances (5.5)–(5.7)

$$\mathcal{R} = \mathcal{R}_1 + \mathcal{R}_2 + \mathcal{R}_3 = \frac{1}{\pi a l_1 L_p} + \frac{8\eta_{\text{eff}} l_2}{\pi a^4} \tag{5.8}$$

[1]The resistance along the (un)loading zone is typically two orders of magnitude smaller than the resistance across the membrane

The flow is driven by the osmotic pressure $\mathbb{R}\mathbb{T}c^*$ so the average flow velocity $\bar{u}$ can be written as

$$\bar{u} = \frac{1}{\pi a^2}\frac{\mathbb{R}\mathbb{T}c^*}{\mathcal{R}} \tag{5.9}$$

$$= \frac{1}{\pi a^2}\left(\frac{1}{\pi a l_1 L_p} + \frac{8\eta_{\text{eff}} l_2}{\pi a^4}\right)^{-1}\mathbb{R}\mathbb{T}c^* \tag{5.10}$$

$$= \left(\frac{a^2 l_1 L_p}{a^3 + 8\eta_{\text{eff}} L_p l_1 l_2}\right)\mathbb{R}\mathbb{T}c^* \tag{5.11}$$

As a quick check, we can compare this velocity to the one found in Eq. (2.7) (p. 14) which was calculated without taking the viscous resistance (Eq. 5.6) into account. There, we found a characteristic osmotic velocity of 10^{-2} m/s, two orders of magnitude larger than the observed velocity of 2.8×10^{-4} m/s. Using the parameters

$$l_1 = 0.1 \text{ m}, \quad l_2 = 1 \text{ m}, \quad a = 10^{-5} \text{ m}, \quad L_p = 5 \times 10^{-14} \text{ m/(s Pa)}, \quad \text{and} \quad \mathbb{R}\mathbb{T}c^* = 1 \text{ MPa},$$

we find from Eq. (5.11) that

$$\bar{u} = 3.9 \times 10^{-4} \text{ m/s}, \tag{5.12}$$

in good agreement with the experiments. In non-dimensional units (see Sec. 3.5, p. 24) with the axial length scale l chosen to be the length of the translocation zone i.e. $l = l_2$ we find that the average axial velocity $\bar{U}$ can be written as

$$\bar{U} = \left(\frac{1}{\frac{2}{L_1} + M\ddot{u}}\right), \tag{5.13}$$

such that for large values of $M\ddot{u}$

$$\bar{U} \simeq \frac{1}{M\ddot{u}}, \tag{5.14}$$

while for small values of $M\ddot{u}$,

$$\bar{U} \simeq \frac{L_1}{2}. \tag{5.15}$$

5.1.3 Non-dimensional formulation of the equations of motion

To simplify the mathematical treatment of the full model, we use non-dimensional variables. As outlined above, we employ the scaling used in Sec. 3.5 with the axial length scale L chosen to be the length of the translocation zone $l = l_2$. In these units we have a loading zone (zone 1, $0 < X < X_1$) of length $L_1 = l_1/l_2$, a translocation zone (zone 2, $X_1 < X < X_2$) of length $L_2 = l_2/l_2 = 1$ and an unloading zone (zone 3, $X_2 < X < X_3$) of length $L_3 = l_3/l_2$. Since the equations of motion are different in each of the zones, we will use subscripts. The velocity in the loading zone is denoted U_1, in the translocation zone U_2 and in the unloading zone U_3. Similar subscripts are used for the concentration C.

In steady state, the governing equation for the velocity U in all three zones is

$$\partial_X^2 U_i = \partial_x C_i + M\ddot{u}\, U_i, \tag{5.16}$$

where $i = 1, 2, 3$. The concentration C is governed by

$$\begin{aligned} C_1 &= 1 && (5.17)\\ \partial_x (U_2 C_2) &= 0 && (5.18)\\ C_3 &= C_2(X_2)\left(1 - \frac{X - X_2}{X_3 - X_2}\right). && (5.19) \end{aligned}$$

The boundary conditions require continuity of the velocity U and its first derivative with respect to X

$$\begin{aligned} U_1(0) &= 0, && (5.20)\\ U_2(X_1) &= U_1(X_1), && (5.21)\\ \partial_X U_2(X_1) &= \partial_X U_1(X_1), && (5.22)\\ U_3(X_2) &= U_2(X_2), && (5.23)\\ \partial_X U_3(X_2) &= \partial_X U_2(X_2), && (5.24)\\ U_3(X_3) &= 0. && (5.25) \end{aligned}$$

The conservation equation (5.18) implies that for any two positions in the translocation zone interval $X_a, X_b \in [X_1, X_2]$ we have that

$$U_2(X_a)C_2(X_a) = U_2(X_b)C_2(X_b). \tag{5.26}$$

In particular, since $C_2(X_1) = C_1(X_1) = 1$, we have that

$$U_2(X_2)C_2(X_2) = U_2(X_1). \tag{5.27}$$

This means that we can eliminate C from the equations of motion entirely and get

$$\begin{aligned} \partial_X^2 U_1 &= M\ddot{u}\, U_1, && (5.28)\\ \partial_X^2 U_2 &= -\frac{U_1(X_1)}{U_2^2}\partial_X U_2 + M\ddot{u}\, U_2, && (5.29)\\ \partial_X^2 U_3 &= -\frac{U_2(X_1)}{U_2(X_2)(X_3 - X_2)} + M\ddot{u}\, U_3, && (5.30) \end{aligned}$$

To determine C upon solving this system of equations, we simply use Eqns. (5.17), (5.26) and (5.19). In non-dimensional units, the mean velocity in the translocation zone is

$$\bar{U} = \int_{X_1}^{X_2} U_2 \,\mathrm{d}X, \tag{5.31}$$

since $X_2 - X_1 = 1$.

5.2 Analytical solution of the 3–zone model

A general, closed form solution of Eqns. (5.28)-(5.30) is not currently available. It is, however, possible to solve the problem analytically in the in the limits $M\ddot{u} \ll 1$ and $M\ddot{u} \gg 1$. In the following, we will give a brief summary of the solutions which depend on the Münch number $M\ddot{u}$, the size of the loading zone L_1 and the ratio $\omega = \frac{L_3}{L_1}$. The problem is solved for all ω, but with special emphasis on the case $\omega = 1$ commonly used in the literature. Please refer to Appendix A for a thorough analysis the solution procedure.

5.2.1 Solution for $M\ddot{u} \ll 1$

In the limit $M\ddot{u} \ll 1$ the equations of motion are

$$\partial_X^2 U_1 = 0, \tag{5.32}$$

$$\partial_X^2 U_2 = -\frac{U_1(X_1)}{U_2^2}\partial_X U_2, \tag{5.33}$$

$$\partial_X^2 U_3 = -\frac{U_2(X_1)}{U_2(X_2)(X_3 - X_2)}. \tag{5.34}$$

We write the solution in domains 1 and 3 as

$$U_1(X) = B_1 X + B_2, \tag{5.35}$$

$$U_3(X) = -\frac{1}{2}\frac{U_2(X_1)}{U_2(X_2)}\frac{1}{(X_3 - X_2)}(X - X_3)^2 + B_3(X - X_3) + B_4. \tag{5.36}$$

For U_2, only the inverse function $X(U_2)$ is available explicitly

$$X(U_2) = \frac{U_1(X_1)}{B_5}\left[\frac{U_2}{U_1(X_1)} - \frac{1}{B_5}\log\left(\frac{1 + \frac{B_5 U_2}{U_1(X_1)}}{1 + B_5}\right)\right] + B_6. \tag{5.37}$$

To fulfill the boundary conditions we find that the constants $B_1, B_2, \ldots, B_6$ are given by

$$B_1 = \frac{1}{\omega}\left(1 + \omega - \sqrt{1 + 2\omega}\right), \tag{5.38}$$

$$B_2 = 0, \tag{5.39}$$

$$B_3 = \frac{1}{\omega}\left(1 - \sqrt{1 + 2\omega}\right), \tag{5.40}$$

$$B_4 = 0, \tag{5.41}$$

$$B_5 = \frac{1}{\omega}\left(1 - \sqrt{1 + 2\omega}\right), \tag{5.42}$$

$$B_6 = \frac{L_1\omega}{\sqrt{1 + 2\omega} - 1}, \tag{5.43}$$

and that $U_2(X_2) = \frac{1}{2}L_1(1 - B_1)\omega$. We compare this analytical solution to numerical solutions of the full equation system in Sec. 5.4.

The mean translocation velocity in the translocation zone $\bar{U}$ is

$$\bar{U} = \frac{1}{2}\left(\sqrt{1+2\omega}-1\right)L_1 - \left(\frac{4+6\omega-\omega^2+\sqrt{1+2\omega}\left(\omega^2-4-2\omega\right)}{8\omega}\right)L_1^2. \tag{5.44}$$

In most cases the prefactor of second order term (in L_1) is very small. For $\omega = 1$ we find that

$$\bar{U} = \frac{\sqrt{3}-1}{2}L_1 - \frac{9-5\sqrt{3}}{8}L_1^2 \simeq 0.36L_1 - 0.043L_1^2. \tag{5.45}$$

It is often the case in plants that $L_1 \ll 1$, so we can safely use

$$\bar{U} \simeq \frac{\sqrt{3}-1}{2}L_1, \tag{5.46}$$

as an estimate for $\bar{U}$. Apart from a small numerical difference in the prefactor ($\sqrt{3}-1 \simeq 0.732$ vs. 1), this is in good agreement with the result found in Eq. (5.15) using the resistor model.

5.2.2 Solution for $M\ddot{u} \gg 1$

In the limit $M\ddot{u} \gg 1$ the equations of motion are

$$\partial_X^2 U_1 = M\ddot{u}\, U_1, \tag{5.47}$$

$$\partial_X^2 U_2 = -\frac{U_1(X_1)}{U_2^2}\partial_X U_2 + M\ddot{u}\, U_2, \tag{5.48}$$

$$\partial_X^2 U_3 = -\frac{U_2(X_1)}{U_2(X_2)(X_3-X_2)} + M\ddot{u}\, U_3, \tag{5.49}$$

In the loading and unloading zones the solutions are

$$U_1(X) = A_1 \sinh\sqrt{M\ddot{u}}\, X + A_2 \cosh\sqrt{M\ddot{u}}\, X, \tag{5.50}$$

$$U_3(X) = A_3 \sinh\sqrt{M\ddot{u}}\,(X-X_2) + A_4 \cosh\sqrt{M\ddot{u}}\,(X-X_2) + \frac{K}{M\ddot{u}}, \tag{5.51}$$

where $K = \frac{U_2(X_1)}{U_2(X_2)(X_3-X_2)}$ and $A_2 = 0$ since $U_1(0) = 0$. For U_2, we have that

$$U_2(X) = \frac{U_1(X_1)}{\sqrt{1-2M\ddot{u}\, U_1(X_1)(X-X_1)}}. \tag{5.52}$$

With the solution given in Eq. (5.52), we can now determine the constants A_3 and A_4 and $K = \frac{U_2(X_1)}{U_2(X_2)(X_3-X_2)}$. The only free parameter is A_1 which has to be determined such that $U_3(X_3) = 0$. Using the computer algebra system MATHEMATICA 7.0.0, we do this as explained in Appendix A.2. The expressions are generally complicated functions of $M\ddot{u}$, X_1, X_2 and X_3. For $\omega = 1$, we e.g. find that A_1 is given by

$$A_1 = \frac{M\ddot{u}\,(4+X_1)\coth[M\ddot{u}^*] - \operatorname{csch}[M\ddot{u}^*]\left(4M\ddot{u} + \operatorname{csch}[M\ddot{u}^*]\sqrt{M\ddot{u}^{3/2}X_1\sinh[M\ddot{u}^*]^2\left(M\ddot{u}^*\cosh[M\ddot{u}^*]^2 - 4\sinh[M\ddot{u}^*] + 2\sinh[2M\ddot{u}^*]\right)}\right)}{4M\ddot{u}^2(2+X_1)\cosh[M\ddot{u}^*] - 2\left(4M\ddot{u}^2 + M\ddot{u}^{3/2}X_1\sinh[M\ddot{u}^*]\right)}, \tag{5.53}$$

where $M\ddot{u}^* = \sqrt{M\ddot{u}}X_1$. We compare this analytical solution to numerical solutions of the full equation system in Sec. 5.4.

In spite of the complexity of the analytical expression for the A_i's, the mean translocation velocity in the translocation zone $\bar{U}$ can be approximated by a simple function of $M\ddot{u}$. We thus find that

$$\bar{U} \simeq \frac{1}{M\ddot{u}} \tag{5.54}$$

as long as $M\ddot{u}\ (X_3 - X_2) \gg 1$. Once again, this is in good agreement with the resistor model result given in Eq. (5.14).

5.3 Solution summary for $\omega = 1$

In the special case $\omega = 1$ we have for the average translocation velocity $\bar{U}$ that

$$\bar{U} = \begin{cases} \frac{\sqrt{3}-1}{2} L_1 & \text{if } M\ddot{u} \ll 1, \\ \frac{1}{M\ddot{u}} & \text{if } M\ddot{u} \gg 1. \end{cases}$$

Inspired by Eq. (5.13) we therefore write

$$\bar{U} \simeq \frac{1}{\frac{2}{(\sqrt{3}-1)L_1} + M\ddot{u}}, \tag{5.55}$$

or in dimensional units

$$\bar{u} \simeq \left(\frac{a^2 l_1 L_p}{\frac{a^3}{\sqrt{3}-1} + 8\eta_{\text{eff}} L_p l_1 l_2} \right) \mathbb{R}\mathbb{T}c^*. \tag{5.56}$$

We compare this prediction to numerical solutions of the full equation system in Sec. 5.4. The dependence of $\bar{u}$ on the parameters in the problem is discussed in detail in Sec. 6.3, p. 64. From Eq. (5.56), we can further calculate the characteristic time t_0 it takes for a sugar molecule to traverse the translocation zone

$$t_0 = \frac{l_2}{\bar{u}} = \frac{l_2 \left(\frac{a^3}{\sqrt{3}-1} + 8\eta_{\text{eff}} L_p l_1 l_2 \right)}{a^2 l_1 L_p} \frac{1}{\mathbb{R}\mathbb{T}c^*}. \tag{5.57}$$

When l_2 becomes very large we recover the result obtained numerically by Thompson and Holbrook [79] that $t_0 \propto l_2^2$.

5.4 Comparison between numerical and analytical solutions

5.4.1 Numerical solutions of the 3–zone model

To evaluate the accuracy of the analytical solutions presented above, we have solved Eqns. (5.28)-(5.30) numerically. We have used MATLAB's `ode45`-routine which uses a Runge-Kutta (4,5) solver [63]. The equations are solved using a shooting method from

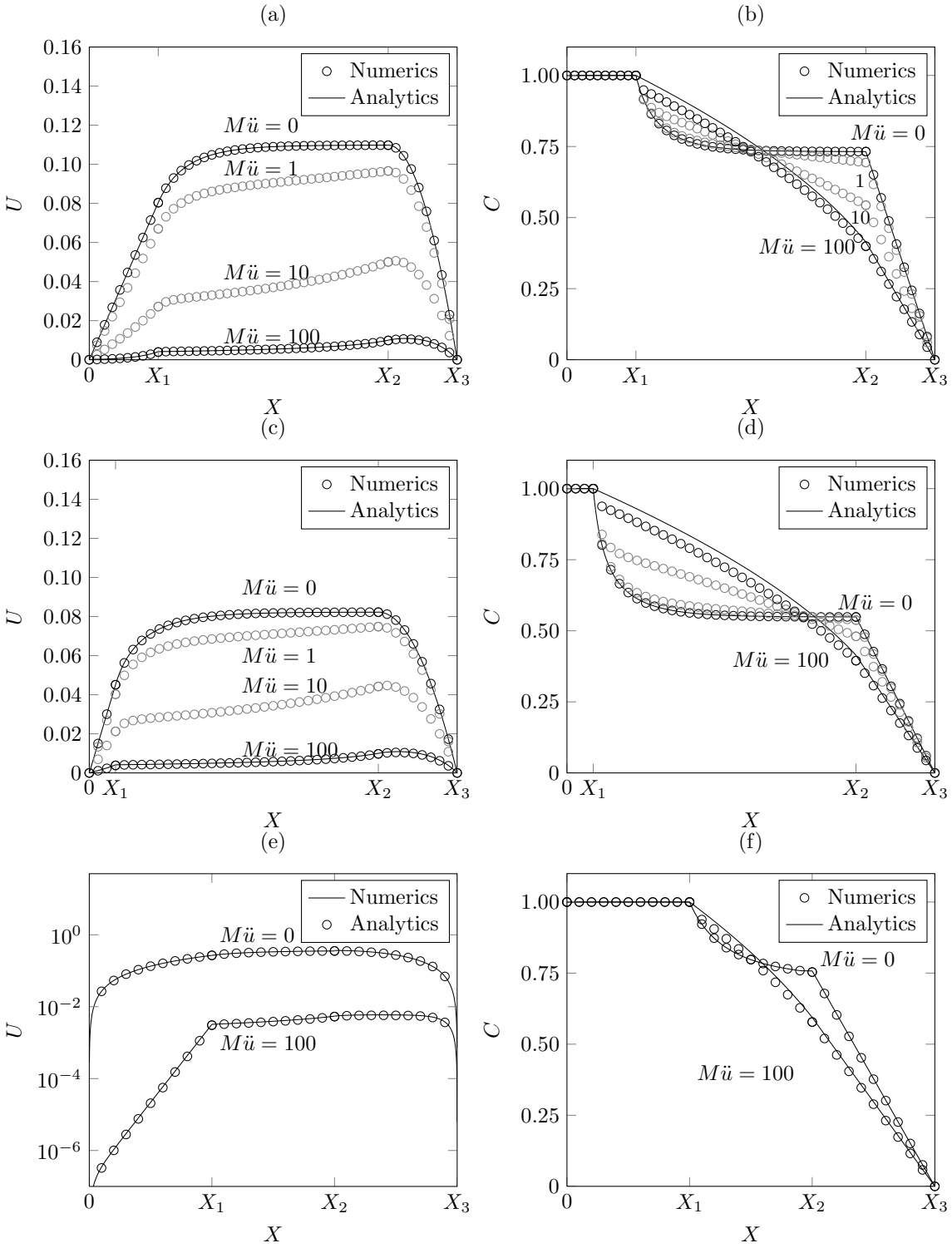

Figure 5.1: Comparison between numerical and analytical solutions of the 3–zone model. (a), (c), and (e): Numerical (circles) and analytical (lines) solutions for velocity U plotted as a function of axial position X. (b), (d), and (f): Numerical (circles) and analytical (lines) solutions for concentration C plotted as a function of axial position X. The values of Münch number $M\ddot{u}$ used are indicated next to the points. Parameters used are (a) and (b): $X_1 = 0.3$, $X_2 = 1.3$, and $X_3 = 1.6$. (c) and (d): $X_1 = 0.1$, $X_2 = 1.1$, and $X_3 = 1.4$. (e) and (f): $X_1 = 1$, $X_2 = 2$, and $X_3 = 3$. Note the logarithmic coordinate axis in (e).

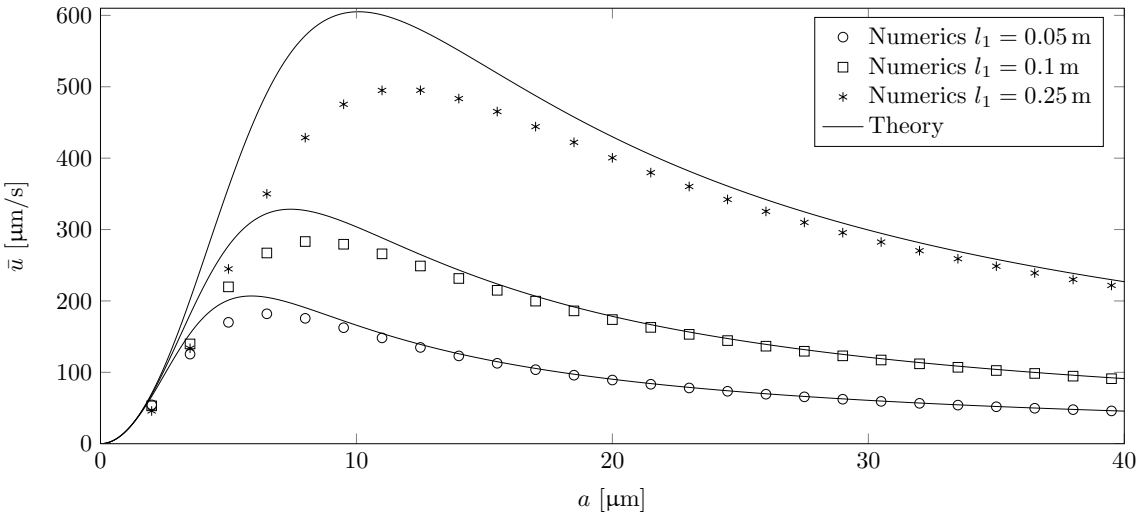

Figure 5.2: Comparison between numerical and analytical solutions of the 3-zone model. Numerically computed dimensional mean translocation velocities $\bar{u}$ (points) plotted as a function of radius a for a plant with a stem length $l_2 = 1$ m. The leaf and root sizes are $l_1 = l_3 = 0.05$ m (circles), $l_1 = l_3 = 0.1$ m (squares), and $l_1 = l_3 = 0.25$ m (stars). The solid lines shows the velocity predicted by Eq. (5.56). Parameters used are $L_p = 5 \times 10^{-14}$ m/(Pa s), $\mathbb{RT}c^* = 1$ MPa, and $\eta_{\mathrm{eff}} = 7 \times 10^{-3}$ Pa s.

left to right with the initial conditions $U_1(0) = 0$ and $\partial_X U_1(0) = 1$. To fulfill the boundary condition at X_3, the numerical procedure varies $\partial_X U_1(0)$ until the solution fulfills the condition $U_3(X_3) = 0$. After a thorough convergence test we obtain solutions similar to those shown in Fig. 5.1.

5.4.2 Comparison between numerical and analytical solutions

Using the numerical procedure outlined in Sec. 5.4.1, we have solved Eqns. (5.28)-(5.30) numerically. The results are shown in Fig. 5.1 where the numerical solutions for the velocity U and concentration C are compared with the analytical results obtained in the $M\ddot{u} \ll 1$ and $M\ddot{u} \gg 1$ limits. We generally find very good agreement between the two. The reason for the discrepancy between the analytical and numerical solution for the concentration C for $M\ddot{u} = 100$ is that the analytical solution for large $M\ddot{u}$ does not fulfill the condition $\partial_X U_2(X_1) = \partial_X U_1(X_1)$ exactly.

To evaluate the accuracy of the expression for the mean dimensional translocation velocity $\bar{u}$ given in Eq. (5.56), we have compared it to the results of the numerical simulation. To obtain the dimensional velocity from the non-dimensional solutions we use

$$\bar{u} = u_x^* \bar{U} = \frac{2 l_2 L_p \mathbb{RT} c^*}{a} \bar{U}, \tag{5.58}$$

cf. the scaling procedure discussed in Sec. 3.5, p. 24. Fig. 5.2 shows the numerically

computed dimensional mean translocation velocity $\bar{u}$ plotted as a function of radius a for a plant with a stem length $l_2 = 1$ m, and three different leaf/root sizes. We generally find good qualitative and quantitative agreement between the numerical simulations and the analytical result. The agreement is especially good (to within $\sim 10\%$) when the leaf is short compared to the stem, i.e. when $L_1 = \frac{l_1}{l_2}$ is small. We find equally good agreement between numerics and theory for plants with other stem lengths. We note the existence of a maximum in the dimensional translocation velocity which we discuss in detail in Chapter 6.

5.5 Conclusion and Summary

In this chapter, we have studied analytical and numerical solutions of the one-dimensional equations of motion in the 3-zone model. We have analysed the problem using first a simple hydraulic resistor model and second a full analytical solution in the limits $M\ddot{u} \ll 1$ and $M\ddot{u} \gg 1$. The analytical solutions obtained gives a full understanding of the flow and concentration profiles as a function of axial position in the two limits. The solutions depend on three non-dimensional numbers: The Münch number $M\ddot{u}$, the relative size of the loading and translocation zone $L_1 = \frac{l_1}{l_2}$, and the relative size of the loading and unloading zone $\omega = \frac{l_3}{l_1}$. To evaluate the accuracy of the analytical solutions, we have solved the equations of motion numerically. We have found good agreement between theory and numerics. From the analytical solutions, we have derived an analytical expression for the average axial translocation velocity $\bar{u}$ as a functions of the parameters in the problem, cf. Eq. (5.56).

Chapter 6

Optimality of the Münch mechanism

In this chapter we apply the results of the theoretical analysis of osmotically driven flows obtained in Chapters 3, 4 and 5 to translocation processes in plants. We begin by showing that the 3-zone model is able to reproduce translocation velocity measurements made on plants, and that it therefore gives us a basic understanding of how the velocity scales as a functions of the parameters in the problem. We then consider an interesting prediction of the model; that the osmotic Münch flow mechanism has a maximum in translocation velocity for a particular value of the phloem sieve tube radius a_c. We derive an expression for a_c which takes the form of an allometric scaling law, and show that a large group of plants follow this prediction. Finally, we discuss the implications for the Lang relay hypothesis and for the feasibility of the osmotic flow mechanism for long distance transport in plants. The author believes that the results presented in this chapter constitutes the most significant contribution to the phloem translocation literature obtained over the course of the PhD project.

The theoretical analysis of the optimality of the Münch mechanism was made by the author during and after a visit to the lab of Noel Michele Holbrook and Maciej Zwieniecki at Harvard University in 2008. It was published in [29][1] (see Appendix F) in a paper written in collaboration with Tomas Bohr, Jinkee Lee, Henrik Bruus, Noel Michele Holbrook and Maciej Zwieniecki. Maciej Zwieniecki performed the *in-vivo* phloem flow velocity measurements referred to in the text.

6.1 Introduction to optimality and allometric scaling laws

Plants display a remarkable variety of different structures and vary by many order of magnitude in size. Despite this incredible diversity and complexity, many fundamental biological processes show a striking simplicity when viewed as a function of size, by what is know as allometric scaling laws. The laws describe how biological parameters vary

[1] The scaling analysis presented here differs slightly from that given in [29]. To avoid lengthy mathematical discussions and the use of numerical solutions in the comparison with experimental data the author has chosen Eq. (5.11), p. 53, as the starting point for the discussion. This means that the expression for the critical radius a_c derived here differs from that found in [29] by a factor $2^{1/3}$ which is easily absorbed by the geometric factor G, cf. Eq. (6.7).

with scale, regardless of the otherwise large qualitative differences among of the species being considered. These scaling laws emerge from underlying physical mechanisms that are independent of the specific species, but which impose certain constraints on the system as a whole as a result of selection pressure for a specific property [87, 52].

As we have seen in Chapter 2, the phloem tissue of plants is responsible for the distribution of sugar and hormonal and signaling molecules. On the biological motivation for examining the optimality of the Münch mechanism, the author and collaborators write in [29] that

> ...phloem distributes hormonal and signaling molecules that allow for the integration of distal parts in lieu of a designated nervous system [43, 83]. This additional signalling task could result in selection pressure to optimize translocation velocity by providing plants with the ability to respond rapidly to environmental perturbations [46]. ([29], p. 1)

The question we pose in the following is whether an allometric scaling analysis can be applied to translocation in the phloem. If we assume that the flow inside plants is driven according to the Münch hypothesis, what consequences does it have for the relation between, say, the size of the leaf, the length of the stem and the radius of the phloem tubes if we assume that plants are optimized for rapid translocation in the phloem?

To make progress on this we will use the results derived in Chapter 5.

6.2 Comparison between the 3-zone model and plant velocity measurements

The equations of motion derived in Chapter 3 and analyzed in Chapter 5 have been shown by several authors to accurately describe osmotically driven flows in artificial systems [16, 40, 30, 28, 29], see also Chapter 7.

To shown that they are a relevant description of the processes that occur in plants, we must make an assessment of to what extend the theory is able to reproduce empirical data. Quoting once again Knoblauch and Peters [36]:

> While there is no shortage of mathematical formalizations of various aspects of phloem transport..., the question remains whether any such theoretical description mirrors physical reality in a biologically meaningful way can only be decided empirically. ([36], p. 1442)

One such empirical comparison can be made by considering the characteristic flow velocity $\bar{u}$ for the 3-zone model derived in Chapter 5 (Eq. (5.11), p. 53). The expression for $\bar{u}$ has the form

$$\bar{u} \simeq \left(\frac{a^2 l_1 L_p}{\frac{a^3}{\sqrt{3}-1} + 8 L_p \eta_{\text{eff}} l_1 l_2} \right) \Pi \tag{6.1}$$

and thus relates the translocation velocity to characteristic physical properties of the plant and the available osmotic driving pressure $\mathbb{RT}c^* = \Pi$.

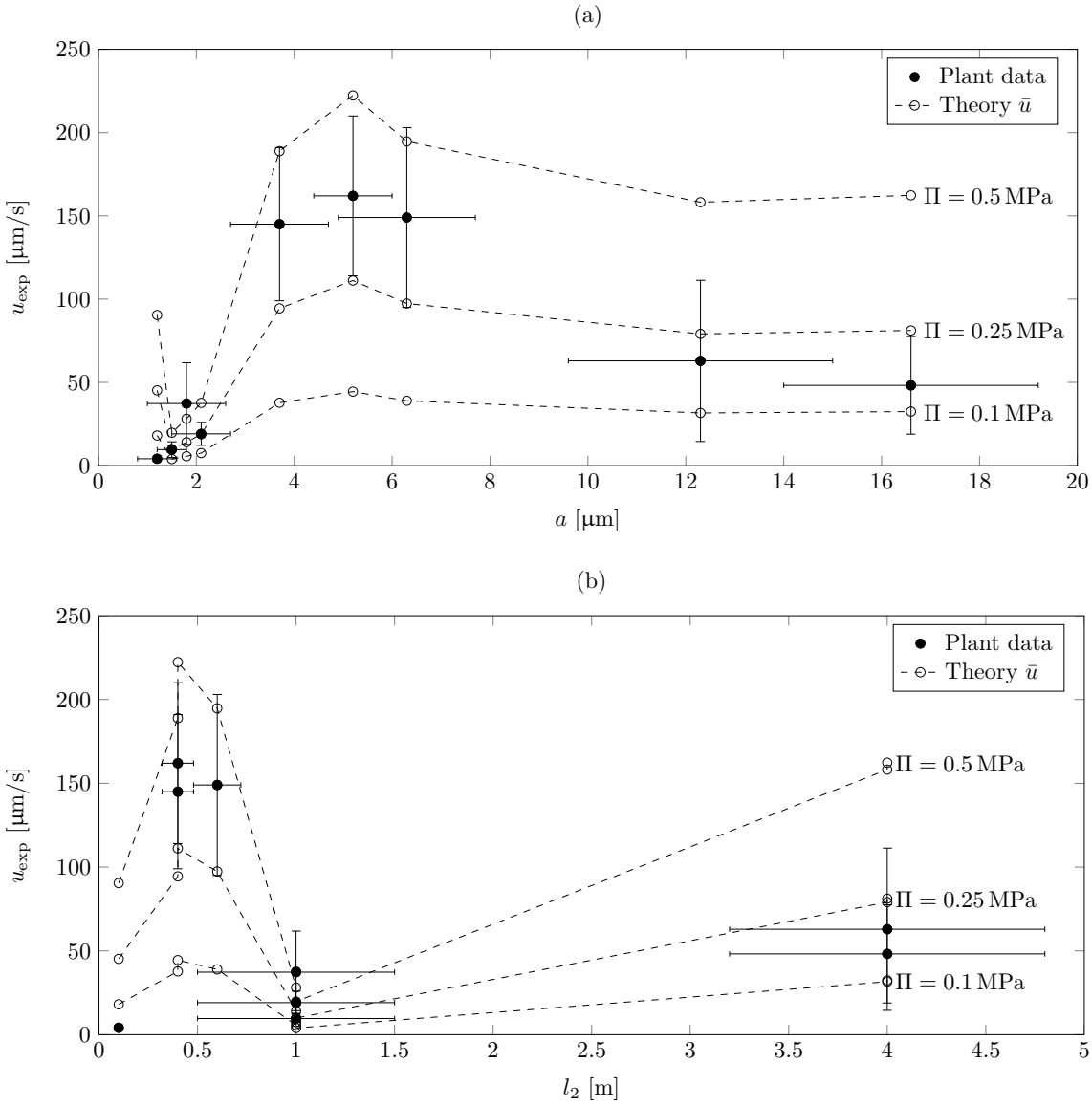

Figure 6.1: Comparison between plant velocity measurements and theory. (a) Measured flow velocity u_{exp} (black dots) plotted as a function of the sieve tube radius a for the 7 different species listed in Table 6.1. Also shown is the velocity $\bar{u}$ predicted by Eq. (6.1) (open circles connected by dashed lines) plotted for $\Pi = 0.1$ MPa $- 0.5$ MPa as indicated on the right. (b) Measured flow velocity u_{exp} (black dots) plotted as a function of the stem length l_2. Also shown is the velocity $\bar{u}$ predicted by Eq. (6.1) (open circles connected by dashed lines) plotted for $\Pi = 0.1$ MPa $- 0.5$ MPa as indicated on the right. Throughout, $L_p = 5 \times 10^{-14}$ m/(Pa s) and $\eta_{\mathrm{eff}} = 7 \times 10^{-3}$ Pa s was used.

A data set which allows for direct comparison with Eq. (6.1) is given in Table 6.1, p. 75. Here, experimental data obtained from *in-vivo* phloem flow velocity measurements made on 7 different species are listed along with values of the relevant physical parameters[2]. When comparing the experimental data to the prediction of Eq. (6.1), we will treat the membrane permeability L_p and the liquid viscosity η_{eff} as constants. We make this assumption based on a thorough study by Thompson and Holbrook [79]. They found that representative values are $L_p = 5 \times 10^{-14}$ m/(Pa s) and $\eta = 2 \times 10^{-3}$ Pa s, such that $\eta_{\text{eff}} = 7 \times 10^{-3}$ Pa s. Characteristic values of the osmotic pressure are $\Pi = 0.2$ MPa $- 2$ MPa, obtained from the sugar concentrations listed in Table 2.1, p. 11.

A comparison between the velocity predicted by Eq. (6.1) and the measured values listed in Table 6.1 is shown in Fig. 6.2. In (a), the velocity is plotted as a function of the radius a of the sieve tubes, while (b) shows the velocity plotted as a function of the stem length l_2. The prediction of the velocity $\bar{u}$ given in Eq. (6.1) is shown as open circles connected by dashed lines as guides to the eye. We observe a good qualitative and quantitative agreement between the prediction of Eq. (6.1) and the experimental data for the curves with $\Pi = 0.1$ MPa $- 0.5$ MPa. Although these value of the osmotic pressure Π are at the low end of the spectrum, we note that the factor Π entering into Eq. (6.1) represents the difference in osmotic pressure between the root and the leaf, a number which can be significantly lower than the values found by simply considering the sugar concentration as pointed out by Turgeon [82].

6.3 Optimality of the Münch mechanism

We now move on to an allometric scaling analysis of translocation in the phloem. To make progress on this, we must first convince ourselves that a maximum in translocation velocity is imposed by the Münch osmotic flow mechanism. We begin by considering the dependence of the translocation velocity $\bar{u}$ given in Eq. (6.1) on the sieve tube radius a, the leaf size l_1 and the stem size l_2. With 2 of the 3 parameters kept constant, $\bar{u}$ behaves as illustrated in Fig. 6.2. The velocity grows asymptotically as a function of the leaf size l_1 to the value

$$\bar{u}(l_1 \to \infty) = \frac{a^2}{8\eta l_2}\Pi, \tag{6.2}$$

and decays as $\frac{1}{l_2}$ when the stem length becomes very large. When the stem is very short we find that

$$\bar{u}(l_2 \to 0) = \left(\sqrt{3} - 1\right) \frac{l_1 L_p}{a}\Pi. \tag{6.3}$$

While the velocity $\bar{u}$ has no maximum points as a function of l_1 and $l_2 > 0$, it does have an extrema as a function of the radius a, at the value $a = a_c$ as indicated in Fig. 6.2(c). As sketched in Fig. 6.3(a), the existence of such a maximum in translocation velocity is quite

[2]We note that the stem length of these plants are $l_2 \sim 1$ m and that the values of the ratio $L_1 = \frac{l_1}{l_2}$ lie in the range $0.05 - 0.25$. We can therefore expect that Eq. (6.1) gives a reasonably accurate estimate of $\bar{u}$ from the 3-zone mode cf. the discussion in Sec. 5.4.2, p. 59. For plants with much larger values of L_1 one needs to solve the 3-zone model numerically in each individual case. The author and co-workers used this approach in [29].

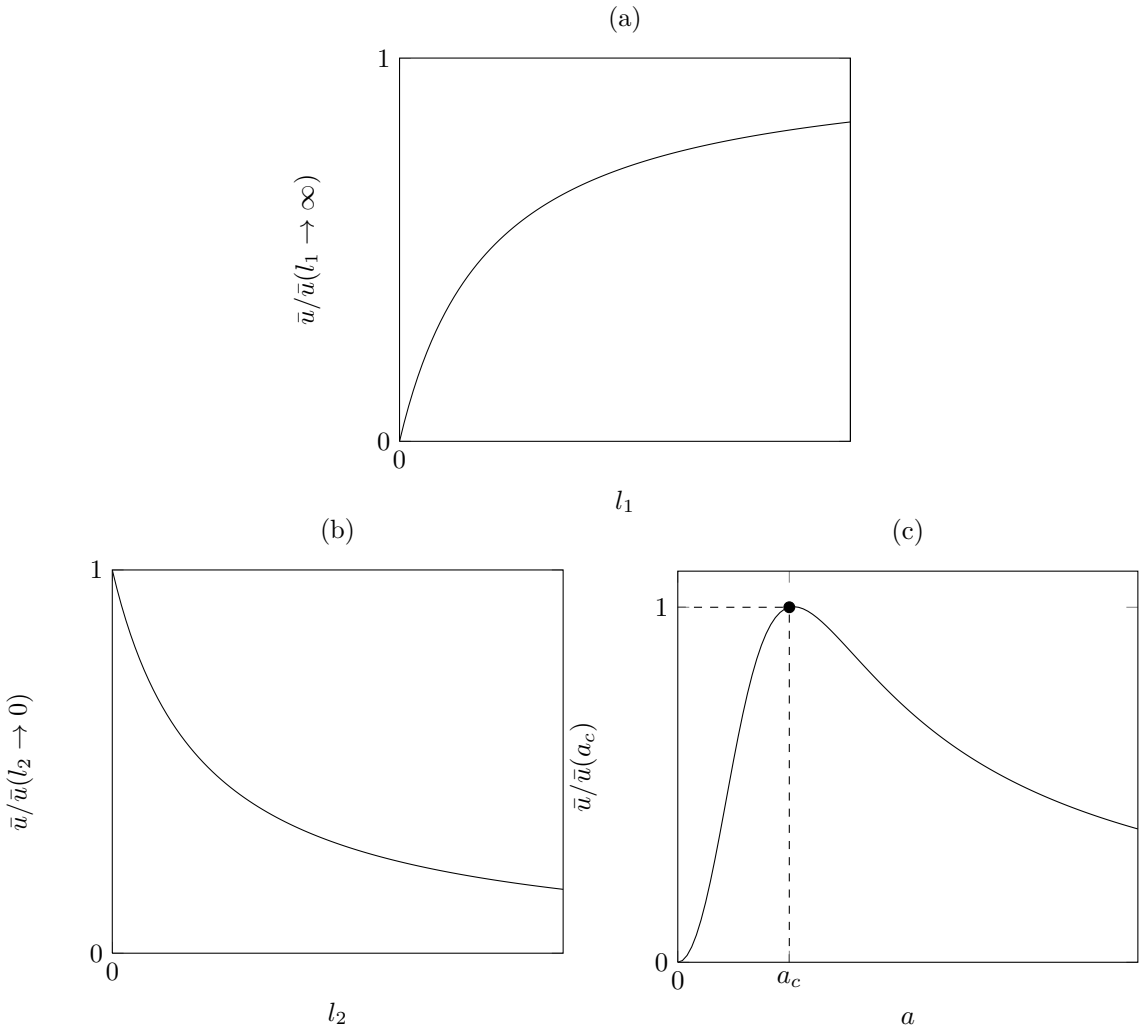

Figure 6.2: Plots showing the asymptotic behavior of the velocity $\bar{u}$ given in Eq. (6.1) as a function of a, l_1, and l_2. (a) Plot of $\bar{u}/\bar{u}(l_1 \to \infty)$ as a function of the leaf size l_1 for constant a and l_2. As $l_1 \to \infty$, $\bar{u}$ approaches $\frac{a^2}{8\eta l_2}\Pi$. (b) Plot of $\bar{u}/\bar{u}(l_2 \to 0)$ as a function of stem length l_2 for constant a and l_2. As $l_2 \to 0$, $\bar{u}$ approaches $\left(\sqrt{3}-1\right)\frac{l_1 L_p}{a}\Pi$. (c) Plot of $\bar{u}$ as a function of radius a for constant l_1 and l_2. At the critical radius $a = a_c$, the velocity $\bar{u}$ has an maximum point (indicated by the black dot) given by Eq. (6.5). The value of $a = a_c$ at which this occurs is given in Eq. (6.4).

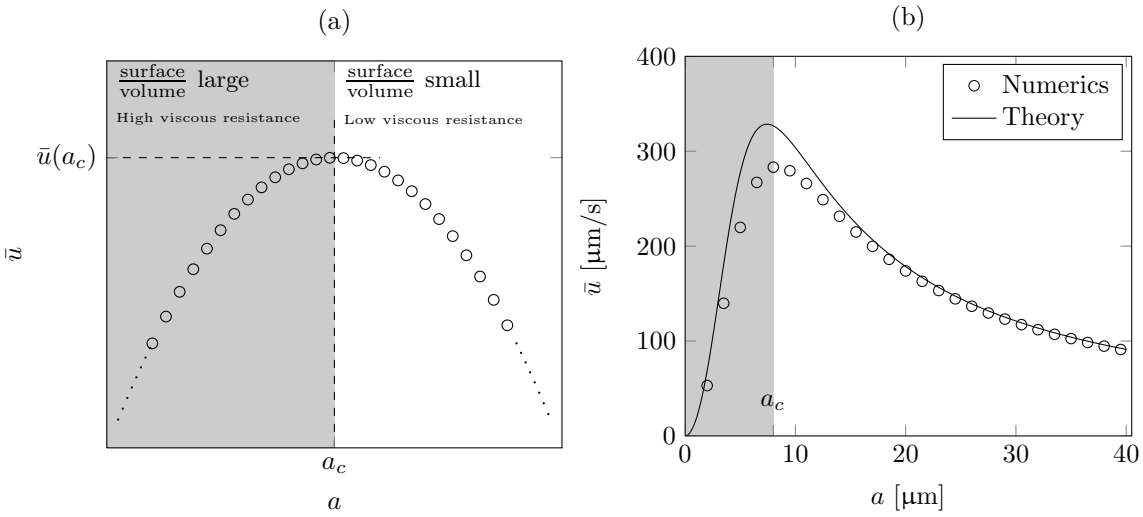

Figure 6.3: Optimized velocity for osmotically driven flows. (a) Heuristic argument for existence of a maximum in translocation velocity for osmotically driven flows. The flow velocity $\bar{u}$ (open circles) is plotted as a function of the tube radius a. The osmotic drive takes place across the tube surface and the velocity therefore grows as the the surface-to-volume ratio $\sigma = \frac{2}{a}$ increases, i.e. when the radius decreases. Very thin tubes, on the other hand, offer high viscous resistance to the flow; and thus there is an optimum radius a_c and velocity $\bar{u}(a_c)$ at the intersection between the dashed lines, where the osmotic pump is most effective and the resistance not too large. (b) Example of numerically computed mean translocation velocity $\bar{u}$ (dots) as a function of radius a calculated from the 3-zone model showing the existence of a maximum in translocation velocity. The solid line shows the velocity predicted by Eq. (6.1). Close to the maximum of the solid curve, at $a = 7.5$ µm, the transition between the two types of flow occurs and the velocity is at a maximum. This is consistent with the numerical simulations which yields $a_c \simeq 8.0$ µm as indicated on the ordinate axis. Parameters used are $L_p = 5 \times 10^{-14}$ m/(Pa s), $l_1 = l_3 = 0.1$ m, $l_2 = 1$ m, $\Pi = 1$ MPa, and $\eta_{\text{eff}} = 7 \times 10^{-3}$ Pa s. We also find good agreement between numerics and theory for other values of l_1 and l_2.

easy to understand: the osmotic flow takes place across the cell surface and is therefore more effective in terms of the axial velocity for thinner tubes where the surface-to-volume ratio $\sigma = \frac{2}{a}$ is larger. Very thin tubes, on the other hand, offer high viscous resistance to the flow, and thus there is an optimum radius a_c, where the osmotic pump is effective and the resistance not too large.

To estimate the radius at which this maximum occurs, we use the expression for the mean translocation velocity $\bar{u}$ given in Eq. (6.1) This velocity is plotted as a function of the phloem sieve tube radius a in Fig. 6.3(b), along with the results of numerical simulation of the 3-zone model. In accordance with the numerical result, the solid curve shows a maximum which we can calculate by considering the nominator of $\partial_a \bar{u} = 2al_1L_p\left(\frac{a^3}{\sqrt{3}-1} + 8\eta L_p l_1 l_2\right) - \frac{3}{\sqrt{3}-1}a^4 l_1 L_p$. The velocity has a maximum when this is zero, i.e. when

$$a^3 = a_c^3 = 16(\sqrt{3}-1)L_p\eta_{\text{eff}}l_1l_2. \tag{6.4}$$

As shown in Fig. 6.3(b) the numerically determined value of the optimized radius ($a_c = 8$ μm in this particular example) lies very close to that predicted by Eq. (6.4), $a_c = 7.5$ μm.

From Eqns. (6.1) and (6.4), we may further calculate the velocity $\bar{u}(a_c)$ at the critical radius

$$\bar{u}(a_c) = \frac{a_c^2}{24\eta_{\text{eff}}l_2}\Pi = \frac{\left(2-\sqrt{3}\right)^{1/3}}{3}\frac{(L_pl_1)^{2/3}}{(\eta_{\text{eff}}l_2)^{1/3}}\Pi. \tag{6.5}$$

Thus an increase in leaf size (with fixed stem size) will lead to an increase in the velocity $\bar{u}(a_c)$, while an increase in stem size (with fixed leaf size) will lead to a decrease. We thus assume that these external length scales are set by other biological constraints such as the cost of building, supporting and maintaining photosynthetic surfaces.

It is also interesting to consider the characteristic transit time $t_0(a_c)$ for a sugar molecule to traverse the translocation zone

$$t_0(a_c) = \frac{l_2}{\bar{u}(a_c)} = \frac{3}{\left(2-\sqrt{3}\right)^{1/3}}\frac{\eta_{\text{eff}}^{1/3}}{(L_pl_1)^{2/3}}\frac{l_2^{4/3}}{\Pi}. \tag{6.6}$$

We observe that the transit time t_0 at the critical radius grows as $l_2^{4/3}$, significantly slower than the dependence $t_0 \propto l_2^2$ found numerically by Thompson and Holbrook [79] in the non-optimized case of very large l_2.

6.3.1 Allometric scaling law for the optimality of the Münch mechanism

In summary, we have that the expression for the critical radius a_c given in Eq. (6.4) predicts a scaling relation of the form

$$a_c^3 = GL_p\eta_{\text{eff}}l_1l_2, \tag{6.7}$$

where $G = 16(\sqrt{3}-1) \simeq 10$ is a geometric factor[3]. If plants are optimized for rapid translocation in the phloem, we expect to find that they have appropriate combinations of

[3]We notice that in terms of the non-dimensional parameters $M\ddot{u}$ and L_1, the scaling relation given in Eq. (6.7) corresponds to $M\ddot{u} = \frac{16}{G}\frac{1}{L_1}$.

the four length scales: a, $L_p\eta_{\text{eff}}$, l_1, and l_2. This prediction thus relates physics occurring at length scales spanning more than 10 orders of magnitude: from the molecular scale – through the length scale $L_p\eta_{\text{eff}}$ which is closely related to the hydrodynamic pore-size of transport proteins – to the long-distance translocation scale which spans many 10s of meters.

6.4 Comparison with plant data

Table 6.2, p. 76, list values of phloem sieve tube radius a, leaf size l_1 and stem length l_2 for 19 different species from [29]. The data is represented visually in Fig. 6.4, and show the general trend that large plants tend to have large sieve tube and large leaves.

To test the scaling relation given in Eq. (6.7) the product $l_1 l_2$ is potted as a function of sieve tube radius a in Fig. 6.4(d) and again in Fig. 6.5 where the individual species are labeled by numbers referring to Table 6.2. A visual inspection of Fig. 6.5 reveals that the data points lie close to the predicted scaling exponent of 3 (solid line). By method of least squares fitting we will now determine the statistical estimate of the exponent and prefactor.

6.4.1 Determining the scaling exponent

When examining the data given in Table 6.2 we consider scaling relations of the form

$$a^\alpha = \beta l_1 l_2, \tag{6.8}$$

once again treating L_p and η_{eff} as constants. To determine the constants α and $\beta = GL_p\eta_{\text{eff}}$, it is convenient to consider instead the logarithm of this equation

$$\alpha \log a = \log \beta + \log l_1 l_2, \tag{6.9}$$

which with $\xi = \log a$, $\zeta = \log l_1 l_2$ and $B = -\log \beta$ becomes

$$\zeta = \alpha \xi + B. \tag{6.10}$$

A least squares fit [75] yields

$$\alpha_{\text{ls}} = 2.58 \pm 0.25, \tag{6.11}$$

quite close to the predicted scaling $\alpha = 3$ with a correlation coefficient of $r_c = 0.93$ as reported by the author and co-workers in [29]. The standard least squares correlation method, however, does not take into account the uncertainty on both sets of variables, i.e. the error on the radius a and on the product $l_1 l_2$. A more appropriate method is therefore a Model II least squares cubic regression analysis (see [52] p. 328 and [90] p. 1083). Using that technique, we find

$$\alpha_{\text{lsc}} = 3.32 \pm 0.37, \tag{6.12}$$

consistent with the $\alpha = 3$ prediction. Generally, the least squares method obtains the lowest value for the scaling exponent whereas Model II type regressions provides an upper

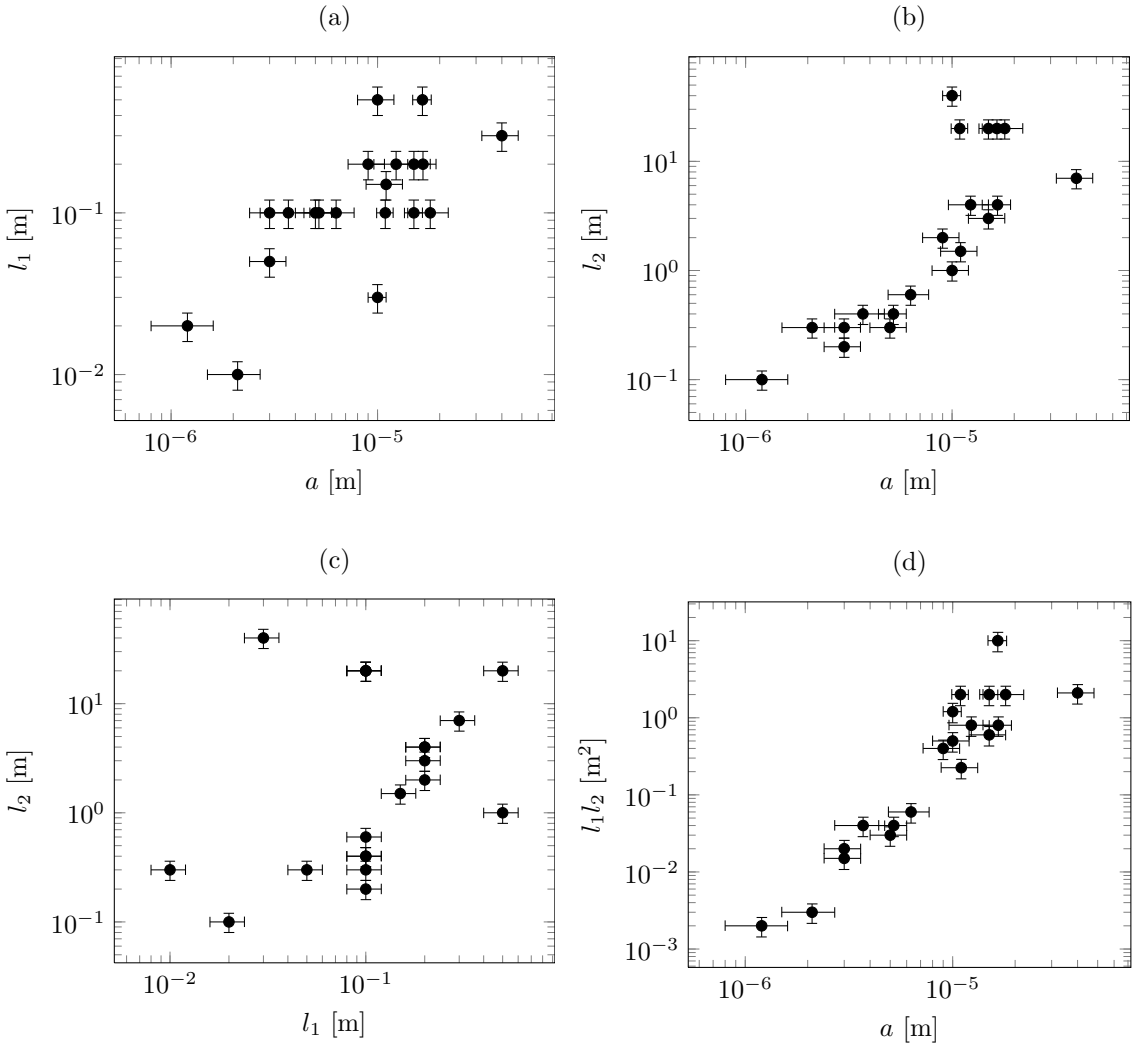

Figure 6.4: Visual representation of the plant data given in Table 6.2. (a) Leaf length l_1 plotted as a function of sieve tube radius a. (b) Stem length l_2 plotted as a function of sieve tube radius a. (c) Stem length l_2 plotted as a function of leaf length l_1. (d) Product of leaf and stem length $l_1 l_2$ plotted as a function of sieve tube radius a.

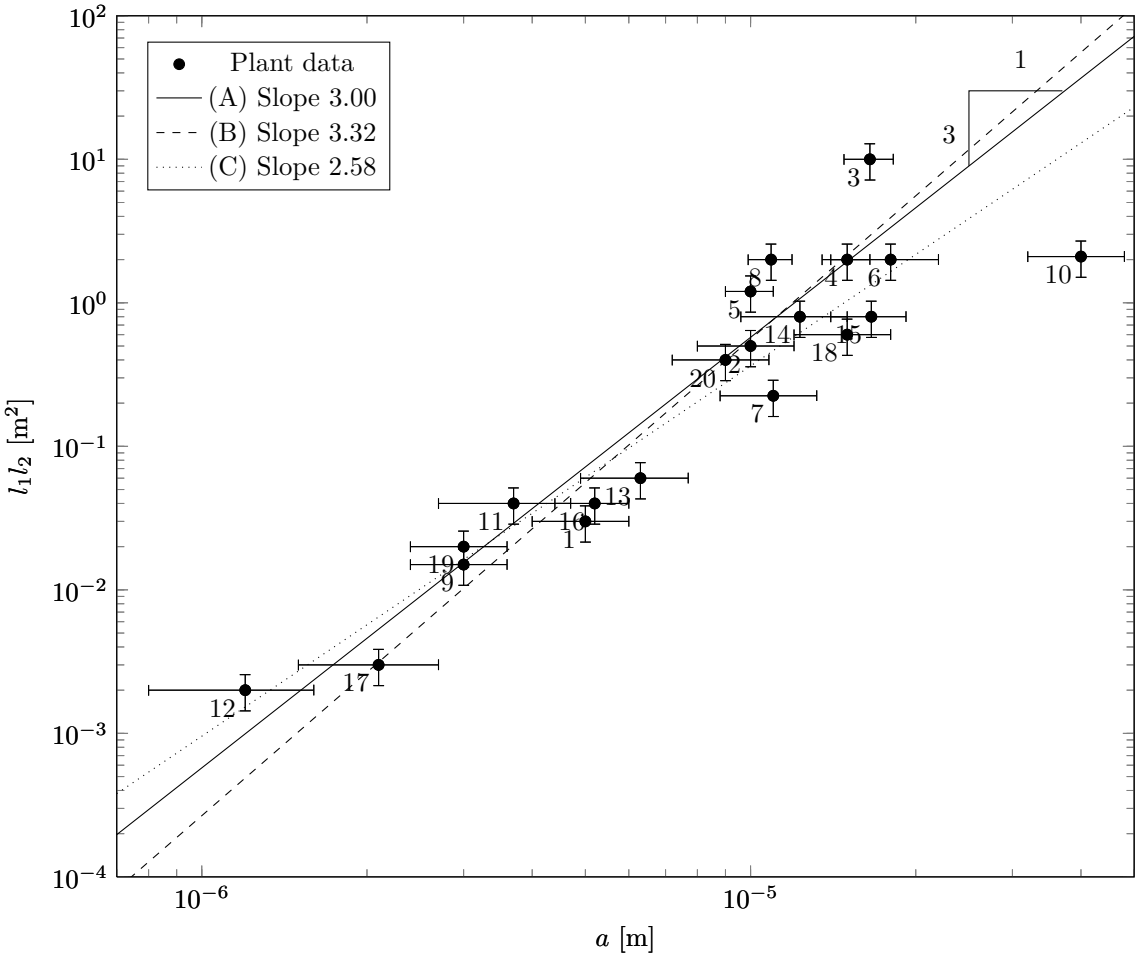

Figure 6.5: Comparison between the predicted scaling law $a^3 \propto l_1 l_2$ and the plant data given in Table 6.2. Log-log plot of measured $l_1 l_2$ as a function of measured radius a (black dots). The prediction of Eq. (6.7) (A, solid line, slope 3.00), Eq. (6.12) (B, dashed line, slope 3.32), and Eq. (6.11) (C, dotted line, slope 2.58) are also shown. The numbers next to the points indicated the species as listed in Table 6.2.

limit on α [52]. Figure 6.5 shows a comparison between the experimental data and the exponents derived from the regression analysis.

In summary we find good agreement between the predicted scaling relation and the experimental data on plants ranging in sieve tube radius a from $a = 1$ µm (*Tradescantia virginiana*, no. 12) to $a = 40$ µm (*Cucurbita malepo*, no. 10) and stem length l_2 from $l_2 = 0.1$ m (*Tradescantia virginiana*, no. 12) to $l_2 = 40$ m (*Robinia pseudoacacia*, no. 5). We note that a number of plants lie quite far from the predicted scaling. Two such points are *Cucurbita malepo* (no. 10), and *Sabal palmetto* (no. 3). The major difference between *Cucurbita malepo* the rest of the data set is presumably that it has very large sieve tubes, much like the *Cucurbita maxima* shown in Fig. 2.2, p. 10. On the other hand, the phloem of *Sabal palmetto* is located further inside the stem than what is usually the case. As discussed in Chapter 4, this also makes a difference for the hydraulic resistance of the sieve plates.

6.4.2 Determining the scaling prefactor

Data from the literature suggest that the scaling prefactor $\beta = GL_p\eta_{\text{eff}} \simeq 3.5 \times 10^{-15}$ m since $G \simeq 10$, $L_p = 5 \times 10^{-14}$ m/(Pa s), and $\eta_{\text{eff}} = 7 \times 10^{-3}$ Pa s. It can be determined from the data in Table 6.2 under the assumption that $\alpha = 3$ by a least squares fit to $a^3 = \beta l_1 l_2$. This yields

$$\beta_{\text{ls}} = (1.74 \pm 1.30) \times 10^{-15}\text{m}, \tag{6.13}$$

which is in the same order of magnitude as predicted by the literature data.

6.5 Discussion

In a discussion of the scaling analysis presented above the author and collaborators write in [29] that

> Plants, which span tens of metres and proliferate in hundreds of cubic metres of soil and air, experience diverse and often rapid fluctuations in environmental conditions. To respond to such environmental heterogeneity requires the rapid distribution of both energy and information in the form of chemical signals to enhance plant productivity and competitiveness. The phloem provides uninterrupted coupling between most distal parts of all plants and links plants' multibranched dendritic structure into a single functional microfluidic system [6]. Concordance between our theoretical model, studies of osmotically driven flow in synthetic phloem, and measurements of flow and geometric properties made on real plants gives confidence in the Münch theory of phloem flow and suggests that plants are optimized for rapid translocation of sugar, thereby gaining a competitive edge in terms of their ability to respond rapidly to environmental stimuli. Our analysis provides a general scaling law for phloem dimensions that maximizes translocation velocity, suggesting that evolutionary selection on the efficacy of signal transduction has shaped the structure and function of this supracellular transport pathway. ([29], p. 7)

The author thus believes that the physical constraints imposed by the optimality of the Münch mechanism has played an important role in the evolution of the phloem vascular system of plants. If we accept this hypothesis, we are able to shed new light on a number of conjectures found in the phloem literature.

6.5.1 Lang's relay hypothesis

One such conjecture is known as Lang's Hypothesis. In 1979, Alexander Lang [41] proposed that in order to maximize the rate of transport of sugar, the phloem translocation pathway might be split into a number of separate compartments. He writes that

> the phloem is envisaged as comprising a series of 'function units' of perhaps a few centimeters to several meters in length, each unit consisting of a file of sieve elements disposed end to end, the units having a short length of overlap between one and the next. ([41], p. 142)

Lang continues to describe how, in this short overlapping region, sugar is actively transferred between the two functional units which are otherwise physically separate, thus not allowing for a flow of liquid from one unit to the next. This concept is illustrated in Fig. 6.6, where the flow is from top to bottom, and the number in each box represents the sugar concentration. Lang estimates that about 2 % of the sugar is consumed by the reloading process at each reloading zone, but that this can lead to an increase of a factor of 10 in the rate of transport and that is is thus worth the extra expense in terms of the sugar lost.

There is, however, no clear experimental evidence for the existence of the relay zones proposed by Lang (see e.g. [50]). The hypothesis is none the less still widely cited as a method that plants may use for accelerating the rate of phloem transport [36]. Using the scaling analysis developed in the previous sections, we can evaluate the efficiency of the flow according to Lang's hypothesis. If we let l_2 be the length of the functional unit and l_1 be the length of overlap between two adjacent units, the situation is completely analogous to the 3-zone model. If the flow is optimized according to the Münch mechanism, we thus expect to find that the radius a_c of the sieve tube in the functional unit is

$$a_c = (GL_p\eta_{\text{eff}}l_2l_1)^{1/3}. \tag{6.14}$$

Lang provides no estimates of the size of the unit other than those given in the quote above. For a tree we may take a unit length of $l_2 = 1$ m and an overlapping region of length, say, $l_1 = 0.05$ m. This gives an optimum radius of

$$a_c = 5.6\ \mu\text{m}, \tag{6.15}$$

calculated with $G = 10$, $L_p = 5 \times 10^{-14}$ m/(Pa s) and $\eta = 7 \times 10^{-3}$ Pas. Trees, however, typically have radii in the range $10 - 20$ μm, 2-4 times larger than predicted by Eq. (6.15) (see Table 6.2). For a_c to be equal to 10 μm, one must choose the overlapping length $l_1 = 0.35$ m such that a total of 70% of adjacent functional units are overlapping. If such large overlapping regions exists they should be easy to observe.

From this analysis we conclude that we find no evidence in Fig. 6.5 to support Lang's relay hypothesis.

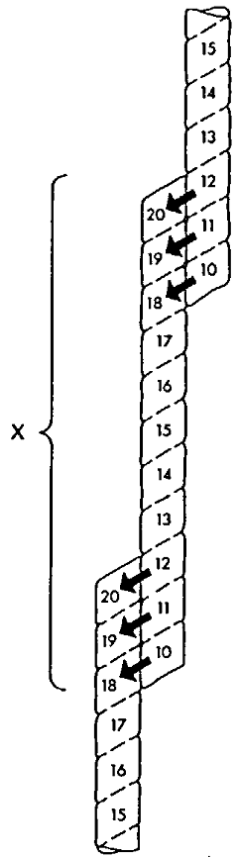

Figure 6.6: Lang's relay hypothesis. The phloem is envisaged as comprising a series of function units (indicated by the X) of perhaps a few centimeters to several meters in length, each unit consisting of a file of sieve elements disposed end to end, the units having a short length of over-lab between one and the next. In this short overlapping region, sugar is actively transferred between the two functional units which are otherwise physically separate, thus not allowing for a flow of liquid from one unit to the next. The flow is from top to bottom, and the number in each box represents the sugar concentration. From [41], Fig. 1. Reproduced with permission.

6.5.2 Is osmosis adequate for translocation in tall trees?

The question whether osmotically driven translocation is adequate to account for the rates of transport observed in tall trees is still an open question. Without some form of actively aided transport (such as the Lang relay mechanism discussed above), there is general agreement that osmosis is insufficient [82, 36]. This view has been promoted by the author of the present thesis himself in [30]. The argument put forward is that the hydraulic resistance of a 100 m tall tree is much to large to overcome for osmosis alone, and that flow rates would therefore be unreasonably slow. This is especially pronounced in gymnosperms where the hydraulic resistance of the sieve plates may be much larger than that found in the angiosperms studied in Chapter 4, see e.g. [68].

It is therefore somewhat surprising that the trees found in Table 6.2 (species 3, 4, 5, 6, and 8) all fall reasonably close to the $a^3 \propto l_1 l_2$ line in Fig. 6.5. If we use Eq. (6.1) to estimate the velocity $\bar{u}$ we find that they lie in the range from 16×10^{-6} m/s (*Robinia pseudoaccacia*) to 100×10^{-6} m/s (*Sabal palmetto*) and thus fall within the range of velocities measured on much smaller plants, cf. Table 6.1. The lone gymnosperm, *Pinus strobus*, has a predicted velocity of 40×10^{-6} m/s, although on must not forget that Eq. (6.1) was derived assuming that the sieve pores are open. These velocities were calculated with $L_p = 5 \times 10^{-14}$ m/(Pa s), $\eta_{\text{eff}} = 7 \times 10^{-3}$ Pa s and $RTc^* = 0.5$ MPa, the highest value of the osmotic pressure consistent with our findings in Fig. 6.2.

We further note that at the optimum radius, the characteristic transit time t_0 scales as $t_0(a_c) \propto l_2^{4/3}$ (cf. Eq. (6.6)) in contrast to the non-optimized result $t_0 \propto l_2^2$ found by Thompson and Holbrook in [79]. Tall trees may therefore have significantly shorter osmotic transit times than previously believed. For *Sabal palmetto*, we thus find from Eq. (6.6) that $t_0(a_c) \simeq 31$ h, while for *Robinia pseudoaccacia* $t_0(a_c) = 516$ h. The very large t_0 found for *Robinia pseudoaccacia* may reflect the fact that we have chosen the size of the leaflets, which are about 3 cm long, and not the size of the compound leaf which can grow up to, say, 25 cm in length. With $l_2 = 25$ cm we find that $t_0(a_c) \simeq 126$ h which still a significant amount of time.

From these observations it is still an open question whether the osmotic pumping is sufficient to account for phloem translocation in tall trees. More experimental data, and in particular velocity measurements made in tall trees correlated with measurements of leaf and stem sizes, is needed.

6.6 Conclusion

In this chapter we have applied the results of the 3-zone model introduced in Chapter 5 to translocation in the phloem. We have shown that the model is a fair description of the processes that occur in plants by comparing experimental velocity data to the results of the model with good results. An interesting prediction of the model is that the osmotic pumping mechanism has a maximum in translocation velocity for a special, optimal, value of the phloem sieve tube radius a_c. The expression for a_c has the form of an allometric scaling law

$$a^\alpha = G L_p \eta_{\text{eff}} l_1 l_2. \tag{6.16}$$

Table 6.1: Experimental data for phloem sieve tube radius a, leaf size l_1, stem length l_2 and flow velocity u_{exp}. The uncertainties indicate standard errors on measurements. Data from [29], see Appendix F. The measurement technique used to obtain the velocity values is discussed in said paper. Measurement (7-9) were made after the submission of the manuscript and are not included in [29].

No.	Species	a [μm]	l_2 [m]	l_1 [m]	u_{exp} [μm/s]
1	*Glycine max*	3.7 ± 1.0	0.40 ± 0.08	0.10 ± 0.02	145 ± 46
2	*Tradascantia virginiana*	1.2 ± 0.4	0.10 ± 0.02	0.020 ± 0.004	4.13 ± 1.64
3	*Cucumis sativus*	6.3 ± 1.4	0.60 ± 0.12	0.10 ± 0.02	149 ± 54
4	*Cucurbita maxima*	12.3 ± 2.7	4.0 ± 0.8	0.20 ± 0.04	62.9 ± 48.4
5	*Cucurbita maxima*	16.6 ± 2.6	4.0 ± 0.8	0.20 ± 0.04	48.2 ± 29.3
6	*Solanum lycopersicum*	5.2 ± 0.8	0.40 ± 0.08	0.10 ± 0.02	162 ± 48
7	*Populus balsamifera*	1.8 ± 0.8	1.0 ± 0.5	0.10 ± 0.01	37.7 ± 24.5
8	*Gnetum gnemon*	2.1 ± 0.6	1.0 ± 0.5	0.10 ± 0.01	19.1 ± 6.9
9	*Gossypium hirstum*	1.5 ± 0.3	1.0 ± 0.5	0.10 ± 0.01	9.62 ± 4.70

The scaling exponent α has been determined from a statistical analysis of experimental data from 19 plant species by least squares regression $\alpha_{\text{ls}} = 2.58 \pm 0.25$ and least squares cubic regression $\alpha_{\text{lsc}} = 3.32 \pm 0.37$. Both values are close to the exponent $\alpha = 3$ derived under the assumption that the translocation velocity is at a maximum. This analysis thus provides a general scaling law for phloem dimensions that maximizes the translocation velocity, suggesting that evolutionary selection on efficacy of sugar transport and signal transduction has shaped the structure and function of this transport pathway. This is a remarkable result, since it relates structures in plants spanning up to 10 orders of magnitude in size from the length of the stem l_2, measured in meters, to the size of the pores in the membrane, measured in nanometers, through the length $L_p\eta_{\text{eff}}$.

Table 6.2: Experimental data for phloem sieve tube radius a, leaf size l_1 and stem size l_2. The uncertainties indicate standard errors on measurements. Data from [29], see Appendix F.

No.	Species	a [µm]	l_2 [m]	l_1 [m]
1	*Beta vulgaris*	5.0 ± 1.0	0.3 ± 0.06	0.10 ± 0.02
2	*Yucca flaccida*	10.0 ± 2.0	1.0 ± 0.2	0.5 ± 0.1
3	*Sabal palmetto*	16.5 ± 1.7	20 ± 4	0.5 ± 0.1
4	*Tilia americana*	15.0 ± 1.5	20 ± 4	0.10 ± 0.02
5	*Robinia pseudoaccacia*	10.0 ± 1.0	40 ± 8	0.030 ± 0.006
6	*Vitis vinifera*	18.0 ± 4.0	20 ± 4	0.10 ± 0.02
7	*Gossypium bardadense*	11.0 ± 2.2	1.5 ± 0.3	0.15 ± 0.03
8	*Pinus strobus*	10.9 ± 1.0	20 ± 4	0.10 ± 0.02
9	*Festuca arundinacea*	3.0 ± 0.6	0.30 ± 0.06	0.05 ± 0.01
10	*Cucurbita malepo*	40.0 ± 8.0	7.0 ± 1.4	0.30 ± 0.06
11	*Glycine max*	3.7 ± 1.0	0.40 ± 0.08	0.10 ± 0.02
12	*Tradascantia virginiana*	1.2 ± 0.4	0.10 ± 0.02	0.020 ± 0.004
13	*Cucumis sativus*	6.3 ± 1.4	0.60 ± 0.12	0.10 ± 0.02
14	*Cucurbita maxima*	12.3 ± 2.7	4.0 ± 0.8	0.20 ± 0.04
15	*Cucurbita maxima*	16.6 ± 2.6	4.0 ± 0.8	0.20 ± 0.04
16	*Solanum lycopersicum*	5.2 ± 0.8	0.40 ± 0.08	0.10 ± 0.02
17	*Anacyclus purethrum*	2.1 ± 0.6	0.30 ± 0.06	0.010 ± 0.002
18	*Ecbalium elaterium*	15.0 ± 3.0	3.0 ± 0.6	0.20 ± 0.04
19	*Eragostis plana*	3.0 ± 0.6	0.2 ± 0.04	0.10 ± 0.02
20	*Heracleum mantegazzianum*	9.0 ± 1.8	2.0 ± 0.4	0.20 ± 0.04

Chapter 7

Microfluidic experiments

Throughout the PhD project, the author has found great sources of inspiration and insight in the experiments conducted by Münch, Eschrich *et al.*, and Lang discussed in Sec. 2.4, p. 16. Realizing, however, the fundamental shortcoming of these experiments – that they were conducted at length scales far from those found in plants – prompted the author and advisors Henrik Bruus and Tomas Bohr to conduct experiments aimed at using channel dimension that approached those found in the plants.

The following paper, [28], presented unabridged in Sec. 7.1–7.8 describes our experimental study of osmotically driven flows in microfluidic channels separated by a semipermeable membrane. To stay true to the original manuscript the notation in the present chapter differs slightly from that found in Chapters 1-6. Please refer to Table 7.1, p. 91, for a list of symbols. The design, fabrication and testing of the microfluidic devices was carried out by the author at the Technical University of Denmark. The experiments and part of the theoretical analysis was conducted at Harvard University in collaboration with Jinkee Lee during a visit in the lab of Noel Michele Holbrook. See further acknowledgements in Sec. 7.8.

While it is difficult to determine the long-term impact of the results presented, the paper has been well recieved in the plant vascular biology community. Knoblauch and Peters [37] writes that

> Phloem-inspired artificial microfluidics systems such as that of Jensen *et al.* (2009) provide an extremely powerful approach to the empirical testing of mathematical and other hypotheses of phloem transport. To date, the plant transport community has not yet connected to the engineers in the lab-on-a-chip field, but we expect that in the near future, "micro-Münch-models" will influence the way we think about the phloem on the conceptual level in a similar way as Münch's original models did 80 years ago. ([36], p. 1442)

and ends their paper by stating that

> We expect that over the next decade or so, artificial microfluidics systems, designed as structural analogs of natural sieve tubes (Jensen *et al.* 2009), will mature into indispensible and versatile tools in our efforts to make the phloem less of a miracle and more of a mechanism. ([36], p. 1448)

Start of paper

K. H. Jensen, J. Lee, T. Bohr and H. Bruus
Osmotically driven flows in microchannels separated by a semipermeable membrane
Lab on a Chip **9**(14), pp. 2093–2099 (2009)

7.1 Abstract

We have fabricated lab-on-a-chip systems with microchannels separated by integrated membranes allowing for osmotically driven microflows. We have investigated these flows experimentally by studying the dynamics and structure of the front of a sugar solution traveling in $200\,\mu$m wide and $50 - 200\,\mu$m deep microchannels. We find that the sugar front travels with constant speed, and that this speed is proportional to the concentration of the sugar solution and inversely proportional to the depth of the channel. We propose a theoretical model, which, in the limit of low axial flow resistance, predicts that the sugar front indeed should travel with a constant velocity. The model also predicts an inverse relationship between the depth of the channel and the speed, and a linear relation between the sugar concentration and the speed. We thus find good qualitative agreement between the experimental results and the predictions of the model. Our motivation for studying osmotically driven microflows is that they are believed to be responsible for the translocation of sugar in plants through the phloem sieve element cells. Also, we suggest that osmotic elements can act as on-chip integrated pumps with no movable parts in lab-on-a-chip systems.

7.2 Introduction

Osmotically driven flows are believed to be responsible for the translocation of sugar in plants, a process that takes place in the phloem sieve element cells [73]. These cells form a micro-fluidic network which spans the entire length of the plant measuring from 10 μm in diameter in small plants to 100 μm in diameter in large trees [73]. The mechanism driving these flows is believed to be the osmotic pressures that build up relative to the neighboring water-filled tissue in response to loading and unloading of sugar into and out of the phloem cells in different parts of the plant [73]. This mechanism, collectively called the pressure-flow hypothesis, is much more efficient than diffusion, since the osmotic pressure difference caused by a difference in sugar concentration creates a bulk flow directed from large concentrations to small concentrations, in accordance with the basic needs of the plant.

Experimental verification of flow rates in living plants is difficult [37], and the experimental evidence from artificial systems backing the pressure-flow hypothesis is scarce and

consists solely of results obtained with centimetric sized setups [16, 40, 30]. However, many theoretical and numerical studies of the sugar translocation in plants have used the pressure-flow hypothesis [79, 80, 24] with good results. To verify that these results are indeed valid, we believe that it is of fundamental importance to conduct a systematic survey of osmotically driven flows at the micrometer scale. Finally, osmotic flows in microchannels can act as migration enhancers [1] or as microscale on-chip pumps with no movable parts. Examples of previous off-chip osmotic pumps are the device developed by by Park *et al.* [55] and the osmotic pills developed by Shire Laboratories and pioneered by F. Theeuwes [76]. Also, there is a direct analogy between osmotically driven flows powered by concentration gradients, and electroosmotically driven flows in electrolytes [9, 19] powered by electrical potential gradients.

7.3 Experimental setup

7.3.1 Chip design and fabrication

To study osmotically driven flows in microchannels, we have designed and fabricated a microfluidic system consisting of two layers of 1.5 mm thick polymethyl methacrylate (PMMA) separated by a semipermeable membrane (Spectra/Por Biotech Cellulose Ester dialysis membrane, MWCO 3.5 kDa, thickness $\sim 40\,\mu$m), as sketched in Fig. 8.2(a)-(d). Channels of length 27 mm, width 200 μm and depth $50 - 200\,\mu$m were milled in the two PMMA layers by use of a MiniMill/Pro3 milling machine [18, 11]. The top channel contains partly the sugar solution, and partly pure water, while the bottom channel always contains only pure water. To facilitate the production of a steep concentration gradient by cross-flows, a 200 μm wide cross-channel was milled in the upper PMMA layer perpendicular to and bi-secting the main channel. Inlets were produced by drilling 800 μm diameter holes through the wafer and inserting brass tubes into these. By removing the surrounding material, the channel walls in both the top and bottom layers acquired a height of $100\,\mu$m and a width of $150\,\mu$m. After assembly, the two PMMA layers were positioned such that the main channels in either layer were facing each other. Thus, when clamping the two layers together using two 30 mm paper clamps, the membrane acted as a seal, stopping any undesired leaks from the channels as long as the applied pressure did not exceed approximately 1 bar.

7.3.2 Measurement setup and procedures

In our setup, the osmotic pressure pushes water from the lower channel, through the membrane, and into the sugar-rich part of the upper channel. This displaces the solution along the upper channel thus generating a flow there, as shown in Fig. 7.2. To measure this flow inside the upper channel, particle and dye tracking were used. In both cases inlets 1, 2, 3 and 5 (see Fig. 8.2) were connected via silicone tubing (inner diameter 0.5 mm) to disposable syringes. Syringes 2, 3 and 5 was filled with demineralised water and syringe 1 was filled with a solution of sugar (sucrose or dextran (mol. weight: 17.5 kDa, Sigma-Aldrigde, type D4624)) and 5 % volume red dye (Flachsmann Scandinavia, Red Fruit

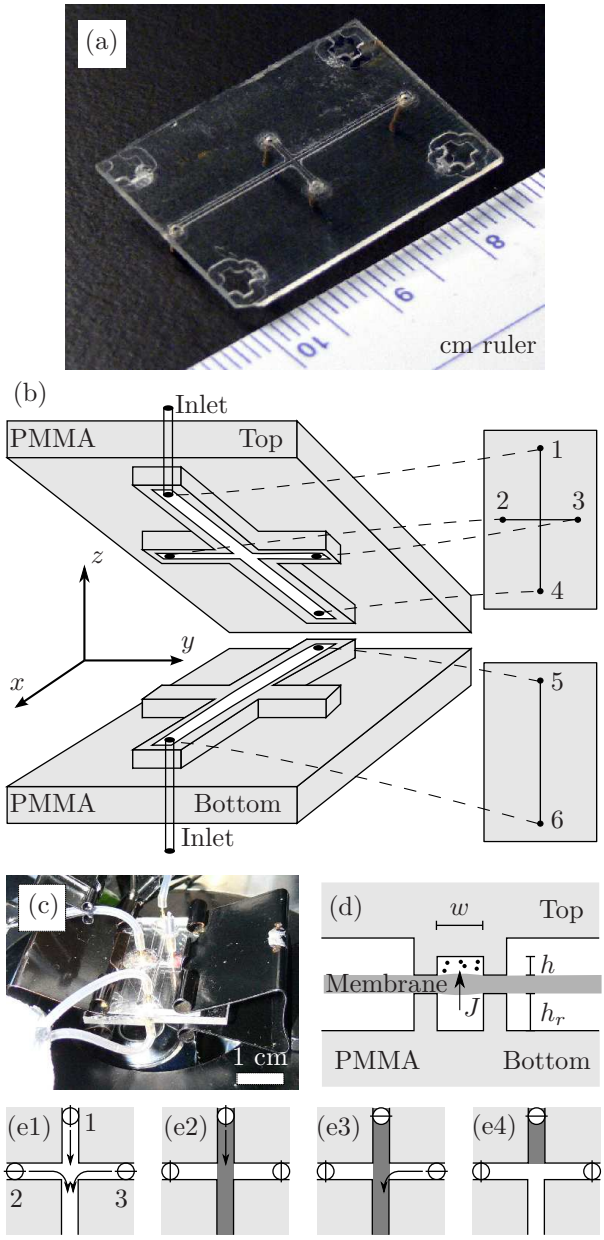

Figure 7.1: (a) Picture of the top part (upside down) of the chip showing the elevated channel and the four brass inlet tubes (pointing down). The crosses in the four corners were used for alignment. (b) Schematics of the two PMMA layers (gray) showing the elevated channels (white) facing each other. All six inlet positions (black dots) are marked, but for clarity only two brass tubes are shown. (c) Picture of the fully assembled setup. (d) Schematic cross-section closeup of the two PMMA layers (gray) clamped together with the semipermeable membrane (dark gray) in between. The sugar in the upper channel (black dots) and the water influx J from the lower channel (arrow) are also marked. (e1)-(e4) Valve settings (circles) and cross-flow flushing procedure (arrows) for creating a sharp front in the top channel between the sugar/dye solution (dark gray) and the pure water (white). See details in the text.

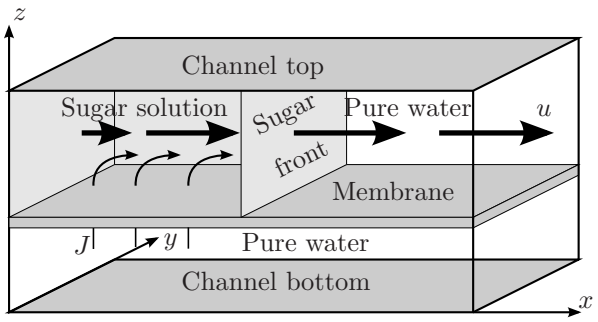

Figure 7.2: A sketch of the osmotically driven flow. The osmotic pressure forces water from the lower channel, through the membrane, and into the sugar-rich part (light gray region) of the upper channel. The water flux J (curved arrows), which pushes the sugar front forward, is related to the sugar concentration by Eq. (7.3). The resulting flow velocity u is represented by the thick horizontal arrows.

Dye, type 123000) in the dye tracking experiments and 0.05 % volume sulfate modified 1 μm polystyrene beads (Sigma Aldrigde, L9650-1ML, density 1050 kg/m^3) in the particle tracking experiments. Inlets 4 and 6 were connected to the same water bath to minimize the hydrostatic pressure difference between the two sides of the membrane. The liquid height in the water bath was carefully aligned to the top channel to avoid any difference in liquid height that might have resulted in a flow in the opposite direction. When conducting both dye tracking and particle tracking experiments, the initialization procedure shown in Fig. 8.2(e1)-(e4) was used: First (e1), inlet valves 1, 2 and 3 were opened and all channels were flushed thoroughly with pure water (white) to remove any air bubbles and other impurities. Second (e2), after closing inlets 2 and 3 a sugar solution (dark gray) was injected through inlet 1 filling the main channel in the upper layer. Third (e3), inlet 1 was closed and water was carefully pumped through inlet 2 to produce a sharp concentration front at the cross, as shown in Fig. 8.2(e4) and 7.3(b).

Sugar front motion recorded by dye tracking

The motion of the sugar front in the upper channel was recorded by taking pictures of the channel in 10 s intervals using a Leica MZ 16 microscope. This yielded images as those displayed in Fig. 7.3(a), clearly showing a front (marked by arrows) of the sugar/dye solution moving along the channel. To obtain the position $\lambda(t)$ of the sugar front as a function of time t, the distance from the initial front position λ_0 to the current position $\lambda(t)$ was measured using ImageJ software. The position of the sugar front was taken to be at the end of the highly saturated dark region. In this way, the position of the front could be measured at each time step with an accuracy of ± 200 μm. As verified in earlier works [16, 30], we assumed that the sugar and dye traveled together, which is reasonable since the Péclet number is $Pé \sim 10$ (see Section 7.5). Experiments with dye alone were carried out. These showed, that the osmotic pumping due to the dye molecules was negligible. We

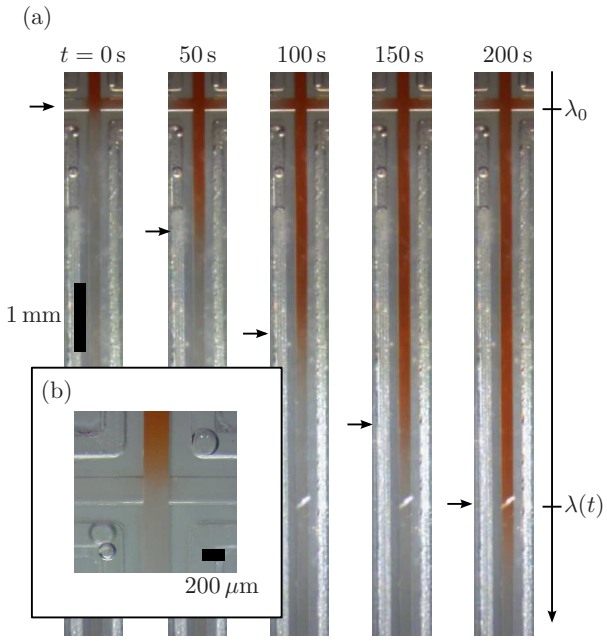

Figure 7.3: (a): Images showing the sugar front moving in the 200 μm×200 μm channel. The time between each image is 50 s. The arrows indicate the position of the sugar front as it moves down along the channel. (b): Closeup of the cross junction just after a sharp sugar/water interface has been created.

only applied the dye tracking method on the 200 μm deep channel, since the 100 μm and 50 μm deep channels were too shallow for sufficient scattering of red light by the solution to get a clear view of the front.

Sugar front motion recorded by use of particle tracking

The flow velocity inside the upper channel was recorded by tracking the motion of 1 μm beads in the water 3 mm ahead of the initial sugar front position. Images were recorded every 200 − 1000 ms for up to 400 s using a Unibrain Fire-i400 1394 digital camera attached to a Nikon Diaphot microscope with the focal plane at $h/2$ and a focal depth of approximately 10 μm. Sedimentation times for the particles were 1800 s for the 200 μm channel and 450 s for the 50 μm channel. Since only the first 150 s were used when determining the front velocity, this did not interfere with our measurements. At the point of observation, well ahead of the front, the flow behaved as if it were pressure driven (see the insert in Fig. 7.5) and the standard laminar flow profile [10] was used to determine the average flow velocity.

7.4 Experimental results

7.4.1 Dye tracking

Figure 7.4 shows the position of the sugar front in the 200 μm deep channel as a function of time obtained by dye tracking. The data sets correspond to different concentrations of sucrose and dextran as indicated in the legends. Initially, the sugar front moves with constant speed, but then it gradually decreases, more so for low than high concentrations. The solid black lines are linear fits for the first 100 s giving the initial velocity of the front. As a function of time the front smears out over a region of growing width w_f. In Fig. 7.4(c) w_f is plotted vs. time for the 10.1 mM dextran experiment along with a fit to $w_f = (2Dt)^{1/2}$ showing that the sugar front broadens by molecular diffusion. Here, D is the molecular diffusion constant.

7.4.2 Particle tracking

Figure 7.5 shows the velocity as a function of time obtained by particle tracking in a $200\,\mu\text{m}\times 200\,\mu\text{m}$ channel. For the first 150 s the velocity is approximately constant after which it starts decreasing as the sugar front passes the point of observation. We interpret the mean value of the initial plateau of the velocity graph as the speed of the sugar front. Figs. 7.6(a) and (b) shows the velocity of the sugar front as a function of dextran concentration and of channel depth obtained in this way.

7.5 Theoretical analysis

When modeling the flow inside the channel, we use an approach similar to that of Eschrich *et al.* [16]. They introduced a 1D model with no axial flow resistance and zero diffusivity in a setting very similar to ours. To formalize this, we consider the two most important non-dimensional numbers in the experiments: the Münch number M [30] and the Péclet number $Pé$ [10]. These numbers characterize the ratio of axial to membrane flow resistance and axially convective to diffusive fluxes respectively. In our experiments

$$M = \frac{wLL_p\alpha RTc}{\frac{wh^3}{\eta L}\alpha RTc} = \frac{\eta L^2 L_p}{h^3} \sim 10^{-6}, \tag{7.1}$$

and

$$Pé = \frac{w_f u}{D} \sim 10. \tag{7.2}$$

Here η is the viscosity (typically 1.5 mPa s), w_f is the width of the sugar front (typically 500 μm), and D the molecular diffusivity of sugar (typically 10^{-10} m^{2}s^{-1} for sucrose and the dye and 10^{-11} m^{2}s^{-1} for dextran)

7.5.1 Equation of motion

Since $M \ll 1$ and $Pe \gg 1$, we shall neglect the axial flow resistance and the diffusion of the sugar in our analysis. In this way, let $\lambda(t)$ denote the position of the sugar/dye front

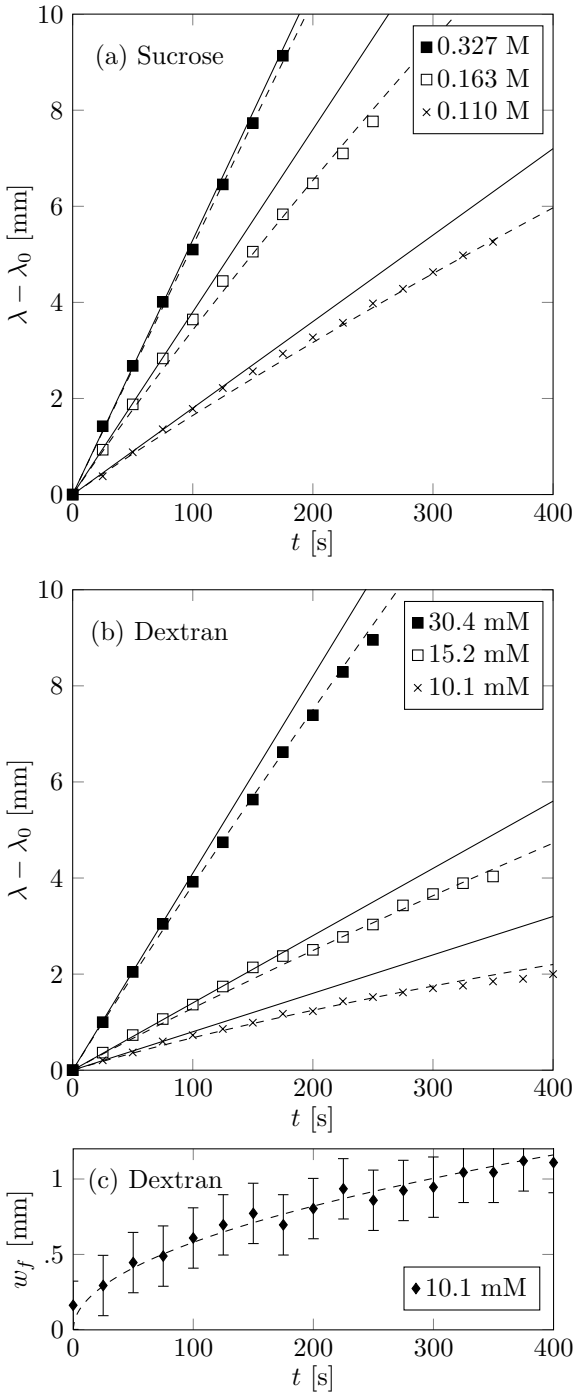

Figure 7.4: Measured position λ of the sugar front as a function of time t in the $200\,\mu\text{m}\times200\,\mu\text{m}$ channel for various concentrations of (a) sucrose and (b) dextran. The solid black lines are linear fits for $0\,\text{s} < t < 100\,\text{s}$. The dashed lines are fits to Eq. (7.13). (c) The width w_f of the sugar front as a function of time for the 10.1 mM dextran experiment. The dashed black line is a fit to $(2Dt)^{1/2}$ with $D = 1.7 \times 10^{-9}\,\text{m}^2\,\text{s}^{-1}$, 5 times larger than the value given in Tabel 7.1. This, however, is in good agreement with Taylor dispersion theory [74, 42], since $Pé \simeq 15$.

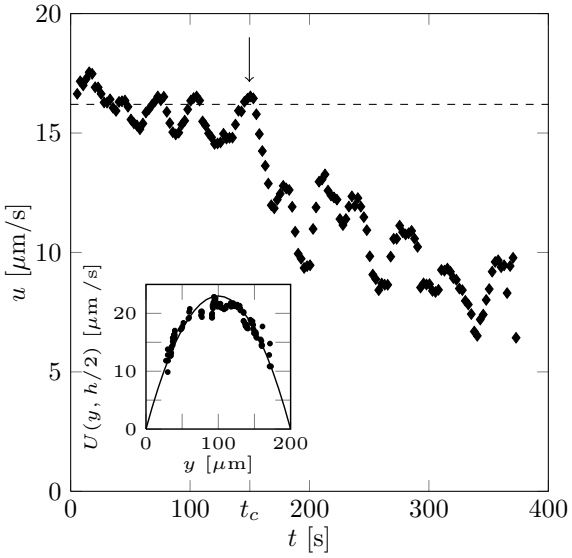

Figure 7.5: The average flow velocity u in the 200 μm deep channel as a function of time t measured 3 mm ahead of the initial front position. At $t_c \simeq 150\,\mathrm{s}$ (indicated by the arrow), the sugar front begins to reach the observation point, and the velocity decreases rapidly. For $t > t_c$, the velocity was not determined accurately. The insert shows a typical velocity profile $U(y, h/2)$ in the center plane across the $200\,\mu\mathrm{m}\times 200\,\mu\mathrm{m}$ channel obtained by particle tracking. The solid black line is a fit to the velocity profile for a rectangular channel used when obtaining the average flow velocity.

in the upper channel, and let V denote the volume behind the front. The flux J of water across the membrane from the lower to the upper channel, see Fig. 8.2(d), is given by

$$J = L_p\left(\Delta p + \Delta\Pi\right) \simeq L_p \alpha R T c, \tag{7.3}$$

where L_p is the membrane permeability, Δp the hydrostatic and $\Delta\Pi$ the osmotic pressure difference across the membrane. In our experiments $\Delta p = 0$, and from the van 't Hoff relation follows $\Delta\Pi \simeq \alpha R T c$, where α is the osmotic non-ideality coefficient, R is the gas constant, T is the absolute temperature, and c is the concentration of sugar molecules. Since the concentration is independent of x behind the front and zero ahead of it, J is also independent of x. By the conservation of sugar this allows us to a first approximation to write the concentration as

$$c(x,t) = \begin{cases} c_0 \frac{\lambda_0}{\lambda(t)} & x \le \lambda(t), \\ 0 & x \ge \lambda(t). \end{cases} \tag{7.4}$$

Moreover, the rate of change of the expanding volume V behind the front can be related

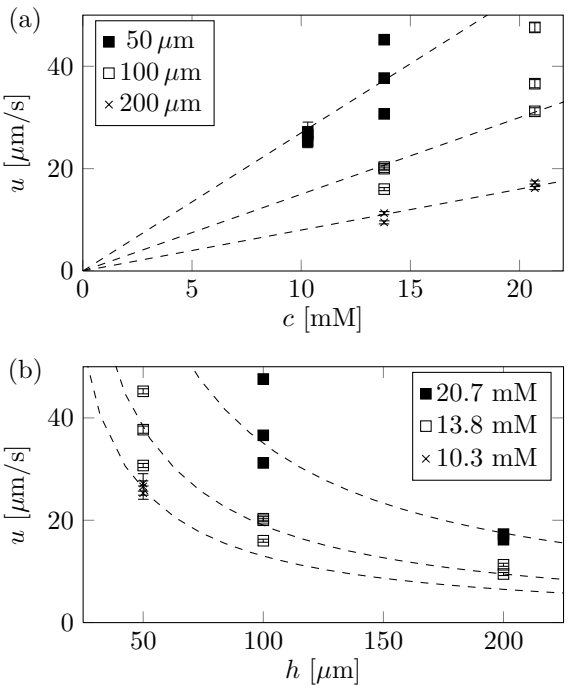

Figure 7.6: Front velocity u obtained by particle tracking. (a) The velocity u plotted against dextran concentration c_0. The dashed lines are fits to c provided as guides to the eye. (b) The velocity u plotted against channel depth h. The dashed lines are fits to $1/h$ provided as guides to the eye.

to J as

$$\begin{aligned} \frac{\mathrm{d}V}{\mathrm{d}t} &= w\int_0^L J(x)\mathrm{d}x \\ &= wL_p\alpha RTc_0\frac{\lambda_0}{\lambda(t)}\int_0^{\lambda(t)}\mathrm{d}x \\ &= w\lambda_0 L_p\alpha RTc_0. \end{aligned} \tag{7.5}$$

However, we also have that

$$\frac{\mathrm{d}V}{\mathrm{d}t} = hw\frac{\mathrm{d}\lambda(t)}{\mathrm{d}t}, \tag{7.6}$$

which implies together with Eq. (7.5) that

$$\lambda(t) = \lambda_0 + \frac{\lambda_0}{h}L_p\alpha RTc_0 t = \lambda_0 + ut, \tag{7.7}$$

where the velocity u of the front is given by

$$u = \frac{\lambda_0}{h}L_p\alpha RTc_0. \tag{7.8}$$

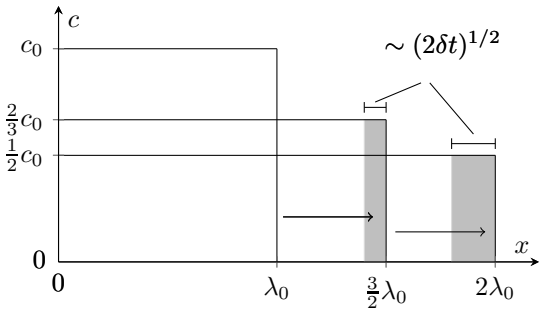

Figure 7.7: The time evolution of the sugar concentration profile given by Eq. (7.4). The gray regions represents the sugar lost from the observed region by diffusion, see Eq. (7.9).

7.5.2 Corrections to the equation of motion

In the previous section, we considered the motion of a sharp sugar front, as given by the stepwise concentration profile in Eq. (7.4), and found that this moved with constant velocity. However, as can be seen in Fig. 7.4(a,b) the front velocity gradually decreases. To explain this, we consider two effects. First, we observe that in Fig. 7.3(a) there exists a region of growing size separating the sugar/dye-filled region from the region of pure water. Even though the sugar and the dye diffuse at different rates, we shall assume that some of the sugar also lies ahead of the visible front. Since the sugar in this region is located ahead of the front, the osmotic pumping in the observed volume behind the front is lowered, thus slowing down the motion of the observed front. Second, we note that sugar leaking across the membrane also lowers the osmotic pumping behind the front. This effect should be especially pronounced for sucrose, since its molecular weight is smaller than the cut-off of the membrane. Common to these two effects is, however, that they are driven by diffusion. In the first case, sugar diffuses from the pumping region to a region ahead of the front and in the second it diffuses across the membrane. The nature of these two effects makes them impossible to distinguish from one another. Lumping them together as one diffusion process characterized by an effective diffusion constant δ, we may rewrite Eq. (7.4) as

$$c(x,t) = \begin{cases} c_0 \frac{\lambda_0}{\lambda(t)+\ell_D} & x \leq \lambda(t), \\ 0 & x \geq \lambda(t). \end{cases} \tag{7.9}$$

where $\ell_D = (2\delta t)^{1/2}$. Here δ is a fitting parameter which has the dimension of a diffusion coefficient and which includes both of the effects mentioned above. In this way, the amount of sugar lost from the observed volume by diffusion is $\Delta c \simeq c_0 (2\delta t)^{1/2}$, as indicated in Fig. 7.7.

Using Eqs. (7.5) and (7.6) the time derivative of λ becomes

$$\frac{\mathrm{d}\lambda}{\mathrm{d}t} = \frac{L_p \alpha R T c_0 \lambda_0}{h} \frac{\lambda}{\lambda + \ell_D}. \tag{7.10}$$

Rescaling using $\lambda = s\lambda_0$ and $t = \tau\frac{\lambda_0}{u}$, we get that

$$\frac{\mathrm{d}s}{\mathrm{d}\tau} = \frac{s}{s + \left(\frac{\tau}{P\acute{e}_g}\right)^{1/2}}, \tag{7.11}$$

where we have introduced the global Péclet number related to the loss of sugar by diffusion,

$$P\acute{e}_g = \frac{2\lambda_0^2 L_p \alpha R T c_0}{\delta h} = \frac{2\lambda_0}{\delta} u. \tag{7.12}$$

Given the experimental conditions, $P\acute{e}_g$ is typically of the order $10^1 - 10^2$. Thus, for $\left(\frac{\tau}{P\acute{e}_g}\right)^{1/2} \ll 1$, Eq. (7.11) can be solved by an expansion,

$$s = s_0 + \tau\left(1 - \frac{2}{3s_0}\left(\frac{\tau}{P\acute{e}_g}\right)^{1/2} + \mathcal{O}\left[\left(\frac{\tau}{P\acute{e}_g}\right)\right]\right). \tag{7.13}$$

We have made numerical simulations of the full 1-D coupled velocity-concentration equation system for the special case of diffusion ahead of the front. Our results show, that the simple model in Eq. (7.13) captures the essential dynamics of the motion of the sugar front. The dashed lines in Figs. 7.4(a) and (b) are fits to Eq. (7.13), with values of δ varying between $2 \times 10^{-7}\,\mathrm{m^2\,s^{-1}}$ and $4 \times 10^{-9}\,\mathrm{m^2\,s^{-1}}$, showing good qualitative agreement between theory and experiment. However, since we have not tracked the sugars directly, these cannot immediately be compared with the values for sucrose ($D = 4.6 \times 10^{-10}$ m^2/s) and dextran ($D = 7.0 \times 10^{-11}$ m^2/s). To completely resolve this issue, experiments with eg. fluorescently tagged sugar molecules where the concentration on both sides of the membrane is measured are needed.

7.6 Discussion

7.6.1 Comparison of theory and experiment

To compare the experimental data with theory, we have in Fig. 7.8 plotted the empirically obtained velocities u_{exp} against those predicted by Eq. (7.8). For nearly all the dextran and sucrose experiments we see a good agreement between experiment and theory, although Eq. (7.8) systematically overestimates the expected velocities.

We interpret the quantitative disagreement as an indication of a decreasing sugar concentration in the top channel due to diffusion of sugar into the membrane as well as the presence of a low-concentration boundary layer near the membrane, a so-called unstirred layer [58].

7.6.2 Osmotic pumps in lab-on-a-chip systems

Depending on the specific application, flows in lab-on-a-chip systems are conventionally driven by either syringe pumps or by using more advanced techniques such as off-chip

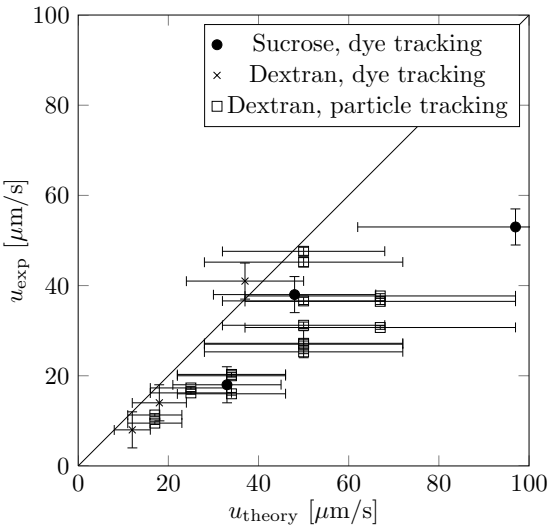

Figure 7.8: The experimental values of the front velocity u_{exp} plotted against the theoretical results u_{theory} from Eq. (7.8).

osmotic pumps [55], electronically controlled pressure devices, electro-osmotic pumps [2], evaporation pumps [54], or capillary pumps [8]. Most of these techniques involves the integration of either movable parts or complicated electronics into the lab-on-a-chip device. As an application of our design and fabrication method, we suggest the use of integrated osmotic pumps in lab-on-a-chip systems. This could be done by integrating in the device a region where the channel is in contact through a membrane with a large reservoir containing an osmotically active agent. By using a sufficiently large reservoir, say $1\,\text{cm}^3$, and a $100\,\mu\text{m}\times 100\,\mu\text{m}$ channel with a flow rate of $100\,\mu$m/s it would take more than 10 days to reduce the reservoir concentration by 50% and thus decreasing the pumping rate by 50%. We emphasize that such osmotic pumping would be completely steady, even at very low flow rates.

7.7 Conclusions

We have studied osmotically driven, transient flows in 200 μm wide and $50 - 200$ μm deep microchannels separated by a semipermeable membrane integrated in a microfluidic PMMA chip. These flows are generated by the influx of water from the lower channel containing pure water, through the semipermeable membrane, into the large sugar concentration placed in one end of the top channel. We have observed that the sugar front in the top channel travels with constant speed, and that this speed is proportional to the concentration of the sugar solution and inversely proportional to the depth of the channel. We propose a theoretical model, which, in the limit of low axial flow resistance, predicts that the sugar front should travel with a constant velocity. The model also predicts an

inverse relationship between the depth of the channel and the speed and a linear relation between the sugar concentration and the speed. We compare theory and experiment with good qualitative agreement, although the detailed mechanism behind the deceleration of the flow is still unknown. Finally, we suggest that on-chip osmotic elements can potentially act as pumps with no movable parts in lab-on-a-chip systems.

7.8 Acknowledgements

It is a pleasure to thank Emmanuelle Rio, Christophe Clanet, Frederik Bundgaard, Jan Kafka and Oliver Geschke for assistance and advice on chip design and manufacturing. We also thank Alexander Schulz, Michele Holbrook, Maciej Zwieniecki and Howard Stone for many useful discussions of the biological and phycial aspects of osmotically driven flows. This work was supported by the Danish National Research Foundation, Grant No. 74 and by the Materials Research Science and Engineering Center at Harvard University.

End of paper

K. H. Jensen, J. Lee, T. Bohr and H. Bruus
Osmotically driven flows in microchannels separated by a semipermeable membrane
Lab on a Chip **9**(14), pp. 2093–2099 (2009)

Table 7.1: List of parameters in alphabetic order after the symbol.

Parameter	Symbol	Value and/or unit
Sugar concentration	c	mol/L
Initial concentration	c_0	mol/L
Diffusive concentration loss	Δc	mol/L
Diffusion constant	D	m^2/s
Sucrose, see Ref. [4]	D	$4.6 \times 10^{-10}\ \mathrm{m}^2/\mathrm{s}$
Dextran, see Ref. [30]	D	$7.0 \times 10^{-11}\ \mathrm{m}^2/\mathrm{s}$
Dye, see Ref. [4]	D	$3.4 \times 10^{-10}\ \mathrm{m}^2/\mathrm{s}$
Height of channel	h	$50, 100, 200\ \mu\mathrm{m}$
Height of reservoir	h_r	$200\ \mu\mathrm{m}$
Flux across membrane	J	m/s
Length of channel	L	27 mm
Membrane permeability	L_p	1.8 pm/(Pa s)
Diffusion length	l_D	m
Münch number	M	
Hydrostatic pressure	p	Pa
Péclet number, local	$Pé$	
Péclet number, global	$Pé_g$	
Gas constant	R	8310 Pa L/(K mol)
Position of sugar front	s	
Absolute temperature	T	K
Time	t	s
x-velocity of sugar front	U	m/s
Mean x-velocity of sugar front	u	m/s
Volume behind sugar front	V	m^3
Width of channel	w	$200\ \mu\mathrm{m}$
Width of sugar front	w_f	m
Cartesian coordinates	x, y, z	m
Osmotic coefficients:		
Dextran ($T = 293\,\mathrm{K}$)	α	41, see Ref. [30]
Sucrose ($T = 293\,\mathrm{K}$)	α	1, see Ref. [47]
Fitting parameter	δ	m^2/s
Viscosity	η	Pa s
Position of sugar front	λ	m
Position of initial sugar front	λ_0	13.5 mm
Osmotic pressure	Π	Pa

Chapter 8

Self-consistent unstirred layers in osmotically driven flows

The one-dimensional equations of motion analyzed in Chapters 3-6 where derived under the assumption that the concentration is well-mixed across the cross-section of the tube. This approximation is valid if the radial transport of solute molecules due to diffusion is much faster than the transport due to advection. To quantify exactly when this condition is fulfilled, one generally needs to solve the coupled concentration-osmotic flow problem. Since this question is relevant to a number of industrial membrane transport problems (such as desalination) it has been analyzed by a number of workers. One of the main contributors is T. J. Pedley who in a series of papers published in the late 1970s and early 1980s solved the coupled problem in a number different geometries [59, 60, 56, 57, 58]. His solutions quantify to what degree the solution is well-mixed, but only in situations where the osmotic flow across the membrane is a small perturbation to a much larger, externally driven, bulk velocity component. This situation is relevant to many industrial application, where e.g. an external stirring mechanism is present, but not to plants where osmosis itself drives the bulk flow.

The author, Tomas Bohr, and Henrik Bruus thus decided to look for analytical solutions of the self-consistent problem i.e. the problem where osmosis itself is driving the bulk flow. We studied the flow between parallel plates because the flow field was already known in the literature, and thus allowed for a simple analysis of the concentration part of problem. This change in geometry, of course, makes the applicability of our results to plants difficult to access. However, since we show that all geometries behave nearly the same under a proper rescaling, we believe that the low value of the radial Péclet number found in plants ($Pe \simeq 0.01$, cf. Eq. (3.49), p. 26) implies that the concentration is well mixed across the tube cross-section.

The following paper, [27], presented unabridged in Sec. 8.1–8.7, describes our theoretical analysis of parallel plate problem. The author conducted all of the numerical simulations and most of the theoretical analysis. To stay true to the published manuscript the notation differs slightly from that found in Chapters 1–6. Please refer to Table 8.1, p. 108, for a list of parameters.

Start of paper

K. H. Jensen, T. Bohr and H. Bruus
Self-consistent unstirred layers in osmotically driven flows
Journal of Fluid Mechanics **662**, pp. 197–208 (2010)

8.1 Abstract

It has long been recognized, that the osmotic transport characteristics of membranes may be strongly influenced by the presence of unstirred concentration boundary layers adjacent to the membrane. Previous experimental as well as theoretical works have mainly focused on the case where the solutions on both sides of the membrane remain well-mixed due to an external stirring mechanism. We investigate the effects of concentration boundary layers on the efficiency of osmotic pumping processes in the absence of external stirring i.e. when all advection is provided by the osmosis itself. This case is relevant in the study of intracellular flows, e.g. in plants. For such systems, we show that no well-defined boundary layer thickness exists and that the reduction in concentration can be estimated by a surprisingly simple mathematical relation across a wide range of geometries and Péclet numbers. Osmosis, boundary layers, biological flows.

8.2 Introduction

Osmotic transport characteristics of membranes are strongly influenced by the presence of unstirred concentration boundary layers adjacent to the membrane [58]. As first demonstrated by Dainty [15], these boundary layers lead to a decrease in the efficiency of the osmotic pumping process. To see this, consider an ideal semipermeable membrane (i.e. a membrane permeable to solvent molecules but impermeable to solute molecules) separating two solutions of the same solute at different bulk concentrations, say zero and unity, as shown in Fig. 8.1(a). If there were no transport of solvent across the membrane, these concentrations would persist all the way to the membrane. However, if there is a flux J of solvent due to osmosis across the membrane from the region of low concentration (say the left side) to the region of high concentration, the solutes will be pushed away from the membrane on the high-concentration side of the membrane. As a result, the concentration of solute in the vicinity of the membrane on the high-concentration side will be lower. The concentration difference between the two sides of the membrane is thus decreased, and this in turn reduces the magnitude of the osmotically driven flux J, which in the absence of hydrostatic pressure differences across the membrane is given by

$$J = \gamma, \tag{8.1}$$

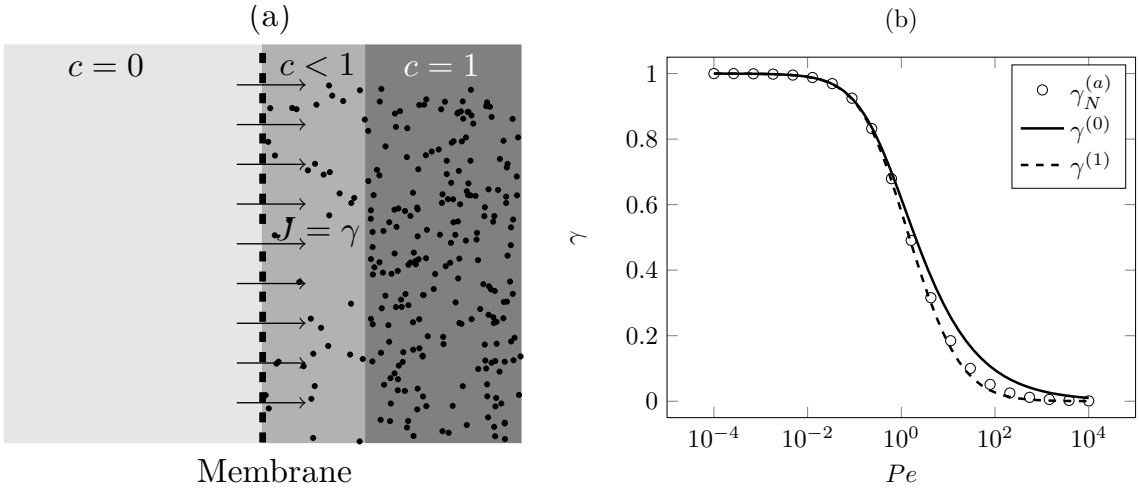

Figure 8.1: (a) Sketch of solute concentration distributions on either side of a semipermeable membrane separating two well-stirred solutions of the same solute at different bulk concentrations $c = 0$ (left side) and $c = 1$ (right side). Because of the transport of solvent across the membrane due to osmosis (sketched by the arrows) from left to right, there will be a tendency for the concentration γ of solute in contact with the membrane to be lower than unity just on the right side of the membrane. Since the flux of solvent J is proportional to the difference in concentration, we have that $J = \gamma$. (b) Numerically computed membrane concentration γ_N as a function of the Péclet number Pe for the parallel plate geometry (circles) shown in Fig. 8.2(a). Also shown are the expressions given by Eq. (8.10) (solid) and Eq. (8.17) (dashed). See Sec. 3 for details.

according to the standard equations of non-equilibrium thermodynamics [39]. Here, J is the volume flux pr. area pr. unit time, γ is the solute concentration immediately to the right (high concentration side) of the membrane, and both quantities are non-dimensional as described in Sec. 8.3.1.

A large number of papers has presented both experiments (see e.g. [62]) and theory (see e.g. [59, 56, 57, 58] and [3]) for the situation described above. Most of these workers have focused on the case where the solution on both sides of the membrane remain well-stirred such that a well defined boundary layer exists. For a number of different geometries, the thickness of the boundary layer has been determined as a function of systems parameters and the functional dependence on the osmotic pumping efficiency γ has be found.

A major limitation of the above theoretical and experimental work is, however, that it is concerned only with situations in which the solutions on both sides of the membrane remain well-mixed due to an external stirring mechanism. In nearly all cases, it is assumed that the flow generated by osmosis through Eq. (8.1) is negligible in determining the bulk flow, and only of significance close to the membrane.

The goal of the present work is to examine theoretically the situation in which the advecting bulk flow is itself driven by Eq. (8.1) and no external stirring is present. An important example, the one that inspired this work, is the flow in phloem cells of plants, where the osmotic pressure differences are believed to be responsible for the flow of the sugar solutions (the so-called Münch mechanism, see e.g. [79], [30]). In the present paper, we compute the concentration and flow profiles for various simple geometries. For these systems, we will show that no localized boundary layer exists, and second that the drop in concentration γ can be calculated by a simple mathematical relation valid across a wide range of geometries and Péclet numbers.

8.3 Governing equations and geometries

In the analysis of the problem describe above, we shall consider steady osmotically driven flows confined between two infinite parallel plates at low Reynolds numbers. We thus consider systems such as those sketched in Fig. 8.2(a)-(c), and explained further in Sec. 8.3.3, in which a solute of concentration c is diffusing and being advected by a velocity field $\mathbf{u}$, arising due to an osmotic flow across a membrane (indicated by dashed lines).

8.3.1 Non-dimensional variables

To simplify the mathematical expressions we are using non-dimensional variables throughout this paper. The explicit scalings are: Lengths are given by the plate-to-plate distance h, concentrations are in units of the characteristic concentration c_0, velocities are given by the characteristic osmotic velocity $u_0 = L_p RT c_0$, where L_p is the permeability of the membrane, R is the molar gas constant, and T is the absolute temperature. Moreover, pressure is given in terms of shear-stress pressure $p_0 = \eta u_0/h$.

The Reynolds number is given by $Re = \rho u_0 h/\eta \ll 1$, so we treat only Stokes flow in this paper. The Péclet number is given by $Pe = u_0 h/D$, where D is the diffusivity of the solute. In most cases we assume that $Re \ll 1$ while Pe is finite which implies that the

Schmidt number $Sc = \frac{\eta}{\rho D}$ is very large. This is consistent with the situation in plants cells, where the Schmidt number is of order 10^4.

8.3.2 Steady state equations of motion - Stokes flow

The equations of motion governing the velocity field $\mathbf{u} = (u, v)$ and pressure field p are the Stokes equation and the continuity equation

$$\nabla p = \nabla^2 \mathbf{u}, \tag{8.2}$$

$$\nabla \cdot \mathbf{u} = 0. \tag{8.3}$$

The equation governing the concentration field is

$$\mathbf{u} \cdot \nabla c = \frac{1}{Pe} \nabla^2 c. \tag{8.4}$$

The velocity boundary condition at the membrane interface Ω, is that the normal velocity component $\mathbf{n} \cdot \mathbf{u}$ is given by

$$\mathbf{n} \cdot \mathbf{u}(x, y) = c(x, y), \quad \text{for } (x, y) \in \Omega. \tag{8.5}$$

The concentration boundary condition is that the normal component of the solute flux across the membrane must be zero, ie.

$$\frac{1}{Pe} \mathbf{n} \cdot \nabla c(x, y) + \mathbf{n} \cdot \mathbf{u}(x, y) c(x, y) = 0, \quad \text{for } (x, y) \in \Omega. \tag{8.6}$$

Solutions to Eqns. (8.2)-(8.6) for arbitrary geometries are not readily available. Thus in Sec. 8.4 we study full numerical solutions to our problem, and from the observed behavior of these we establish and verify approximate analytical solutions in Sec. 8.5.

8.3.3 Geometries

We consider the three geometries shown in Fig. 8.2. Outside the indicated membranes a solution of concentration $c = 0$ is present. First, in (a), left-right symmetric flow between two parallel plates separated a non-dimensional distance of 1 is analyzed. At the the upper plate, a source region of length $2\ell_m$ is kept at a constant concentration $c = 1$. On the lower plate, facing the constant concentration zone, is a membrane (indicated by the dashed line) also of length $2\ell_m$. Second, in (b), up-down symmetric flow between two parallel plates (separated by a distance 1) with a solid-wall source region ($c = 1$) at a right angle to the membrane is considered. The length of the membrane zone is $\ell_m^{(\mathrm{b})}$, and the distance from the source region to the membrane region is H. Finally, in (c), left-right and up-down symmetric flow around a solid cylinder of radius r is embedded exactly half way between two plates (separated by a distance 1) is considered. At the surface of the cylinder is a source region ($c = 1$). The length of the membrane zone is $\ell_m^{(\mathrm{c})}$. At the cylinder surface we impose a no-slip boundary condition.

In the following, we will investigate geometry (a) analytically and numerically, while geometries (b) and (c) will only be considered numerically.

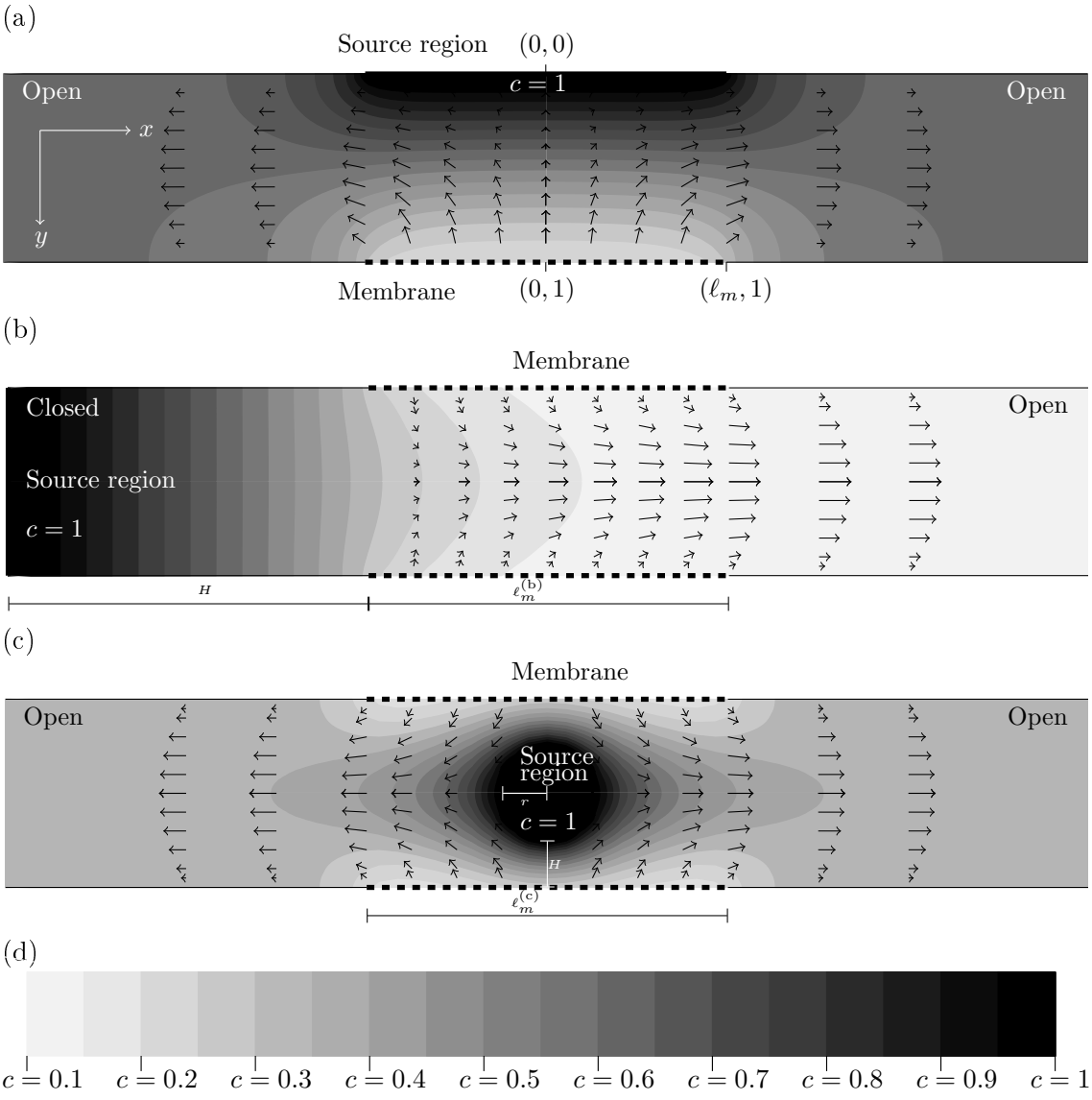

Figure 8.2: Sketch of the geometries considered. (a) Flow between parallel plates. On the upper plate, a region is kept at a constant concentration $c = 1$. On the lower plate, facing the constant concentration zone at distance $H = 1$, is a membrane of length $2\ell_m$ in this case plotted for $\ell_m = 1$. By osmosis, liquid flows across the membrane, thereby diluting the concentration near the membrane. (b) Flow between parallel plates with a membrane of length $\ell_m^{(\mathrm{b})} = 2$ at a right angle to the concentration source. The distance between the two zones are $H = 2$. (c) A cylinder of radius $r = \frac{1}{4}$, embedded exactly half way between the two plates. At the surface of the cylinder the concentration is kept constant at $c = 1$. The length of the membrane zone is $\ell_m^{(\mathrm{c})} = 2$ and $H = \frac{1}{4}$. In (a)-(c), numerically computed concentration contours (see (d)) are shown (Plotted for $Pe' = 10$, see Sec. 5). The velocity field is indicated by the arrows. (d) Contour scale bar for the concentration contour plots in (a)-(c).

8.4 Numerical results for the left-right symmetric parallel plate problem

The steady-state behavior of the systems shown in Fig. 8.2 was solved using the numerical methods described in Appendix 8.8. The figure shows typical concentration and velocity profiles obtained in this way. Varying the Péclet number Pe, a number of such simulations were made and the following qualitative observations were made.

In geometry (a), for $Pe \ll 1$, the concentration in the membrane zone ($0 < x < \ell_{\mathrm{m}}$) hardly varies at all along the x-direction, and the variation along the y-direction is linear. This is illustrated in Fig. 8.3 which shows cross-sections taken along the y-direction at four different x values. For $x > \ell_{\mathrm{m}}$ the concentration is flat, having been smoothed by diffusion. Near $x = \ell_{\mathrm{m}}$ a transition takes place between the linear concentration gradient and the flat concentration plateau near the outlet. This is illustrated in Fig. 8.4 where cross-sections taken along the x direction are shown.

To quantify the efficiency of the osmotic pumping process, we calculate the mean concentration at the membrane γ as a function of the Péclet number Pe, plotted in Fig. 8.1(b). For small values of Pe, γ tends to the inlet concentration $c = 1$. This is reasonable since any depletion of the membrane concentration would be counteracted by the strong diffusion. For larger values of Pe, equilibrium between diffusive and advective forces leads to values of $\gamma < 1$ thus reducing the efficiency of the osmotic pump.

One further observation is, that as shown in Fig. 8.3 (e)-(f), the velocity field $\mathbf{u} = (u, v)$ is well described by a squeeze flow [10]

$$u(x, y) = 6xy(1 - y)\gamma, \tag{8.7a}$$

$$v(x, y) = y^2(2y - 3)\gamma. \tag{8.7b}$$

Despite of the richness found in the numerical solutions illustrated in Figs. 8.2, 8.3, 8.4 and 8.1(b), the system can be described theoretically using a few simple assumptions regarding the flow and velocity field at very low Péclet numbers. From there, the solutions can be extended using perturbation methods to be valid across a wider range of parameter values.

8.5 Theory for the left-right symmetric parallel plate problem

Inspired by the qualitative results discussed above, we will begin by modeling the concentration profile of Fig. 8.2(a) using that for $Pe \ll 1$ concentration profile is linear in the membrane zone. Near the outlet, the concentration profile is flattened by diffusion and the resulting concentration value is simply the mean of the values at the source region and at the membrane:

$$c(x, y) = \begin{cases} 1 - (1 - \gamma)y, & \text{for } x < \ell_{\mathrm{m}}, \\ \frac{1}{2}(1 + \gamma), & \text{for } x > \ell_{\mathrm{m}}. \end{cases} \tag{8.8}$$

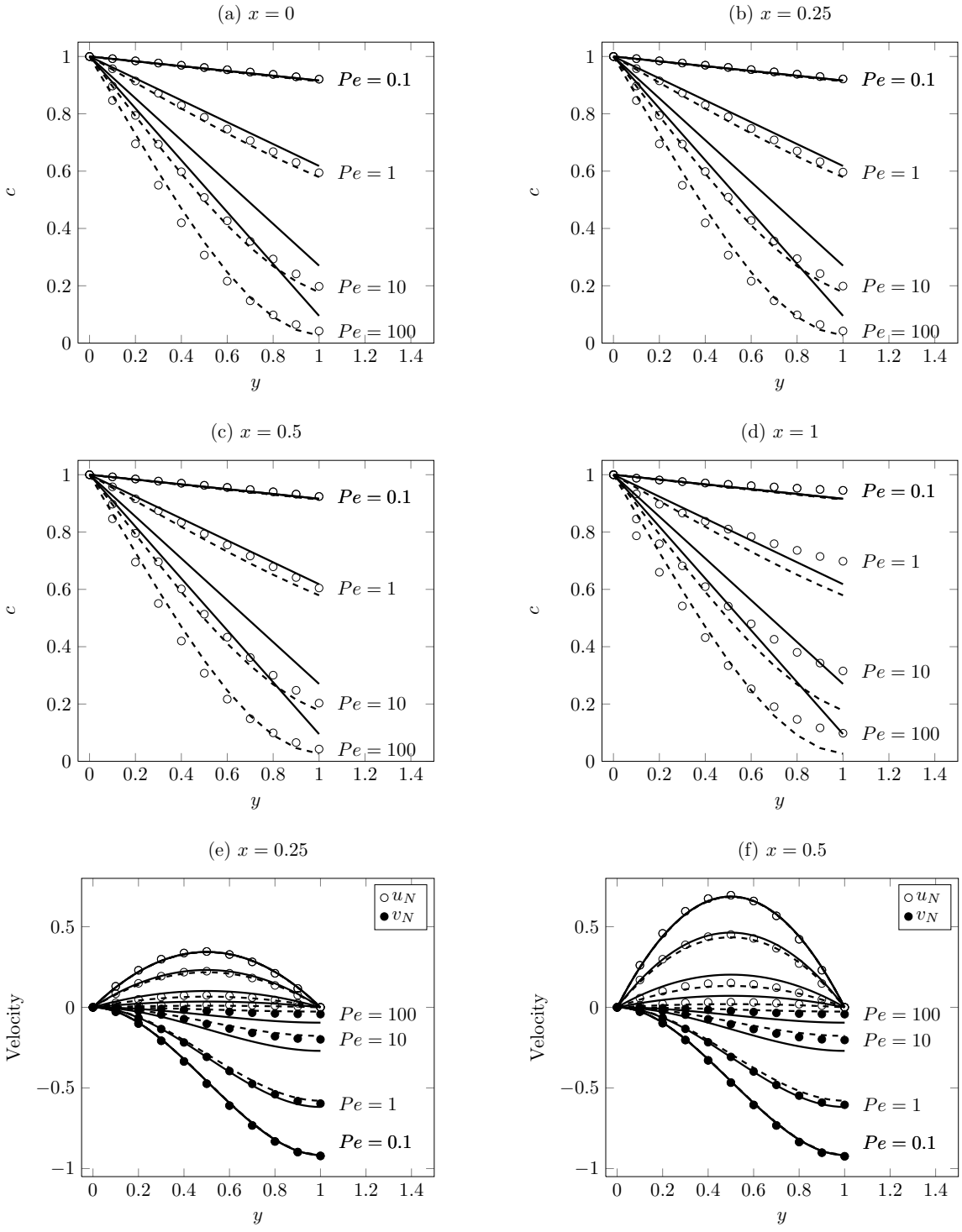

Figure 8.3: (a)-(d) Numerically computed concentration profiles c (circles) plotted against y for different values of x (as indicated above the plots) and the Péclet number Pe (as indicated next to the data points). All plots were obtained for the geometry in Fig. 8.2(a) with $\ell_{\mathrm{m}} = 1$. Also shown are the expressions given by Eq. (8.8) (solid lines) and Eq. (8.16) (dashed lines). (f)-(e) Numerically computed velocity profiles u_N (circles) and v_N (dots) plotted against y for different values of the Péclet number Pe (as indicated next to the data points). Also shown are the velocity profiles given by Eqns. (8.7a) and (8.7b) for u and v respectively The solid lines are plotted with γ obtained from Eq. (8.10) while the dashed lines uses $\gamma^{(1)}$ from Eq. (8.17).

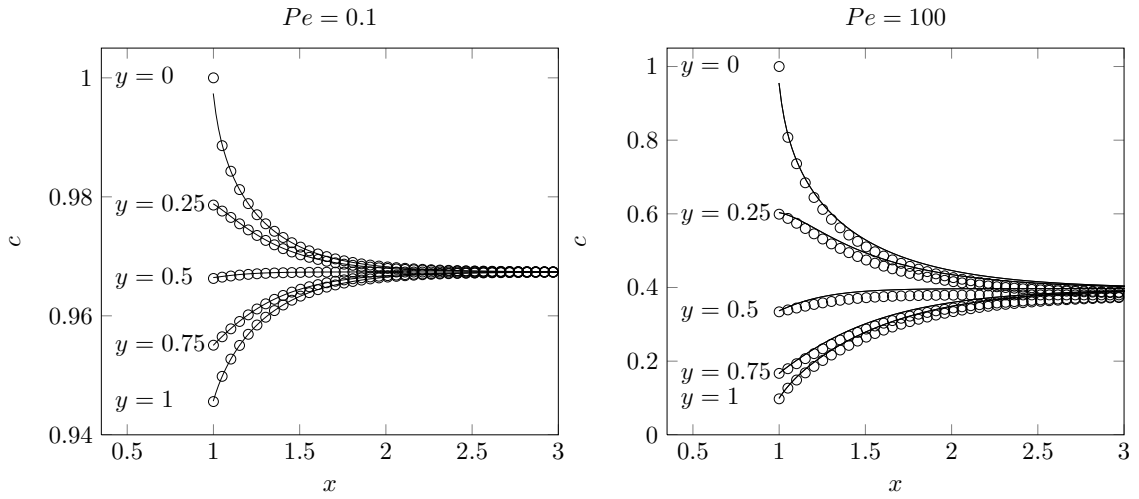

Figure 8.4: Numerically computed concentration profiles c (circles) plotted against x for different values of y (as indicated next to the plots) and the Péclet number Pe (as indicated above the plots). All plots were obtained with $\ell_{\mathrm{m}} = 1$. Also shown is the expressions given by the solution to Eq. (8.18) (solid lines).

To estimate the concentration at the membrane γ we use the boundary condition (8.6),

$$\frac{1}{Pe}\partial_y c = -\gamma^2. \tag{8.9}$$

With Eq. (8.8) this leads to

$$\gamma = \frac{\sqrt{1+4Pe}-1}{2Pe}, \tag{8.10}$$

an expression which does not, except for the length scale h in the Péclet number, depend on the specific geometry. Fig. 8.1(b) shows the numerical results compared with Eqns. (8.8) and (8.10).

8.5.1 A detailed look at the concentration profile for $x < \ell_{\mathrm{m}}$

For $Pe \geq 1$, the assumption of a linear concentration profile given in Eq. (8.8) is no longer valid. To determine a more accurate concentration distribution in the membrane zone we consider the equation governing the concentration field

$$\partial_x^2 c + \partial_y^2 c = Pe\big(u\partial_x c + v\partial_y c\big). \tag{8.11}$$

Starting with the result from Eq. (8.8), we will expand the solution of Eq. (8.11) in powers of Pe as $c = c^{(0)} + Pe\,c^{(1)} + Pe^2 c^{(2)} + \ldots$, with

$$c^{(0)} = 1 - (1-\gamma)y. \tag{8.12}$$

To first order in Pe the governing equation becomes

$$\partial_x^2 c^{(1)} + \partial_y^2 c^{(1)} = u\partial_x c^{(0)} + v\partial_y c^{(0)}. \tag{8.13}$$

The boundary conditions are that $c = 1$ on the top boundary and that $c = \gamma$ on the membrane. We will assume that the terms $\partial_x^2 c^{(1)}$ and $u\partial_x c^{(0)}$ are small compared to $\partial_y^2 c^{(1)}$ and $v\partial_y c^{(0)}$. We further use, that the velocity field $\mathbf{u} = (u, v)$ can be described by a squeeze flow. Inserting $c^{(0)}$, we get that

$$\begin{aligned} \partial_y^2 c^{(1)} &= v\partial_y c^{(0)} = \gamma y^2 (2y-3)\left[-(1-\gamma)\right] \\ &= -\alpha y^2(2y-3), \end{aligned} \tag{8.14a}$$

where $\alpha = \gamma(1-\gamma)$. Finally, $c^{(1)}$ becomes

$$c^{(1)} = -\frac{\alpha}{20}\left(2y^5 - 5y^4 + 3y\right). \tag{8.15}$$

Thus, to first order in Pe, the concentration distribution is

$$c(x,y) = 1 - (1-\gamma)y - \frac{\alpha Pe}{20}\left(2y^5 - 5y^4 + 3y\right). \tag{8.16}$$

The corresponding correction to γ calculated from the membrane boundary condition in Eq. (8.9) is

$$\gamma^{(1)} = \frac{\sqrt{\frac{49}{400}Pe^2 + \frac{33}{10}Pe + 1} - 1 - \frac{7}{20}Pe}{\frac{13}{10}Pe}, \tag{8.17}$$

which is shown as the dashed line in Fig. 8.1(b) To compare Eqns. (8.16) and (8.17) with our numerical simulations, Fig. 8.3 shows numerically obtained concentration profiles plotted as a function of y along with Eq. (8.16) for $x = 0$, 0.25, 0.5 and $x = 1$.

8.5.2 A detailed look at the concentration profile for $x > \ell_{\mathrm{m}}$

For $x > \ell_{\mathrm{m}}$ we shall assume, that the flow is parallel to the x-axis, such that the equation of motion is now

$$\partial_x^2 c + \partial_y^2 c = Pe\ u\partial_x c, \tag{8.18}$$

where u is a now parabolic velocity profile $u = 6\gamma y(1-y)\ell_{\mathrm{m}}$ and $v = 0$. As c is even in y we expand it in a cosine-series $c(x,y) = c_0 + \sum_{n=1}^{\infty} c_n(x)\cos(n\pi y)$ and the equation for the coefficients $c_n(x)$ has the form $\partial_x^2 c_n - n^2\pi^2 c_n - \sum_{m=1}^{\infty} A^{nm}\partial_x c_m = 0$, where the matrix elements A^{nm} are given in Appendix 8.9. Truncating to the lowest two orders $(n, m = 1, 2)$ we search for the exponentially decaying solutions $c_i(x) = c_i^0 \exp(\lambda_i x)$ satisfying

$$(\lambda_1^2 - A^{11}\lambda_1 - \pi^2)(\lambda_2^2 - A^{22}\lambda_2 - 4\pi^2) = 0, \tag{8.19}$$

with negative values of λ_1 and λ_2. The most important eigenvalue is the one with the smallest absolute value since it will determine the asymptotic decay. It seems likely that this eigenvalue is associated to the lowest modes and thus it should be given as

$$\lambda^* = \frac{1}{2}\left(A^{11} - \sqrt{(A^{11})^2 + 4\pi^2}\right). \tag{8.20}$$

In the limit $Pe \ll 1$, we find that $\lambda^* \simeq -\pi$. Taking the first order result (8.17), we find $Pe\gamma^{(1)} \to 20/7$ for $Pe \gg 1$, which implies that $A^{11} = \frac{20}{7}\ell_m\left(1 - 3/\pi^2\right)$. As long as ℓ_m is not too large (i.e. when $A^{11} \ll 2\pi$) we once again obtain $\lambda^* \simeq -\pi$. If on the other hand $A^{11} \gg 2\pi$, we find that $\lambda^* \to 7\pi^4\ell_{\mathrm{m}}/(20(\pi^2 - 3)) \approx -4.96\ell_{\mathrm{m}}$.

For $\ell_m = 1$ and $Pe = (0.1, 1, 10, 100)$ we find numerically among the first 10 eigenvalues $\lambda_N^* = (-3.11, -2.93, -2.47, -1.88)$ while Eq. (8.20), with Eq. (8.17) used for calculating γ, gives $\lambda^* = (-3.11, -2.95, -2.58, -2.38)$, only differing significantly at the fourth eigenvalue.

8.6 Results from other geometries

To test the validity of Eq. (8.10) for geometries other than Fig. 8.2(a), for which it was originally derived, we show in Fig. 8.5 numerically obtained values of the mean membrane concentration γ_N plotted against Pe for the geometries found in Fig. 8.2 (b) and (c). In Fig. 8.5(a) γ_N is plotted against the usual Péclet number while in (b) it is plotted against the rescaled Péclet number

$$Pe' = \frac{Hhu_0}{D}, \tag{8.21}$$

where H is the minimum distance between the membrane and the constant concentration zone in units of the plate-to-plate distance h, as indicated in Fig. 8.2 (b) and (c). As is clearly seen, the data collapse is significant when using Pe'. The result obtained in Eq. (8.17), while only valid for geometry (a), is shown for comparison.

The fact the data collapse even for geometry (b) is surprising, since there the gradient from the source region to the membrane region is along the x-direction and therefore Eqns. (8.4)-(8.6), which even to lowest order in Pe constitute a highly nonlinear problem, do not directly reduce to Eq. 8.9. We interpret the data collapse as being due to the fact that the concentration gradient in the x-direction induces a gradient of equal size in a direction normal to the membrane, in this case the y-direction. This can be seen directly in Fig. 8.6 where the concentration x-derivative $\partial_x c$ is constant (-0.33 in this case) in the region separating the source and membrane zones, and equal to the y-derivative of the concentration $\partial_y c$ at the membrane interface.

This shows that the relative orientation of the source and membrane regions does not play a large role in determining the flow. This however is hardly surprising since one would not expect e.g. a change in orientation of the membrane to strongly influence the inflow at a given concentration, at least when the non-dimensional separation distance H is much larger than unity. The mathematical reason is presumably that the concentration field to lowest order in Pe satisfies the Laplace equation (Eq. (8.4) with $u = 0$) and thus that the integral of $(\nabla c)^2$ over the domain is minimal, favouring solutions where the size of the concentration gradient is nearly constant.

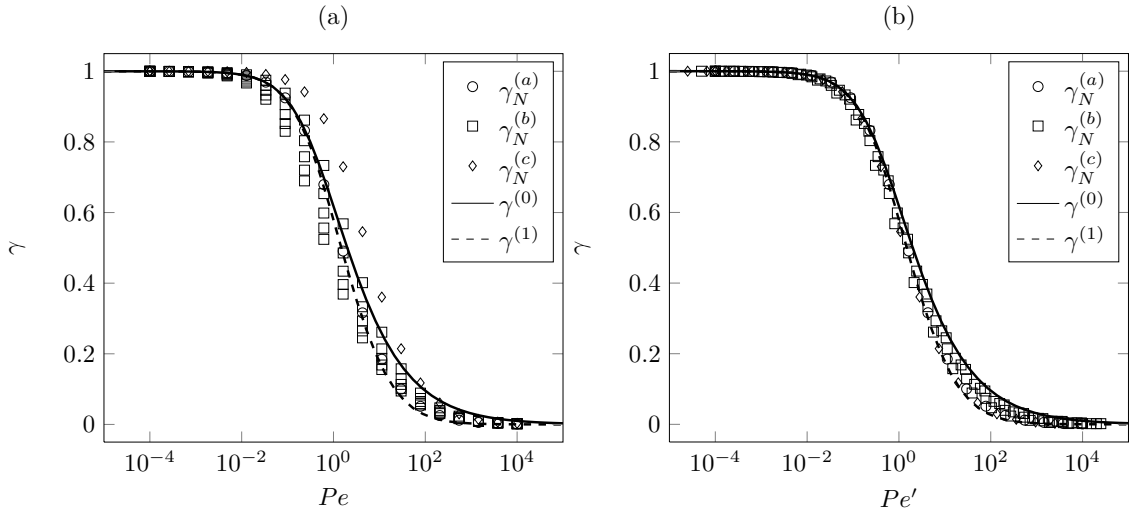

Figure 8.5: (a) Numerically computed mean membrane concentration γ_N as a function of the Péclet number $Pe = \frac{hu_0}{D}$ for the three geometries of Fig. 2. For geometry {a} plot of $\gamma_N^{(\mathrm{a})}$ for $H = 1$ (circles); for geometry {b} plot of $\gamma_N^{(\mathrm{b})}$ for H between 1/2 and 5/2 and $\ell_m^{(\mathrm{b})} = 1/2$ (squares); and for geometry {c} plot of $\gamma_N^{(\mathrm{c})}$ for $H = 1/4$, $\ell_m^{(\mathrm{c})} = 1/4$, and $r = 1/4$ (diamonds). The curves show the prediction given by Eq. (8.10) (solid curve) and Eq. (8.17) (dashed curve). (b) As in panel (a) except now γ_N is shown as a function of the modified Péclet number $Pe' = HPe = \frac{Hhu_0}{D}$.

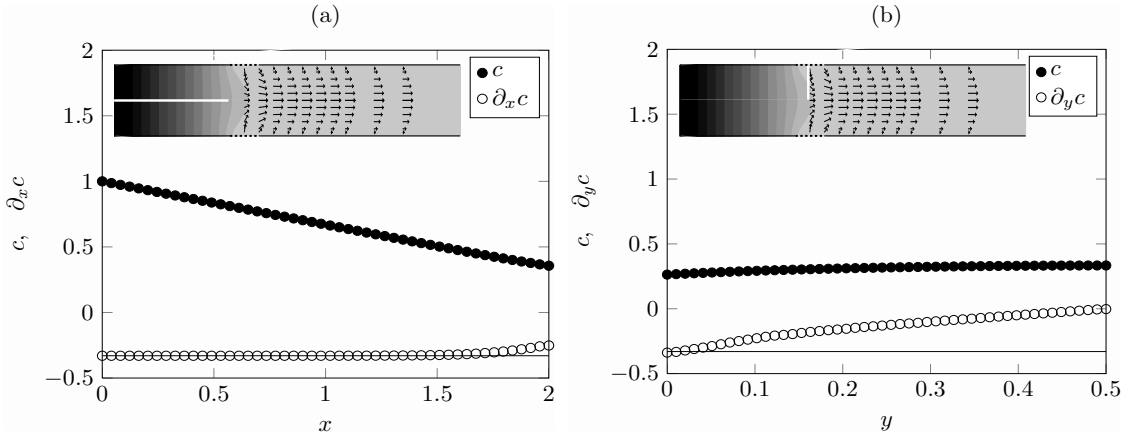

Figure 8.6: Flow and concentration field for geometry (b). (a) Cross-section plot of the concentration c (black circle) and the concentration x-derivative $\partial_x c$ (open circles) plotted along the solid white line shown in the inset for $H = 2$, $\ell_m^{(\mathrm{b})} = \frac{1}{2}$ and $Pe' = 10$. The solid black line indicates $\partial_x c = -0.33$. The concentration source is at $x = 0$ and the membrane starts at $x = 2$. (b) Cross-section plot of the concentration c (black circles) and the concentration y-derivative $\partial_y c$ (open circles) plotted along the solid white line shown in the inset for the same parameters as in (a). The solid black line indicates $\partial_y c = -0.33$, the value at the membrane ($y = 0$).

8.7 Conclusion

In this paper, we have studied new solutions to osmotically driven flow problems, where the distribution and fluxes of solutes and liquid have generated self-consistent flow and concentration patterns. We have presented a general analytical solution method, and have applied this method to a specific example, obtaining detailed knowledge of the flow- and concentration fields in the parallel plate geometry (c.f. Fig. 8.2(a)). This geometry has also been studied numerically, and we find good agreement between our analytical solution method and the numerics. Further, we have studied two topologically different geometries numerically varying the governing parameter, the Péclet number, by eight orders of magnitude. Using a scaled Péclet number, we obtain a data collapse over all eight orders of magnitude. This shows, that the while the detailed nature of the solutions depend on the geometry in question, cf. Fig. 8.2(a)-(c), the osmotic pumping efficiency is largely independent of the geometry, as long as the correct length scale for the problem is chosen.

This work was supported by the Danish National Research Foundation, Grant No. 74.

8.8 Numerical methods

The problem posed by Eqns. (8.2)-(8.6) was solved using the commercial finite element (FEM) software package COMSOL Multiphysics 3.4. See e.g. [32] for a detailed discussion

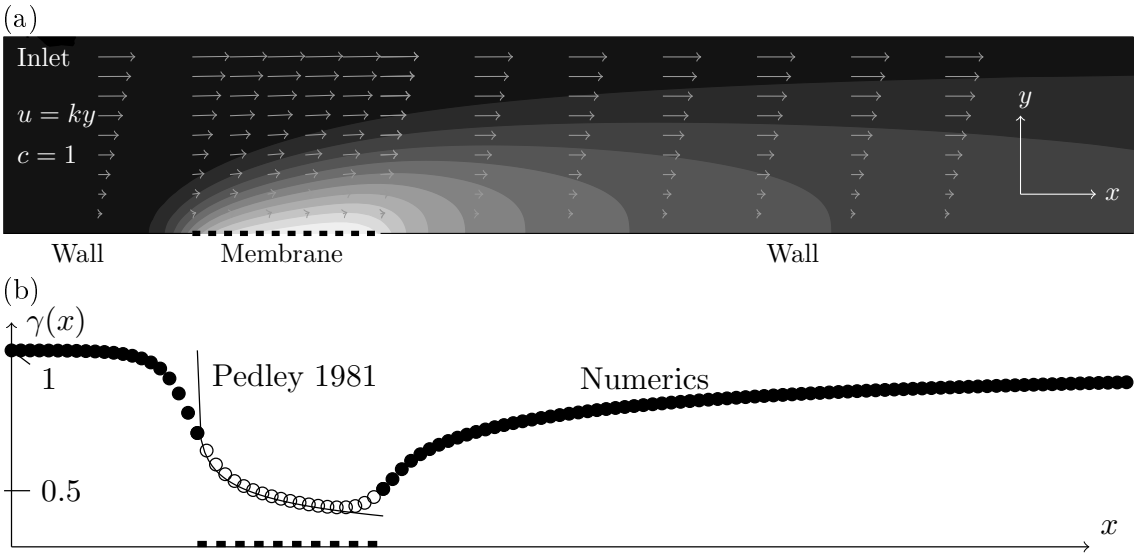

Figure 8.7: Comparison between our numerical method and Pedley's analytical solution for a shear flow above a membrane as shown in (a). To the left, a solution of concentration $c = 1$ is entering the computational with a velocity profile $(u, v) = (ky, 0)$. As the solution passes above the membrane, the flow and concentration profiles are perturbed, creating a characteristic boundary layer. (a) also shows concentration contours (scale bar in Fig. 8.3(c)) and velocity arrow plot for $k = 25$ and $Pe = 10$. (b) Plot of the numerically computed concentration at the lower wall $\gamma(x)$ as a function of position x (open circles at the membrane, and solid circles on the wall). The solid line represents Pedley's analytical solution [57].

of applying the FEM method to solve Stokes flow problems. To validate our numerical code, we used the analytical solution provided by [57] for a shear flow above a membrane. Fig. 8.7 shows a comparison between our numerical method and Pedley's analytical solution.

8.9 Solution of the diffusion-advection eigenvalue problem

The matrix elements A^{nm} in Sec. 8.5.2 are

$$A^{nm} = 2\beta\int_0^1 \cos(n\pi y)\cos(m\pi y)y(1-y)\,\mathrm{d}y = \begin{cases} -2\beta\frac{\left(1+(-1)^{m+n}\right)\left(m^2+n^2\right)}{\left(m^2-n^2\right)^2\pi^2} & \text{for } n \neq m, \\ \frac{2\beta}{12}\left(1-\frac{3}{n^2\pi^2}\right) & \text{for } n = m, \end{cases} \tag{8.22}$$

where $\beta = 6Pe\,\gamma\ell_{\mathrm{m}}$. Note, that $A^{nm} = 0$ for odd values of $n+m$. The eigenvalue problem becomes the diagonalization of the matrix

$$\mathbf{M} = \begin{pmatrix} 0 & 1 & 0 & 0 & 0 & 0 & \cdots \\ 1^2\pi^2 & A^{11} & 0 & 0 & 0 & A^{13} & \cdots \\ 0 & 0 & 0 & 1 & 0 & 0 & \cdots \\ 0 & 0 & 2^2\pi^2 & A^{22} & 0 & 0 & \cdots \\ 0 & 0 & 0 & 0 & 0 & 1 & \cdots \\ 0 & A^{31} & 0 & 0 & 3^2\pi^2 & A^{33} & \cdots \\ \vdots & \vdots & \vdots & \vdots & \vdots & \vdots & \ddots \end{pmatrix}, \tag{8.23}$$

from which the coefficients c_n can be determined to obtain the solution to Eq. (8.18). Fig. 8.4 shows the results for $N = 20$, $Pe = 0.1$ and $Pe = 100$ plotted together with the corresponding numerical solutions. Across the whole range of Pe values, we find good agreement with the numerical results.

End of paper

K. H. Jensen, T. Bohr and H. Bruus
Self-consistent unstirred layers in osmotically driven flows
Journal of Fluid Mechanics **662**, pp. 197–208 (2010)

Table 8.1: List of parameters in alphabetic order after the symbol.

Parameter	Symbol	Value and/or unit
Matrix element	A^{nm}	
Concentration	c	
Characteristic concentration	c_0	mol/L
Diffusivity	D	m^2/s
Mini. dist. from membrane to constant conc. zone	H	
Plate-to-plate distance	h	m
Membrane permeability	L_p	m/(Pa s)
Length of membrane zone	ℓ_m	
Normal vector	$\mathbf{n}$	
Pressure	p	
Peclet number	Pe	
Gas constant	R	8.31 J/(K mol) [4]
Radius of cylinder	r	
Reynolds number	Re	
Schmidt number	Sc	
Temperature	T	K
Osmotic velocity	u_0	m/s
Velocity field	$\mathbf{u} = (u, v)$	
Cartesian coordinates	x, y	
Concentration at membrane interface	γ	
Viscosity	η	Pa s
Matrix eigenvalue	λ_n	
Density	ρ	kg/m^3
Membrane interface	Ω	

Chapter 9

Conclusion and outlook

Conclusion

The present thesis has been devoted to a theoretical investigation of osmotically driven flows in microfluidic systems and their relation to sugar transport in plants. We have analyzed the fluid mechanics of these flows to shed new light on the quantitative and qualitative properties of the translocation process that occur in the phloem vascular system of plants.

Using a simple model framework, where we think of the plant as consisting of a leaf, a stem and a root zone, we have found new analytical solutions to the equations of motion. These allow us to fully characterize the dependence of the flow speed on the parameters of the problem such as leaf size, stem length, and phloem sieve tube radius. We have compared the results of the model to *in-vivo* measurements made on 7 different plant species with good results.

An interesting prediction of the model is that the osmotically driven Münch flow mechanism has a maximum in translocation velocity for a special value of the radius $a = a_c$. The existence of such a maximum is quite easy to understand: the osmotic flow takes place across the cell surface and is therefore more effective in terms of the axial velocity for thinner tubes where the surface-to-volume ratio is larger. Very thin tubes, on the other hand, offer high viscous resistance to the flow, and thus there is an optimum radius a_c, where the osmotic pump is effective and the resistance not too large. We have derived an analytical expression for a_c which takes the form of an allometric scaling law relating the radius of the sieve tube a_c to the length of the stem l_2 and the size of the leaf l_1; $a_c^3 \propto l_1 l_2$. We have compared this prediction to plant data and have found good agreement between observations and our result for plants varying several orders of magnitude in size. This suggests that the physical constraints imposed by the optimality of the Münch mechanism have played a significant role in the evolution of the phloem vascular system of plants.

We have studied several aspects of the flow process in detail. First, we have tried to quantify the effect of the perforated sieve plates that separate adjacent phloem cells on the hydraulic resistance of the phloem translocation pathway. Our findings suggest that the presence of sieve plate contributes significantly to the total hydraulic resistance, and that one needs to take this into account when modeling long-distance transport in plants.

Second, we have studied the effect of unstirred concentration boundary layers on the flow in order to quantify how well-mixed the concentration field is. We have found that at the Péclet numbers relevant to plants the concentration is nearly uniformly distributed across the tube.

Finally, we have designed, fabricated and conducted osmotic experiments using a new type of biomimicking microfluidic devices with channels approaching the dimensions found in plants. We have found that the experiments follow the Münch theory with reasonable accuracy.

Outlook

The equations of motion analyzed in the present thesis were derived under a number of assumptions that identifies which physical effects are believed to be most significant.These approximations are not due to the author, but are widely used throughout the phloem transport literature.

The applicability of a number of these assumptions are, however, not well established and needs to be tested empirically. It is therefore an important task for future research in this field to analyze and identify the quantitative effect that each of these approximations has on the flow. The analytical results relating the translocation velocity to the characteristic sizes of the plant organs derived in the present thesis can act as a starting point for this type of analysis. By studying deviations from the predictions of the model, one can identify plants that have behaviors very far from the predictions and thereby learn of the qualitative and quantitative features which makes the assumption valid or invalid.

The author would like, mainly out of personal interest, to highlight the fact that most current phloem models completely neglect the branched structure of the phloem transport network. These networks are present on many scales in plants and are known to play a significant role in the structure of translocation networks in virtually all living creatures from the largest animals to the smallest microbes [87]. This is most likely also the case for the phloem network.

Finally, the author believes that future research should also focus on gymnosperms. For this group of plants, some of which are very tall trees, the feasibility of the Münch mechanism for long distance transport is even more controversial than for the angiosperms studied in the present thesis. A first step in this direction would be to study the hydraulic resistance of sieve plates and optimized Münch scaling behavior in gymnosperms.

Appendix A

Analytical solution of the 3-zone model

In this appendix we provide analytical solution to Eqns. (5.28)-(5.30)

$$\partial_X^2 U_1 = M\ddot{u}\, U_1, \tag{A.1}$$
$$\partial_X^2 U_2 = -\frac{U_1(X_1)}{U_2^2}\partial_X U_2 + M\ddot{u}\, U_2, \tag{A.2}$$
$$\partial_X^2 U_3 = -\frac{U_2(X_1)}{U_2(X_2)(X_3 - X_2)} + M\ddot{u}\, U_3, \tag{A.3}$$

with the set of boundary conditions

$$U_1(0) = 0, \tag{A.4}$$
$$U_2(X_1) = U_1(X_1), \tag{A.5}$$
$$\partial_X U_2(X_1) = \partial_x U_1(X_1), \tag{A.6}$$
$$U_3(X_2) = U_2(X_2), \tag{A.7}$$
$$\partial_X U_3(X_2) = \partial_X U_2(X_2), \tag{A.8}$$
$$U_3(X_3) = 0. \tag{A.9}$$

Along the way, we will use the notation

$$L_1 = X_1, \tag{A.10}$$
$$L_2 = X_2 - X_1 = 1, \tag{A.11}$$
$$L_3 = X_3 - X_2, \tag{A.12}$$
$$\omega = \frac{L_3}{L_1}. \tag{A.13}$$

It is immediately apparent that Eqns. (A.1) and (A.3) can be solved directly for all values of $M\ddot{u}$:

$$U_1(X) = A_1 \sinh\sqrt{M\ddot{u}}\,X + A_2 \cosh\sqrt{M\ddot{u}}\,X, \tag{A.14}$$

$$U_3(X) = A_3 \sinh\sqrt{M\ddot{u}}\,(X - X_2) + A_4 \cosh\sqrt{M\ddot{u}}\,(X - X_2) + \frac{U_2(X_1)}{U_2(X_2)(X_3 - X_2)}\frac{1}{M\ddot{u}}. \tag{A.15}$$

At present time, solutions of Eq. (A.2) are only avaliable as numerical approximations. In the limits $M\ddot{u} \gg 1$ and $M\ddot{u} \ll 1$, the system can, however, be solved analytically.

A.1 Solution for $M\ddot{u} \ll 1$

In the limit $M\ddot{u} \ll 1$ the equations of motion (A.1)-(A.3) become

$$\partial_X^2 U_1 = 0, \tag{A.16}$$

$$\partial_X^2 U_2 = -\frac{U_1(X_1)}{U_2^2}\partial_X U_2, \tag{A.17}$$

$$\partial_X^2 U_3 = -\frac{U_2(X_1)}{U_2(X_2)}\frac{1}{(X_3 - X_2)}. \tag{A.18}$$

We can write the solutions in domains 1 and 3 as

$$U_1(X) = B_1 X + B_2, \tag{A.19}$$

$$U_3(X) = -\frac{1}{2}\frac{U_2(X_1)}{U_2(X_2)}\frac{1}{(X_3 - X_2)}(X - X_3)^2 + B_3(X - X_3) + B_4, \tag{A.20}$$

In domain 2, we can integrate once

$$\partial_X U_2 = \frac{U_1(X_1)}{U_2} + B_5. \tag{A.21}$$

As long as $\partial_X U_2 \neq 0$, this means that

$$\partial_{U_2} X = \frac{1}{B_5}\left(1 - \frac{U_1(X_1)}{U_1(X_1) + B_5 U_2}\right), \tag{A.22}$$

which has the solution

$$X(U_2) = \frac{U_1(X_1)}{B_5}\left[\frac{U_2}{U_1(X_1)} - \frac{1}{B_5}\log\left(\frac{1 + \frac{B_5 U_2}{U_1(X_1)}}{1 + B_5}\right)\right] + B_6. \tag{A.23}$$

In the limit $\partial_X U_2 = 0$, we find

$$U_2 = -\frac{U_1(X_1)}{B_5}. \tag{A.24}$$

The derivatives of the solutions U_1, U_2 and U_3 are

$$\partial_X U_1 = B_1, \tag{A.25}$$

$$\partial_X U_2 = \frac{U_1(X_1)}{U_2} + B_5, \tag{A.26}$$

$$\partial_X U_3 = \frac{U_2(X_1)}{U_2(X_2)} \frac{X_3 - X}{X_3 - X_2} + B_3. \tag{A.27}$$

A.1.1 Calculation of the constants $B_1, B_2, \ldots, B_6$

The calculations determining the constants $B_1, B_2, \ldots, B_6$

$$B_1 = \frac{1}{\omega}\left(1 + \omega - \sqrt{1+2\omega}\right), \tag{A.28}$$

$$B_2 = 0, \tag{A.29}$$

$$B_3 = \frac{1}{\omega}\left(1 - \sqrt{1+2\omega}\right), \tag{A.30}$$

$$B_4 = 0, \tag{A.31}$$

$$B_5 = \frac{1}{\omega}\left(1 - \sqrt{1+2\omega}\right), \tag{A.32}$$

$$B_6 = \frac{L_1 \omega}{\sqrt{1+2\omega} - 1}. \tag{A.33}$$

are given below. They are found using the boundary conditions in Eqns. (A.4)-(A.9).

Calculation of B_2

It is clear from Eq. (A.4) ($U_1(0) = 0$) that

$$B_2 = 0 \tag{A.34}$$

Calculation of B_4

Similarly, we find from Eq. (A.9) ($U_3(X_3) = 0$) that

$$B_4 = 0 \tag{A.35}$$

Calculation of B_5

To determine B_5 we use Eq. (A.6) ($\partial_X U_2(X_1) = \partial_X U_1(X_1)$) and Eq. (A.5) ($U_2(X_1) = U_1(X_1)$) and find that

$$B_1 = \frac{U_1(X_1)}{U_2(X_1)} + B_5 = 1 + B_5. \tag{A.36}$$

Thus

$$B_5 = B_1 - 1 \tag{A.37}$$

Calculation of B_3

To determine B_3 we use Eq. (A.8) ($\partial_X U_3(X_2) = \partial_X U_2(X_2)$) and find that

$$\frac{U_1(X_1)}{U_2(X_2)} + B_5 = \frac{U_1(X_1)}{U_2(X_2)} + B_3, \tag{A.38}$$

such that

$$B_3 = B_5 = B_1 - 1. \tag{A.39}$$

Calculation of B_1

To determine B_1 consider Eq. (A.7)

$$U_2(X_2) = U_3(X_2) = -\frac{1}{2}\frac{U_2(X_1)}{U_2(X_2)}L_3 - B_3 L_3 = -\frac{1}{2}\frac{B_1 L_1 L_3}{U_2(X_2)} - (B_1 - 1)L_3. \tag{A.40}$$

This leads to a second order equation for $U_2(X_2)$

$$U_2(X_2)^2 + (B_1 - 1)L_3 U_2(X_2) + \frac{1}{2}B_1 L_1 L_3 = 0, \tag{A.41}$$

which has the solution

$$U_2(X_2) = \frac{(1 - B_1)L_3 \pm \sqrt{(B_1 - 1)^2 L_3^2 - 2B_1 L_1 L_3}}{2}. \tag{A.42}$$

Using $\omega = \frac{L_3}{L_1}$ this becomes

$$U_2(X_2) = L_1 \frac{(1 - B_1)\omega \pm \sqrt{(B_1 - 1)^2 \omega^2 - 2B_1 \omega}}{2}. \tag{A.43}$$

For $U_2(X_2)$ to be real, positive and unique, we require that the term in the square root vanishes

$$(B_1 - 1)^2 \omega^2 - 2B_1 \omega = 0. \tag{A.44}$$

This is illustrated for $\omega = 1$ in Fig. A.1, and implies that B_1 must be given by

$$B_1 = \frac{1}{\omega}\left(1 + \omega - \sqrt{1 + 2\omega}\right), \tag{A.45}$$

where we have chosen the "$-$" solution of Eq. (A.44) to ensure that $U_2(X_2)$ is positive.

Calculation of B_6

From Eq. (A.23) it follows that

$$X_1 = X(U_2(X_1)) = \frac{U_1(X_1)}{B_5}\left[\frac{U_2(X_1)}{U_1(X_1)} - \frac{1}{B_5}\log\left(\frac{1 + \frac{B_5 U_2(X_1)}{U_1(X_1)}}{1 + B_5}\right)\right] + B_6 \tag{A.46}$$

$$= \frac{B_1 L_1}{B_5} + B_6, \tag{A.47}$$

such that

$$B_6 = L_1\left(1 - \frac{B_1}{B_5}\right). \tag{A.48}$$

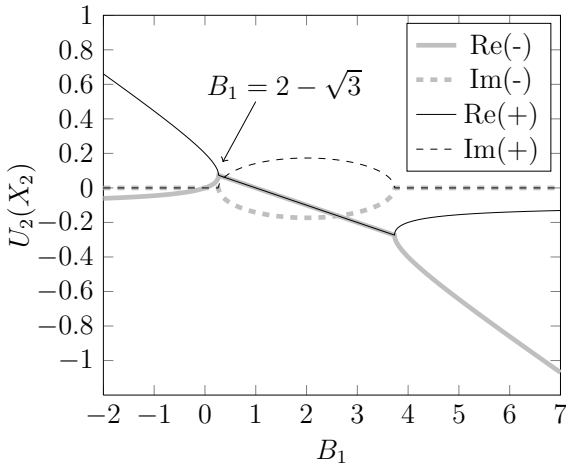

Figure A.1: Plot of $U_X(X_2)$ as a function of B_1 for $\omega = 1$ and $L_1 = 0.2$ from Eq. (A.43). The real and imaginary part of the two solutions (+ and −, as indicated in the legend) to Eq. (A.43) are shown. For the solution to be physical, we require that $U_2(X_2)$ is real, positive and unique. This happens when $B_1 = \frac{1}{\omega}\left(1 + \omega - \sqrt{1 + 2\omega}\right) = 2 - \sqrt{3} \simeq 0.268$.

A.1.2 Additional results

For the calculation of the mean translocation velocity, the ratio $\chi = U_2(X_2)/U_1(X_1)$ is useful. We have that

$$U_1(X_1) = B_1 L1 = \frac{L_1}{\omega}\left(1 + \omega - \sqrt{1 + 2\omega}\right), \tag{A.49}$$

and

$$U_2(X_2) = \frac{1}{2} L_1 \left(1 - B_1\right) \omega. \tag{A.50}$$

Thus

$$\chi = \frac{U_2(X_2)}{U_1(X_1)} = \frac{1}{2}\left(1 + \sqrt{1 + 2\omega}\right). \tag{A.51}$$

A.1.3 Calculation of $\bar{U}$ for $M\ddot{u} \ll 1$

The mean velocity in the translocation zone is

$$\bar{U} = \frac{1}{X_3 - X_2} \int_{X_2}^{X_3} U_2(X)\, dX, \tag{A.52}$$

This quantity can be found from Eq. (A.23). If we define I_1, I_2, I_3, I_4 as the area of the regions shown in Fig. A.2, we have that

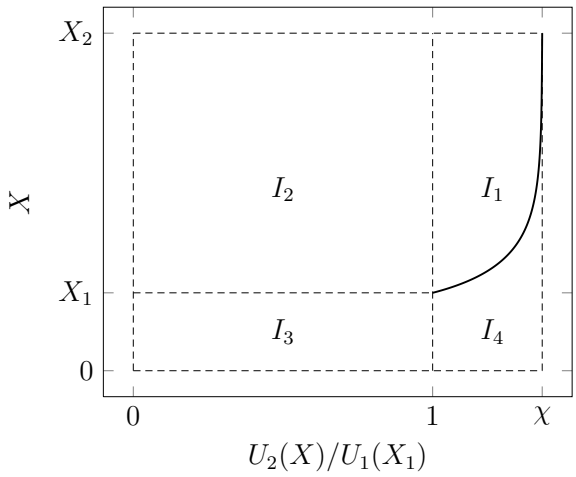

Figure A.2: Plot of X (solid line above I_4) as a function of $\frac{U_2(X)}{U_1(X_1)}$ from Eq. (A.23). The four domains I_1, I_2, I_3 and I_4 used in the calculation of $\bar{U}$ are indicated.

$$
\begin{aligned}
I_0 = I_1 + I_2 + I_3 + I_4 &= X_2\chi, && \text{(A.53)}\\
I_2 &= 1, && \text{(A.54)}\\
I_3 &= L_1, && \text{(A.55)}\\
I_4 &= \int_1^{\chi} X\left(\frac{U_2}{U_1(X_1)}\right) d\left(\frac{U_2}{U_1(X_1)}\right). && \text{(A.56)}
\end{aligned}
$$

We shall now evaluate I_4, using along the way that $\lim_{x\to 0} x\log x = 0$

$$
\begin{aligned}
I_4 &= \int_1^{\chi}\left(\frac{U_1(X_1)}{B_5}\left[\frac{U_2}{U_1(X_1)} - \frac{1}{B_5}\log\left(\frac{1+\frac{B_5U_2}{U_1(X_1)}}{1+B_5}\right)\right] + B_6\right) d\left(\frac{U_2}{U_1(X_1)}\right) && \text{(A.57)}\\
&= \frac{1}{8}L_1\left(\omega - 2 + (2+\omega)\sqrt{1+2\omega}\right). && \text{(A.58)}
\end{aligned}
$$

The mean velocity $\bar{U}$ can then be calculated from

$$
\begin{aligned}
\bar{U} &= U_1(X_1)(I_1 + I_2), && \text{(A.59)}\\
&= U_1(X_1)(I_0 - I_3 - I_4) && \text{(A.60)}\\
&= \frac{1}{2}\left(\sqrt{1+2\omega} - 1\right)L_1 - \left(\frac{4 + 6\omega - \omega^2 + \sqrt{1+2\omega}\left(\omega^2 - 4 - 2\omega\right)}{8\omega}\right)L_1^2. && \text{(A.61)}
\end{aligned}
$$

In most cases, the second order term (in L_1) is very small. The function $f(\omega) = \frac{1}{2}\left(\sqrt{1+2\omega} - 1\right)$ showing the importance of the relative size of L_1 and L_3 is shown in Fig. A.3. For the special case $\omega = 1$,we find that

$$
\begin{aligned}
\bar{U}(\omega = 1) &= \frac{\sqrt{3}-1}{2}L_1 - \frac{9 - 5\sqrt{3}}{8}L_1^2 && \text{(A.62)}\\
&\simeq 0.36L_1 - 0.043L_1^2. && \text{(A.63)}
\end{aligned}
$$

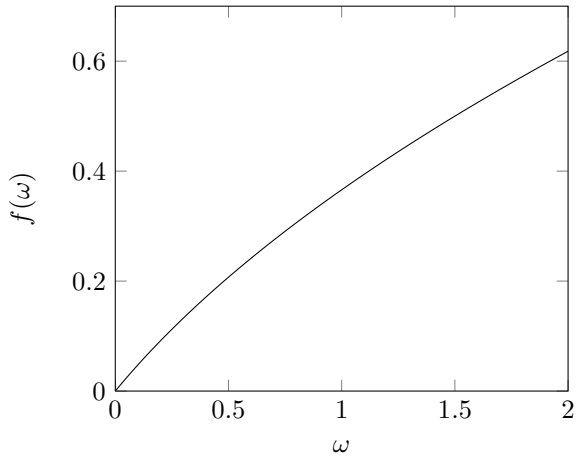

Figure A.3: The function $f(\omega) = \frac{1}{2}\left(\sqrt{1+2\omega}-1\right)$ plotted as a function of $\omega = L_3/L_1$ showing the importance of the relative size of L_1 and L_3 in Eq. (A.61).

A.2 Solution for $M\ddot{u} \gg 1$

In the limit $M\ddot{u} \gg 1$ the equations of motion (A.1)-(A.3) are

$$\partial_X^2 U_1 = M\ddot{u}\, U_1, \tag{A.64}$$

$$\partial_X^2 U_2 = -\frac{U_1(X_1)}{U_2^2}\partial_X U_2 + M\ddot{u}\, U_2, \tag{A.65}$$

$$\partial_X^2 U_3 = -K + M\ddot{u}\, U_3, \tag{A.66}$$

where $K = \frac{U_2(X_1)}{U_2(X_2)(X_3-X_2)}$. The equations in domains 1 and 3 can be readily solved

$$U_1(X) = A_1 \sinh\sqrt{M\ddot{u}}\, X + A_2 \cosh\sqrt{M\ddot{u}}\, X, \tag{A.67}$$

$$U_3(X) = A_3 \sinh\sqrt{M\ddot{u}}\,(X-X_2) + A_4 \cosh\sqrt{M\ddot{u}}\,(X-X_2) + \frac{K}{M\ddot{u}}. \tag{A.68}$$

Here, $A_2 = 0$ because of the boundary condition at $X = 0$, while A_3 and A_4 are determined by the continuity condition on U and $\partial_X U$ at $X = X_2$.

$$A_3 = \frac{1}{\sqrt{M\ddot{u}}}\partial_X U_2(X_2), \tag{A.69}$$

$$A_4 = U_2(X_2) - \frac{K}{M\ddot{u}}. \tag{A.70}$$

In the translocation zone, we shall solve the equation

$$\partial_X^2 U_2 = -\frac{U_1(X_1)}{U_2^2}\partial_X U_2 + M\ddot{u}\, U_2, \tag{A.71}$$

by assuming that U_2 can be written as $U_2 = \frac{U_2'}{M\ddot{u}}$, where U_2' is of the order 1. Inserting this, and keeping only terms of order $M\ddot{u}$ and M^2, we get that

$$M\ddot{u}\, U_1(X_1)\partial_X U_2' = U_2'^3. \tag{A.72}$$

Since we require that $U_2(X_1) = U_1(X_1)$ this implies that

$$U_2(X) = \frac{U_1(X_1)}{\sqrt{1 - 2M\ddot{u}\, U_1(X_1)(X - X_1)}} \tag{A.73}$$

Please note that this solution does not fulfill the condition $\partial_X U_2(X_1) = \partial_X U_1(X_1)$ exactly. This is due to the fact that we have ignored the term $\partial_X^2 U_2$. This, however, turns out to play very little role when comparing the analytical solution to the numerical results.

With the solution given in Eq. (A.73), we can now determine the constants A_3 and A_4 and $K = \frac{U_2(X_1)}{U_2(X_2)(X_3 - X_2)}$. The only free parameter is A_1 which has to be determined such that $U_3(X_3) = 0$. Using MATHEMATICA 7.0.0, we can then determine the A's using the code

```
Clear[A1, A2, A3, A4, X, X1, X2, X3, M, v1, v2, v3, K];
A2 = 0;
X2 = X1 + 1;
v1[X_] = A1*Sinh[Sqrt[M]*X] + A2*Cosh[Sqrt[M]*X];
v0 = v1[X1];
v2[X_] = v0/(Sqrt[1 - 2*M*v0*(X - X1)]);
K = v2[X1]/v2[X2]*1/(X3 - X2);
Dv2[X_] = D[v2[X], X];
A3 = 1/Sqrt[M]*Dv2[X2];
A4 = v2[X2] - K/M;
v3[X_] = A3*Sinh[Sqrt[M]*(X - X2)] + A4*Cosh[Sqrt[M]*(X - X2)] + K/M;
v3[X3];
Solve[v3[X3] == 0, A1];
FullSimplify[%]
A3
A4
```

The expressions are generally very complicated functions of $M\ddot{u}$, X_1, X_2 and X_3. For $\omega = 1$, we e.g. find that A_1 is given by

$$A_1(\omega{=}1) = \frac{M\ddot{u}\,(4+X_1)\coth[M\ddot{u}^*] - \operatorname{csch}[M\ddot{u}^*]\left(4M\ddot{u} + \operatorname{csch}[M\ddot{u}^*]\sqrt{M\ddot{u}^{3/2}X_1\sinh[M\ddot{u}^*]^2\left(M\ddot{u}^*\cosh[M\ddot{u}^*]^2 - 4\sinh[M\ddot{u}^*] + 2\sinh[2M\ddot{u}^*]\right)}\right)}{4M\ddot{u}^2(2+X_1)\cosh[M\ddot{u}^*] - 2\left(4M\ddot{u}^2 + M\ddot{u}^{3/2}X_1\sinh[M\ddot{u}^*]\right)}, \tag{A.74}$$

where $M\ddot{u}^* = \sqrt{M\ddot{u}}\,X_1$.

Calculating the mean velocity in the translocation zone for $M\ddot{u} \gg 1$

From the solution in Eq. (A.73) we can now calculate the mean velocity

$$\bar{U} = \frac{1}{X_3 - X_2}\int_{X_2}^{X_3} U_2(X)\, dX = \frac{1 - \sqrt{1 - 2M\ddot{u}\, U_1(X_1)}}{M\ddot{u}}. \tag{A.75}$$

Despite of the complexity of the expression for A_1, we find that as long as the product $M\ddot{u}\,(X_3 - X_2)$ is large, the product $M\ddot{u}\,U_1(X_1)$ is nearly constant and equal approximately equal to 0.5. This implies that

$$\bar{U} \simeq \frac{1}{M\ddot{u}}. \tag{A.76}$$

To see why this is so, consider the equation for U_3

$$U_3(X) = A_3 \sinh\sqrt{M\ddot{u}}\,(X - X_2) + A_4 \cosh\sqrt{M\ddot{u}}\,(X - X_2) + \frac{K}{M\ddot{u}}. \tag{A.77}$$

It is clear that $K \leq \frac{1}{X_3 - X_2}$. Thus, since $U_3(X_3) = 0$, and if $(X_3 - X_2)M\ddot{u}$ is sufficiently large we must have that

$$0 = A_3 \sinh\sqrt{M\ddot{u}}\,(X_3 - X_2) + A_4 \cosh\sqrt{M\ddot{u}}\,(X_3 - X_2) + \frac{K}{M\ddot{u}} \simeq (A_3 + A_4)\exp\left(\sqrt{M\ddot{u}}\,(X_3 - X_2)\right). \tag{A.78}$$

This implies that $A_3 = -A_4$. Eqns. (A.69)-(A.70) then leads to

$$\frac{1}{\sqrt{M\ddot{u}}}\partial_X U_2(X_2) = -U_2(X_2) \tag{A.79}$$

or

$$\frac{\sqrt{M\ddot{u}}\,U_1^2(X_1)}{(1 - 2M\ddot{u}\,U_1(X_1))^{3/2}} = -\frac{U_1(X_1)}{(1 - 2M\ddot{u}\,U_1(X_1))^{1/2}}. \tag{A.80}$$

since $X_2 - X_1 = 1$. Rewriting, we get that

$$\sqrt{M\ddot{u}}\,U_1(X_1) = 2M\ddot{u}\,U_1(X_1) - 1, \tag{A.81}$$

or

$$U_1(X_1) = \frac{1}{2M\ddot{u} - \sqrt{M\ddot{u}}} \simeq \frac{1}{2M\ddot{u}}. \tag{A.82}$$

In this way, $M\ddot{u}\,U_1(X_1) \simeq 1/2$ as found above.

Appendix B

Horwitz's derivation of the equations of motion

Following Horwitz [25], we consider a tube with cross section area A and perimeter S submerged in a large water reservoir as shown in Fig. B.1. The tube is filled with a solution of sugar and water with concentration c, flow velocity u and hydrostatic pressure p. Both $c = c(x)$, $u = u(x)$, and $p = p(x)$ are one-dimensional variables that does not depend on the radial position. The walls are made of a semipermeable membrane with permeability L_p that allows water, but not sugar, to flow across driven by osmotic and hydrostatic pressure differences at a rate $j_w = L_p(\mathbb{R}\mathbb{T}c - p)$. Here, $\mathbb{R}$ is the gas constant and $\mathbb{T}$ is the temperature. Sugar is added/removed from the tube at a rate υ by some active mechanism decoupled from the osmotic pumping.

B.1 Conservation of volume

Consider now a small section of the tube from x_0 to $x_0 + \Delta x$. Taking into account the advective flow of water along the tube and the radial influx due to osmosis, the conservation equation for volume is

$$Sj_w\Delta x + A(u(x_0) - u(x_0 + \Delta x)) = 0. \tag{B.1}$$

Letting $\Delta x \to 0$ we find that

$$\partial_x u = \frac{S}{A} j_w = \frac{S}{A} L_p(\mathbb{R}\mathbb{T}c(x) - p(x)). \tag{B.2}$$

For a cylindrical tube with radius a, this is simply

$$\partial_x u = \frac{2L_p}{a}(\mathbb{R}\mathbb{T}c - p). \tag{B.3}$$

This can be further reduced by using Hagen-Pouiseuille relation between pressure gradient and flow velocity in a cylindrical tube $\partial_x p = -\frac{8\eta}{a^2}u$ such that

$$\partial_x^2 u = \frac{2L_p}{a}\left(\mathbb{R}\mathbb{T}\partial_x c + \frac{8\eta}{a^2}u\right). \tag{B.4}$$

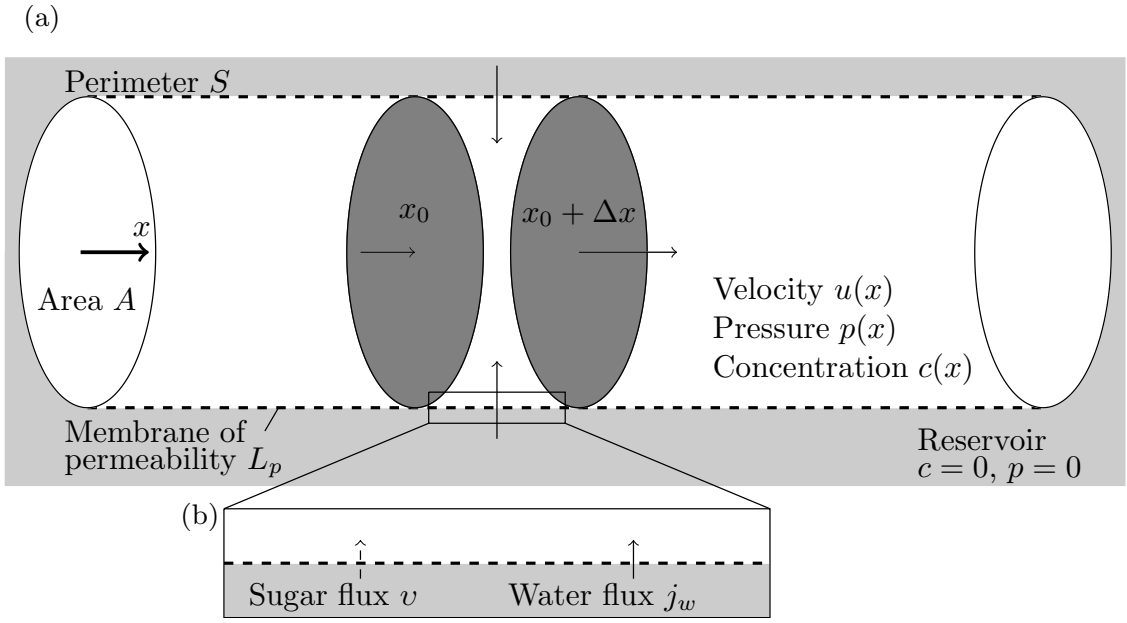

Figure B.1: Sketch of the geometry used in Horwitz's deriviation of the transport equations. (a) An incompressible liquid is moving inside a tube with cross section area A and perimeter S with mean velocity u (arrows). A solute of concentration c is dissolved in the liquid and is moving due to the motion of the liquid and molecular diffusion. The tube is submerged in a large reservoir (gray region) and has a walls made from a semipermeable membrane (dashed line) with permeability L_p that allow the liquid but not the solute to pass. (b) Closeup of the situation at the membrane (dashed line). The presence of the membrane facilitates a flow of water driven by osmotic and hydrostatic pressure differences across the wall. This occurs at a rate $j_w = L_p\,(\mathbb{R}\mathbb{T}c - p)$ indicated by the solid arrow at the membrane interface (See Fig. 3.1). Sugar is added to/removed from the tube at a rate υ by an active mechanism decoupled from the osmotic pumping as indicated by the dashed arrow. The osmotically driven flow across the membrane accelerates the liquid as it moves along the tube as indicated by the growing size of the arrows in (a).

B.2 Conservation of sugar

Consider again a small section of the tube of length Δx. Taking into account the advective and diffusive flow of sugar along the tube and the radial influx due to loading and unloading, the conservation equation is

$$\begin{aligned} 0 &= \partial_t c \Delta x A \\ &- A\left(u(x)c(x) - u(x_0+\Delta x)c(x+\Delta x)\right) \\ &+ AD\left(\partial_x c(x) - \partial_x c(x_0+\Delta x)\right) \\ &- A\Delta x \upsilon, \end{aligned} \tag{B.5}$$

where D is the diffusion coefficient of the sugar and υ is the loading/unloading rate. Letting $\Delta x \to 0$, this reduces to the familiar advection-diffusion equation

$$\partial_t c + \partial_x(cu) = D\partial_x^2 c + \upsilon. \tag{B.6}$$

B.2.1 Mathematical formulation of the loading/unloading processes

The form of the trans-membrane loading function υ in Eq. (B.6) varies depending on whether one considers loading or unloading. Several mathematical formulation has been used in the literature to approximate the quantitative properties of the loading processes. The most widely used formulations are

$$\upsilon = \begin{cases} k_0, & \text{(a) constant loading [13, 84],} \\ k_1 x + k_2, & \text{(b) linear loading [70],} \\ k_3 c, & \text{(c) concentration dependent loading [79],} \\ (k_4 x + k_5)c, & \text{(d) concentration dependent linear loading [70],} \\ k_6(c_T - c), & \text{(e) concentration dependent loading with target concentration } c_T \text{ [38],} \\ \frac{k_7 c}{k_8 + c}, & \text{(f) Michaelis-Menten loading [45].} \end{cases} \tag{B.7}$$

The k's are loading constants which can be determined experimentally (see e.g. [45]).

Appendix C

Themodynamics of osmosis

In this appendix we consider the thermodynamics of osmosis. We derive transport equations for flow of water and solute across a membrane which is permeable to both substances. The derivation is due to Schultz [67] and Heimburg [21].

C.1 Non-equlibrium thermodynamics

The process of osmosis can best be described by the formalism of non-equlibrium thermodynamics [67]. We thus consider a linear phenomenological relation between a thermodynamic flux j'_n and the corresponding conjugate force ξ_n

$$j'_n = L_{nn}\xi_n, \tag{C.1}$$

which is valid if the system is close to equilibrium. Here, L_{nn} is a proportionality constant with the unit of conductance. The driving force ξ_n is related to the difference in chemical potential of the substance n between different regions of the system

$$\xi_n = \Delta\mu_n \tag{C.2}$$

Ohm's law of current flow, Fourier's law of heat flow, Fick's law of diffusion and the Poiseuille's equation describing volume flow are all examples of Eq. (3.1). If the system is characterized by several forces and fluxes (e.g. if the membrane is non-ideal) there may be interactions between fluxes and non-conjugate forces

$$j'_n = L_{nn}\xi_n + \sum_{m\neq n} L_{nm}\xi_m, \tag{C.3}$$

where according to the Onsager relations $L_{nm} = L_{mn}$. The flux of particles as a consequence of temperature gradients (the Soret effect) and the flux of heat due to concentration gradients (the Dufour effect) are well known examples of Eq. (C.3). It can be shown that the relation between the rate of internal entropy production $\partial_t s$, the absolute temperature $\mathbb{T}$, and the forces and fluxes is given by

$$\mathbb{T}\partial_t s = \sum_n j'_n \xi_n. \tag{C.4}$$

The quantity $\mathbb{T}\partial_t s$ is known as the dissipation function and is a measure of the tendency of the non-equilibrium process to proceed.

C.2 Osmotically driven flow across non-ideal membranes

In the present discussion we consider a membrane separating two chambers at pressures p_1 and p_2. The chambers contain a dilute aqueous solutions of a solute at concentrations c_1 and c_2. The chemical potentials of the water μ_w in the two compartments are

$$\mu_{w,1} = = (\mu_{w,1})_0 + \bar{v}_w p_1 + \mathbb{RT} \log\left(\frac{n_{w,1}}{n_{w,1}+n_{s,1}}\right), \tag{C.5}$$

$$\mu_{w,2} = = (\mu_{w,2})_0 + \bar{v}_w p_2 + \mathbb{RT} \log\left(\frac{n_{w,2}}{n_{w,2}+n_{s,2}}\right), \tag{C.6}$$

$$\tag{C.7}$$

where $\bar{v}_w$ is the partial molar volume of water, $(\mu_w)_0$ are reference values, and n_w and n_s are the number of water and solvent molecules respectively. Since the solutions are dilute, the logarithmic term can be expanded

$$\log\left(\frac{n_w}{n_w+n_s}\right) = -\log\left(1+\frac{n_s}{n_w}\right) \simeq -\frac{n_s}{n_w} = -\bar{v}_w c \tag{C.8}$$

where c is the concentration of the solute. The difference in chemical potential $\Delta\mu_w$ is thus

$$\Delta\mu_w = \mu_{w,2} - \mu_{w,1} \simeq \bar{v}_w (p_2 - p_1) - \bar{v}_w \mathbb{RT} (c_2 - c_1) = \bar{v}_w \Delta p - \bar{v}_w \Delta\Pi. \tag{C.9}$$

For the solute, the chemical potentials are

$$\mu_{s,1} = = (\mu_{s,1})_0 + \bar{v}_s p_1 + \mathbb{RT} \log\left(\frac{n_{s,1}}{n_{w,1}+n_{s,1}}\right), \tag{C.10}$$

$$\mu_{s,2} = = (\mu_{s,2})_0 + \bar{v}_s p_2 + \mathbb{RT} \log\left(\frac{n_{s,2}}{n_{w,2}+n_{s,2}}\right), \tag{C.11}$$

$$\tag{C.12}$$

In this case we cannot generally get rid of the logarithm since its argument is not close to one. If the concentrations are of similar magnitude, we can however write[1]

$$\Delta\mu_s = \mu_{s,2} - \mu_{s,1} \simeq \bar{v}_s (p_2 - p_1) + \mathbb{RT}\left(\frac{c_2 - c_1}{c_1}\right) = \bar{v}_s \Delta p + \frac{\Delta\Pi}{c_1} \tag{C.13}$$

The dissipation equation (C.4) is

$$\mathbb{T}\partial_t s = j'_w (\bar{v}_w \Delta p - \bar{v}_w \Delta\Pi) + j'_s \left(\bar{v}_s \Delta p - \frac{\Delta\Pi}{c_1}\right). \tag{C.14}$$

[1] See [67] for a detailed treatment of the expansion of the logarithmic term.

Upon rearrangement this becomes

$$\mathbb{T}\partial_t s = \left(j'_w \bar{v}_w + j'_s \bar{v}_s\right) \Delta p + \left(\frac{j'_s}{c_1} - \bar{v}_w j'_w\right) \Delta\Pi. \tag{C.15}$$

where $j'_v = (j'_w \bar{v}_w + j'_s \bar{v}_s)$ is simply the volume flow and $j'_D = \frac{j'_s}{c_1} - \bar{v}_w j'_w$ the difference between the velocities of the oppositely directed flows of solute and water. In this notation we have that

$$\mathbb{T}\partial_t s = j'_v \Delta p + j'_D \Delta\Pi. \tag{C.16}$$

We can now write the phenomenological equations (C.3)

$$j'_v = L_{pp}\Delta p + L_{pD}\Delta\Pi, \tag{C.17}$$
$$j'_D = L_{Dp}\Delta p + L_{DD}\Delta\Pi, \tag{C.18}$$

where $L_{pD} = L_{Dp}$ from the Onsager relation. Using the notation $\sigma_s = -\frac{L_{pD}}{L_{pp}}$ the volume flux j'_v given in Eq. (C.17) can be written as

$$j'_v = L_{pp}\left(\Delta p - \sigma_s \Delta\Pi\right), \tag{C.19}$$

The quantity σ_s is know as a reflection coefficient, and is a measure of the degree to which a membrane is permeable to the solute. If $\sigma_s = 1$ it is perfectly impermeable, at we obtain the ideal membrane transport Eq. (3.5), p. 21 . If on the other hand $\sigma_s = 0$ the membrane is equally permeable to solute and water. The solute flux j'_s is given by

$$j'_s = (1 - \sigma_s) c_1 j'_v + \omega_s \Delta\Pi \tag{C.20}$$

where $\omega_s = c_1 \frac{L_{pp}L_{DD} - L_{pD}^2}{L_{pp}}$.

Appendix D

Sieve plate data

This appendix contains data for the *Curcubita maxima* sieve plate shown in Fig. 4.2(a), p. 41. The data was kindly provided by M. Knoblauch and D. L. Mullendore. See [48] for details on how the measurements were made.

```
Sieve tube element length = 154.3*1e-6 m
Sieve tube element radius = 29.005*1e-6 m
Sieve plate thickness = 0.966*1e-6 m
Sieve pore radii = 1e-6 m*[
4.6217562188
4.535683898
4.4759094422
4.4217524916
4.4092803846
4.3677122045
4.2630274694
4.1897320191
4.0190780657
4.0004081138
3.949318219
3.8845114525
3.8100328702
3.7462617435
3.6640493165
3.6027107679
3.4075444176
3.3399556362
3.3347985877
3.2392481984
3.1734984532
3.1716001618
3.1506399347
```

```
3.1418881591
3.1069116639
3.0930327149
3.0704154025
3.0041217282
2.9721574733
2.866337958
2.8470601859
2.7970542884
2.76487436
2.5305560114
2.4114607257
2.2080530822
2.1395724912
2.0323186401
2.0041789728
1.9136916469
1.7785203023
1.6526258
1.597558372
1.5867494774
1.2926936506
1.2208011857
0.9684655618
0.887807481
0.8276143905
0.7478736748
]
```

Appendix E

Paper published in the Journal of Fluid Mechanics (2009)

J. Fluid Mech. (2009), *vol.* 636, *pp.* 371–396. © Cambridge University Press 2009
doi:10.1017/S002211200900799X

Osmotically driven pipe flows and their relation to sugar transport in plants

KÅRE H. JENSEN[1,2], EMMANUELLE RIO[1,3], RASMUS HANSEN[1], CHRISTOPHE CLANET[4] AND TOMAS BOHR[1]†

[1]Center for Fluid Dynamics, Department of Physics, Technical University of Denmark, Building 309, 2800 Kgs. Lyngby, Denmark

[2]Center for Fluid Dynamics, Department of Micro- and Nanotechnology, Technical University of Denmark, DTU Nanotech Building 345 East, 2800 Kgs. Lyngby, Denmark

[3]Laboratoire de Physique des Solides, Univ. Paris-Sud, CNRS, UMR 8502, F-91405 Orsay Cedex, France

[4]IRPHE, Universités d'Aix-Marseille, 49 Rue Frédéric Joliot-Curie BP 146, F-13384 Marseille Cedex 13, France

(Received 28 May 2008; revised 28 April 2009; accepted 28 April 2009)

In plants, osmotically driven flows are believed to be responsible for translocation of sugar in the pipe-like phloem cell network, spanning the entire length of the plant – the so-called Münch mechanism. In this paper, we present an experimental and theoretical study of transient osmotically driven flows through pipes with semi-permeable walls. Our aim is to understand the dynamics and structure of a 'sugar front', i.e. the transport and decay of a sudden loading of sugar in a water-filled pipe which is closed in both ends. In the limit of low axial resistance (valid in our experiments as well as in many cases in plants) we show that the equations of motion for the sugar concentration and the water velocity can be solved exactly by the method of characteristics, yielding the entire flow and concentration profile along the tube. The concentration front decays exponentially in agreement with the results of Eschrich, Evert & Young (*Planta* (*Berl.*), vol. 107, 1972, p. 279). In the opposite case of very narrow channels, we obtain an asymptotic solution for intermediate times showing a decay of the front velocity as $M^{-1/3}t^{-2/3}$ with time t and dimensionless number $M \sim \eta\kappa L^2 r^{-3}$ for tubes of length L, radius r, permeability κ and fluid viscosity η. The experiments (which are in the small M regime) are in good quantitative agreement with the theory. The applicability of our results to plants is discussed and it is shown that it is probable that the Münch mechanism can account only for the short distance transport of sugar in plants.

1. Introduction

The translocation of sugar in plants, which takes place in the phloem sieve tubes, is not well understood on the quantitative level. The current belief, called the pressure-flow hypothesis (Nobel 1999), is based on the pioneering work of Ernst Münch in the 1920s (Münch 1930). It states, that the motion in the phloem is purely passive, due to the osmotic pressures that build up relative to the neighbouring xylem in response to

† Email address for correspondence: tbohr@fysik.dtu.dk

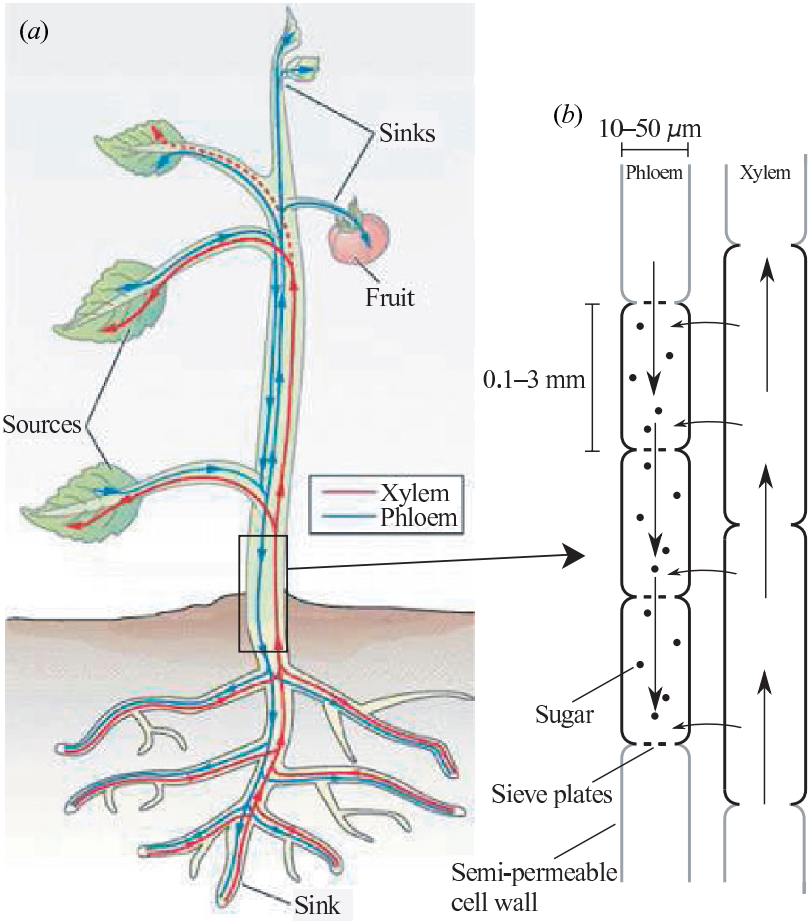

FIGURE 1. In plants, two separate pipe-like systems are responsible for the transport of water and sugar. The xylem conducts water from the roots to the shoot while the phloem conducts sugar and other nutrients from places of production to places of growth and storage. The mechanism believed to be responsible for sugar translocation in the phloem, called the Münch mechanism or the pressure-flow hypothesis (Nobel 1999), states the following: As sugar is produced via photosynthesis in sources it is actively loaded into the tubular phloem cells. As it enters the phloem, the chemical potential of the water inside is lowered compared to the surrounding tissue, thereby creating a net flux of water into the phloem cells. This influx of water in turn creates a bulk flow of sugar and water towards the sugar sink shown in (*b*), where active unloading takes place. As the sugar is removed, the chemical potential of the water inside the phloem is raised resulting in a flow of water out of the sieve element.

loading and unloading of sugar in different parts of the plant, as shown in figure 1. This mechanism is much more effective than diffusion, since the osmotic pressure differences caused by different sugar concentrations in the phloem create a bulk flow directed from large concentrations to small concentrations, in accordance with the basic need of the plant. Such flows are often called osmotically driven pressure flows (Thompson & Holbrook 2003), or osmotically driven volume flows (Eschrich, Evert & Young 1972).

To study the osmotically driven flows, Eschrich *et al.* (1972) conducted simple model experiments. Their set-up consisted of a semi-permeable membrane tube submerged in a water reservoir, modelling a phloem sieve element and the surrounding water-filled tissue. At one end of the tube a solution of sugar, water and dye was introduced to mimic the sudden loading of sugar into a phloem sieve element. In the case of the closed tube, they found that the sugar front velocity decayed exponentially in

time as it approached the far end of the tube. Also, they found the initial velocity of the sugar front to be proportional to concentration of the sugar solution. Through simple conservation arguments, they showed that for a flow driven according to the pressure-flow hypothesis, the velocity of the sugar front is given by

$$u_f = \frac{L}{t_0}\exp\left(-\frac{t}{t_0}\right) \quad \text{where} \quad t_0 = \frac{r}{2\kappa\Pi}, \tag{1.1}$$

where t is time, L is the length of the sieve element and r its radius, κ is the permeability of the membrane and Π is the osmotic pressure of the sugar solution. For dilute solutions, $\Pi \approx RTc$ (Landau & Lifshitz 1980), where R is the gas constant, T the absolute temperature and c the concentration in moles per volume. The conservation argument for (1.1) is the following: for incompressible flow in a wide rigid semi-permeable tube of length L imbedded in water, we imagine part of the tube initially filled with sugar solution and the rest with pure water. For a wide tube with slow flow, viscous effects and thus the pressure gradient along the tube is negligible and the pressure is simply equal to the osmotic pressure Π averaged over the tube, i.e. $RT\bar{c}$ where $\bar{c}$ is the constant average sugar concentration. The water (volume) flux through the part of the tube ahead of the sugar front x_f (where there is no osmosis) is $-2\pi r\kappa RT\bar{c}(L - x_f)$, where κ is the permeability of the tube and the flow is negative since water flows out. This will be equal to the rate of change of volume ahead of x_f and thus, due to incompressibility, is equal to $-\pi r^2 \mathrm{d}x_f/\mathrm{d}t$. Putting these two expressions together we get

$$\frac{\mathrm{d}x_f}{\mathrm{d}t} = \frac{2L_p RT\bar{c}}{r}(L - x_f) = \frac{1}{t_0}(L - x_f) \tag{1.2}$$

leading to $u_f = \mathrm{d}x_f/\mathrm{d}t$ given by (1.1).

In the experiments performed by Eschrich *et al.* (1972) good qualitative agreement with (1.1) was obtained, but on the quantitative level the agreement was rather poor. We thus chose to perform independent experiments along the same lines. Eschrich *et al.* (1972) used dye to track the sugar, and in one of our set-ups we can check this method by directly following the sugar without using dye. Also, we make independent measurements of the membrane properties, which then allow detailed comparison with the predictions showing good quantitative agreement.

Simultaneously with the experiments, we develop the theory for osmotic flows. The above derivation of the front propagation is simplified by the lack of viscosity and diffusion and, indeed, by the very assumption that a well-defined sugar front exists. To go beyond this we must use the coupled equations for the velocity and concentration fields as they vary along the tubes and in time. Here we follow the footsteps of a large number of authors, as discussed later. Our main contribution is the analysis of the decay of an initially localized sugar concentration in a channel closed in both ends described by (4.9) and (4.10). Here we point out that the main dimensionless number (termed as *Münch number*) can be chosen as

$$M = \frac{16\eta L^2\kappa}{r^3}, \tag{1.3}$$

where η is the fluid viscosity. We show how to simplify the equations and obtain exact solutions in the regimes $M \ll 1$ (the regime of the experiments in this paper and of those of Eschrich *et al.*) and asymptotic solutions for $M \gg 1$. Both regimes are found in plants and we propose an effective way for numerical integration of the equations in the general case using Green's functions. In the regime $M \ll 1$ the solubility of the

Quantity	Magnitude	Reference
Radius (μm)	4.5 (Fava bean), 4 (Winter squash), 6–25	Knoblauch & van Bel (1998), Taiz & Zeiger (2002), Nobel (1999)
Length (mm)	0.09 (Fava bean), 0.1–3	Knoblauch & van Bel (1998), Nobel (1999)
Flow velocity ($m\,h^{-1}$)	0.5–1, 0.2–2	Knoblauch & van Bel (1998), Nobel (1999)
Elastic modulus (MPa)	17, 5.6–7.4 (Ash)	Thompson & Holbrook (2003*a*), Niklas (1992)
Permeability ($10^{-11}\,m\,s^{-1}\,Pa^{-1}$)	5,1.1 (Zitella translucence)	Thompson & Holbrook (2003*a*), Eschrich *et al.* (1972)
Sucrose concentration (M)]	0.3–0.9	Taiz & Zeiger (2002)

TABLE 1. Characteristic properties of phloem sieve elements.

equations is shown by mapping them to a damped Burgers equation (5.6), which can be solved by the method of characteristics. An analogous relation was pointed out earlier by Frisch (1976), but for a different boundary condition (open in one end) where the damping term disappears. Some results for $M \ll 1$ were also given by Weir (1981), but the lack of generality of his approach to the time-dependent problem makes his results hard to extend.

In table 1 we show characteristic data for single sieve elements, which build up the phloem conducts in plants. If one naively applies these results to the flow inside such sieve elements, taking $L = 1\,\mathrm{mm}$, $r = 10\,\mu\mathrm{m}$, $\kappa = 10^{-11}\,\mathrm{m\,s^{-1}\,Pa^{-1}}$ and concentration $\bar{c} = 0.5\,\mathrm{M}$, one gets a characteristic velocity from (1.1) of $9\,\mathrm{m\,h^{-1}}$, almost an order of magnitude larger than the range of velocities given in the table. Here one has to remember that the characteristic velocity from (1.1) is valid for a *transient* flow caused by an initial sudden sugar loading, whereas the velocities quoted in the table are characteristic for the normal steady-state operation of the plants. For large distances (e.g. those occurring in tall trees), the viscous effects embodied in (1.3) become large. Thus the value of M for the single sieve element considered above is $M \approx 1.6 \times 10^{-4}$ whereas the value for a phloem tube spanning a distance of 10 m would be greater by a factor 10^8, i.e. $M \approx 1.6 \times 10^4$ (see also table 3 for characteristic values for M). In this regime (1.1) is no longer valid and, in fact, as seen in § 5.2 (5.46), the characteristic velocity will be reduced by a factor $M^{-1/3}$, now making it an order of magnitude *smaller* than the velocities quoted in the table. This seems to indicate that large distance transport in trees cannot rely solely on the Münch mechanism and indeed the sieve elements are living cells and active transport may play a key role (see, e.g. Taiz & Zeiger 2002). For future studies in this direction it is important to be able to separate these effects clearly and thus to understand the passive osmotic component as clearly and simply as possible, which is the aim of the present paper.

The layout of the paper is as follows: §§ 2 and 3 describe our experimental set-ups and the experimental results obtained. In § 4, the flow equations are developed and in § 5 we present solutions for the cases $M \ll 1$ and $M \gg 1$. Finally, § 6 contains a detailed comparison between theory and experiments. After the conclusions (§ 7), two appendices follow. Appendix A provides information about the experimental materials used and appendix B discusses the numerical methods (based on Green's functions) used for solving the flow equations in the general case.

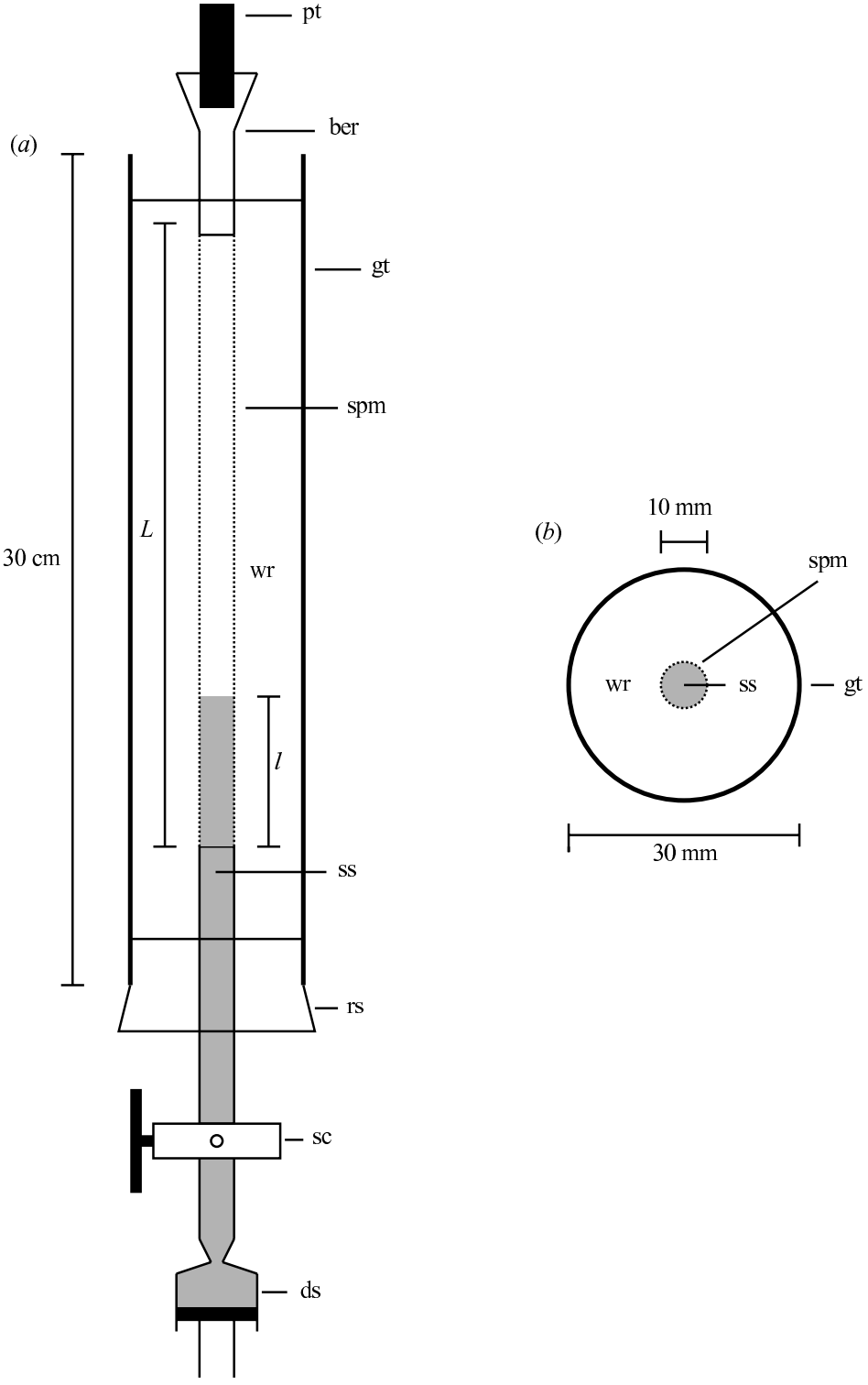

FIGURE 2. Set-up I used to observe the movement of a sugar–dye solution (ss) inside a semi-permeable membrane tube (spm). L: length of membrane tube; l: initial sugar front height; ds: disposable syringe; gt: glass tube; rs: rubber stopper; sc: stopcock; wr: water reservoir; bc: brass cylinder; pt: pressure transducer.

2. First experimental set-up

2.1. *Set-up and methods*

Set-up I is presented in figure 2. It is based on the design by Eschrich *et al.* with the addition of a pressure transducer that allows us to measure the gauge pressure

	1	2	3	4	5
Mean sugar concentration, $\bar{c}$ (mM)	1.5 ± 0.3	2.10 ± 0.03	2.4 ± 0.2	4.2 ± 0.7	6.8 ± 0.1
Osmotic pressure, Π (bar)	0.14 ± 0.02	0.15 ± 0.01	0.31 ± 0.03	0.39 ± 0.01	0.68 ± 0.02
Membrane tube length, L (cm)	28.5	20.8	28.5	28.5	20.6
Initial front height, l (cm)	4.9	3.7	6.6	6.5	4.8

TABLE 2. Data for the experimental runs shown in figure 3.

(which is what we from now on will refer to as 'pressure') inside the membrane tube continuously. More precisely, it consisted of a 30 cm long, 30 mm wide glass tube in which a semi-permeable membrane tube of equal length and a diameter of 10 mm was inserted. At one end, the membrane tube was fitted over a glass stopcock equipped with a rubber stopper. On the other end, the membrane tube was fitted over a brass cylinder equipped with a holder to accommodate a pressure transducer for measuring the pressure inside the membrane tube.

After filling the 30 mm wide glass tube with water, water was pressed into the semi-permeable tube with a syringe. Care was taken so that no air bubbles were stuck inside the tube. For introducing the sugar solution into the tube, a syringe was filled with the solution and then attached to the lower end of the stopcock which was kept closed. After fitting the syringe, the stopcock was opened and the syringe piston was very slowly pressed in, until a suitable part of the tube had been filled with the solution. Care was also taken to avoid any mixing between the sugar solution and the water already present in the semi-permeable tube. The physical characteristics of the membranes and of the sugar we used are discussed in appendix A. To track the movement of the sugar solution it was mixed with a red dye and data was recorded by taking pictures of the membrane tube at intervals of 15 min using a digital camera.

2.2. *Experimental results obtained with set-up I*

An example of a set of data is shown in figure 3. In figure 3(*a*) are the raw images, which after processing give figure 3(*b*) showing the position of the sugar front, x_f, as a function of time. The error bars on x_f are estimated to be ± 1 mm, but are too small to be seen. Finally, figure 3(*c*) shows the pressure inside the tube as a function of time. At first, a linear motion of the front is observed with a front velocity of ~ 1 cm h^{-1}. This is then followed by a decrease in the front velocity as the front approaches the end of the tube. The pressure is seen to rise rapidly during the first hour before settling to a constant value, indicated by the dashed line. This constant value is taken to be the osmotic pressure Π of the sugar solution. Looking at figure 3(*a*), one observes that diffusion has the effect of dispersing the front slightly as time passes. Below the front, the concentration seems to be uniform throughout the cross-section of the tube, and there is no indication of large boundary layers forming near the membrane walls.

Similar experiments with different sugar concentrations were made and a plot of the results can be seen in figure 3(*d,e*). The experimental conditions for the five different sets of experiments are given in table 2. Qualitatively the motion of the front and the pressure increase follows the same pattern. One notices that the speed with which the fronts move is related to the mean sugar concentration inside the membrane tube, with the high-concentration solutions moving faster than the low-concentration ones.

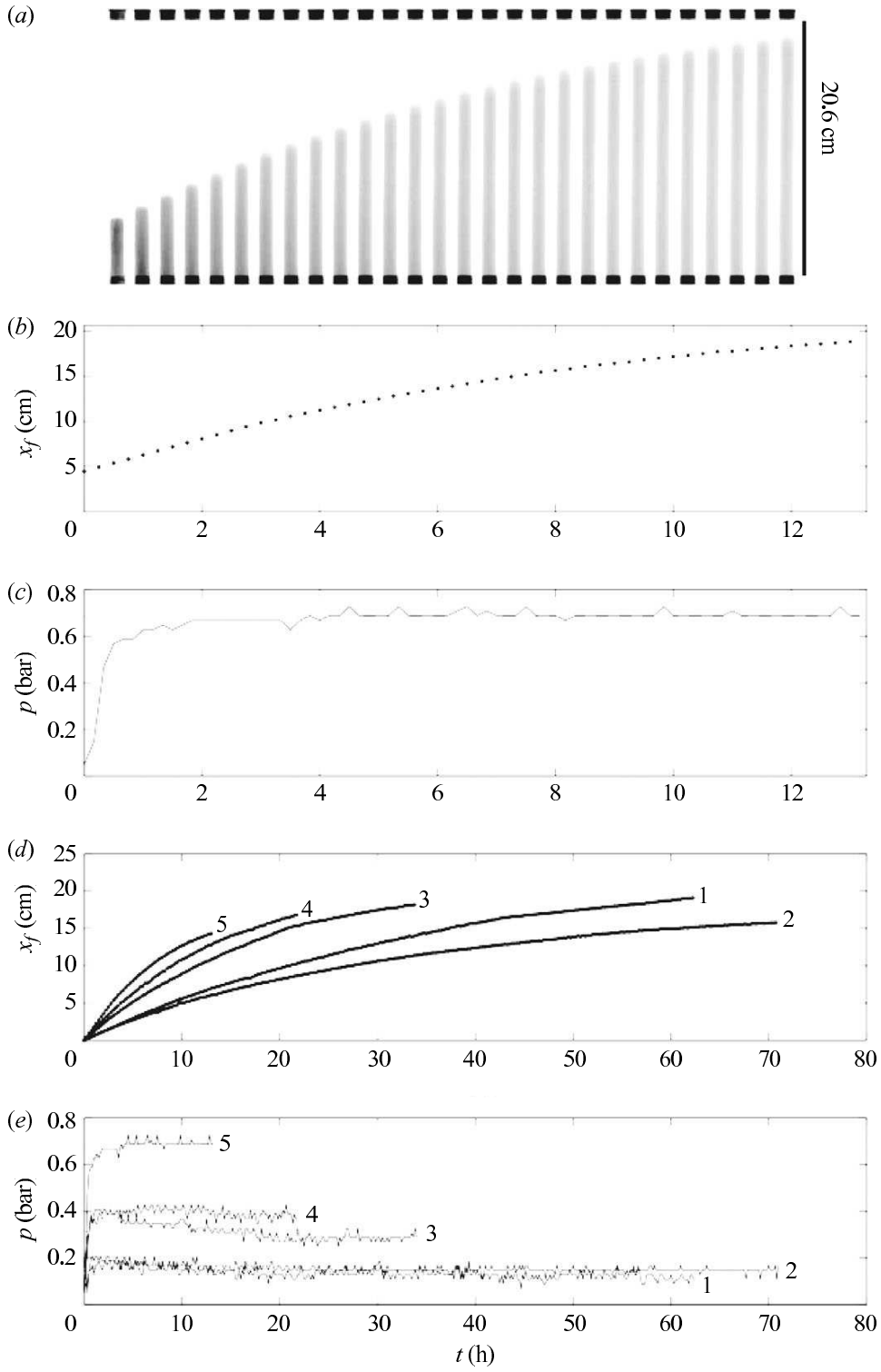

FIGURE 3. Experimental results from set-up I. (*a*) Time series of pictures taken in experiment 5. Time increases from left to right in steps of 30 min. See details of the sugar solutions used in table 2. (*b*) Plot of the front position versus time obtained from the images above. (*c*) Plot of the gauge pressure inside the tube versus time. The dashed line is the osmotic pressure of the solution, taken to be the average value of the pressure from $t = 2$ h until the end of the experiment. (*d*) Plots of the sugar front position versus time for different sugar concentrations, as indicated in table 2. (*e*) Plots of the pressure inside the membrane tube for different sugar concentrations.

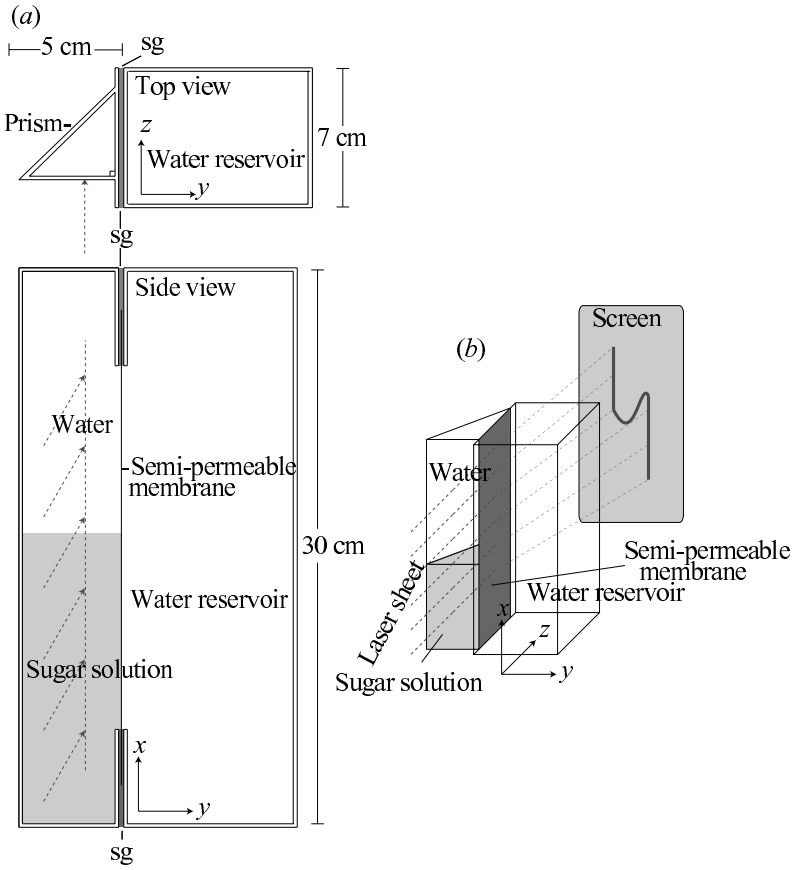

FIGURE 4. Set-up II dedicated to the tracking of the sugar front via index of refraction changes. It consists of a hollow isosceles glass prism and a Plexiglas cuboid in osmotic contact through a membrane. A pressure transducer was attached to the top of the glass prism to measure the pressure inside.

The reason why 2 is moving slower than 1 is that experiment 2 was conducted in a slightly shorter membrane tube than the one used in experiment 1, thereby decreasing the characteristic velocity as we shall see later.

3. Second experimental set-up

3.1. *Set-up and methods*

Set-up II is presented in figure 4. This set-up allows us to track the real front location, without the use of colorant, directly via the variation of the index of refraction. It consisted of a hollow isosceles glass prism and a Plexiglas cuboid in osmotic contact through a membrane. To track the time evolution of the sugar front inside the prism, we used the refraction of a laser sheet passing through it. The laser sheet was generated by shining a laser beam, generated by a Melles Griot 3.1 mW laser, through a glass rod. When passing through the prism, light would deviate depending on the local index of refraction, producing a typical S shape as shown in figure 4. The index of refraction varies linearly with sugar concentration and thus by looking at the refracted laser sheet projected onto a screen, we were able to reconstruct the concentration profile inside the prism. A camera recorded images of the screen at regular intervals to track the moving concentration profile.

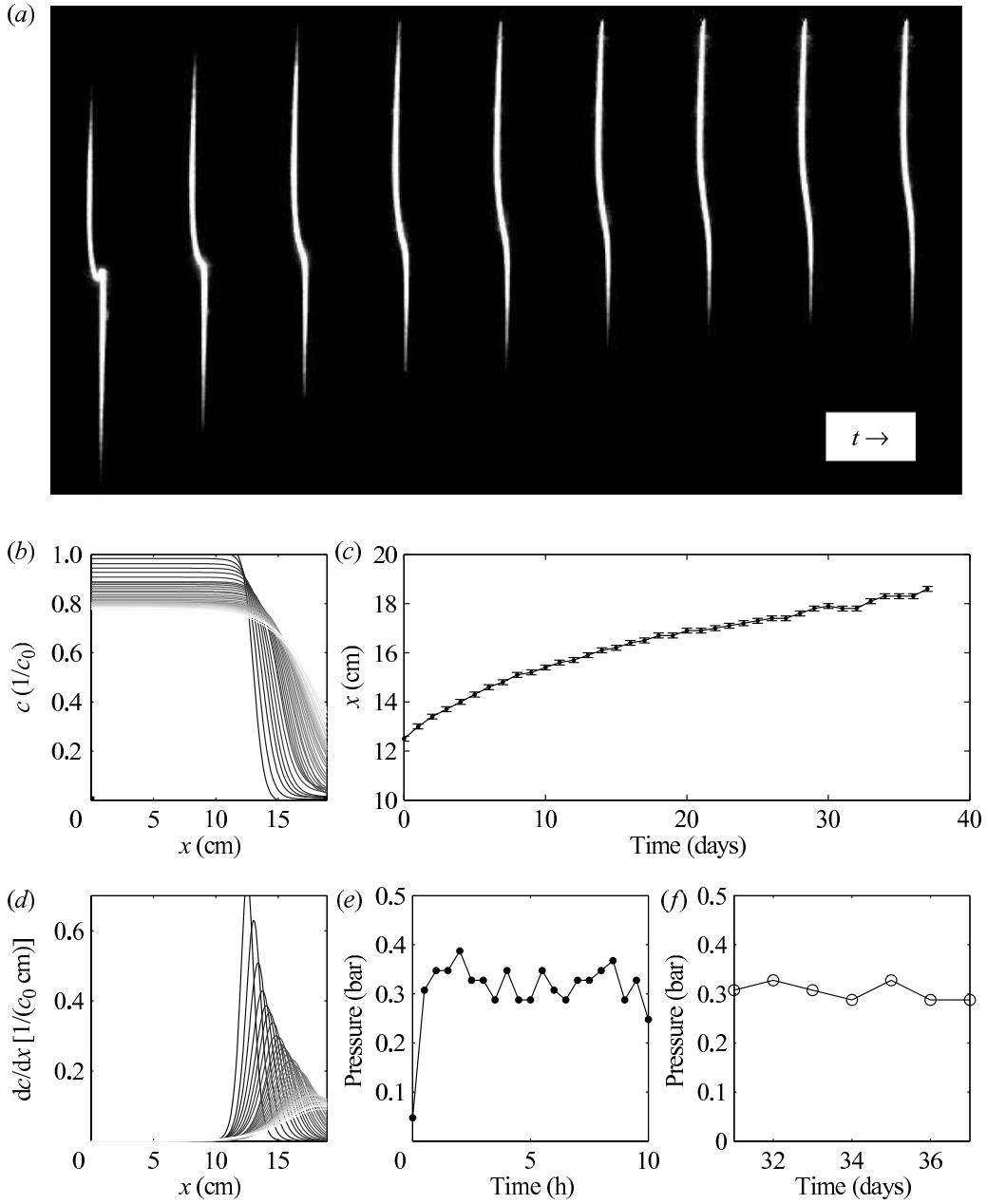

FIGURE 5. Results from set-up II. In (*a*) the raw data images are shown. In (*b*) the concentration profile extracted from (*a*) is shown. (*c*) shows the front position extracted from (*b*) by finding the maximum of the concentration gradient, shown in (*d*). Finally, (*e*, *f*) show the pressure inside the prism.

3.2. *Experimental results obtained with set-up II*

3.2.1. *Effect of osmosis*

Figure 5 shows the data collected using set-up II. In figure 5(*a*), a time series of pictures is depicted showing the refracted laser-light projected onto a screen, the time gap between each image being 1 day. Comparing the upper and lower parts of each picture, one generally observes a deflection to the right at the bottom, corresponding to a high sugar concentration at the bottom of the prism. In the intermediate region one sees a dip in the refracted light, corresponding to a strong concentration gradient. The dip gradually flattens while it advances upwards, representing a sugar front which advances while it broadens. This process can be seen directly in figure 5(*b*),

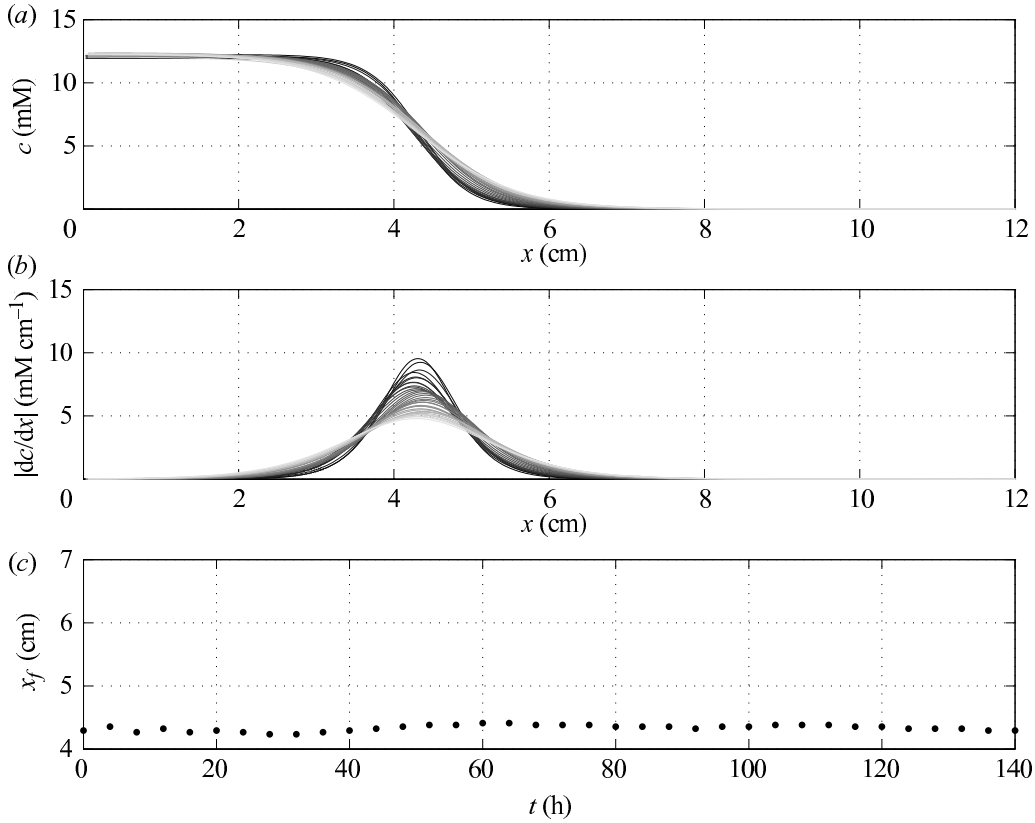

FIGURE 6. Results from a control experiment with set-up II, where concentration varies only due to diffusion. (*a*) Time evolution of the concentration profile, (*b*) time evolution of the profile of concentration gradient and (*c*) time evolution of the sugar front location.

which shows the time evolution of the sugar concentration obtained from the images. Starting from a steep concentration profile, we see that the front moves upwards while it flattens. In figure 5(*d*) the time evolution of the concentration gradient is depicted, clearly showing a peak which broadens while it moves forward. Finally, in figure 5(*e*, *f*), the position of the sugar front and the pressure inside the prism is plotted as a function of time. The error bars on x_f are ± 1 mm, as discussed below.

3.2.2. *Effect of diffusion*

To study the effect of diffusion on the dynamics of the sugar front separately, an experiment was made with set-up II, in which the water reservoir was not filled. The experiment was then conducted in the usual way, and the motion of the front was recorded. The results of this are shown in figure 6. Starting from a steep concentration gradient, we observe that the front flattens but otherwise does not move much.

Comparing figures 5 and 6 we observe, that while the front moves 2 cm due to osmosis in 6 days, it does not seem to move at all in 6 days due to diffusion. Thus, while diffusion has a flattening effect, it plays little role in the forward motion of the front.

Since the front did not move due to diffusion, the fluctuations in the front position seen in figure 6(*c*) gives a measure of the uncertainty of a single measurement of the front position. Taking the standard deviation of the fluctuations gives an uncertainty of ± 1 mm, shown as error bars in figure 5(*c*).

More details on this second experiment can be found in Jensen (2007).

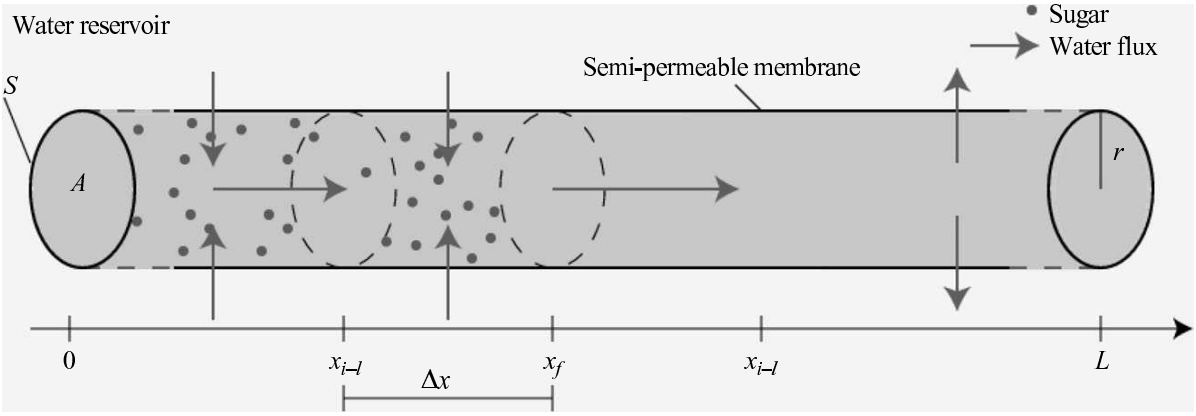

FIGURE 7. Sketch of the tube.

4. Theoretical analysis

4.1. *Front propagation via flow equations*

The equations of motion for osmotically driven flows have been derived and analysed thoroughly several times in the literature (Weir 1981) and have been studied carefully numerically (Henton 2002; Thompson & Holbrook 2003*a*, *b*). For the sake of completeness, we shall include a short derivation of these.

We consider a tube of length L and radius r, as shown in figure 7. The tube has a constant cross-section of area $A = \pi r^2$ and circumference $S = 2\pi r$ and its walls are made of a semi-permeable membrane with permeability κ. Inside the tube is a solution of sugar in water with concentration $c(x) = c(x, t)$. Throughout this paper, we study the transient dynamics generated by an asymmetrical initial concentration distribution, where the sugar is initially localized to one end of the tube with a concentration level c_0. The tube is surrounded by a water reservoir, modelling the water surrounding the membrane tube in set-up I.

We shall assume that $L \gg r$ and that the radial component of the flow velocity inside the tube is much smaller than the axial component, as is indeed the case in the experiments. With these assumptions, we will model the flow in the spirit of lubrication theory and consider only a single average axial velocity component $u(x, t)$. Also, we will assume that the concentration c is independent of the radial position ρ an assumption that can be verified experimentally in set-up II.

Let us now consider the equation for volume conservation by looking at a small section of the tube between x_{i-1} and x_i. The volume flux into the section due to advection is

$$A(u_{i-1} - u_i), \tag{4.1}$$

where the axial flow velocities are taken to be u_{i-1} and u_i at x_{i-1} and x_i, respectively. The volume flux inwards across the membrane due to osmosis (Schultz 1980) is

$$S\Delta x\kappa(RTc(x, t) - p(x, t)), \tag{4.2}$$

where p is the local difference of pressure across the membrane and c is the local concentration. For clarity we use the van't Hoff value $\Pi = RTc$ for the osmotic pressure, which is valid only for dilute (ideal) solutions. In appendix A.3, we show that the linear relation between Π and c is verified experimentally as $\Pi = (0.1 \pm 0.01\,\text{bar mM}^{-1})c$. Assuming conservation of volume, we get

$$A(u_{i-1} - u_i) + S\Delta x\kappa(RTc - p) = 0. \tag{4.3}$$

Letting $\Delta x \to 0$ and using that the cross-section to perimeter ratio reduces to $r/2$, this becomes

$$\frac{r}{2}\frac{\partial u}{\partial x} = \kappa(RTc - p). \tag{4.4}$$

For these very slow and slowly varying flows, the time dependence of the Navier–Stokes equation can be neglected and the velocity field is determined by the instantaneous pressure gradient through the Poiseuille or Darcy relation (for a circular tube)

$$u = -\frac{r^2}{8\eta}\frac{\partial p}{\partial x}, \tag{4.5}$$

where η is the dynamic viscosity of the solution, typically $\sim 1.5 \times 10^{-3}$ Pa s in our experiments.

Differentiating (4.4) with respect to x and inserting the result from (4.5) we get for the conservation of water that

$$RT\frac{\partial c}{\partial x} = \frac{r}{2\kappa}\frac{\partial^2 u}{\partial x^2} - \frac{8\eta}{r^2}u. \tag{4.6}$$

The final equation expresses the conservation of sugar advected with velocity u and diffusing with molecular diffusivity D

$$\frac{\partial c}{\partial t} + \frac{\partial uc}{\partial x} = D\frac{\partial^2 c}{\partial x^2}. \tag{4.7}$$

The set of equations (4.6) and (4.7) is equivalent to those of Thompson & Holbrook (2003*b*) except for the fact that we have removed the pressure by substitution, and that we do not consider elastic deformations of the tube.

4.1.1. *Non-dimensionalization of the flow equations*

To non-dimensionalize (4.6) and (4.7), we introduce the following scaling

$$c = c_0 C, \qquad u = u_0 U, \qquad x = LX, \qquad t = t_0 \tau,$$

L has been chosen such that the spatial domain is now of the unit interval $X \in [0, 1]$, $u_0 = L/t_0$ and c_0 is the initial concentration level in one end of the tube. Choosing further

$$t_0 = \frac{r}{2\kappa RTc_0}, \quad M = \frac{16\eta L^2\kappa}{r^3} \quad \text{and} \quad \bar{D} = \frac{D}{u_0 L} = \frac{Dr}{2RTc_0L^2\kappa}, \tag{4.8}$$

and inserting in (4.6) and (4.7), we get the non-dimensional flow equations

$$\frac{\partial^2 U}{\partial X^2} - MU = \frac{\partial C}{\partial X}, \tag{4.9}$$

$$\frac{\partial C}{\partial \tau} + \frac{\partial UC}{\partial X} = \bar{D}\frac{\partial^2 C}{\partial X^2}. \tag{4.10}$$

The parameter M corresponds to the ratio of axial to membrane flow resistance, which we shall refer to as the *Münch number*. This is identical to the parameter $\hat{F}$ in Thompson & Holbrook (2003*b*). The second parameter $\bar{D}$ is the Peclet number. Thus, the longer the tube the less important the diffusion becomes and the more important the pressure gradient due to viscous effects becomes.

Values of the parameters M and $\bar{D}$ in different situations can be seen in table 3. The typical magnitude of the parameters M and $\bar{D}$ in plants are found from the

	M	$\bar{D}$
Set-up I	2×10^{-8}	6×10^{-5}
Set-up II	10^{-9}	2×10^{-2}
Single sieve element ($L=1$ mm)	5×10^{-4}	5×10^{-4}
Leaf ($L=1$ cm)	5×10^{-2}	5×10^{-5}
Branch ($L=1$ m)	5×10^{2}	5×10^{-7}
Small tree ($L=10$ m)	5×10^{4}	5×10^{-8}

TABLE 3. Values of the parameters M and $\bar{D}$ in various situations.

following values (also given in table 3):

$$r=10\,\mu\text{m},\quad \eta=1.5\times10^{-3}\,\text{Pa s},\quad u_0=2\,\text{m h}^{-1},\quad \kappa=2\times10^{-11}\,\text{m (Pa s)}^{-1}.$$

We observe, that M and $\bar{D}$ are small in both experiments, and that for short distance transport in plants this is also the case. However, over length scales comparable to a branch ($L=1$ m) or a small tree ($L=10$ m) M is large, so in this case the pressure gradient is not negligible.

When deriving the equations for osmotically driven flows, we have assumed that the concentration inside the tube was a function of x and t only. However, the real concentration inside the tube will also depend on the radial position ρ in the form of a concentration boundary layer near the membrane, in the literature called an *unstirred layer* (Pedley 1983). Close to the membrane, the concentration c_m is lowered compared to the bulk value c_b because sugar is advected away from the membrane by the influx of water. This, in turn, results in a lower influx of water, ultimately causing the axial flow inside the tube to be slower than expected. In our experiments we see no signs of such boundary layers and apparently their width and their effect on the bulk flow are very small.

5. Solutions of the flow equations

We will now analyse (4.9) and (4.10). We will show that they can be solved quite generally for $M=\bar{D}=0$ by the method of characteristics. For an arbitrary initial condition, this method will generally yield an implicit solution.

For arbitrary values of M and $\bar{D}$, we cannot solve the equations of motion analytically and thus have to incorporate numerical methods. This topic has been the focus of much work both in the steady-state case (Thompson & Holbrook 2003*a*) and in the transient case (Henton 2002). However, no formulation fully exploiting the partially linear character of the equations capable of handling all different boundary conditions has so far been presented. Therefore, we show that using Green's functions, the equations of motion can be transformed into a single integro-differential equation, which can be solved using standard numerical methods with very high precision. This technical numerical part is detailed in appendix B.

5.1. *Results for small Münch number*

In the limit $M=\bar{D}=0$ the equations become

$$\frac{\partial^2 U}{\partial X^2}=\frac{\partial C}{\partial X}, \tag{5.1}$$

$$\frac{\partial C}{\partial \tau}+\frac{\partial UC}{\partial X}=0. \tag{5.2}$$

By integrating (5.1) with respect to X, we get

$$\frac{\partial U}{\partial X} = C + F(\tau). \tag{5.3}$$

If we choose $U(0) = U(1) = 0$, $F(\tau)$ becomes

$$F(\tau) = -\int_0^1 C \, \mathrm{d}X \equiv -\bar{C}(\tau). \tag{5.4}$$

Using (5.3) in (5.2) gives

$$\frac{\partial}{\partial X}\left[\frac{\partial U}{\partial \tau} + U\left(\frac{\partial U}{\partial X} + \bar{C}\right)\right] = -\frac{\mathrm{d}\bar{C}}{\mathrm{d}\tau} = 0, \tag{5.5}$$

where the last equality follows from integrating X from 0 to 1, observing that all terms in the square bracket vanish at the end points due to the boundary condition $u(X=0,\tau) = u(X=1,\tau) = 0$. Thus $\bar{C}$ is a constant in time since the tube is closed. Integrating with respect to X and using the boundary conditions on U, this becomes

$$\frac{\partial U}{\partial \tau} + U\frac{\partial U}{\partial X} = -\bar{C}U. \tag{5.6}$$

Equation (5.6) is a damped Burgers equation (Gurbatov, Malakhov & Saichev 1991), which can be solved using Riemann's method of characteristics. The characteristic equations are

$$\frac{\mathrm{d}U}{\mathrm{d}\tau} = -\bar{C}U \tag{5.7}$$

$$\frac{\mathrm{d}X}{\mathrm{d}\tau} = U. \tag{5.8}$$

Equation (5.7) has the solution

$$U = U_0(\xi)\exp(-\bar{C}\tau), \tag{5.9}$$

where the parametrization $\xi(X,\tau)$ of the initial velocity has to be found from

$$X = \xi + \frac{1}{\bar{C}}U_0(\xi)(1 - \exp(-\bar{C}\tau)), \tag{5.10}$$

where $\xi = X$ at $\tau = 0$.

5.1.1. *Exact solutions for simple initial conditions*

An experimental condition close to that of our experiments is to use a Heaviside step function as initial condition on C, making C initially constant in some interval $[0, \lambda]$

$$C(X, \tau = 0) = C_I H(\lambda - X) = \begin{cases} C_I & \text{for} \quad 0 \leqslant X \leqslant \lambda. \\ 0 & \text{for} \quad \lambda < X \leqslant 1. \end{cases} \tag{5.11}$$

Equation (5.3) now enables us to find the initial condition on the velocity

$$U(X, \tau = 0) = \int_0^X (C(X', 0) - \bar{C}) \, \mathrm{d}X' = \int_0^X (C(X', 0) - \lambda C_I) \, \mathrm{d}X' \tag{5.12}$$

$$= \begin{cases} (C_I - \bar{C})X & \text{for} \quad 0 \leqslant X \leqslant \lambda. \\ \bar{C}(1 - X) & \text{for} \quad \lambda < X \leqslant 1. \end{cases} \tag{5.13}$$

From (5.13), we have

$$U_0(\xi) = \begin{cases} (C_I - \bar{C})\xi & \text{for} \quad 0 \leqslant \xi \leqslant \lambda. \\ \bar{C}(1-\xi) & \text{for} \quad \lambda < \xi \leqslant 1. \end{cases} \tag{5.14}$$

Then, solving for $\xi(X, \tau)$ in (5.10) gives

$$\xi(X,\tau) = \begin{cases} \dfrac{X}{1 + (1/\lambda)(1-\lambda)(1-\exp(-\bar{C}\tau)} & \text{for} \quad X \in I_1, \\ \dfrac{X - 1 + \exp(-\bar{C}\tau)}{\exp(-\bar{C}\tau)} & \text{for} \quad X \in I_2, \end{cases} \tag{5.15}$$

where the intervals I_1 and I_2 are defined by

$$I_1 = [0, 1 - (1-\lambda)\exp(-\bar{C}\tau)], \tag{5.16}$$

$$I_2 = [1 - (1-\lambda)\exp(-\bar{C}\tau), 1]. \tag{5.17}$$

Finally, $U(X, \tau)$ is calculated from (5.9)

$$U(X,\tau) = \begin{cases} \dfrac{(C_I - \bar{C})\exp(-\bar{C}\tau)X}{(1/\lambda)(1-\lambda)(1-\exp(-\bar{C}\tau))} & \text{for} \quad X \in I_1, \\ \bar{C}(1-X) & \text{for} \quad X \in I_2, \end{cases} \tag{5.18}$$

which is equivalent to the result obtained by Weir (1981). The solution is plotted in figure 8(*a*, *b*). We can now calculate the instantaneous sugar front position X_f and velocity U_f using the right boundary of I_1 from (5.16)

$$X_f(\tau) = 1 - (1-\lambda)\exp(-\bar{C}\tau), \tag{5.19}$$

$$U_f(\tau) = \frac{\mathrm{d}X_f}{\mathrm{d}\tau} = \bar{C}(1-\lambda)\exp(-\bar{C}\tau). \tag{5.20}$$

Similarly, $C(X, \tau)$ is given by

$$C(X,\tau) = \frac{\bar{C}}{1 - (1-\lambda)\exp(-\bar{C}\tau)} H(X_f - X). \tag{5.21}$$

Going back to dimensional variables, (5.19) and (5.20) become

$$x_f(t) = L - (L-l)\exp\left(-\frac{t}{t_0}\right) \quad \text{and} \tag{5.22}$$

$$u_f(t) = \frac{L}{t_0}\exp\left(-\frac{t}{t_0}\right), \tag{5.23}$$

where L is the length of the membrane tube, l is the initial front position and the decay time t_0 is in accordance with the simple argument given in § 1.

As noted earlier we can use the method of characteristics on arbitrary initial conditions, including the more realistic case, where the initial jump in concentration is replaced by a continuous variation, say, a linear decrease from C_I to 0 taking place between λ_1 and λ_2, i.e.

$$C(X, \tau = 0) = \begin{cases} C_I & \text{for} \quad 0 \leqslant X \leqslant \lambda_1. \\ C_I \dfrac{\lambda_2 - X}{\lambda_2 - \lambda_1} & \text{for} \quad \lambda_1 \leqslant X \leqslant \lambda_2. \\ 0 & \text{for} \quad \lambda_2 < X \leqslant 1. \end{cases} \tag{5.24}$$

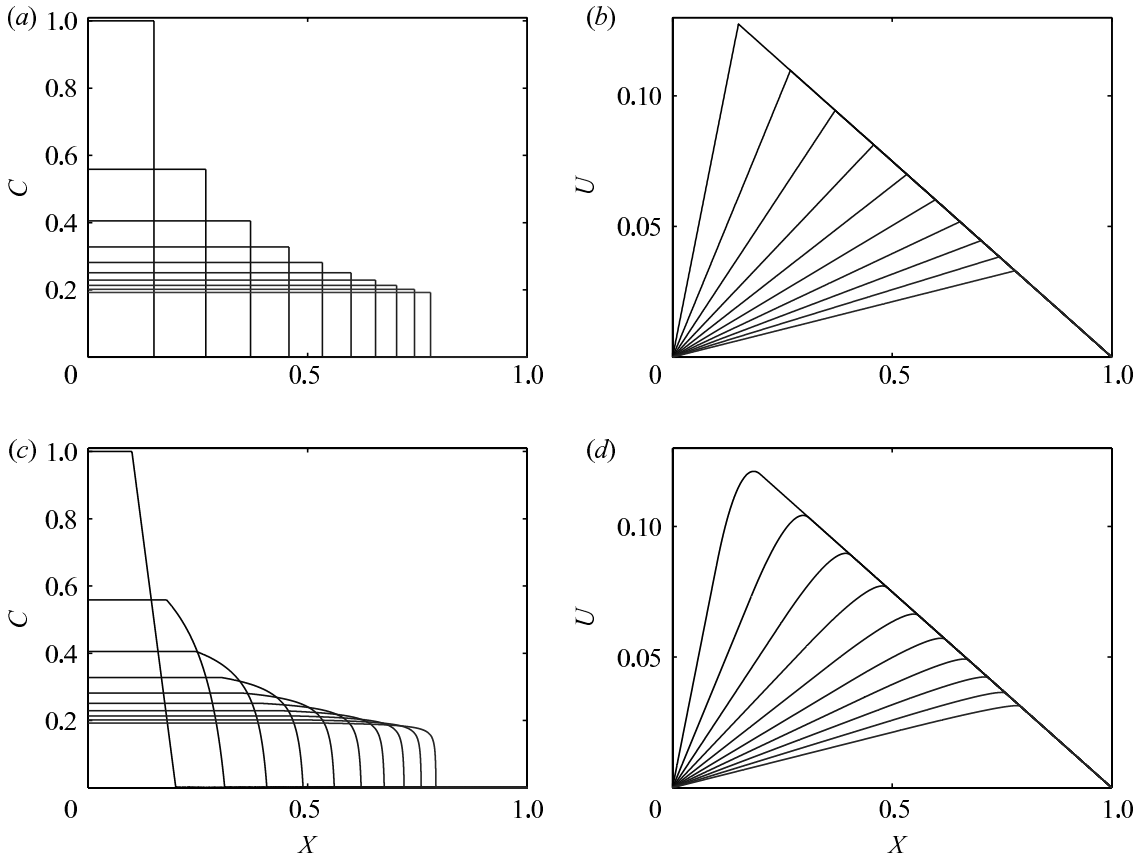

FIGURE 8. (a, b) Plot of the analytical solution for a piecewise constant initial concentration. $\lambda = 0.1$, $C_I = 1$ and $\bar{C} = 0.1$. (c, d) Plot of the analytical solution for a piecewise linear initial concentration. $\lambda_1 = 0.05$, $\lambda_2 = 0.15$, $C_I = 1$ and $\bar{C} = 0.1$. Time increases from black to gray in steps of one unit of time.

Using (5.3) yields the initial velocity

$$U(X, \tau = 0) = \begin{cases} (C_I - \bar{C})X & \text{for} \quad 0 \leqslant X \leqslant \lambda_1, \\ A_1 X^2 + B_1 X + C_1 & \text{for} \quad \lambda_1 \leqslant X \leqslant \lambda_2, \\ \bar{C}(1 - X) & \text{for} \quad \lambda_2 < X \leqslant 1, \end{cases} \tag{5.25}$$

where $\bar{C} = C_I(\lambda_1 + \lambda_2)/2$, and the constants are given by

$$A_1 = -\frac{C_I}{2(\lambda_2 - \lambda_1)}, \quad B_1 = \frac{C_I \lambda_2}{\lambda_2 - \lambda_1} - \bar{C}, \quad C_1 = C_I \lambda_1 + \frac{C_I}{\lambda_2 - \lambda_1}\left(\lambda_1 \lambda_2 + \lambda_1^2/2\right). \tag{5.26}$$

Finding $\xi(X, \tau)$ from (5.10) now gives

$$\xi(X, \tau) = \begin{cases} \dfrac{X}{1 + (1/\lambda)(1 - \lambda)(1 - \exp(-\bar{C}\tau)} & \text{for} \quad X \in I_1, \\ A_2 \xi_2^2 + B_2 \xi_2^2 + C_2 & \text{for} \quad X \in I_2, \\ \dfrac{X - 1 + \exp(-\bar{C}\tau)}{\exp(-\bar{C}\tau)} & \text{for} \quad X \in I_3, \end{cases} \tag{5.27}$$

where

$$A_2 = \frac{A_1}{\bar{C}}(1 - \exp(-\bar{C}\tau)), \quad B_2 = 1 + \frac{B_1}{\bar{C}}(1 - \exp(-\bar{C}\tau)), \quad C_2 = \frac{C_1}{\bar{C}}(1 - \exp(-\bar{C}\tau)). \tag{5.28}$$

Here

$$\xi_2 = \frac{-B_2 + \sqrt{B_2^2 - 4A_2(C_2 - X)}}{2A_2}, \tag{5.29}$$

where the plus solution has been chosen to ensure that $\xi \to X$ as $\tau \to 0$. Finally,

$$I_1 = \left[0, \lambda_1 + \frac{\lambda_1}{\bar{C}}(C_I - \bar{C})(1 - \exp(-\bar{C}\tau))\right], \tag{5.30}$$

$$I_2 = \left[\lambda_1 + \frac{\lambda_1}{\bar{C}}(C_I - \bar{C})(1 - \exp(-\bar{C}\tau)), 1 + (\lambda_2 - 1)\exp(-\bar{C}\tau)\right], \tag{5.31}$$

$$I_3 = \left[1 + (\lambda_2 - 1)\exp(-\bar{C}\tau), 1\right]. \tag{5.32}$$

Plugging into (5.9) gives $U(X, \tau)$ as

$$U(X,\tau) = \begin{cases} \dfrac{(C_I - \bar{C})\exp(-\bar{C})X}{1 + (1/\lambda)(1-\lambda)(1 - \exp(-\bar{C}\tau)} & \text{for} \quad X \in I_1, \\ \left(A_1\xi_2^2 + B_1\xi_2^2 + C_1\right)\exp(-\bar{C}\tau) & \text{for} \quad X \in I_2, \\ \bar{C}\,(1 - X) & \text{for} \quad X \in I_3, \end{cases} \tag{5.33}$$

as shown in figure 8 along with C found from (5.3), i.e.

$$C = \frac{\partial U}{\partial X} + \bar{C}. \tag{5.34}$$

Note that the interval I_2 does not shrink to 0 in time ($I_2 \to [\lambda_1 C_1/\bar{C}, 1]$ for $\tau \to \infty$), but the curvature around the right-hand end point grows without bound so that the limiting shape of the concentration profile again becomes a discontinuous Heaviside function.

5.2. *Results for large Münch number*

In the limit of large $M \gg 1$ we cannot neglect the pressure gradient along the channel and this term dominates the advective term in (4.9), i.e. the second derivative in U. Thus

$$\frac{\partial C}{\partial X} = -MU \tag{5.35}$$

$$\frac{\partial C}{\partial \tau} + \frac{\partial CU}{\partial X} = \bar{D}\frac{\partial^2 C}{\partial X^2} \tag{5.36}$$

giving the nonlinear diffusion equation

$$\frac{\partial C}{\partial \tau} = M^{-1}\frac{\partial}{\partial X}\left[C\frac{\partial C}{\partial X}\right] + \bar{D}\frac{\partial^2 C}{\partial X^2}. \tag{5.37}$$

If we neglect molecular diffusion the resulting universal nonlinear diffusion equation can be written as

$$\frac{\partial C}{\partial \tau} = M^{-1}\frac{\partial}{\partial X}\left[C\frac{\partial C}{\partial X}\right]. \tag{5.38}$$

This can be done as long as $M^{-1}C \gg \bar{D} \approx 10^{-5}$. If M becomes even larger normal diffusion will take over. Equation (5.38) belongs to a class of equations which have been studied, e.g. in the context of intense thermal waves by Zeldovich *et al.* and flow through porous media by Barenblatt (1996) in the 1950s. The Münch number M can be removed by rescaling the time according to $\tau = Mt$, so when M is large we get

very slow motion with a time scale growing linearly with M. Equation (5.38) admits scaling solutions of the form

$$C(X,\tau) = \left(\frac{\tau}{M}\right)^{\alpha} \Phi(\xi) \quad \text{with} \quad \xi = X\left(\frac{\tau}{M}\right)^{\beta} \tag{5.39}$$

as long as $\alpha + 2\beta + 1 = 0$. The total amount of sugar is, however, conserved. In our rescaled units

$$\int_0^1 C(X,\tau)\,\mathrm{d}X = \lambda, \tag{5.40}$$

where, as before, λ is the fraction of the tube initially containing the sugar. We can only hope to find a scaling solution in the intermediate time regime, where the precise initial condition has been forgotten, but the far end ($X = 1$) is not yet felt. Thus we can replace integral (5.40) with

$$\int_0^{\infty} C(X,\tau)\,\mathrm{d}X = \lambda \tag{5.41}$$

which implies that $\alpha = \beta = -1/3$ and

$$C(X,\tau) = \left(\frac{\tau}{M}\right)^{-1/3} \Phi(\xi) \quad \text{with} \quad \xi = X\left(\frac{\tau}{M}\right)^{-1/3}. \tag{5.42}$$

Inserting this form into (5.38), we obtain the differential equation for Φ

$$\frac{1}{2}\frac{\mathrm{d}^2\Phi^2}{\mathrm{d}\xi^2} + \frac{1}{3}\frac{\mathrm{d}(\xi\Phi)}{\mathrm{d}\xi} = 0 \tag{5.43}$$

which can be integrated once to

$$\Phi\frac{\mathrm{d}\Phi}{\mathrm{d}\xi} + \frac{1}{3}\xi\Phi = \text{constant}. \tag{5.44}$$

Due to the boundary condition $\partial C/\partial X = 0$ in the origin, the constant has to vanish and we find the solution

$$\Phi(\xi) = \frac{1}{6}(b^2 - \xi^2) \tag{5.45}$$

which is valid only for ξ smaller than the constant b. For $\xi > b$, Φ is identically 0. The fact that the solution – in contrast to the linear diffusion equation – has *compact support*, is an interesting characteristic of a large class of nonlinear diffusion equations (Barenblatt 1996). The value of b is determined by conservation integral (5.41) giving $\int_0^{\infty} \Phi\,\mathrm{d}\xi = 1$, and thus $b = (9\lambda)^{1/3}$.

The final solution thus has the form

$$C(X,\tau) = \begin{cases} \dfrac{M}{6\tau}((X_f(\tau))^2 - X^2) & \text{for} \quad X < X_f(\tau) = \left(9\lambda\dfrac{\tau}{M}\right)^{1/3} \\ 0 & \text{for} \quad X > X_f(\tau) \end{cases} \tag{5.46}$$

which shows that the sugar front moves as $X_f(\tau) \sim \tau^{1/3}$ and the concentration at the origin decays as $C(0,\tau) \sim \tau^{-1/3}$. To check the validity of this solution, also when the initial condition has support in a finite region near the origin, we plot $(\tau/M)^{1/3}C(X,\tau)$ against $\xi = X(\tau/M)^{-1/3}$ in figure 9(*c*). The corresponding solution for U is found from

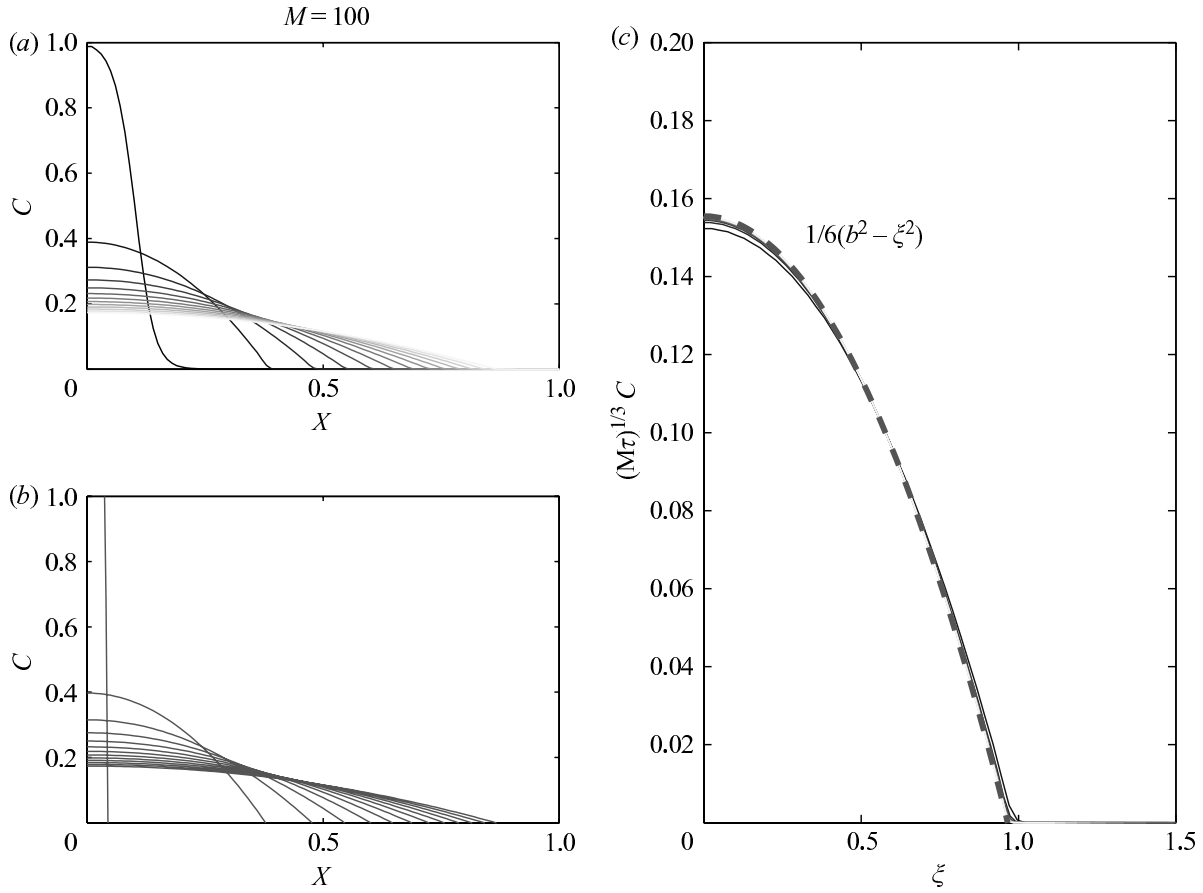

FIGURE 9. (*a*) Numerical simulation of (5.38) compared with (*b*) scaling solution (5.46) and (*c*) (5.45), which is shown as a dashed line. The initial condition has the form $C(X,0)=1-[1+\exp(-(X-\lambda)/\epsilon)]^{-1}$, where $\lambda=0.1$ and $\epsilon=2\times10^{-2}$ and the curves are equidistant in time. When λ controlling the size of the region of non-zero initial sugar concentration becomes larger, a more accurate scaling solution is found by letting $\tau\to\tau+\tau_0$ and treating τ_0 as an unknown parameter. In (*c*), we have omitted the first curve (the initial condition).

(5.35) as

$$U(X,\tau)=\begin{cases}\dfrac{X}{3\tau} & \text{for} \quad X<X_f(\tau)\\ 0 & \text{for} \quad X>X_f(\tau)\end{cases} \tag{5.47}$$

and $\partial^2U/\partial X^2=0$ justifying the neglect of $\partial^2U/\partial X^2$ in going from (4.9) to (5.35) for large M. It is seen that the velocity of the sugar front $X_f'(\tau)=(\lambda/(3M))^{1/3}\tau^{-2/3}$ is identical to $U(X_f(\tau),\tau)$ from (5.47).

6. Comparison between theory and experiment

In §§2.2 and 3.2, we have presented experiments demonstrating the movement of a sugar solution inside a membrane tube surrounded by a reservoir of water. We now wish to consider whether the theory is in agreement with the experimental results.

6.1. *Set-up I*

The plot in figure 10 shows the relative front position, $(L-x_f)/(L-l)$, plotted against time for five different experiments conducted with set-up I. The numbers 1–5 indicate the sugar concentrations used (cf. table 2). One clearly sees, that the relative front position approaches zero faster for high concentrations than for low. Typical

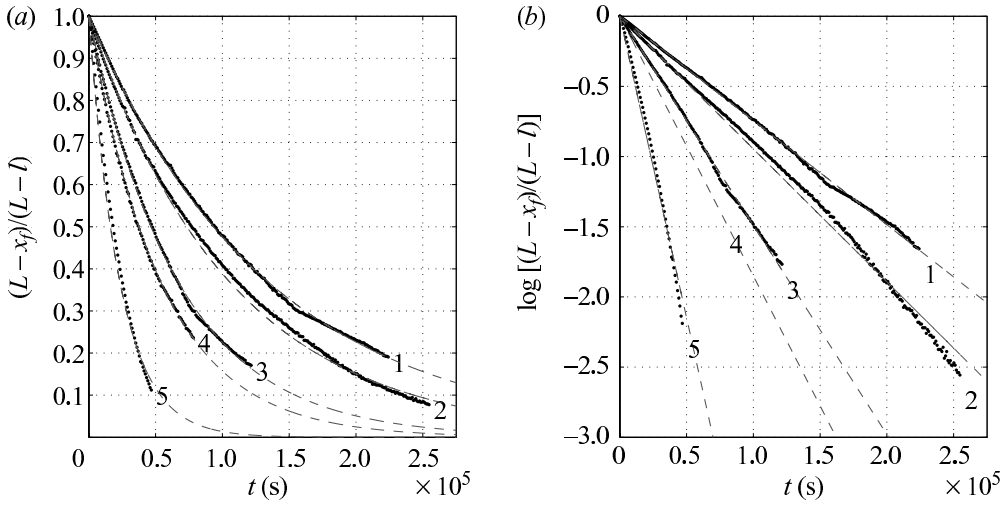

FIGURE 10. (*a*) Experimental (black dots) and fits to (5.22) for the relative front position versus time, shown as dashed lines. (*b*) Semi-logarithmic version of (*a*).

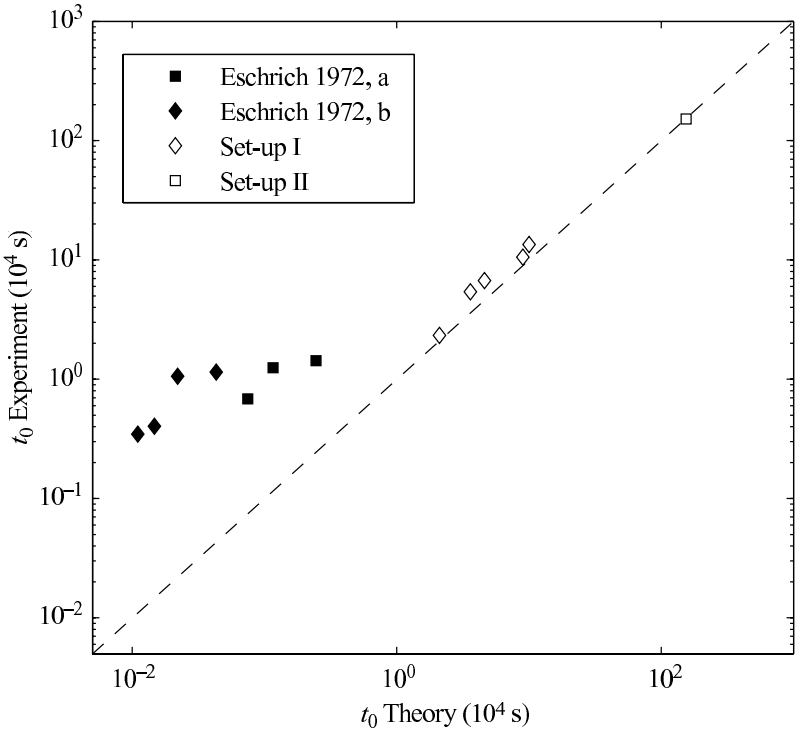

FIGURE 11. Our experimentally obtained values of t_0 plotted together with the results found by Eschrich *et al.* (1972). Data points marked with an 'a' represent results from closed tube experiments and points marked with a 'b' represent results from semi-closed experiments taken from figures 8 and 9 of the original paper.

values of M and $\bar{D}$ are $M \sim 10^{-8}$ and $\bar{D} \sim 10^{-5}$, so it is reasonable to assume that we are in the domain where the analytical solution for $M = \bar{D} = 0$ is valid. To test the result from (5.19) against the experimental data, the plot in figure 10 shows the logarithm of the relative front position plotted against time. For long stretches of time the curves are seen to approximately follow straight lines in good qualitative agreement with theory. The dashed lines are fits to (5.19), and we interpret the slopes as $-\frac{1}{t_0}$, the different values plotted in figure 11 against the theoretical values. The theoretically and experimentally obtained values of t_0 are in good quantitative

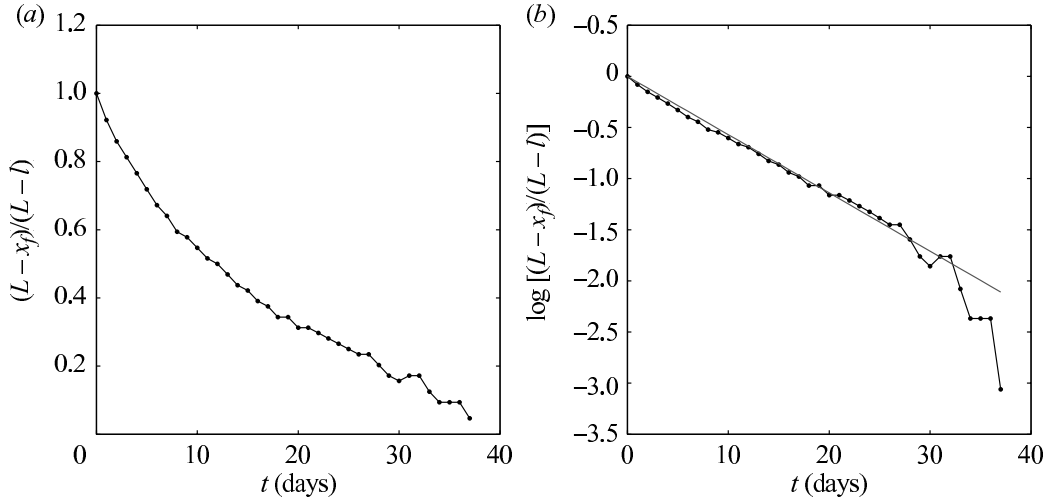

FIGURE 12. (*a*) Experimental data obtained using set-up II showing the relative front position (black dots) as a function of time. (*b*) Lin–log plot of the experimental data shown on the left. The solid line is a fit to (5.22) with $t_0 = 1.6 \times 10^6$ s.

agreement, within 10 %–30 %. Generally, theory predicts somewhat smaller values of t_0 than observed, implying that the observed motion of the sugar front is a little slower than expected from the pressure-flow hypothesis. Nevertheless, as can be seen in figure 11 these results are a considerable improvement to the previous results obtained by Eschrich *et al.* as we find much better agreement between experiment and theory.

6.2. *Set-up II*

The plot in figure 12 shows the relative front position, $(L - x_f)/(L - l)$, plotted against time for the experiment conducted with set-up I. On the semi-logarithmic plot, the curves are seen to follow straight lines in good qualitative agreement with the simple theory for $M = \bar{D} = 0$. As can be seen in figure 11, we also found very good quantitative agreement between the experiment and theory for set-up II.

To test how well the motion of the sugar front observed in the experiments with set-up II was reproduced by our model, we solved the equations of motion numerically starting with the initial conditions from figure 5. For $M = \bar{D} = 0$, the results are shown in figure 13(*b*). While the front positions are reproduced relatively well, the shape of the front is not, so diffusion must play a role. This can be seen in figure 13(*c*) which shows the result of simulation with $M = 10^{-9}$, $D = 6.9 \times 10^{-11}\ \mathrm{m^2\ s^{-1}}$. Clearly, the model which includes diffusion reproduces the experimental data significantly better.

To study the shape of the front in greater detail, consider the plots in figure 13(*d–f*). Here the gradient of the concentration curves on the left in figure 13 is shown. In figure 13(*d*) we clearly see a peak moving from left to right while it gradually broadens and flattens. In figure 13(*e*) also we see the peak advancing, but the flattening and broadening is much less pronounced. In figure 13(*f*) we see that the model which includes diffusion reproduces the gradual broadening and flattening of the front very well.

7. Conclusion

In this paper we have studied osmotically driven transient pipe flows. The flows are generated by concentration differences of sugar in closed tubes, fully or partly

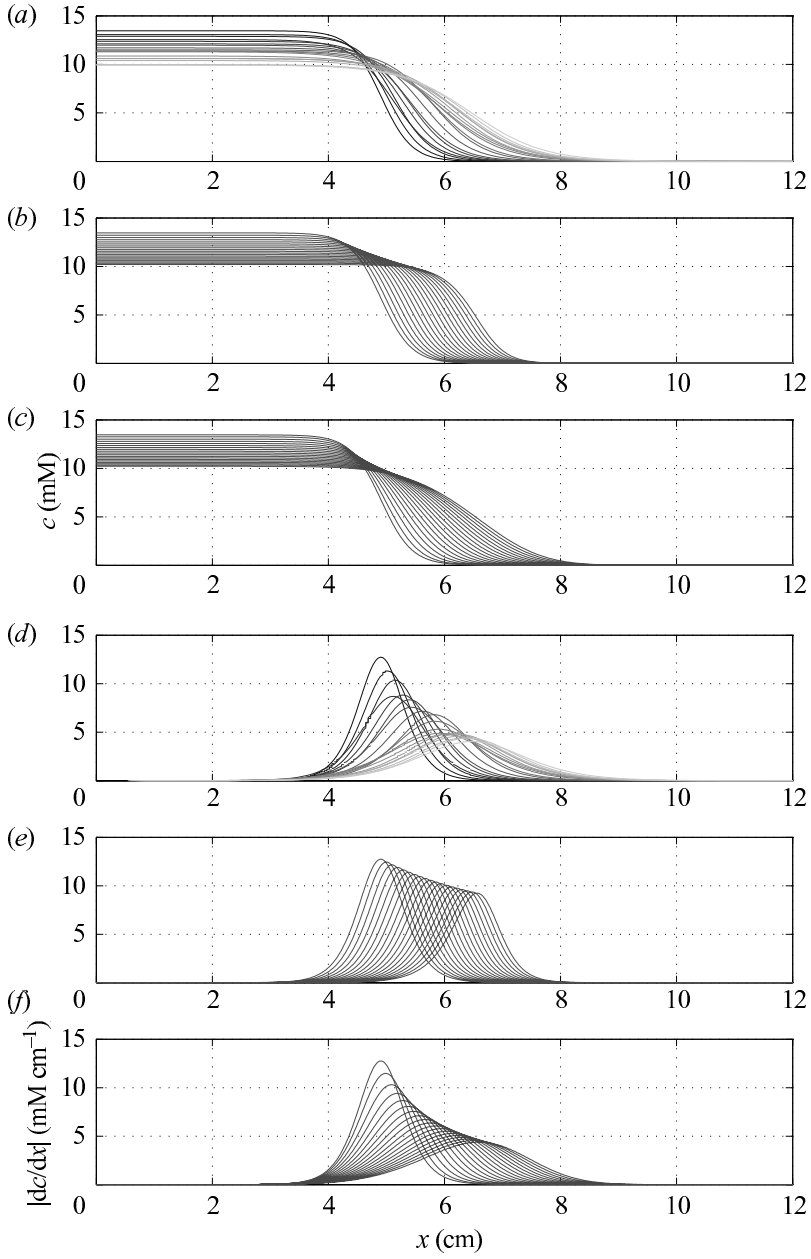

FIGURE 13. Results from set-up II showing the experimental data (a,d) and the numerical model for $M=D=0$ (b,e) and for $M=10^{-9}$, $D=6.9\times10^{-11}$ m^2 s^{-1} (c, f).

enclosed by semi-permeable membranes surrounded by pure water. The flows are initiated by a large concentration in one end of the tube and we study the approach to equilibrium, where the sugar is distributed evenly within the tube. Experimentally, we have used two configurations: the first is an updated version of the set-up of Eschrich *et al.* where the flow takes place in a dialysis tube and the sugar is followed by introducing a dye. The advantage is the relatively rapid motion, due to the large surface area. The disadvantage is that the sugar concentration cannot be inferred accurately by this method and for this reason we have introduced our second set-up, where the sugar concentration can be followed directly by refraction measurements.

On the theoretical side, we first re-derive the governing flow equations and introduce the dimensionless Münch number M. We then show that analytical solutions can be obtained in the two important limits of very large and very small M. In the general case we show how numerical methods based on Green's functions are very effective.

Finally, we compare theory and experiment with very good agreement. In particular the results or the velocity of the front (as proposed by Eschrich *et al.*) can be verified rather accurately.

Concerning the application to sap flow, the quantitative study we performed leads to the following conclusions: for a large tree it seems improbable that sugar transport, e.g. from leaf to root by this sole passive mechanism would be sufficiently efficient. In this case active transport processes might play an important role. On the other hand, transport over short distances, e.g. locally in leaves or from a leaf to a nearby shoot might be more convincingly described by the pressure-flow hypothesis.

It is a pleasure to thank Francois Charru, Marie-Alice Goudeau-Boudeville, Herv Cochard, Pierre Cruiziat, Alexander Schulz, N. Michele Holbrook and Vakhtang Putkaradze for many useful discussions. Much appreciated technical assistance was provided by Erik Hansen. This work was supported by the Danish National Research Foundation, Grant No. 74.

Appendix A. Materials: sugar and membrane

A.1. *Sugar*

The sugar used was a dextran (Sigma-Aldrich, St Louis, MO, USA, type D4624) with an average molecular weight of 17.5 kDa. The dye used was a red fruit dye (Flachsmann Scandinavia, Rød Frugtfarve, type 123000) consisting of an aqueous mixture of the food additives E-124 and E-131 with molecular weights of 539 Da and 1159 Da, respectively (PubChem-Database 2007). Even though the molecular weights are below the MWCO of the membrane, the red dye was not observed to leak through the membrane. This, however, was observed when using another type of dye, Methylene blue, which has a molecular weight of 320 Da.

A.2. *Membrane*

The membrane used in both set-ups was a semi-permeable dialysis membrane tube (Spectra/Por Biotech cellulose ester dialysis membrane) with a radius of 5 mm, a thickness of 60 μm and a MWCO (molecular weight cut off) of 3.5 kDa. The permeability L_p was determined by applying a pressure and measuring the flow rate across the membrane

$$L_p = (1.8 \pm 0.2) \times 10^{-12}\,\mathrm{m\ (Pa\,s)^{-1}}. \tag{A 1}$$

A.3. *Osmotic strength of dextran*

Figure 14(left) shows the relation between dextran concentration and osmotic pressure found from the experiments shown in figure 3. A linear fit gives

$$\Pi = (0.1 \pm 0.01\ \mathrm{bar\ mM^{-1}})c \tag{A 2}$$

where Π has unit bar, and c is measured in mM. This is in good agreement with values given by Jonsson (1986).

Appendix B. Numerical methods for non-zero M and $\bar{D}$

For non-zero values of M and $\bar{D}$, the equations of motion,

$$\frac{\partial^2 U}{\partial X^2} - MU = \frac{\partial C}{\partial X} \tag{B 1}$$

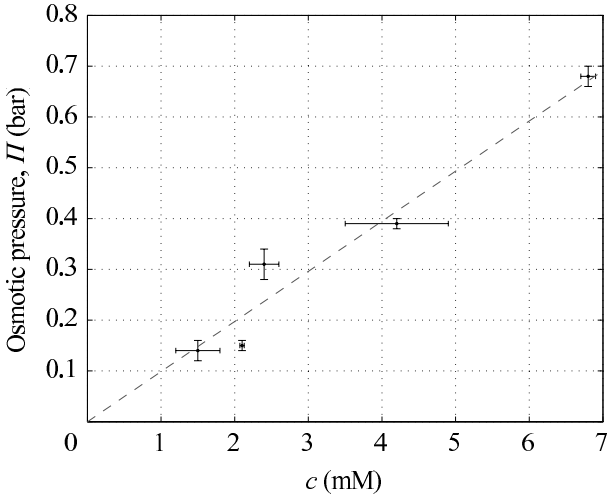

FIGURE 14. van't Hoff relation for 17.5 kDa dextran.

and

$$\frac{\partial C}{\partial \tau} + \frac{\partial CU}{\partial X} = \bar{D}\frac{\partial^2 C}{\partial X^2} \tag{B 2}$$

cannot be solved analytically. However, they can be written as a single integro-differential equation, which is straightforward to solve on a computer. If we choose a set of linear boundary conditions, $B_X[U] = a_i$, for (B 1), the solution can be written as

$$U = \int_0^1 G(X,\xi)\frac{\partial C}{\partial \xi}\mathrm{d}\xi + U_2. \tag{B 3}$$

Here, $G(X,\xi)$ is the Green's function for the differential operator $\partial^2/\partial X^2 - M$ with boundary conditions $B_X[U] = 0$ and U_2 fulfils the homogeneous version of (B 1) with $B_X[U] = a_i$. Plugging this into (B 2) yields

$$\frac{\partial C}{\partial \tau} + \frac{\partial}{\partial X}\left(C\left(\int_0^1 G(X,\xi)\frac{\partial C}{\partial \xi}\mathrm{d}\xi + U_2\right)\right) = \bar{D}\frac{\partial^2 C}{\partial X^2}. \tag{B 4}$$

For the closed tube, i.e. for the boundary conditions $U(0,\tau) = U(1,\tau) = 0$, $G(X,\xi)$ is given by

$$G(X,\xi) = \begin{cases} -\dfrac{\sinh(a(1-X))}{a\sinh a}\sinh a\xi & \text{for} \quad \xi < X, \\ -\dfrac{\sinh aX}{a\sinh a}\sinh(a(1-\xi)) & \text{for} \quad \xi > X, \end{cases} \tag{B 5}$$

and $U_2 = 0$. To increase numerical accuracy, it is convenient to transform (B 4) by defining

$$\frac{\partial f}{\partial X} = C - \bar{C} \tag{B 6}$$

and choosing $f(0) = f(1) = 0$ such that $f(X) = \int_0^X (C - \bar{C})\mathrm{d}\xi$. Inserting in (B 4), we get

$$\frac{\partial f}{\partial t} = \bar{D}\frac{\partial^2 f}{\partial X^2} - \left(f(X) - \int_0^1 \frac{\partial K(X,\xi)}{\partial \xi} f(\xi)\mathrm{d}\xi\right)\left(\frac{\partial f}{\partial X} + \bar{C}\right), \tag{B 7}$$

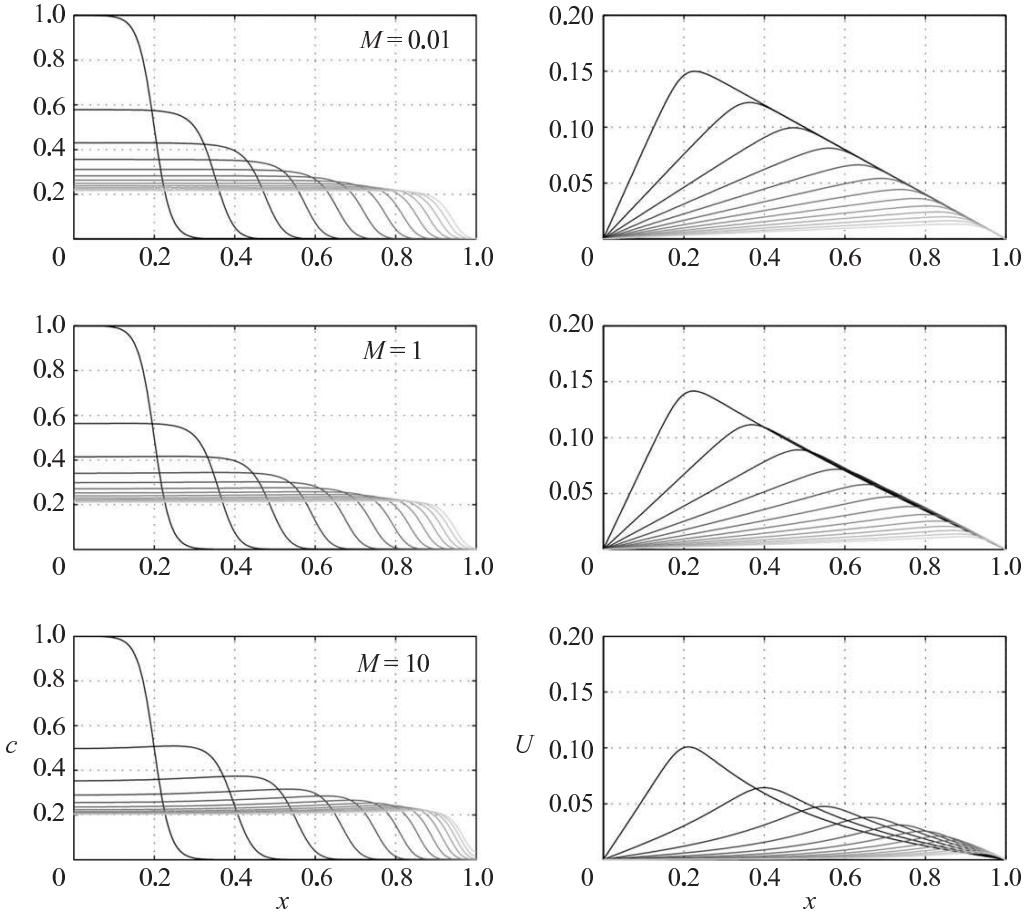

FIGURE 15. Results of numerical simulation of (B 4) using the boundary conditions $U(0,\tau)=U(1,\tau)=0$ for different values of M. $\bar{D}$ is kept constant at 10^{-5}. The initial condition was $C(X,0)=1-1/(1+\exp(-(X-\lambda)/\epsilon))$ where $\lambda=0.2$ and $\epsilon=2\times10^{2}$.

where

$$\frac{\partial K(X,\xi)}{\partial \xi}=\begin{cases}-a\dfrac{\sinh(a(1-X))}{\sinh a}\sinh a\xi & \text{for} \quad \xi < X,\\ -a\dfrac{\sinh aX}{\sinh a}\sinh(a(1-\xi)) & \text{for} \quad \xi > X.\end{cases} \tag{B 8}$$

To solve (B 7) we used MATLAB's built-in time solver `ode23t` which is based on an explicit Runge–Kutta formula along with standard second-order schemes for the first- and second-order derivatives. For the spatial integration, the trapezoidal rule was used (Press 2001). Results of a numerical simulation for different values of M are shown in figure 15.

REFERENCES

BARENBLATT, G. I. 1996 *Scaling, Self-Similarity, and Intermediate Asymptotics*. Cambridge University Press.

ESCHRICH, W., EVERT, R. F. & YOUNG, J. H. 1972 Solution flow in tubular semipermeable membranes. *Planta(Berl.)* **107**, 279–300.

FRISCH, H. L. 1976 Osmotically driven flow in narrow channels. *Trans. Soc. Rheol.* **20**, 23–27.

GURBATOV, S. N. MALAKHOV, A. N. & SAICHEV, A. I. 1991 *Nonlinear Random Waves and Turbulence in Nondispersive Media: Waves, Rays, Particles*. Manchester University Press.

HENTON, S. M. 2002 Revisiting the Münch pressure-flow hypothesis for long-distance transport of carbohydrates: modelling the dynamics of solute transport inside a semipermeable tube. *J. Exp. Bot.* **53**, 1411–1419.

JONSSON, G. 1986 Transport phenomena in ultrafiltration: membrane selectivity and boundary layer phenomena. *J. Pure Appl. Chem.* **58**, 1647–1656.

JENSEN, K. H. 2007 Osmotically driven flows and their relation to sugar transport in plants. MSc Thesis, The Niels Bohr Institute, University of Copenhagen.

KNOBLAUCH, M. & VAN BEL, A. J. E. 1998 Sieve tubes in action. *The Plant Cell* **10**, 35–50.

LANDAU, L. D. & LIFSHITZ, E. M. 1980 *Statistical Physics*. Pergamon Press.

MÜNCH, E. 1930 *Die Stoffbewegung in der Pflanze*. Verlag von Gustav Fisher.

NIKLAS, K. J. 1992 *Plant Biomechanics – An Engineering Approach to Plant Form and Function*. The University of Chicago Press.

NOBEL, P. S. 1999 *Physicochemical & Environmental Plant Physiology*. Academic Press.

PEDLEY, T. J. 1983 Calculation of unstirred layer thickness in membrane transport experiments: a survey. *Quart. Rev. Biophys.* **16**, 115–150.

PRESS, W. H. 2001 *Numerical Recipes in Fortran 77*, Vol. 1 Cambridge University Press.

PUBCHEM–DATABASE 2007 http://pubchem.ncbi.nlm.nih.gov/ *National Library of Medicine*

SCHULTZ, S. G. 1980 *Basic Principles of Membrane Transport*. Cambridge University Press.

TAIZ, L. & ZEIGER, E. 2002 *Plant Physiology*. Sinauer Associates.

THOMPSON, M. V. & HOLBROOK, N. M. 2003*a*, Application of a single-solute non-steady-state phloem model to the study of long-distance assimilate transport. *J. Theor. Biol.* **220**, 419–455.

THOMPSON, M. V. & HOLBROOK, N. M. 2003*b*, Scaling phloem transport: water potential equilibrium and osmoregulatory flow. *Plant, Cell Environ.* **26**, 1561–1577.

WEIR, G. J. 1981 Analysis of Münch theory. *Math. Biosci.* **56**, 141–152.

Appendix F

Paper published in the Journal of the Royal Society Interface (2011)

Downloaded from rsif.royalsocietypublishing.org on January 23, 2011

JOURNAL OF THE ROYAL SOCIETY Interface

FirstCite® e-publishing

J. R. Soc. Interface
doi:10.1098/rsif.2010.0578
Published online

Optimality of the Münch mechanism for translocation of sugars in plants

K. H. Jensen[1,†], J. Lee[2,†], T. Bohr[3], H. Bruus[1], N. M. Holbrook[4,*] and M. A. Zwieniecki[5]

[1]*Centre for Fluid Dynamics, Department of Micro- and Nanotechnology, Technical University of Denmark, DTU Nanotech Building 345 East, 2800 Kongens Lyngby, Denmark*
[2]*Division of Engineering, Brown University, Providence, RI 02912, USA*
[3]*Centre for Fluid Dynamics, Department of Physics, Technical University of Denmark, DTU Physics Building 309, 2800 Kongens Lyngby, Denmark*
[4]*Department of Organismic and Evolutionary Biology, and* [5]*Arnold Arboretum, Harvard University, Cambridge, MA 02138, USA*

Plants require effective vascular systems for the transport of water and dissolved molecules between distal regions. Their survival depends on the ability to transport sugars from the leaves where they are produced to sites of active growth; a flow driven, according to the Münch hypothesis, by osmotic gradients generated by differences in sugar concentration. The length scales over which sugars are produced (L_{leaf}) and over which they are transported (L_{stem}), as well as the radius r of the cylindrical phloem cells through which the transport takes place, vary among species over several orders of magnitude; a major unsettled question is whether the Münch transport mechanism is effective over this wide range of sizes. Optimization of translocation speed predicts a scaling relation between radius r and the characteristic lengths as $r \sim (L_{\mathrm{leaf}}\, L_{\mathrm{stem}})^{1/3}$. Direct measurements using novel *in vivo* techniques and biomimicking microfluidic devices support this scaling relation and provide the first quantitative support for a unified mechanism of sugar translocation in plants spanning several orders of magnitude in size. The existence of a general scaling law for phloem dimensions provides a new framework for investigating the physical principles governing the morphological diversity of plants.

Keywords: phloem transport; sugar translocation; microfluidics; biomimetics; osmotic pumping

1. INTRODUCTION

Vasculatures of plants and animals are among the most elegant and complex of microfluidic systems. In plants, xylem transports water from soil to leaves, while phloem distributes the products of photosynthesis throughout the plant. Flow generation in both systems occurs in the absence of any mechanical pump. Xylem flow is generated by evaporation and driven by tension gradient in the vessels [1]. The physics of transport under tension creates a safety–efficiency optimization problem that constrains the design of xylem vessels [2]. The mechanism driving phloem transport is believed to be the movement of water via osmosis in response to the loading and unloading of sugar in different parts of the plant and sustained along the tubes by continuous maintenance of the osmotic gradient across the perimeter of the phloem tube, as shown in figure 1 [3,4]. Phloem operates under positive pressure and the assumed mode of its generation results in the delivery of sugars being controlled by their loading and unloading rates [5,6], rather than by the velocity of the flow. However, phloem distributes hormonal and signalling molecules that allow for the integration of distal parts in lieu of a designated nervous system [7,8]. This additional signalling task could result in the selection pressure to optimize translocation velocity by providing plants with the ability to respond rapidly to environmental perturbations [9]. Here we ask if phloem is indeed optimized for speed. Further, we investigate if a single scaling law can describe the design principles of phloem tubes governing the speed of translocation given the wide range of length scales existing in nature. Phloem tube radii range from 1 to 40 μm, their length from 0.01 to 100 m, with transport velocities from 0.01 to 1 m h^{-1} [10–12].

Studies of long-distance transport in plants are inherently difficult because the fluxes are intracellular, protected by physical barriers [13] or biological activity (e.g. forisomes and p-proteins [14,15]), and occur under large tensions or pressures [16]. In principle, these properties require *in vivo* approaches, which are prone to methodological challenges. However, recent biomimetic approaches have helped answer long-standing questions regarding water transport in the xylem [17] and to resolve optimization laws governing the placement of

*Author for correspondence (holbrook@oeb.harvard.edu).
†These authors contributed equally to the study.

Received 20 October 2010
Accepted 21 December 2010

This journal is © 2011 The Royal Society

Downloaded from rsif.royalsocietypublishing.org on January 23, 2011

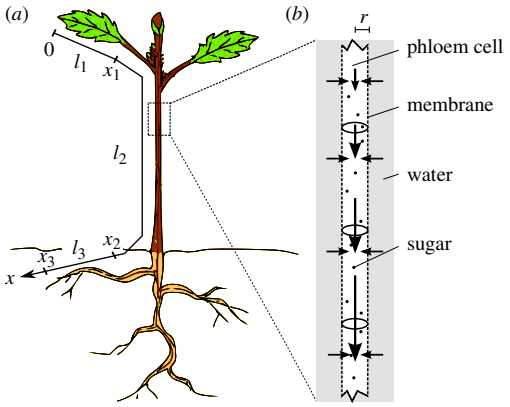

Figure 1. (*a*) Schematic of a plant in which sugar and signalling molecules travel from sources, e.g. leaves, to places of storage and growth, e.g. fruits or roots. In our model, the plant is divided into three zones, a source/loading zone of length l_1 (the leaf; $0 < x < x_1$), a translocation zone of length l_2 (the stem; $x_1 < x < x_2$) and a sink/unloading zone of length l_3 (the root; $x_2 < x < x_3$). (*b*) Diagram of how the Münch flow mechanism is thought to drive sugar translocation in plants. The surfaces of the cylindrical phloem cells of radius r are covered by a semi-permeable membrane. Sugar loaded actively into the cells at the sugar source draws water by osmosis from the surrounding tissue, thereby generating flow as the sugar solution is displaced downstream. (Online version in colour.)

veins within leaves [18], both processes being part of the transpiration stream [1]. Progress in the fabrication of microfluidic devices has made it possible to mimic phloem transport [19], providing a physical model to test Münch theory [20]. Here, we use synthetic phloem to resolve design properties underlying the delivery of photoassimilate and chemical signals between distal plant parts and to provide a mechanistic basis for the implementation of our mathematical model of phloem function.

Many of the published models of phloem transport incorporate details of sugar loading and unloading (e.g. [21–24]). In contrast, our goal was to study a simplified model, which agrees with the general trends previously reported, but which due to its simplicity lends itself to a scaling analysis. To determine if real plants follow the scaling relation predicted by our mathematical model, we examined phloem dimensions and transport velocities in real plants using a novel, non-invasive, dye-tracing method that offers a significant improvement to the previously used techniques such as traditional dye tracing [25], biomass accumulation [26] or tracing radioactive carbon [27], while accommodating a broader range of plant materials than magnetic resonance imaging [12]. We also compared published data on sieve tube radii with the optimal radii calculated from our model.

2. MATERIAL AND METHODS

To study osmotically driven flows in microchannels, we designed and fabricated a microfluidic system consisting of two layers of 1.5 mm thick polymethyl methacrylate (PMMA) separated by a semi-permeable membrane (Spectra/Por Biotech cellulose ester dialysis membrane, MWCO 3.5 kDa, thickness 40 μm), as shown in figure 2*a*. Channels of length 27 mm, width 200 μm and depth $h = 100–200$ μm were milled in the two PMMA layers using a MiniMill/Pro3 milling machine [19]. The top channel contains partly the sugar solution and partly pure water, while the bottom channel always contains only pure water. Inlets were produced by drilling 800 μm diameter holes through the wafer and inserting brass tubes into these. By removing the surrounding material, the channel walls in both the top and bottom layers acquired a height of 100 μm and a width of 150 μm. After assembly, the two PMMA layers were positioned such that the main channels in either layer were facing each other. Thus, when clamping the two layers together using four 10 mm paper clamps, the membrane acted as a seal, stopping any undesired leaks from the channels as long as the applied pressure did not exceed approximately 100 kPa.

The top channel was connected at one end to a syringe pump (NE-1000, New Era syringe pump, NY), which continuously injected a solution of water, dextran (17.5 kDa, Sigma-Aldrich) 1 μm polystyrene beads (Sigma-Aldrich, L9650-1ML, density 1050 kg m^{-3}) into the channel at flow velocities of 2–4 μm s^{-1}. At the other end, the channel was left open with the outlet terminating in an open reservoir. Both ends of the lower 'pure water' channel were connected to this reservoir to minimize the hydrostatic pressure difference across the membrane and to prevent axial flow in this channel. The flow velocity inside the upper channel was recorded by tracking the motion of the beads. Image sequences were recorded at different positions along the channel using a Unibrain Fire-i400 1394 digital camera attached to a Nikon Diaphot microscope with the focal plane at $h/2$ and a focal depth of approximately 10 μm. The flow behaved as if it were pressure-driven and the standard laminar flow profile was used to determine the average flow velocity [19].

To determine rates of phloem transport *in vivo*, an aqueous solution (100 mg l^{-1}) of 5(6)-carboxyfluorescein diacetate was placed onto gently abraded upper leaf epidermis from where it was loaded into the phloem by the plant (figure 2*b*) [28,29]. We tracked the dye, as it moved in the phloem of petioles or stems, by photobleaching flow velocity techniques that were previously used in microfluidic systems [30,31]. However, these single-detector techniques required modification to accommodate measurements on living plant tissues (low velocities, tissue light scattering and absorption, the need to maintain favourable growth conditions). We used two solid-state, high-gain photodiodes (SED033 used with IL1700 Research Radiometer, International Light Technologies) separated by a known distance to determine travel time of the photobleached pulse. The photodiodes were connected to the stem/petiole via bifurcated, 4 mm diameter optical fibres to obtain a sufficient signal-to-noise ratio despite extremely low light intensities. Excitation light was delivered via 490 nm short-pass filters (Omega Optical, USA), while photodiodes were fitted with 510 nm long-pass filters (Omega Optical). Excitation light was generated by narrow

Downloaded from rsif.royalsocietypublishing.org on January 23, 2011

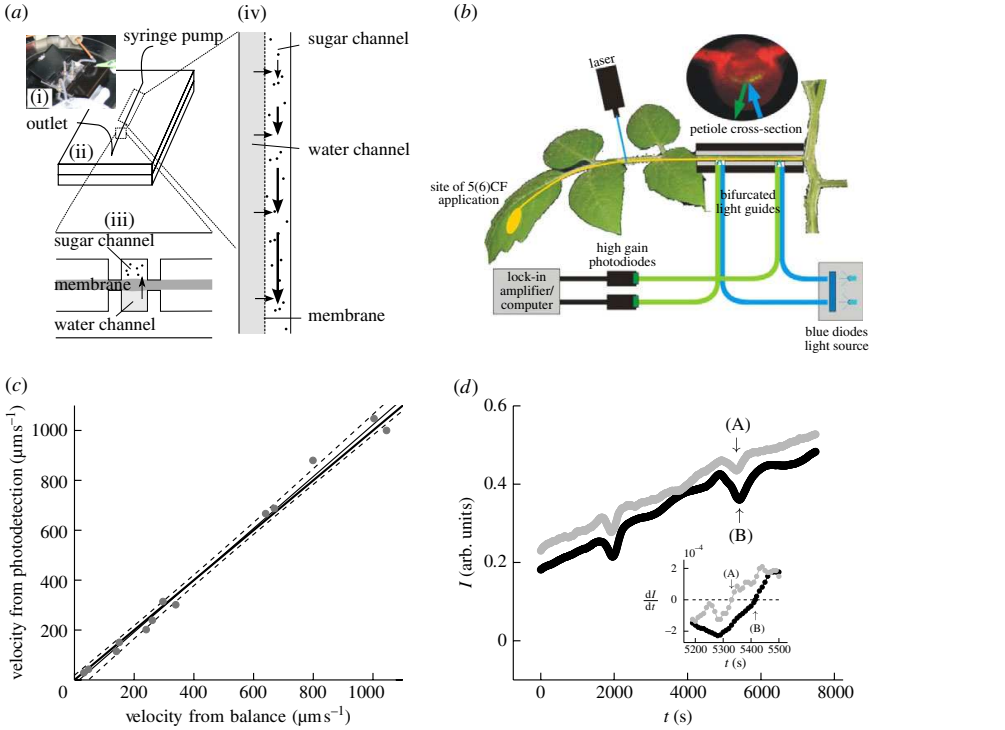

Figure 2. (*a*) Microfluidic set-up. (i) Picture of the microfluidic device used to biomimic the phloem transport system. (ii,iii) Schematic of the microfluidic device. Two microchannels are in osmotic contact through a semi-permeable membrane. One, the bottom channel, remains filled with pure water while the other contains a sugar solution injected slowly at one end by a syringe pump. (iv) Close-up showing the flow mechanism driving sugar translocation in the microfluidic system. (*b*) Sketch of the set-up used to determine phloem flow rate in tomato petioles. (*c*) Comparison of flow velocities in a 1.19 mm diameter glass capillary determined by our photobleaching technique and by a standard mass flow-rate technique (filled circles, measurements; thin line, regression; dashed line, 95% confidence interval; thick line, one to one relation). (*d*) Two consecutive measurements of the relative intensity I of the fluorescence versus time t detected by the two photodiodes shown in (*b*). The flow velocity u is determined by measuring the traversal time between the two diodes, marked by arrows (A,B), of a minimum in I induced by photobleaching of the dye using a short (less than 30 s) laser pulse. The inset shows $\partial I/\partial t$ versus time; the intensity minima (indicated by arrows (A,B)) are given by $\partial I/\partial t = 0$ (black circles, sensor 1; grey circles, sensor 2). (Online version in colour.)

band blue diodes (470 nm, Roithner LaserTechnik GmbH, Switzerland). Fibres were attached to the plant through custom-made, light-tight clips. A bleached pulse was produced ahead of the detection system by a 20 mW laser of wavelength 473 nm (Dragon Laser, China) as sketched in figure 2*b*. All filters and laser parameters were chosen to accommodate properties of the 5(6)-carboxyfluorescein diacetate dye.

The set-up was tested by comparing flow velocity determined by photodetection with values $u = Q/(2\pi r^2)$ obtained from volume flow rate Q as measured by a microbalance (Sartorius 210DX ± 0.01 mg) and the radius r of the capillary tube (figure 2*c*). We generated velocities from 20 to 1000 $\mu m\,s^{-1}$, similar to the measured *in vivo* phloem velocities. The signal output is Gaussian-shaped, figure 2*d*, due to the convolution of the 4 mm wide detection window (set by the optical fibre diameter) and the internal dispersion-widened bleaching pulse combined with light scattering in the plant tissues. Thus, the flow velocity u was determined by measuring the traversal time between the two diodes of a minimum intensity of fluorescence following the photobleaching of the dye using a 30 s laser pulse. The same procedure was used on the plants (figure 2*d*). We note that the technique is independent of dye loading rate and tissue light properties.

3. RESULTS

In plants, phloem transport initiates in the leaves, where sugar is actively loaded into sieve tubes, and ends in growth or storage zones, where sugar is unloaded. We may think of the plant aligned with x-axis as being divided into three zones: (i) a loading zone $(0 < x < x_1)$ of length $l_1 = x_1$ (essentially the length of the leaf); (ii) a translocation zone $(x_1 < x < x_2)$ of length $l_2 = x_2 - x_1$ (essentially the length the plant, typically much larger than l_1); and (iii) an unloading zone $(x_2 < x < x_3)$ of length $l_3 = x_3 - x_2$, where the sugar is consumed (figure 1; table 1). The flow rate through a phloem tube depends on the osmotic driving force, the radius r of the tube, its length l_2 and the effective viscosity η of the fluid including the effect of sieve plates [6,32]. The most important characteristic of this relation is that, fixing all other parameters,

Downloaded from rsif.royalsocietypublishing.org on January 23, 2011

Table 1. Nomenclature.

parameter	symbol	value and/or unit
length	x	m
viscosity	η	Pa s
membrane permeability	L_p	$\mathrm{m\,s^{-1}\,Pa^{-1}}$
length of leaf	l_1, L_leaf	m
length of stem	l_2, L_stem	m
length of root	l_3	m
radius of phloem tube	r	m
optimal radius	r_c	m
water flow through tube wall	J	$\mathrm{m\,s^{-1}}$
pressure	p	Pa
osmotic flow velocity scale	U	$\mathrm{m\,s^{-1}}$
Münch number	$M\ddot{u}$	dimensionless
leaf to stem length ratio	α	dimensionless
dimensionless sugar concentration gradient in root	β	dimensionless
volume flux	Q	$\mathrm{m^3\,s^{-1}}$
gas constant	R	$\mathrm{m^3\,Pa\,K^{-1}\,mol^{-1}}$
temperature	T	K
wall resistance	R_w	$\mathrm{Pa\,m^{-3}\,s}$
tube resistance	R_t	$\mathrm{Pa\,m^{-3}\,s}$
velocity	u	$\mathrm{m\,s^{-1}}$
dimensionless velocity	v	dimensionless
dimensionless length	ξ	dimensionless
dimensionless concentration	ς	dimensionless
height of channel	h	m
intensity of fluorescence	I	arb. units
time	t	s

it is non-monotonic in r giving maximal flow rate at a particular value denoted r_c. This is easily understood since the behaviour for large and small r is strongly dependent on the ratio of the resistance of the flow in the channel to the resistance (or the inverse of the permeability L_p) across the semi-permeable membrane, a non-dimensional quantity we call the Münch number $M\ddot{u}$ [33],

$$M\ddot{u} = 16\frac{\eta L_\mathrm{p} l_2^2}{r^3}. \tag{3.1}$$

For wide tubes ($M\ddot{u} \ll 1$) there is essentially no viscous pressure gradient along the tube, but the efficacy of the osmotic pump is small. On the other hand, for narrow tubes ($M\ddot{u} \gg 1$), where the osmotic driving force is strong, the viscous pressure gradient in the tube becomes important and the flow is impeded.

The water flow J across the membrane of the tube at position x is determined by the local difference $c(x)$ in sugar concentration and in pressure $p(x)$ across the membrane. In a tube at temperature T,

$$J(x) = L_\mathrm{p}[RTc(x) - p(x)] \tag{3.2a}$$

and together with conservation of fluid volume, this leads to the Münch equation for the gradient of the velocity $u(x)$ in the translocation zone

$$\frac{\partial u}{\partial x} = \frac{2L_\mathrm{p}}{r}\,(RTc - p), \quad \text{for } x_1 < x < x_2. \tag{3.2b}$$

Here, we assume ideality of the sugar solution, a semi-permeable membrane with unity reflection coefficient, and slow flow velocities relative to transverse diffusion such that radial gradients are weak. Also, we are assuming that the external pressure and concentration do not vary—aside from hydrostatic pressure differences owing to height variations. This is clearly a strong simplification since of course the phloem flow is not independent of the state of the xylem. However, all of our phloem flow measurements were conducted under low-light thus minimizing transpiration-induced gradients in xylem pressure [12]. The neglect of external variations in the sugar concentration is partly due to the way our model is formulated, since the strong variations in concentrations between leaf and root are modelled as *internal* variations in the tube.

The pressure gradient for such slow flows is given by the Hagen–Poiseuille–Darcy relation

$$\frac{\partial p}{\partial x} = -\left(\frac{8\eta}{r^2}\right)u \tag{3.2c}$$

valid even taking into account the radial, osmotic inflow [34,35]. We verified (figure 3*a*) the description (3.2*a*)–(3.2*c*) of osmotic transport by comparing measurements of osmotically driven flows through microfluidic channels (described in detail in [19]) with analytical solutions of the flow problem in the limit $M\ddot{u} \ll 1$ (see appendix A), under the boundary conditions of a fixed concentration and velocity at x_1 and a fixed pressure ($p = 0$) at x_2, boundary conditions used in previous experimental studies [36,37]. Fabrication of devices working in the limit $M\ddot{u} \gg 1$ is difficult owing to the properties of currently available artificial membranes, channel lengths and bonding burst pressures, and we have not been able to realize this limit.

To examine how velocity scales with the full range of radial and axial phloem dimensions found in plants we formulated a simple model (see appendix A for further details), which gives a complete overview of the concentration and velocity profiles as a function of $M\ddot{u}$ and the relative size of the loading, translocation and unloading zones. In this analysis, the loading zone is characterized by a constant sugar concentration $c(x) = c_0$, i.e. $\partial c/\partial x = 0$, such that equation (3.2) becomes

$$\frac{\partial^2 u}{\partial x^2} = -\frac{2L_\mathrm{p}}{r}\frac{\partial p}{\partial x} = \frac{16\eta L_\mathrm{p}}{r^3}u(x), \quad \text{for } 0 < x < x_1, \tag{3.3}$$

with the boundary condition $u(0) = 0$, i.e. a vanishing velocity at the beginning of the loading zone. Here, we have taken the derivative of both sides of equation (3.2*b*) in order to eliminate the pressure gradient using equation (3.2*c*). In the translocation zone, the flux $c(x)u(x)$ of sugar is conserved and equal to $c_0u(x_1)$, where c_0 is the loading concentration and $u(x_1)$ is the velocity at the entrance of the translocation zone. This leads to an equation of the form

$$\frac{\partial^2 u}{\partial x^2} = -\frac{2L_\mathrm{p}RTc_0}{r}\frac{u(x_1)}{u^2}\frac{\partial u}{\partial x} + \frac{16\eta L_\mathrm{p}}{r^3}u(x), \quad \text{for } x_1 < x < x_2. \tag{3.4}$$

Downloaded from rsif.royalsocietypublishing.org on January 23, 2011

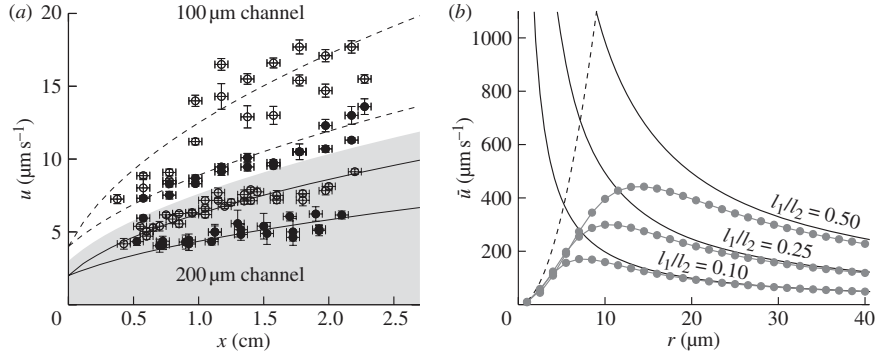

Figure 3. (*a*) Flow velocity $u(x)$ measured in 100 µm (white region) and 200 µm (grey region) deep and 200 µm wide microchannels. The dashed and solid lines are fits to equation (A 4). The sugar concentrations used are 21 mM (open circles) and 13 mM (filled circles). The horizontal error bars indicate the resolution of the microscope stage, while the vertical error bars were obtained via least squares error propagation from the velocity profile. (*b*) Numerically computed mean velocity $\bar{u}$ (dots connected by lines) as a function of radius r assuming $L_p = 5 \times 10^{-14}$ m (Pa s)$^{-1}$, $l_1 = (0.1, 0.25, 0.50)$ m, $l_2 = 1$ m, $RTc_0 = 0.54$ MPa, and $\eta = 5 \times 10^{-3}$ Pa s. The solid and dashed lines show the scaling laws for u predicted by equations (3.6) and (3.7), respectively. These clearly show that $\bar{u}$ grows as r^2 for small r while it decays as $1/r$ for large r. At the intersection between the two lines given by equation (3.8) the transition between the two types of flow occurs and the velocity is at a maximum (filled circles with solid lines, numerics; solid lines, $M\ddot{u} \ll 1$; dashed lines, $M\ddot{u} \gg 1$).

The unloading zone is characterized by a linear decrease in the sugar concentration for $x_2 < x < x_3$, such that both the sugar concentration and the velocity vanish at the end of the tube, $c(x_3) = 0$ and $u(x_3) = 0$. This introduces a coefficient $\beta \equiv (l_2/c_0)(\partial c/\partial x)$, which can be determined only when we know the concentration $c(x_2)$ at the entry of the unloading zone. It can also be expressed in terms of the velocities at the entry of the translocation and unloading zones (equations (A 8*a*) and (A 8*b*)). In the unloading zone, equation (3.2) for u thus becomes

$$\frac{\partial^2 u}{\partial x^2} = -\frac{2L_p RTc_0}{rl_2}\beta + \frac{16\eta L_p}{r^3}u(x), \quad \text{for } x_2 < x < x_3. \tag{3.5a}$$

Our analysis of these equations is carried out in appendix A. An important simplification can be acheived by non-dimensionalization, introducing a non-dimensional length ξ (scaled by the length l_2 of the plant) and a non-dimensional velocity v scaled by the naive osmotic velocity $U = (2l_2/r)L_p RTc_0$ and a non-dimensional concentration ς scaled by c_0. This gives

$$\partial_\xi^2 v = \partial_\xi \varsigma + M\ddot{u}v, \tag{3.5b}$$

where the dimensionless Münch number $M\ddot{u}$ is given by equation (3.1).

This analysis gives us a complete overview of the concentration and velocity profiles as a function of $M\ddot{u}$. Of special interest is the mean velocity $\bar{u}_2$ in the translocation zone, which sets the transit time from one end of the plant to the other. In the limit of very wide tubes, the bulk of the resistance lies in the transport of water across the membrane in the loading and unloading zone with a resistance $R_w = (2\pi r l_1 L_p)^{-1}$. Writing the volume flux $Q = \bar{u}\pi r^2$ as $Q = \Delta p/R_w$, with $\Delta p = RTc_0$, we find that the average flow velocity is $\bar{u} \approx RTc_0 L_p l_1/r$. A more thorough analysis of the problem, assuming for simplicity that $l_3 = l_1$, shows that

$$\bar{u} = \left(\sqrt{3} - 1\right)\frac{RTc_0 L_p}{r} l_1, \quad \text{for } M\ddot{u} \ll 1. \tag{3.6}$$

See appendix A for the full derivation, including a discussion of the case $l_3 \neq l_1$. In the opposite limit of very narrow tubes ($M\ddot{u} \gg 1$), we can argue in the following way: water moving in the system faces three barriers. First, it must pass across the membrane in the loading zone. Then, it has to move along the length of the tube before finally escaping the tube across the membrane in the unloading zone. The first and last of these three resistances are proportional to $1/r$, while the middle part scales as $1/r^4$. Thus, for very small r, the resistance in the tube $R_t = 8\eta l_2(\pi r^4)^{-1}$ will dominate, giving $Q = RTc_0\pi r^4/(8\eta l_2)$, and we find an average flow velocity

$$\bar{u} = \frac{RTc_0}{8\eta l_2} r^2, \quad \text{for } M\ddot{u} \gg 1. \tag{3.7}$$

Figure 3*b* shows the numerical simulations on the full system of equations with the two expressions (3.6) and (3.7) shown as dashed and full lines, respectively. The radius (r_c) yielding the maximum velocity can be estimated as the intersection of these two curves, giving $M\ddot{u} \propto l_2/l_1$ or

$$r_c = \left[8\left(\sqrt{3} - 1\right)\eta L_p\right]^{1/3} l_1^{1/3} l_2^{1/3}. \tag{3.8}$$

Under the assumption that swift translocation of the phloem provides a competitive edge, it would thus be desirable for plants to have sieve tube radii close to the value r_c predicted by equation (3.8).

To explore the design constraints facing the long-distance transport in phloem, and to determine if real plants follow the scaling relation described by equation

Downloaded from rsif.royalsocietypublishing.org on January 23, 2011

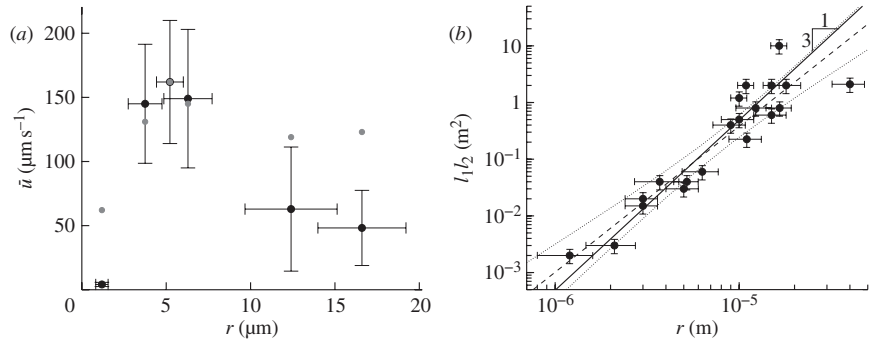

Figure 4. (*a*) *In vivo* determined phloem flow rates (black dots) in petioles (one stem) of six species plotted as a function of phloem radius as later determined on the same plant material. The velocities vary as much as 2.5 orders of magnitude, from 3 $\mu m\,s^{-1}$ (0.01 $m\,h^{-1}$) in *T. virginiana* to 150 $\mu m\,s^{-1}$ (0.6 $m\,h^{-1}$) in *Solanum lycopersicum*. The model predictions (grey dots) calculated from equations (3.5)–(3.7) agree well with the observed data. The error bars indicate the mean and standard errors of $N = 3$–8 measurements. (*b*) Log–log plot of $l_1 l_2$ versus measured radius r (black dots) for 20 plants of sizes ranging from $r =$ 1 μm (*T. virginiana*) to $r = 40$ μm (*Cucurbita pepo*) and $l_2 = 0.1$ m (*T. virginiana*) to $l_2 = 40$ m (*Robinia pseudoacacia*). The prediction of equation (3.8) (thick black line) with parameters $L_p = 5 \times 10^{-14}\,m\,(Pa\,s)^{-1}$ and $\eta = 5 \times 10^{-3}$ Pa s (kinematic viscosity $= 1.85 \times 10^{-3}$, sieve plate factor $= 2.7$) is plotted along with the best fit to the plant data (dashed line, slope 2.6 ± 0.3), showing that the scaling relationship predicted by equation (3.8) falls within the 95% confidence interval (dotted lines). The error bars indicate the standard error in the radius r and lengths l_1 and l_2. See table 2 for further details on the species used.

(3.8), we examined phloem dimensions and transport velocities in real plants in petioles or stems of six species using our novel, non-invasive, dye-tracing method. Results, figure 4*a*, show that phloem velocities vary as much as a factor of 50, from 3 $\mu m\,s^{-1}$ (0.01 $m\,h^{-1}$) in *Tradescantia virginiana* L. to 150 $\mu m\,s^{-1}$ (0.6 $m\,h^{-1}$) in *Solanum lycopersicum* L., values consistent with the range of velocities reported using other techniques [10,12]. Comparison of velocities measured in plants with the prediction of the proposed model, figure 4*a* and equation (A 22), shows that the model reproduces the observed velocities across a wide range of species thus validating the proposed assumptions. The agreement between *in vivo* measurements (figure 4*a*) and theory derived from the analysis of osmotic-driven flow in synthetic channels (figure 3*a*) suggests that phloem flow rates are controlled by the same physical principles in plants as in biomimicking devices—at least in the low *Mü* limit, to which our microfluidic devices are so far limited—despite the anatomical complexity present in the living systems [38].

The proposed scaling law allows for the calculation of a speed-optimized radius when both loading zone and translocation length are known. Thus, we compared published data on sieve tube radii with the optimal radii calculated from equation (3.8) using leaf size as the proxy for the loading and unloading zone (l_1) and plant length as the proxy for the translocation length (l_2). The plant selection consisted of a diverse range of species, encompassed 2.5 orders of magnitude in length, and included small rosettes, grasses, vines and trees. We found good agreement between measured radii and the scaling relationships of l_1 and l_2 predicted by equation (3.8), indicating the widespread optimization of phloem dimensions for rate of translocation, figure 4*b*. Further, we found that the scaling pre-factor in equation (3.8) agrees well with the predicted optimum radii using published values of the membrane permeability L_p and the effective viscosity η. The effects of the increased flow resistance owing to the flow through the sieve plates are taken into account by multiplying the viscosity $\eta = 1.85$ mPa s of a typical plant sugar solution [10] by a so-called sieve plate factor, which typically is between 2 and 5 [6,29], for which we have assumed the value 2.7 thus arriving at the effective viscosity of 5 mPa s used in our simulations.

4. DISCUSSION

Plants are reliant on efficient and robust distribution systems made of microchannels to transport water, energy and signals over distances that range from only a few centimetres to many tens of metres. Building on the basic physical laws for osmosis, we have developed a simple, generic model for osmotically driven flow in a phloem tube with semi-permeable membranes at the wall. A single scaling law based on optimization for this theoretical translocation speed predicts phloem dimensions relative to the lengths of the loading (leaf) and unloading (root) zones and the translocation distance (stem). The existence of this optimization underscores the role of the phloem as a major informational pathway for molecular signal transduction across the plant body. It also explains why a smaller plant with large leaves (e.g. *Cucurbita*) may have larger diameter sieve tubes than found in many trees.

We have shown that our simple model for phloem translocation in plants leads to an understanding of the dependence between the speed of phloem flow and the characteristic dimensions of the plant. The assumption that plants have evolved to optimize their phloem speed then led us to a scaling relation between radius r and the characteristic lengths as $r \approx (A L_{leaf} L_{stem})^{1/3}$, where the constant A (with dimensions of length) is proportional to ηL_p, the product of

Downloaded from rsif.royalsocietypublishing.org on January 23, 2011

the viscosity of the flow and the permeability of the membrane, a prediction which is supported by field-data from plants. It should be noted that the optimization over the radius is done while fixing the lengths L_{leaf} and L_{stem} of the plant. The corresponding optimal velocity can approximately be obtained by inserting $r = r_{\mathrm{c}}$, given by equation (3.8), into equation (3.6) or (3.7), giving

$$u_{\mathrm{opt}} = aRTc_0\, L_{\mathrm{p}}^{2/3}\eta^{-1/3}L_{\mathrm{leaf}}^{2/3}L_{\mathrm{stem}}^{-1/3},$$

where a is a numerical constant. Thus an increase of the leaf size (with fixed stem size) will lead to an increase in the velocity, while an increase of the stem size (with fixed leaf size) will lead to a decrease. We thus assume that these external length scales are set by other biological constraints such as the cost of building, supporting and maintaining photosynthetic surfaces.

The challenges faced by the phloem in moving photo-assimilates over long distances led to the suggestion that the axial pathway is compartmentalized into 'relays', such that solutes are actively reloaded at discrete points [39]. Relays increase the rate of phloem transport, but require additional inputs of energy. Although no empirical evidence exists for relays, their potential contribution to phloem transport has been widely considered [32,40]. Our analysis, which uses the length of the entire plant as proxy for l_2, is not consistent with the presence of relays, suggesting that axial compartmentalization is not a necessary design feature for efficient phloem transport.

Plants, which span tens of metres and proliferate in hundreds of cubic metres of soil and air, experience diverse and often rapid fluctuations in environmental conditions. To respond to such environmental heterogeneity requires the rapid distribution of both energy and information in the form of chemical signals to enhance plant productivity and competitiveness. The phloem provides uninterrupted coupling between most distal parts of all plants and links plants' multi-branched dendritic structure into a single functional microfluidic system [41]. Concordance between our theoretical model, studies of osmotically driven flow in synthetic phloem, and measurements of flow and geometric properties made on real plants gives confidence in the Münch theory of phloem flow and suggests that plants are optimized for rapid translocation of sugar, thereby gaining a competitive edge in terms of their ability to respond rapidly to environmental stimuli. Our analysis provides a general scaling law for phloem dimensions that maximizes translocation velocity, suggesting that evolutionary selection on the efficacy of signal transduction has shaped the structure and function of this supracellular transport pathway.

We thank Howard Stone and Matthew Thompson for comments on the manuscript. This work was supported by the Danish National Research Foundation (grant no. 74), the Andrew W. Mellon Foundation and the Materials Research Science and Engineering Centre at Harvard University.

APPENDIX A

Analysis of the Münch equation (3.2*b*) is facilitated by making it dimensionless using the following rescaling of length, velocity and concentration:

$$x = \xi l_2, \quad u = Uv = \left(\frac{2l_2}{r}L_{\mathrm{p}}RTc_0\right)v \quad \text{and} \quad c = \varsigma c_0, \tag{A 1}$$

whereby the non-dimensional Münch equation becomes

$$\partial_\xi^2 v = \partial_\xi \varsigma + M\ddot{u}v, \quad \text{for } 0 < \xi < \xi_3. \tag{A 2}$$

The three zones are the loading zone ($0 < \xi < \xi_1$) of length $\lambda_1 = \alpha = l_1/l_2$, the translocation zone ($\xi_1 < \xi < \xi_2$) of length $\lambda_2 = 1$, and the unloading zone ($\xi_2 < \xi < \xi_3$) of length $\lambda_3 = \alpha = l_1/l_2$.

The zero-end-pressure phloem transport model. In the literature (see [6] and references therein), the correct choice of boundary conditions remains unclear, primarily due to lack of knowledge of the exact physiological processes in the loading and unloading zones. This has led to a large class of models all based on equation (A 2), but with widely different boundary conditions. The method applied by most workers has been to either ignore the loading and unloading zones by setting simple conditions at the edges of the translocation zone or to use specific loading and unloading functions. A special case of these models examined by Hölttä *et al.* [40] is to set the pressure at the end of the translocation zone to a fixed value, say $p = 0$. In the microfluidic experiments, we have tested this limit experimentally, and we now consider the solution to equation (A 2) under these conditions.

In the microfluidic channel zone, here defined as $0 < \xi < 1$, equation (A 2) becomes

$$\frac{\partial^2 v}{\partial \xi^2} = -\frac{v_0}{v^2}\frac{\partial v}{\partial \xi} + M\ddot{u}v, \quad \text{for } 0 < \xi < 1, \tag{A 3a}$$

with the boundary conditions

$$v(0) = v_0 \tag{A 3b}$$

and

$$p(1) = 0. \tag{A 3c}$$

In the experiments $M\ddot{u}$ is very small, so combining $M\ddot{u} = 0$ with equation (A 3*b*) yields

$$v(\xi) = v_0^{1/2}(v_0 + 2\xi)^{1/2}, \tag{A 4}$$

in good agreement with the experimetal results (figure 3*a*).

The loading/unloading phloem transport model. We now return to the more general three-zone model of the phloem translocation pathway (figure 1). We assume that the loading and unloading zones are of equal size ($l_1 = l_3$), that the concentration c is constant and equal to c_0 in the loading zone and that the concentration profile is linearly decreasing in the unloading zone. The quantity

Downloaded from rsif.royalsocietypublishing.org on January 23, 2011

we wish to calculate is the mean flow velocity $\bar{u}$ in the translocation zone as a function of $M\ddot{u}$ and $\alpha = l_1/l_2$. The boundary conditions on the velocity v is that it is zero at the boundaries,

$$v(0) = v(\xi_3) = 0. \tag{A 5}$$

In the loading zone, the concentration ς is assumed to be constant and equal to unity,

$$\varsigma_1(\xi) = 1, \quad \text{for } 0 < \xi < \xi_1. \tag{A 6}$$

In the translocation zone, we have sugar flux conservation,

$$v_2(\xi)\varsigma_2(\xi) = \varsigma_3(\xi_2)v_3(\xi_2) = v_2(\xi_1), \quad \text{for } \xi_1 < \xi < \xi_2. \tag{A 7}$$

In the unloading zone, we assume that the concentration profile is linear and of the form

$$\varsigma_3(\xi) = -\beta(\xi - \xi_3), \quad \text{for } \xi_2 < \xi < \xi_3, \tag{A 8a}$$

where β is determined from sugar conservation (A 6) and (A 7) in the translocation zone,

$$\beta = \frac{v_2(\xi_1)}{v_2(\xi_2)(\xi_3 - \xi_2)}. \tag{A 8b}$$

The equations of motion are

$$\partial_\xi^2 v_1 = M\ddot{u}v_1, \quad \text{for } 0 < \xi < \xi_1, \tag{A 9a}$$

$$\partial_\xi^2 v_2 = -\frac{v_1(\xi_1)}{v_2^2}\partial_\xi v_2 + M\ddot{u}v_2, \quad \text{for } \xi_1 < \xi < \xi_2, \tag{A 9b}$$

and

$$\partial_\xi^2 v_3 = -\beta + M\ddot{u}v_3, \quad \text{for } \xi_2 < \xi < \xi_3. \tag{A 9c}$$

Here, the indices on v indicate the domain to which it belongs. These equations cannot be solved analytically for arbitrary values of $M\ddot{u}$ and α; however, analytical solutions can be found in the limits $M\ddot{u} \ll 1$ and $M\ddot{u} \gg 1$. These analytical solutions allow us to calculate the mean flow velocity $\bar{u}$ as a function of the parameters in the problem. Keeping, say, l_1 and l_2 fixed while varying the tube radius r, we find that the analytical solutions allow us to determine the point in the parameter space where the average translocation speed $\bar{u}$ is at a maximum.

Solution for $M\ddot{u} \ll 1$. In this limit, the equations of motion (A 9*a*)–(A 9*c*) are

$$\partial_\xi^2 v_1 = 0, \quad \text{for } 0 < \xi < \xi_1, \tag{A 10a}$$

$$\partial_\xi^2 v_2 = -\frac{v_1(\xi_1)}{v_2^2}\partial_\xi v_2, \quad \text{for } \xi_1 < \xi < \xi_2, \tag{A 10b}$$

and

$$\partial_\xi^2 v_3 = -\beta, \quad \text{for } \xi_2 < \xi < \xi_3, \tag{A 10c}$$

with the boundary conditions $v_1(0) = 0$ and $v_3(\xi_3) = 0$. The solutions can be written as

$$v_1(\xi) = C_1\xi + C_2, \tag{A 11a}$$

$$\xi(v_2) = \frac{v_1(\xi_1)}{C_5}\left[\frac{v_2}{v_1(\xi_1)} - \frac{1}{C_5}\log\left(\frac{1 + (C_5 v_2/v_1(\xi_1))}{1 + C_5}\right)\right] + C_6 \tag{A 11b}$$

and

$$v_3(\xi) = -\frac{1}{2}\frac{v_2(\xi_1)}{v_2(\xi_2)}\frac{1}{(\xi_3 - \xi_2)}(\xi - \xi_3)^2 + C_3(\xi - \xi_3) + C_4. \tag{A 11c}$$

By demanding that the velocity and its derivative should be continous at $\xi = \xi_1$ and $\xi = \xi_2$, and that $\alpha \ll 1$, we find the six C coefficients above to be

$$(C_1, C_2, C_3, C_4, C_5, C_6) = \left(2 - \sqrt{3},\ 0,\ 1 - \sqrt{3},\ 0,\ 1 - \sqrt{3},\ \lambda_1\lfloor 1 + \sqrt{3}\rfloor/2\right). \tag{A 12}$$

The mean velocity $\bar{v}$ is then

$$\bar{v} = \frac{\sqrt{3} - 1}{2}\lambda_1 - \frac{9 - 5\sqrt{3}}{8}\lambda_1^2 \approx 0.366\,\lambda_1 - 0.043\,\lambda_1^2, \tag{A 13}$$

which in dimensional units for small values of λ_1, i.e. $l_1 \ll l_2$, becomes equation (3.6).

Solution for $M\ddot{u} \gg 1$. The equations of motion are

$$\partial_\xi^2 v_1 = M\ddot{u}v_1, \quad \text{for } 0 < \xi < \xi_1, \tag{A 14a}$$

$$\partial_\xi^2 v_2 = -\frac{v_1(\xi_1)}{v_2^2}\partial_\xi v_2 + M\ddot{u}v_2, \quad \text{for } \xi_1 < \xi < \xi_2 \tag{A 14b}$$

and

$$\partial_\xi^2 v_3 = -\beta + M\ddot{u}v_3, \quad \text{for } \xi_2 < \xi < \xi_3, \tag{A 14c}$$

with the boundary conditions $v_1(0) = 0$ and $v_1(\xi_3) = 0$. In zones 1 and 3, the solutions are

$$v_1(\xi) = A_1 \sinh\sqrt{M\ddot{u}}\xi + A_2 \cosh\sqrt{M\ddot{u}}\xi, \quad \text{for } 0 < \xi < \xi_1 \tag{A 15a}$$

and

$$v_3(\xi) = A_3 \sinh\sqrt{M\ddot{u}}(\xi - \xi_2) + A_4 \cosh\sqrt{M\ddot{u}}(\xi - \xi_2) + \frac{\beta}{M\ddot{u}}, \quad \text{for } \xi_2 < \xi < \xi_3. \tag{A 15b}$$

Here, $A_2 = 0$ because of the boundary condition at $\xi = 0$, while A_3 and A_4 are determined by the continuity condition on v and $\partial_\xi v$ at $\xi = \xi_2$:

$$A_3 = \frac{1}{\sqrt{M\ddot{u}}}\partial_\xi v_2(\xi_2) \tag{A 15c}$$

and

$$A_4 = v_2(\xi_2) - \frac{\beta}{M\ddot{u}}. \tag{A 15d}$$

Downloaded from rsif.royalsocietypublishing.org on January 23, 2011

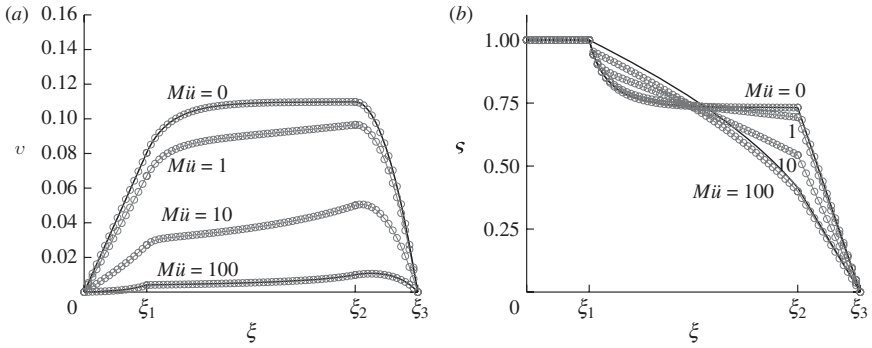

Figure 5. Comparison between analytical and numerical solutions of the non-dimensional phloem flow problem. (*a*) Numerically computed velocity v (circles) as a function of position ξ for $M\ddot{u} = 0$, 1, 10, 100, $\xi_1 = 0.3$, $\xi_2 = 1.3$ and $\xi_3 = 1.6$. The analytical solutions for the velocity (solid lines) given in equations (A 11*a–c*), (A 15*a*,*b*) and (A 18) are shown for comparison. (*b*) Numerically computed concentration ς (circles) as a function of position ξ for the same parameters as in (*a*). The analytical solutions for the concentration (solid lines) were found using the solutions for v given in equations (A 11*a–c*), (A 15*a*,*b*) and (A 18) and the conditions given in equations (A 6), (A 7) and (A 8*a*,*b*). Open circles, numerics; solid lines, analytics.

Table 2. Plant data used in figure 4 for phloem type P (primary = 1, secondary = 2). Sieve lumen radius r, translocation zone length l_2 (plant length), loading zone length l_1 (leaf size) and measured flow velocity are given with corresponding standard deviations. The Münch number $M\ddot{u}$ and the ratio l_1/l_2 were calculated using $L_p = 5 \times 10^{-14}\,\mathrm{m\,s^{-1}\,Pa^{-1}}$, $\eta = 5 \times 10^{-3}$ Pa s. Estimates of l_1 and l_2 follow general knowledge of plants available at online databases (USDA plant database) and visits to the Harvard University Herbaria. References are given in square brackets.

species	habit	P	r (μm)	Δr (μm)	l_2 (m)	Δl_2 (m)	l_1 (m)	Δl_1 (m)	u (μm s^{-1})	Δu (μm s^{-1})	$M\ddot{u}$	l_1/l_2
Beta vulgaris	herbaceous dicot	1	5.0 [42–44]	1.0	0.3	0.06	0.10	0.02			2.88	0.33
Yucca flaccida	woody monocot	1	10.0 [44]	2.0	1.0	0.2	0.5	0.1			4.00	0.50
Sabal palmetto	tree monocot	1	16.5 [44]	1.7	20	4	0.5	0.1			35.6	0.025
Tilia americana	tree dicot	2	15.0 [44]	1.5	20	4	0.10	0.02			474	0.0050
Robinia pseudoacacia	tree dicot	2	10.0 [44]	1.0	40	8	0.030	0.006			6400	0.00075
Vitis vinifera	vine	2	18.0 [44]	4.0	20	4	0.10	0.02			274	0.0050
Gossypium bardadense	herbaceous dicot	1	11.0 [44]	2.2	1.5	0.3	0.15	0.03			6.76	0.10
Pinus strobus	tree conifer	2	10.9 [45]	1.0	20	4	0.10	0.02			1240	0.0050
Festuca arundinacea	herbaceous monocot	1	3.0 [46]	0.6	0.30	0.06	0.05	0.01			13.3	0.17
Cucurbita pepo	creeper dicot	2	40.0 [47]	8.0	7.0	1.4	0.30	0.06			3.06	0.043
Glycine max	herbaceous dicot	1	3.7[a]	1.0	0.40	0.08	0.10	0.02	145	46	12.6	0.25
Tradescantia virginiana	herbaceous monocot	1	1.2[a]	0.4	0.10	0.02	0.020	0.004	4.13	1.64	23.1	0.20
Cucumis sativus	creeper dicot	1	6.3[a]	1.4	0.60	0.12	0.10	0.02	149	54	5.76	0.17
Cucurbita maxima	creeper dicot	1	12.3[a]	2.7	4.0	0.8	0.20	0.04	62.9	48.4	34.4	0.050
Cucurbita maxima	creeper dicot	2	16.6[a]	2.6	4.0	0.8	0.20	0.04	48.2	29.3	14.0	0.050
Solanum lycopersicum	herbaceous dicot	1	5.2[a]	0.8	0.40	0.08	0.10	0.02	162	48	4.55	0.25
Anacyclus purethrum	herbaceous dicot	1	2.1 [10]	0.6	0.30	0.06	0.010	0.002			38.9	0.033
Ecbalium elaterium	creeper dicot	1	15.0 [10]	3.0	3.0	0.6	0.20	0.04			10.7	0.067
Eragostis plana	herbaceous monocot	1	3.0 [48]	0.6	0.2	0.04	0.10	0.02			5.93	0.5
Heracleum mantegazzianum	herbaceous dicot	1	9.0 [49]	1.8	2.0	0.4	0.20	0.04			21.9	0.1

[a]Refers to our own measurements.

Downloaded from rsif.royalsocietypublishing.org on January 23, 2011

In the translocation zone, we shall solve the equation

$$\partial_\xi^2 v_2 = -\frac{v_1(\xi_1)}{v_2^2}\partial_\xi v_2 + M\ddot{u}v_2, \quad \text{for } \xi_1 < \xi < \xi_2, \tag{A 16}$$

by assuming that v_2 can be written as $v_2 = v'_2/M\ddot{u}$, where v'_2 is of the order of unity. Inserting this, and keeping only terms of order $M\ddot{u}$ and $M\ddot{u}^2$, we get that

$$M\ddot{u}v_1(\xi_1)\partial_\xi v'_2 = v_2^{3\prime}. \tag{A 17}$$

Since we must have that $v_2(\xi_1) = v_1(\xi_1)$, we get that

$$v_2(\xi) = \frac{v_1(\xi_1)}{\sqrt{1 - 2M\ddot{u}v_1(\xi_1)(\xi - \xi_1)}}, \quad \text{for } \xi_1 < \xi < \xi_2. \tag{A 18}$$

Note that this solution does not fulfil the condition $\partial_\xi v_2(\xi_1) = \partial_\xi v_1(\xi_1)$. This is due to the fact that we have ignored the term $\partial_\xi^2 v_2$. However, this turns out to play very little role when comparing the analytical solution with the numerical solution of the full problem. Using the continuity conditions at $\xi = \xi_1$ and $\xi = \xi_2$, the mean translocation velocity $\bar{v}$ in the translocation zone is found to be

$$\bar{v} = \frac{1}{M\ddot{u}}, \tag{A 19}$$

which in dimensional units becomes equation (3.7). Representative examples of numerical solutions for the dimensionless velocity and concentration fields together with the analytical solutions for small and large $M\ddot{u}$ are shown in figure 5.

Different sizes of the loading and unloading zone. If $l_1 \neq l_3$, we find that for $M\ddot{u} \gg 1$ the solution (A 19) remains unchanged, while for $M\ddot{u} \ll 1$ the mean velocity instead of equation (A 13) now is given by

$$\bar{v} = \frac{1}{2}\lambda_1\left(\sqrt{1 + 2\chi} - 1\right), \tag{A 20}$$

where $\chi = \lambda_3/\lambda_1$. Thus the scaling relations are not significantly affected as long as χ is of the order of unity.

Optimal radius of the phloem tubes. To maximize the flow velocity, a plant would presumably operate near the maximum in the u–r diagram shown in figure 3*b*. Equating the two expressions (3.6) and (3.7) for $\bar{u}$ in the limits $M\ddot{u} \ll 1$ and $M\ddot{u} \gg 1$ gives the following estimate for the optimal radius r_c:

$$r_c^3 = 8(\sqrt{3} - 1)L_p\eta l_1 l_2. \tag{A 21}$$

Phloem translocation velocity. Figure 4*a* shows the velocities $\bar{u}$ measured experimentally (black circles) using the method described in figure 2. To compare our model with the experimental data, the non-dimensional mean velocity $\bar{v}$ depending on $M\ddot{u}$ and α was first calculated numerically from equations (A 5)–(A 9*c*) using the data for r and l_2 shown in table 2. Then, the dimensional mean velocity $\bar{u}$ was found from

$$\bar{u}(M\ddot{u}, \alpha) = \frac{2l_2}{r}L_p RTc_0 \bar{v}(M\ddot{u}, \alpha), \tag{A 22}$$

with $L_p = 5 \times 10^{-14}$ m (Pa s)$^{-1}$ chosen as the representative value and $RTc_0 = 0.54$ MPa chosen to fit the model to the experimental value for *S. lycopersicum*. These predicted values for $\bar{u}$ (grey circles) are also plotted in figure 3*b* showing good agreement between theory and experiment.

REFERENCES

1 Holbrook, N. & Zwieniecki, M. 2008 Transporting water to the tops of trees. *Phys. Today* **61**, 76–77. (doi:10.1063/1.2835167)

2 Tyree, M. T. & Zimmermann, M. H. 2002 *Xylem structure and the ascent of sap*, 2nd edn. Berlin, Germany: Springer.

3 Knoblauch, M. & Peters, W. S. 2010 Münch, morphology, microfluidics—our structural problem with the phloem. *Plant Cell Environ.* **33**, 1439–1452. (doi:10.1111/j.1365-3040.2010.02177.x)

4 van Bel, A. J. E. & Hafke, J. B. 2005 Physiochemical determinants of phloem transport. In *Vascular transport in plants* (eds N. M. Holbrook & M. A. Zwieniecki), pp. 19–44. San Diego, CA: Elsevier Academic Press.

5 Pickard, W. F. & Abraham-Shrauner, B. 2009 A 'simplest' steady-state Münch-like model of phloem translocation, with source and pathway and sink. *Funct. Plant Biol.* **36**, 629–644. (doi:10.1071/FP08278)

6 Thompson, M. V. & Holbrook, N. M. 2003 Application of a single-solute non-steady-state phloem model in the study of long-distance assimilate transport. *J. Theor. Biol.* **220**, 419–455. (doi:10.1006/jtbi.2003.3115)

7 Lough, T. J. & Lucas, W. J. 2006 Integrative plant biology: role of phloem long-distance macromolecular trafficking. *Ann. Rev. Plant Biol.* **57**, 203–232. (doi:10.1146/annurev.arplant.56.032604.144145)

8 Turgeon, R. & Wolf, S. 2009 Phloem transport: cellular pathways and molecular trafficking. *Ann. Rev. Plant Biol.* **60**, 207–221. (doi:10.1146/annurev/arplant.043008.092045)

9 Mencuccini, M. & Hölttä, T. 2010 The significance of phloem transport for the speed with which canopy photosynthesis and belowground respiration are linked. *New Phytol.* **185**, 189–203. (doi:10.1111/j/1469-8137.2009.03050.x)

10 Canny, M. J. 1973 *Phloem translocation*. Cambridge, UK: Cambridge University Press.

11 Milburn, J. A. 1975 Pressure flow. In *Transport in plants I. Phloem transport* (eds M. H. Zimmermann & J. A. Milburn), pp. 328–353. Berlin, Germany: Springer.

12 Windt, C. W., Vergeldt, F. J., de Jager, P. A. & van As, H. 2006 MRI of long-distance water transport: a comparison of the phloem and xylem flow characteristics and dynamics in poplar, castor bean, tomato and tobacco. *Plant Cell Environ.* **29**, 1715–1729. (doi:10.1111/j1365.3040.2006.01544.x)

13 Sperry, J. S., Meinzer, F. C. & McCulloch, K. A. 2008 Safety and efficiency conflicts in hydraulic architecture: scaling from tissues to trees. *Plant Cell Environ.* **31**, 632–645. (doi:10.1111/j/1365-3040.2007.01765.x)

14 Knoblauch, M., Noll, G. A., Müller, T., Prüfer, D., Schneider-Hüther, I., Scharner, D., van Bel, A. J. E. & Peters, W. S. 2003 ATP-independent contractile proteins from plants. *Nat. Mater.* **2**, 600–603. (doi:10.1038/nmat960)

15 Sjolund, R. D. 1997 The phloem sieve element: a river runs through it. *Plant Cell* **9**, 1137–1146. (doi:10.1105/tpc.9.7.1137)

16 Fisher, D. B. 2000 Long-distance transport. In *Biochemistry and molecular biology of plants* (eds B. B. Buchanan,

Downloaded from rsif.royalsocietypublishing.org on January 23, 2011

W. GruissemR. J. Jones), pp. 730–784. Rockville, MD: American Society of Plant Physiologists.
17 Wheeler, T. D. & Stroock, A. D. 2008 The transpiration of water at negative pressures in a synthetic tree. *Nature* **455**, 208–212. (doi:10.1038/nature07226)
18 Noblin, X., Mahadevan, L., Coomaraswamy, I. A., Weitz, D. A., Holbrook, N. M. & Zwieniecki, M. A. 2008 Optimal vein density in artificial and real leaves. *Proc. Natl Acad. Sci. USA* **105**, 9140–9144. (doi:10.1073/pnas.0709194105)
19 Jensen, K. H., Lee, J., Bohr, T. & Bruus, H. 2009 Osmotically driven flows in microchannels separated by a semipermeable membrane. *Lab Chip* **9**, 2093–2099. (doi:10.1039/b818937d)
20 Münch, E. 1943 Durchlässigkeit der siebröhren fur druckströmungen. *Flora* (*Jena, 1818–1965*) **136**, 223–262.
21 Christy, A. L. & Ferrier, J. M. 1973 A mathematical treatment of Münch's pressure-flow hypothesis of phloem translocation. *Plant Physiol.* **52**, 531–538.
22 Goeschl, J. D., Magnuson, C. E., DeMichele, D. W. & Sharpe, P. J. H. 1976 Concentration-dependent unloading as a necessary assumption for a closed form mathematical model of osmotically driven pressure flow in phloem. *Plant Physiol.* **58**, 556–562.
23 Henton, S. M., Greaves, A. J., Piller, G. J. & Minchin, P. E. H. 2002 Revisiting the Münch pressure-flow hypothesis long-distance transport of carbohydrates: modelling the dynamics of solute transport inside a semipermeable tube. *J. Exp. Bot.* **53**, 1411–1419. (doi:10.1093/jexbot/53.373.1411)
24 Smith, K. C., Magnuson, C. E., Goeschl, J. D. & DeMichele, D. W. 1980 A time-dependent mathematical expression of the Münch hypothesis of phloem transport. *J. Theor. Biol.* **86**, 493–505. (doi:10.1016/0022-5193(80)90348-3)
25 van Bel, A., Ehlers, K. & Knoblauch, M. 2002 Sieve elements caught in the act. *Trends Plant Sci.* **7**, 126–132. (doi:10.1016/S1360-1385(01)02225-7)
26 Canny, M. 1975 Mass transfer. In *Transport in plants I. Phloem transport* (eds M. H. Zimmermann & J. A. Milburn), pp. 139–153. Berlin, Germany: Springer.
27 Minchin, P. E. H. & Thorpe, M. R. 2003 Using the short-lived isotope ^{11}C in mechanistic studies of photosynthate transport. *Funct. Plant Biol.* **30**, 831–841. (doi:10.1071/FP03008)
28 Knoblauch, M. & van Bel, A. J. E. 1998 Sieve tubes in action. *Plant Cell* **10**, 35–50. (doi:10.1105/tpc.10.1.35)
29 Mullendore, D. L., Windt, C. W., Van As, H. & Knoblauch, M. 2010 Sieve tube geometry in relation to phloem flow. *Plant Cell* **22**, 579–593. (doi:10.1105/tpc.109.070094)
30 Bao, J.-B. & Harrison, D. J. 2006 Measurement of flow in microfluidic networks with micrometer-sized flow restrictors. *AIChE J.* **52**, 75–85. (doi:10.1002/aic.10612)
31 Schrum, K. F., Lancaster LII, J. M., Johnston, S. E. & Gilman, S. D. 2000 Monitoring electroosmotic flow by periodic photobleaching of a dilute, neutral fluorophore. *Anal. Chem.* **72**, 4317–4321. (doi:10.1021/ac0005114)
32 Thompson, M. 2006 Phloem: the long and the short of it. *Trends Plant Sci.* **11**, 26–32. (doi:10.1016/j.tplants.2005.11.009)
33 Jensen, K. H., Rio, E., Hansen, R., Clanet, C. & Bohr, T. 2009 Osmotically driven pipe flows and their relation to sugar transport in plants. *J. Fluid Mech.* **636**, 371–396. (doi:10.1017/S002211200900799X)
34 Aldis, G. K. 1988 The unstirred layer during osmotic flow into a tubule. *Bull. Math. Biol.* **50**, 531–545. (doi:10.1016/S0092-8240(88)80007-7)
35 Phillips, R. J. & Dungan, S. R. 1993 Asymptotic analysis of flow in sieve tubes with semi-permeable walls. *J. Theor. Biol.* **162**, 465–485. (doi:10.1006/jtbi.1993.1100)
36 Eschrich, W., Evert, R. F. & Young, J. H. 1972 Solution flow in tubular semipermeable membranes. *Planta* **107**, 279–300. (doi:10.1007/BF00386391)
37 Lang, A. 1973 A working model of a sieve tube. *J. Exp. Bot.* **24**, 896–904. (doi:10.1093/jxb/24.5.896)
38 Esau, K. 1965 *Plant anatomy*. New York, NY: John Wiley & Sons, Inc.
39 Lang, A. 1979 A relay mechanism for phloem translocation. *Ann. Bot.* **44**, 141–145. (doi:0305-7364/79/080141+05S02.00/0)
40 Hölttä, T., Mencuccini, M. & Nikinmaa, E. 2009 Linking phloem function to structure: analysis with a coupled xylem–phloem transport model. *J. Theor. Biol.* **259**, 325–337. (doi:10.1016/j.jtbi.2009.03.039)
41 van Bel, A. J. E. 2003 The phloem, a miracle of ingenuity. *Plant Cell Environ.* **26**, 125–149. (doi:10.1046/j.1365.3040.2003.00963.x)
42 Geiger, D. & Cataldo, D. 1969 Leaf structure and translocation in sugar beet. *Plant Physiol.* **44**, 45–54. (doi:10.1104/pp.44.1.45)
43 Sokolova, S. 1968 Fine structure of petiole phloem cells of *Beta vulgaris* L. *Plant Physiol.* (*Russian*) **15**, 757–763.
44 Tyree, M. T., Christy, A. L. & Ferrier, J. M. 1974 A simpler iterative steady state solution of Münch pressure-flow systems applied to long and short translocation paths. *Plant Physiol.* **54**, 589–600. (doi:10.1104/pp.54.4.589)
45 Murmanis, L. & Evert, R. 1966 Some aspects of sieve cell ultrastructure in *Pinus strobus*. *Am. J. Bot.* **53**, 1065–1078. (doi:10.2307/2440687)
46 Sheehy, J., Mitchell, P., Durnand, J., Gastal, F. & Woodward, F. 1995 Calculation of translocation coefficients from phloem anatomy for use in crop models. *Ann. Bot.* **76**, 263–269. (doi:10.1006/anbo.1995.1095)
47 Crafts, A. & Lorenz, O. 1944 Fruit growth and food transport in cucurbits. *Plant Physiol.* **19**, 131–138. (doi:10.1104/pp.19.1.131)
48 Botha, C. 2005 Interaction of phloem and xylem during phloem loading: functional sympalsmic roles for thin- and thick-walled sieve tubes in monocotyledons. In *Vascular transport in plants* (eds N. M. Holbrook & M. A. Zwieniecki), pp. 115–130. San Diego, CA: Elsevier Academic Press.
49 Fensom, D. 1975 Work with isolated phloem strands. In *Transport in plants I: phloem transport* (eds M. H. Zimmermann & J. A. Milburn), pp. 223–244. Berlin, Germany: Springer.

Bibliography

[1] B. Abecassis, C. Cottin-Bizonne, C. Ybert, A. Ajdari, and L. Bocquet, *Boosting migration of large particles by solute contrasts*, Nature Materials **7** (2008), 785–789.

[2] A. Ajdari, *Pumping liquids using asymmetric electrode arrays*, Phys. Rev. E **61** (2000), no. 1, R45–R48.

[3] G. K. Aldis, *The unstirred layer during osmotic flow into a tubule*, Bull. Math. Bio. **50** (1988), no. 5, 531–545.

[4] P. W. Atkins, *Physical chemistry*, Oxford University Press, 1978.

[5] G. K. Batchelor, *An introduction to fluid dynamics*, Cambridge University Press, 1967.

[6] A. J. E. Van Bel, *The phloem, a miracle of ingenuity*, Plant, Cell and Environment **26** (2003), 125–149.

[7] C. Bouchard and B. P. A. Granjean, *A neural network correlation for the variation of viscosity of sucrose aqueous solutions with temperature and concentration*, LWT - Food Science and Technology **28** (1995), no. 1, 157 – 159.

[8] S. Boudait, O. Hansen, H. Bruus, C. Berendsen, N. K. Bau-Madsen, P. Thomsen, A. Wolff, and J. Jonsmann, *Surface-directed capillary system; theory, experiments and applications*, Lab Chip **5** (2005), 827–836.

[9] A. Brask, J. Kutter, and H. Bruus, *Long-term stable electroosmotic pump with ion exchange membranes*, Lab Chip **5** (2005), 730–738.

[10] H. Bruus, *Theoretical microfluidics*, Oxford University Press, 2008.

[11] F. Bundgaard, G. Perozziello, and O. Geschke, *Rapid prototyping tools and methods for all-topas cyclic olefin copolymer fluidic microsystems*, Proceedings of the Institution of Mechanical Engineers Series C **220** (2007), no. 11, 1625–1632.

[12] M. J. Canny, *Phloem translocation*, Cambridge University Press, 1973.

[13] A. Lawrence Christy and Jack M. Ferrier, *A Mathematical Treatment of Munch's Pressure-Flow Hypothesis of Phloem Translocation*, Plant Physiol. **52** (1973), no. 6, 531–538.

[14] Z. Dagan, S. Weinbaum, and R. Pfeffer, *An infinite-series solution for the creeping motion through an orifice of finite length*, Journal of Fluid Mechanics **115** (1982), 505–523.

[15] J. Dainty, *The polar permeability of plant cell membranes to water*, Protoplasma **57** (1963), 220–228.

[16] W. Eschrich, R. F. Evert, and J. H. Young, *Solution flow in tubular semipermeable membranes*, Planta (Berl.) **107** (1972), 279–300.

[17] Alberts et al., *Essential cell biology*, Garland Science, 2004.

[18] O. Geschke, *Microsystem engineering of lab-on-a-chip devices*, Wiley-VCH, 2004.

[19] M. M. Gregersen, L. H. Olesen, A. Brask, M. F. Hansen, and H. Bruus, *Flow reversal at low voltage and low frequency in a microfabricated ac electrokinetic pump*, Phys. Rev. E **76** (2007), no. 5, 056305.

[20] H. Hasimoto, *On the flow of a viscous fluid past a thin screen at small reynolds numbers*, Journal of the Physical Society of Japan **13** (1958), no. 6, 633–639.

[21] T. Heimburg, *Nonequlibrium thermodynamics in biology*, NBI press, 2006.

[22] N. M. Holbrook, Personal communication, 2011.

[23] N. M. Holbrook and M. A. Zwieniecki, *Vascular transport in plants*, Academic Press, 2005.

[24] T. Hölttä, *Modeling xylem and phloem water flows in trees according to cohesion theory and münch hypothesis*, Trees - Structure and Function **20** (2006), no. 1, 67–78.

[25] L. Horwitz, *Some Simplified Mathematical Treatments of Translocation in Plants*, Plant Physiol. **33** (1958), no. 2, 81–93.

[26] B. Huber, *Die saftströme der pflanzen*, Springer-Verlag, 1956.

[27] K. H. Jensen, T. Bohr, and H. Bruus, *Self-consistent unstirred layers in osmotically driven flows*, Journal of Fluid Mechanics **662** (2010), 197–208.

[28] K. H. Jensen, J. Lee, T. Bohr, and H. Bruus, *Osmotically driven flows in microchannels separated by a semipermeable membrane*, Lab on a Chip **9** (2009), no. 14, 2093–2099.

[29] K. H. Jensen, J. Lee, T. Bohr, H. Bruus, N. M. Holbrook, and M. A. Zwieniecki, *Optimality of the Münch mechanism for translocation of sugars in plants*, Journal of The Royal Society Interface (2011), DOI: 10.1098/rsif.2010.0578.

[30] K. H. Jensen, E. Rio, R. Hansen, C. Clanet, and T. Bohr, *Osmotically driven pipe flows and their relation to sugar transport in plants*, Journal of Fluid Mechanics **636** (2009), 371–396.

[31] K.H. Jensen, M.N. Alam, B. Scherer, A. Lambrecht, and N.A. Mortensen, *Slow-light enhanced light-matter interactions with applications to gas sensing*, Optics Communications **281** (2008), no. 21, 5335 – 5339.

[32] M. J. Jensen, H. A. Stone, and H. Bruus, *A numerical study of two-phase stokes flow in an axisymmetric flow-focusing device*, Physics of Fluids **18** (2006), no. 7, 077103.

[33] J. Jeong and S. Choi, *Axisymmetric stokes flow through a circular orifice in a tube*, Physics of Fluids **17** (2005), no. 5, 053602.

[34] F. C. Johansen, *Flow through Pipe Orifices at Low Reynolds Numbers*, Proceedings of the Royal Society of London. Series A **126** (1930), no. 801, 231–245.

[35] R. P. C. Johnson, *Historical Sketches 21*, Journal of Experimental Botany **37** (1986), no. 9, 1429–1431.

[36] M. Knoblauch and W. S. Peters, *Münch, morphology, microfluidics - our structural problem with the phloem.*, Plant Cell Environment **33** (2010), no. 9, 1439–1452.

[37] M. Knoblauch and A. J. E. van Bel, *Sieve tubes in action*, The Plant Cell **10** (1998), 35–50.

[38] A. Lacointe and P. E. H. Minchin, *Modelling phloem and xylem transport within a complex architecture*, Functional Plant Biology **35** (2008), no. 10, 772–780.

[39] L. D. Landau and E. M. Lifshitz, *Statistical physics*, third ed., Pergamon Press, 1980.

[40] A. Lang, *A working model of a sieve tube*, Journal of Experimental Botany **24** (1973), no. 82, 896–904.

[41] ———, *A relay mechanism for phloem translocationa*, Annals of Botany **44** (1979), no. 2, 141–146.

[42] J. Lee, E. Kulla, A. Chauhan, and A. Tripathi, *Taylor dispersion in polymerase chain reaction in a microchannel*, Phys. Fluids **20** (2008), 093601.

[43] T. J. Lough and W. J. Lucas, *Integrative plant biology: role of phloem long-distance macromolecular trafficking.*, Annual review of plant biology **57** (2006), 203–232.

[44] A MacRobbie, *Phloem translocation - facts and mechanisms - comparative survey*, Biological reviews of the Cambridge philosophical society **46** (1971), no. 4, 429–481.

[45] J. W. Maynard and W. J. Lucas, *A reanalysis of the two-component phloem loading system in beta vulgaris*, Plant Physiol. **69** (1982), no. 3, 734–739.

[46] M. Mencuccini and T. Hölttä, *On light bulbs and marbles. transfer times and teleconnections in plant fluid transport systems.*, New Phytol **187** (2010), no. 4, 888–91.

[47] B. E. Michel, *Solute potentials of sucrose solutions*, Plant Physiol. **50** (1972), 196–198.

[48] D. L. Mullendore, C. W. Windt, H. Van As, and M. Knoblauch, *Sieve Tube Geometry in Relation to Phloem Flow*, Plant Cell **22** (2010), no. 3, 579–593.

[49] E. Münch, *Die stoffbewegung in der pflanze*, Jena, Verlag von Gustav Fisher, 1930.

[50] R. Murphy and D. P. Aikman, *An Investigation of the Relay Hypothesis of Phloem Transport in Ricinus communis L.*, Journal of Experimental Botany **40** (1989), no. 10, 1079–1088.

[51] K. J. Niklas, *Plant biomechanics – an engineering approach to plant form and function*, The University of Chicago Press, 1992.

[52] ———, *Plant allometry: the scaling of form and process*, University of Chicago Press, 1994.

[53] P. S. Nobel, *Physicochemical & environmental plant physiology*, Academic press, 1999.

[54] X. Noblin, L. Mahadevan, I. A. Coomaraswamy, D. A. Weitz, N. M. Holbrook, and M. A. Zwieniecki, *Optimal vein density in artificial and real leaves*, PNAS **105** (2008), no. 27, 9140–9144.

[55] J. Y. Park, C. M. Hwang, S. H. Lee, and S. Lee, *Gradient generation by an osmotic pump and the behavior of human mesenchymal stem cells under the fetal bovine serum concentration gradient*, Lab on a chip **7** (2007), 1673–1680.

[56] T. J. Pedley, *The interaction between stirring and osmosis. part 1*, Journal of Fluid Mechanics **101** (1980), no. 4, 843–861.

[57] ———, *The interaction between stirring and osmosis. part 2*, Journal of Fluid Mechanics **107** (1980), 281–296.

[58] ———, *Calculation of unstirred layer thickness in membrane transport experiments: a survey*, Quarterly Review of Biophysics **16** (1983), no. 2, 115–150.

[59] T. J. Pedley and J. Fischbarg, *The development of osmotic flow through an unstirred layer*, Journal of Theoretical Biology **70** (1978), no. 4, 427 – 447.

[60] T. J. Pedley and J. Fischbarg, *Unstirred layer effects in osmotic water flow across gallbladder epithelium*, Journal of Membrane Biology **54** (1980), 89–102, 10.1007/BF01940563.

[61] W. F. Pickard and B. Abraham-Shrauner, *A simplest steady-state munch-like model of phloem translocation, with source and pathway and sink*, Functional Plant Biology **36** (2009), no. 7, 629–644.

[62] P. Pohl, *The size of the unstirred layer as a function of the solute diffusion coefficient*, Biophysical Journal **75** (1998), 1403–1409.

[63] W. H. Press, *Numerical recipes in fortran 77, volume 1*, second ed., Cambridge University Press, 2001.

[64] G. M. Preston, T. P. Carroll, W. B. Guggino, and P. Agre, *Appearance of Water Channels in Xenopus Oocytes Expressing Red Cell CHIP28 Protein*, Science **256** (1992), no. 5055, 385–387.

[65] R. Roscoe, *The flow of viscous fluids round plane obstacles*, The Philosophical Magazine **40** (1941), 338–351.

[66] R. A. Sampson, *On Stokes's Current Function*, Philosophical Transactions of the Royal Society of London. (A.) **182** (1891), 449–518.

[67] S. G. Schultz, *Basic principles of membrane transport*, Cambridge University Press, 1980.

[68] A. Schulz, *Living sieve cells of conifers as visualized by confocal, laser-scanning fluorescence microscopy*, Protoplasma **166** (1992), 153–164, 10.1007/BF01322778.

[69] H. W. Smith and H. W. Smith, *I. theory of solutions: "a knowledge of the laws of solutions ..."*, Circulation **21** (1960), no. 5, 808–817.

[70] K. C. Smith, C. E. Magnuson, J. D. Goeschl, and D. W. DeMichele, *A time-dependent mathematical expression of the münch hypothesis of phloem transport*, Journal of Theoretical Biology **86** (1980), no. 3, 493 – 505.

[71] J. S. Sperry, U. G. Hacke, and J. K. Wheeler, *Comparative analysis of end wall resistivity in xylem conduits*, Plant, Cell & Environment **28** (2005), no. 4, 456–465.

[72] Statkraft, *Power production based on osmotic pressure*, 2009, Presented by Statkraft at Waterpower XVI, Spokane, USA.

[73] L. Taiz and E. Zeiger, *Plant physiology*, third ed., Sinauer Associates, Inc., 2002.

[74] G. I. Taylor, *Dispersion of soluble matter in solvent flowing slowly through a tube.*, Proc. Roy. Soc. A **291** (1953), 186–203.

[75] J. R. Taylor, *An introduction to error analysis*, second ed., University Science Books, 1997.

[76] F. Theeuwes, *Elementary osmotic pump*, J. Pharm. Sci. **64** (1975), 1987–1991.

[77] M. V. Thompson, *Scaling phloem transport: Elasticity and pressure-concentration waves*, Journal of Theoretical Biology **236** (2005), no. 3, 229 – 241.

[78] ———, *Phloem: the long and the short of it*, Trends in Plant Science **11** (2006), no. 1, 26 – 32.

[79] M. V. Thompson and N. M. Holbrook, *Application of a single-solute non-steady-state phloem model to the study of long-distance assimilate transport*, J Theo Biol **220** (2003), no. 4, 419–455.

[80] ———, *Scaling phloem transport: water potential equilibrium and osmoregulatory flow*, Plant, Cell and Environment **26** (2003), 1561–1577.

[81] ———, *Scaling phloem transport: information transmission*, Plant, Cell & Environment **27** (2004), no. 4, 509–519.

[82] R. Turgeon, *The puzzle of phloem pressure*, Plant Physiology **154** (2010), no. 2, 578–581.

[83] R. Turgeon and S. Wolf, *Phloem transport: cellular pathways and molecular trafficking.*, Annu Rev Plant Biol **60** (2009), 207–221.

[84] M. T. Tyree, A. L. Christy, and J. M. Ferrier, *A Simpler Iterative Steady State Solution of Munch Pressure-Flow Systems Applied to Long and Short Translocation Paths*, Plant Physiol. **54** (1974), no. 4, 589–600.

[85] M. T. Tyree and M. H. Zimmermann, *Xylem structure and the ascent of sap*, Springer, 1983.

[86] C. Y. Wang, *Stokes flow through a thin screen with patterened holes*, AIChE **40** (2004), no. 3, 419–423.

[87] G. B. West and J. H. Brown, *The origin of allometric scaling laws in biology from genomes to ecosystems: towards a quantitative unifying theory of biological structure and organization*, Journal of Experimental Bioliology **208** (2005), no. 9, 1575–1592.

[88] T. D. Wheeler and A. D. Stroock, *The transpiration of water at negative pressures in a synthetic tree*, Nature **455** (2008), no. 7210, 208–212.

[89] C. W. Windt, F. J. Vergeldt, P. De Jager, and H. Van As, *MRI of long-distance water transport: a comparison of the phloem and xylem flow characteristics and dynamics in poplar, castor bean, tomato and tobacco*, Plant, Cell & Environment **29** (2006), no. 9, 1715–1729.

[90] D. York, *Least-squares fitting of a straight line*, Canadian Journal of Physics **44** (1966), no. 5, 1079–1086.